Synthesis, Functionalization and Characterization of Ultrasmall Hybrid Silica Nanoparticles for Theranostic Applications

Vu Long Tran

N°d'ordre NNT : xxx

THESE de DOCTORAT DE L'UNIVERSITE DE LYON

opérée au sein de

l'Université Claude Bernard Lyon 1

Ecole Doctorale de Chimie de Lyon
N° 206
Institut Lumière Matière, UMR5306

Spécialité de doctorat : Chimie de Nanomatériel
Discipline : Chimie

Soutenue publiquement le 22/02/2018, par :

Vu Long Tran

Synthesis, Functionalization and Characterization of Ultrasmall Hybrid Silica Nanoparticles for Theranostic Applications

---

Devant le jury composé de :

Lacombe Sandrine, Professeur, Université Paris Sud	Rapporteur
Subra Gilles, Professeur, Université de Montpellier	Rapporteur
Bégin-Colin Sylvie, Professeur, Université de Strasbourg	Examinateur
Roux Stéphane, Professeur, Université de Franche-Compté	Examinateur
Tillement Olivier, Professeur, Université Lyon 1	Directeur de thèse
Lux François, Maître de Conférences, HDR, Université Lyon 1	Co-directeur de thèse
Cédric Louis, Président de Nano-H S.A.S	Membre invité

UNIVERSITE CLAUDE BERNARD - LYON 1

Président de l'Université	**M. le Professeur Frédéric FLEURY**
Président du Conseil Académique	M. le Professeur Hamda BEN HADID
Vice-président du Conseil d'Administration	M. le Professeur Didier REVEL
Vice-président du Conseil Formation et Vie Universitaire	M. le Professeur Philippe CHEVALIER
Vice-président de la Commission Recherche	M. Fabrice VALLÉE
Directrice Générale des Services	Mme Dominique MARCHAND

COMPOSANTES SANTE

Faculté de Médecine Lyon Est – Claude Bernard	Directeur : M. le Professeur G.RODE
Faculté de Médecine et de Maïeutique Lyon Sud – Charles Mérieux	Directeur : Mme la Professeure C. BURILLON
Faculté d'Odontologie	Directeur : M. le Professeur D. BOURGEOIS
Institut des Sciences Pharmaceutiques et Biologiques	Directeur : Mme la Professeure C. VINCIGUERRA
Institut des Sciences et Techniques de la Réadaptation	Directeur : M. X. PERROT
Département de formation et Centre de Recherche en Biologie Humaine	Directeur : Mme la Professeure A-M. SCHOTT

COMPOSANTES ET DEPARTEMENTS DE SCIENCES ET TECHNOLOGIE

Faculté des Sciences et Technologies	Directeur : M. F. DE MARCHI
Département Biologie	Directeur : M. le Professeur F. THEVENARD
Département Chimie Biochimie	Directeur : Mme C. FELIX
Département GEP	Directeur : M. Hassan HAMMOURI
Département Informatique	Directeur : M. le Professeur S. AKKOUCHE
Département Mathématiques	Directeur : M. le Professeur G. TOMANOV
Département Mécanique	Directeur : M. le Professeur H. BEN HADID
Département Physique	Directeur : M. le Professeur J-C PLENET
UFR Sciences et Techniques des Activités Physiques et Sportives	Directeur : M. Y.VANPOULLE
Observatoire des Sciences de l'Univers de Lyon	Directeur : M. B. GUIDERDONI
Polytech Lyon	Directeur : M. le Professeur E.PERRIN
Ecole Supérieure de Chimie Physique Electronique	Directeur : M. G. PIGNAULT
Institut Universitaire de Technologie de Lyon 1	Directeur : M. le Professeur C. VITON
Ecole Supérieure du Professorat et de l'Education	Directeur : M. le Professeur A. MOUGNIOTTE
Institut de Science Financière et d'Assurances	Directeur : M. N. LEBOISNE

ACKNOWLEDGEMENT

The last three years was a very important part of my life. I have filled it with full of valuable scientific and life experiences thanks to the kind helps of surrounding people.

I would like to express my gratitude to my supervisors Prof. Olivier Tillement, Dr. François Lux and Dr. Cédric Louis for entrusting me with this exciting and important PhD project. Thank you for providing me with your experience, brilliant ideas, solutions and guidance when necessary. The works conducted in this thesis and the final manuscript will not be realized without your helps.

I also would like to thank all members of the jury Prof. Sandrine Lacombe, Prof. Gilles Subra, Prof. Sylvie Bégin-Colin and Prof. Stéphane Roux for spending time evaluating my thesis and helping me further optimize it. Your scientific reviews were crucial for completing this manuscript.

My gratefulness also goes to ARGENT Initial Training Network, Prof. Sandrine Lacombe, the coordinator of the program, Prof. Nigel Mason and all other members of the consortium for giving me the research funding, a variety of important scientific and soft-skills trainings and a wonderful friendly academic network.

I would like to gratefully acknowledge kind helps from different collaborators who were involved in the works described in this thesis Vivek Thakare, Frédéric Boschetti, Franck Denat, Bernard Fenet, Anne Baudouin, Clothilde Zerbino, Rodolphe Antoine, Natalie Mignet, Grégory Ramniceanu, Bich-Thuy Doan, Marc Janier, Jacqueline Sidi-Boudmedine, Jean-Michel Chezal, Elisabeth Miot-Noirault, Guillaume Sudre, Laurent David, Soraia Rosa, Karl Butterworth, Kevin Prise…

My sincere thanks also go to all members of FENNEC team Fabien R., Matteo M., Éloïse T., Arthur M., Shady K., Huong L.T., Marie P., Kevin L., Clélia M., Myléva D., Thomas B., Hélène G., Mahmoud O. M., Dalila N., Zhenhua L., Lionel M., Marie-Geneviève B… for different technical and quotidian assistances, scientific discussions, cultural and language lessons and especially a warm environment in the lab. Thanks all the interns that I had chances to work with Chayma Nouajaa, Mathilde Maillard and Marco Natuzzi for your helps in the syntheses, analyses and functionalizations of the particles. I have learned valuable things from every one of you.

Finally, I would like to thank my family, dad, mum and brother for their loves, guidance and supports. Especially, I will not be able to travel so far without my wife. Thank you for always standing beside me.

RÉSUMÉ

Les nanoparticules (NPs) hybrides peuvent combiner les propriétés physiques uniques des éléments inorganiques pour des applications en imagerie et en thérapeutique avec la biocompatibilité des structures organiques. Cependant, leur utilisation en médecine est encore limitée par des risques potentiels de toxicité à long terme. Dans ce contexte, des NPs hybrides ultrafines pouvant être éliminées rapidement par la voie rénale apparaissent comme de bonnes candidates pour la nanomédicine. La NP à base de silice contenant des chélates du gadolinium appelée AGuIX (Activation et Guidage de l'Irradiation par rayon-X) a été développée avec un diamètre hydrodynamique de moins de 5 nm qui lui permet d'être éliminée rapidement via l'urine après injection intraveineuse. Cette NP s'est révélée être une sonde efficace en imagerie multimodale et un amplificateur local en radiothérapie pour le diagnostic et le traitement du cancer. Elle est en train d'être évaluée dans un essai clinique de phase I par radiothérapie des métastases cérébrales (NANO-RAD, NCT02820454). Néanmoins, la synthèse d'AGuIX est un procédé multi-étapes qui est difficilement modulable.

Ce manuscrit rapporte, pour la première fois, le développement d'un protocole « one-pot » direct pour des nanoparticules de silice ultrafines (USNP) contenant des chélateurs complexés ou non à partir des précurseurs silanes chélatants moléculaires. Dans ce nouveau protocole, la taille des particules et les types des métaux chélatés peuvent être contrôlés facilement. Certaines des propriétés chimiques des USNP ont été clarifiées davantage pendant ce travail exploratoire. Les particules élaborées ont été caractérisées par différentes techniques analytiques complémentaires. Ces nouvelles nanoparticules USNPs présentent des caractéristiques similaires aux AGuIX en terms de propriétes biologiques et de biodistribution.

Dans un second temps, un nouveau protocole de fonctionnalisation d'USNP par des précurseurs silanes chélatants a été développé. Ces chélatants libres fonctionnalisés sur la particule peuvent être alors utilisés afin de complexer des radiométaux pour l'imagerie bimodale. Enfin, d'autres stratégies de fonctionnalisation sont aussi décrites. La nouvelle sonde (17VTh031) combinant un petit chélateur cyclique (NODA) et un fluorophore proche-infrarouge tumeur ciblant (IR783) ainsi que le pyridinium quaternaire ont été greffés sur l'AGuIX pour créer une nouvelle sonde en imagerie multimodale et cibler des tumeurs chondrosarcomes respectivement.

Mots-clés : *nanoparticule de silice ultrafine, cancer, sonde en imagerie multimodale, radiosensibilisateur*

ABSTRACT

Hybrid nanoparticles (NPs) can combine unique physical properties for imaging and therapeutic applications of inorganic elements in bio-friendly organic structures. However, their uses in medicine are limited by the potential risks of long-term toxicities. In this context, ultrasmall renal clearable NPs appear as novel solutions. Silica based NP displaying gadolinium chelates named AGuIX (Activation and Guidance for Irradiation by X-ray) has been developed to have hydrodynamic diameter less than 5 nm which allows rapid elimination through urine after intravenous injection. This NP has been demonstrated as an efficient multimodal imaging probe and a local enhancer for radiotherapy for cancer diagnostics and treatment. It is now being evaluated in a phase I clinical trial by radiotherapy of cerebral metastases (NANO-RAD NCT02820454). Nevertheless, the synthesis of AGuIX implies a multisteps process that can be further improved.

This manuscript shows, for the first time, the development of a straightforward one-pot protocol for ultrasmall silica nanoparticles (USNP) containing complexed or non-complexed chelators from molecular chelating silane precursors. In this new protocol, the size of particle and types of metals can be easily tuned. The chemical properties of USNP have been further clarified during this exploratory work. The produced particles have been characterized by different complimentary analytical techniques. These new nanoparticles USNPs show similar characteristics to AGuIX in terms of biological properties and biodistribution.

Secondly, a new protocol of functionalization for USNP by chelating silane precursors has been developed. These functionalized free chelators on the particle can be used then to complex radiometals for bimodal imaging applications. Finally, other functionalization strategies have also been described. New probe (17VTh031) combining small cyclic chelator (NODA) and tumor targeting near-infrared fluorophore (IR783) as well as quaternary pyridinium have been grafted on AGuIX for creating new multimodal imaging probe and targeting chondrosarcoma tumors respectively.

Keywords: *ultrasmall silica nanoparticle, cancer, multimodal imaging probe, radiosensitizer*

CONTENTS

LIST OF FIGURES

LIST OF TABLES

ABBREVIATIONS

A

ACN: acetonitrile

AGuIX: Activation and Guidance for Irradiation by X-ray

APTES: aminopropyl triethoxysilane

Au: gold

B

BSA: bovine serum albumin

Bi: bismuth

C

CEST: carboxyethylsilanetriol

CT: X-ray computed tomography

Cu: copper

D

D: diffusion coefficient

D_2O: deuterium oxide

DEG: diethylene glycol

DFO: desferoxamine

D_H: hydrodynamic diameter

DLS: dynamic light scattering

DMSO: dimethyl sulfoxide

DOSY: diffusion ordered spectroscopy

DOTA: 1,4,7,10-tetraazacyclododecane-1,4,7,10-tetraacetic acid

DOTAGA: 1,4,7,10-tetraazacyclododecane-1-glutaric acid-4,7,10-tetraacetic acid

DTPA: diethylenetriaminepentaacetic acid

E

EBT: Eriochrome Black T

ECM: extracellular matrix

EPR: enhanced permeation and retention

EPRS: electron paramagnetic resonance spectroscopy

ESI: electrospray ionization

Eu: europium

F

F: fluorine

FDA: Food and Drug Administration

FTIR: Fourrier transformed infra-red

FWHM: full width at half maximum

G

Ga: gallium

GAG: glycosaminoglycan

Gd: gadolinium

GMP: good manufacturing practice

GSH: thiolated glutathione

H

HBTU: 2-(1H-benzotriazol-1-yl)-1,1,3,3-tetramethyluronium hexafluorophosphate

HfO_2: hafnium oxide

Ho: holmium

HPLC: high performance liquid chromatography

I

I: iodine

ICP-OES: inductively-coupled plasma optical emission spectroscopy

ID: injected dose

In: indium

IR: infrared spectroscopy

IT: intratumoral

IV: intravenous

L

Lu: lutetium

M

MCA: multiplicative correlation algorithm

MRI: magnetic resonance imaging

MS: mass spectrometry

MPS: mononuclear phagocytic system

Mn: manganese

MWCO: molecular weight cut-off

N

NHS: *N*-hydroxysuccinimide

NIR: near-infrared

NMR: nuclear magnetic resonance

NSF: nephrogenic systemic fibrosis

NODAGA: 1,4,7-triazacyclononane,1-glutaric acid-4,7-diacetic acid

NOTA: 1,4,7-triazacyclononane,1,4,7-triacetic acid

NP: nanoparticle

O

OI: optical imaging

P

PET: positron emission tomography

PEG: polyethylene glycol

PG: proteoglycan

Pi: post-injection

Pt: platinum

Q

QA: quaternary ammonium (pyridinium)

QC: quality control

R

r_1: longitudinal molar relaxivity

r_2: transverse molar relaxivity

R_g: radius of gyration

RS: radiosensitizing/radiosensitization

RT: radiotherapy

rt: room temperature

S

SAXS: small angle X-ray scattering

SCN: isothiocyanate

SEC: size exclusion chromatography

Si: silicon

SNP: silica nanoparticle

SPECT: single photon emission tomography

SQUID: superconducting quantum interference device

T

TANED: triacetic acid N-(trimethoxysilylpropyl)ethylenediamine

Tb: terbium

Tc: technetium

TEM: transmission electron microscopy

TEOS: tetraethyl orthosilicate

TFA: trifluoroacetic acid

Ti: titanium

TOF: time of flight

t_R: retention time in chromatogram

U

UNP: ultrasmall nanoparticle

USNP: ultrasmall silica nanoparticle

UV : ultraviolet

Y

Y : yttrium

Z

Zr: zirconium

GENERAL INTRODUCTION

Nanoparticles (NPs) for medical applications are exciting research topics. They are objects in the range of 1 nm – 1 μm that have different physical, chemical or biological properties from single, small molecules or bulk materials. Over the last three decades, some NPs have been translated from laboratory researches to real clinical applications. Few have even successfully reached the market, for example, DOXIL liposome.[1] Among different types of NPs that have been studied, hybrid NPs containing both inorganic and organic materials are often of particular interest. They allow exploiting unique physical properties of inorganic materials in optics, magnetism, electronics etc. while avoiding the potential toxicity of these materials towards biological objects thanks to biocompatibility and versatility of organic materials.[2,3] One of novel properties of hybrid NPs that recently attracted much attention is the radiosensitizing (RS) effect.[4,5] This is the ability of NPs containing heavy inorganic elements to increase locally the dose of radiotherapy, one of main pillars of standard cancer treatment along with surgery and chemotherapy.[6–8] One of the most successful examples might be hafnium oxide NPs (NBTXR3) which is now under clinical investigation.[1,9] This concept can become the basis for a new generation of radiotherapy with higher specificity and efficacy. Nevertheless, such NPs are still mainly introduced by local injection to the tumors. Meanwhile, the intravenous administration of hybrid NPs into human body as a systemic treatment is still challenging because they tend to be trapped inside critical organs and imply potential long term toxicity. Researchers have shown that in order for the particles to fully escape this phenomenon, they need to have an ultrasmall hydrodynamic diameter (D_H < 10 nm) without interaction with biomolecules to pass freely through renal membrane.[10–15] This criterion opens a very new field of designing ultrasmall, renal clearable NPs.[3,12] This task is not easy to achieve since very few methods and materials have been reported to give such range of D_H (1 – 10 nm). For the last ten years, our team has developed a top-down method to synthesize ultrasmall (3 – 5 nm) silica NPs, AGuIX, containing gadolinium (Gd) chelates. This NP has been demonstrated as a good sensitizing agent for radiotherapy and imaging agent for multimodal imaging combining magnetic resonance imaging (MRI), radioimaging or optical imaging. However, the synthesis of AGuIX implies a complicated multi-step process that does not allow free control over the particle composition. In this thesis, we explored, for the first time, the feasibility of obtaining ultrasmall silica NPs containing free chelators with one-pot bottom-up method. We have shown that a bulky chelating silane is a key component for this type of synthesis. This method can be easily tuned to produce NPs having different D_H from 3 to 14 nm which are able to chelate different metals at will after being formed. Sophisticated analytical techniques such as small angle X-ray scattering (SAXS), nuclear magnetic resonance (NMR), mass spectrometry (MS) etc. have also been adapted to study the nanostructure of AGuIX and/or new NPs. The possibility of achieving intermediate NPs having only free chelators allowed unprecedented direct investigations by NMR. New particle complexing Gd has been demonstrated as a good contrast agent for magnetic resonance imaging (MRI) in *in vivo* colorectal cancer model. It appeared to maintain favorable biodistribution profile of AGuIX: sufficiently accumulate in the tumors, rapidly escape liver entrapment and efficiently clear out of animal bodies through kidneys.. In the second part of the thesis, different functionalization strategies have been performed on AGuIX to obtain additional properties. First, we have shown that by using chelating silane we can easily functionalize AGuIX with different chelators which are suitable for different metals.

These functionalized NPs can be used as multimodal imaging agent combining MRI with radioimaging by complexing different radionuclides. This possibility has been demonstrated by functionalizing AGuIX with a NODAGA-silane in order to complex specifically ^{64}Cu for positron emission tomography (PET). The new radiolabeled NP is being evaluated by both MRI and PET for their biodistribution in biological cancer models. This method is easy to perform without the need of any additional agents. The chelating silane is also much more stable than classical bioconjugating agents which are often susceptible to hydrolysis over time. Second, AGuIX has been functionalized with a bimodal agent containing NODAGA chelator and a novel near infrared tumor targeting fluorophore (IR783 derivative) to produce a trimodal imaging agent which can be visualized in both MRI, PET and optical imaging. Last but not least, a new strategy for functionalizing quaternary pyridinium on AGuIX has been realized to target tissues rich in extracellular matrix such as cartilages or chondrosarcoma tumors. *In vitro* and *in vivo* experiments are being conducted to evaluate the biodistribution of the ^{111}In labeled functionalized AGuIX by single photon emission tomography (SPECT) and its RS property in chondrosarcoma tumor bearing mice. In conclusion, this thesis contributed to the understanding of nanochemistry underlying ultrasmall silica NPs such as AGuIX, facilitate the future mass production and provide unprecedented structural information of the particle. Our works also elaborate a high flexibility of AGuIX for functionalizing different modalities for cancer imaging and treatment. Especially, the possibility of using silanes for functionalization is an original and direct strategy that can be further developed for other types of ligands.

CHAPTER 1

Ultrasmall hybrid (inorganic/organic) nanoparticles for improving radiotherapy

Chapter 1. Ultrasmall hybrid (inorganic/organic) nanoparticles for improving radiotherapy

1.1. Hybrid nanoparticles (NPs) in cancerology

1.1.1. Advantages of NPs over molecular agents

In the last two decades, the achievements in nanotechnology allow the fabrication and characterization of a lot of nanostructures having the size in nanometric scale (10^{-9} m). They are commonly referred as nanoparticles. These nanostructures become great research topics for future medicine as they can offer several original advantages compared to molecular agents[1,16]:

- The ability to protect, deliver and release a large amount of active molecules to some specific sites based on the chemical design of the nanoparticles;

- The possibility of combining different elements, such as active molecules, functionalized groups or imaging probes, in only one object;

- The ability to target specifically the cancerous tumors thanks to the EPR effect "Enhanced Permeability and Retention", which is the tendency of nanoparticles to accumulate in the tumors rather than in normal tissues[17];

- The optical, thermal, magnetic and electronic properties of nanomaterials induced by their nanometric sizes.

1.1.2. Special properties of hybrid NPs

NPs can be constructed from a wide variety of materials and have a wide range of size (Figure 1-1-A). Among different types of particles, hybrid NPs attract a lot of interests by combining the properties of organic and inorganic materials. Organic materials are certainly important for creating biocompatible interface and chemical versatility but it is the inorganic materials in hybrid NPs which provide unique physical properties for biomedical applications. Some typical examples can be pointed out below (Figure 1-1-B).

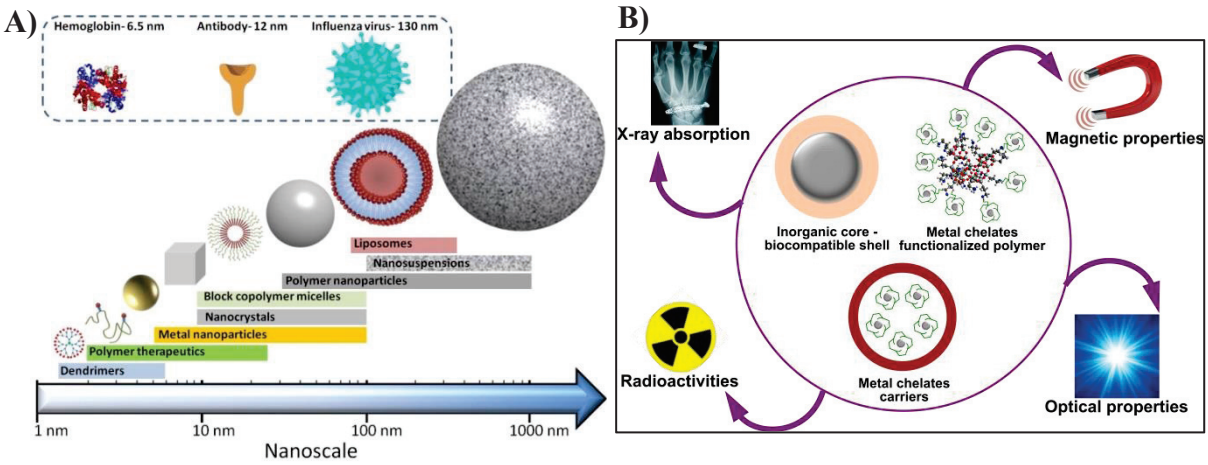

Figure 1-1. A) Different types of nanomedicines and their approximate ranges of sizes. Image taken from www.britishsocietynanomedicine.org; B) Common hybrid nanostructures and their main physical properties.

1.1.2.1. X-ray absorption

Elements with high Z numbers i.e. Au (Z = 79), Pt (Z = 78), Hf (Z = 72), Gd (Z = 64), I (Z = 53), Ba (Z = 56), Bi (Z = 83) etc. are known for their high X-ray attenuation coefficients. This is the basic rationale for their uses as sensitizers for radiotherapy or contrast agents in X-ray computed tomography (CT).[18–23]

1.1.2.2. Magnetic property

Paramagnetic metals such as Gd or Mn can work as efficient positive contrast agents for magnetic resonance imaging (MRI). On the other hand, iron oxide NPs under certain size are found to have superparamagnetic property which can be exploited as negative contrast agents for MRI, targeted drug carriers or heat source for magnetic hyperthermal therapy as a new cancer treatment.[2,24]

1.1.2.3. Optical property

Lanthanide metals i.e. Eu, Tb etc. are extensively studied as imaging probes thanks to their persistent luminescence. Gold nanoclusters also have special luminescent property that could be used for detecting them. Surface plasmon resonance induced on gold NPs after being excited by laser is another interesting heat source for photothermal therapy. Semiconducting NPs made from elements such as Cd, Se, Zn, S etc. (quantum dots) have persistent fluorescence with different wavelengths depending on their sizes. Complexes of macromolecules with metals such as Ru, Pd etc. have been investigated as photosensitizers for photodynamic therapy in cancer treatment.[2,25–27]

1.1.2.4. Radioactivity

Another interesting property that inorganic materials can offer is radioactivity that is extremely useful for both imaging and therapeutic purposes. In complement with common organic compounds containing ^{18}F, ^{123}I, ^{131}I or ^{11}C, inorganic elements provide more options with different emitted particles meaning different energies and penetration lengths as well as different half-lifes which are suitable for a wide range of applications (

Table 1-1). For example, ^{68}Ga, ^{64}Cu, ^{89}Zr, ^{99m}Tc, ^{111}In, ^{67}Ga are some typical radioisotopes for radioimaging while ^{90}Y, ^{177}Lu and ^{223}Ra are among mostly used radiopharmaceuticals for different diseases.[28,29]

Table 1-1. Common radionuclides used in medicine.

Type of chemistry	Isotope	Main emitted particle	Penetration length	Emax (keV)	Percentage of emission (%)	$\tau_{1/2}$	Application
Organic	^{11}C	β+ (then γ)	No limit	385	99.8	20 min	PET
	^{18}F	β+ (then γ)	No limit	250	97	1.83 h	PET
	^{123}I	γ	No limit	159	84	13.2 h	SPECT
	^{131}I	β- γ	Few mm No limit	606 364	90 82	8 days	SPECT + therapy in thyroid diseases
Inorganic	^{64}Cu	β+ (then γ)	No limit	653	17.8	12.7 h	PET
	^{67}Ga	γ	No limit	185 93 9	21 39 55	78 h	SPECT
	^{68}Ga	β+ (then γ)	No limit	1920	89	68 min	PET
	^{89}Zr	β+ (then γ)	No limit	396	23	78.4 h	PET

	^{99m}Tc	γ	No limit	140	88	6 h	SPECT
	^{111}In	γ	No limit	171 245	90 94	68 h	SPECT
	^{90}Y	β-	Few mm	2280	100	64 h	Therapy in different cancers
	^{177}Lu	β- γ	Few mm No limit	497 208	78.6 11	6.6 days	SPECT + therapy in endocrinology
	^{223}Ra	α^{2+}	50 – 100 µm	5780	93.5	11.4 days	Therapy for bone metastasis

1.1.3. Some examples of hybrid NPs used for cancerology in clinics

Until now, some hybrid NPs have been approved for being used in clinics or being tested in ongoing clinical trials (Table 1-2). Iron oxide nanoparticles (Fe_xO_yNPs) are the earliest candidates that were translated to clinical uses. Ferristene and Ferumoxsil are approved as oral contrast agents for imaging gastrointestinal tract. Ferumoxtran-10 (different phase III clinical trials) and Sienna+ (approved in Europe, different phase III trials in the US are being planned) are being developed as intravenous contrast agents for lymph node imaging in cancer diagnoses. MFL AS1 is being tested in a phase II trial in Germany as intravenous agent for hyperthermia therapy in glioblastoma. Gold nanoparticles (AuNPs) have also been extensively studied. Two AuNPs are being investigated in clinical trials for cancer treatments. CYT-6091 has completed phase I trial and is being planned for a phase II trial as a nanocarrier of biopharmaceutics such as tumor necrosis factor α (TNFα) while Auroshell is being investigated in different phase I and II studies as a hyperthermia agent for tumor destruction by laser ablation. Hafnium oxide (HfO_2NP) is another material that is under development for clinical application. NBTXR3 or PEP503 is being studied as RS agent for radiotherapy in several different phase I-II trials. Finally, silica represents another highly potential type of NPs. Among them, C-dot silica NP is under investigation in a phase I study as an intraoperative imaging agent.

Table 1-2. Summary of hybrid NPs used in clinics or under clinical development

Type of NP	Structure	Brandname	Mechanism of action	Indication	Status	Ref.
Iron oxide	10 – 20 nm iron oxide core with dextran coating	Ferumoxtran-10 (Combidex®)	Contrast agent	Lymph node imaging in prostate cancer Or rectal and breast cancer	Phase III: recruiting NCT03223064 NCT02751606	[30]
	Iron oxide core with dextran coating	Sienna+®	Similar	Lymph node imaging	Europe: approved USA: investigational use only (FDA-approved IDE)	[31–33]
	12 nm iron oxide core with aminosilane coating	MFL AS1 Nanotherm® AS1	Hyperthermia based on superparamagnetism (magnetic ablation)	Recurrent glioblastoma multiforme	Phase II: (MF1001) DRKS00005476 (German Clinical Trial)	[34]
	300 nm aggregate of 10 nm iron oxide crystals with siloxane coating	AMI-121 Ferumoxsil Gastromark®	Oral contrast agent	Imaging of upper gastrointestinal tract Imaging of rectum and pelvic organs	FDA approval Phase III: completed	[35,36]
	300 nm of iron oxide NPs coated with polystyrene resin	Ferristene Abdoscan®	Oral contrast agent	Imaging of gastrointestinal tract and pelvic organs	Approved in Sweden Discontinued	[37–39]
	20 – 30 nm of iron oxide NPs coated with polyglucose sorbitol carboxymethyl ether	Ferumoxytol Feraheme®, Rienso®	Carrier of supplemental iron	Parenteral injection for chronic anemia in patients with chronic kidney disease	FDA approval EMA approval	[40–43]
Gold	30 nm Au core with PEG-SH and TNFα coating	CYT-6091 (Aurimune®)	Delivery of cytotoxic agent TNFα	Advanced solid tumors Patients undergoing surgery for primary or metastatic cancers	Phase I: completed NCT00356980 NCT00436410 Phase II: planning	[44–46]

	120 nm silica core with 10 – 20 nm gold coating	Auroshell®	Hyperthermia based on surface plasmon resonance (laser ablation)	Refractory and/or Recurrent Tumors of the Head and Neck MRI/US guided laser therapy for prostate neoplasm	Phase I-II: completed NCT00848042 Phase I: recruiting NCT02680535	[47–49]
Hafnium oxide	50 nm HfO_2 crystals coated by trimetaphosphate	NBTXR3® PEP503®	Intratumoral or intra-arterial injection for radiosensitization	Soft tissue sarcoma Head and neck cancer Head and neck cancer in combination with cisplatin Liver cancer Prostate Cancer Rectal cancer in combination with 5-fluorouracil and capecitabine	Phase II-III: recruiting NCT02379845 Phase I: recruiting NCT01946867 Phase I-II: recruiting NCT02901483 Phase I-II: recruiting NCT02721056 Phase I-II: recruiting NCT02805894 Phase I-II: recruiting NCT02465593	[9,50–52]
Silica	7 nm silica core contained Cy5.5 functionalized by PEG silane and cRGDY peptide	C-dot	Bimodal (PET/optical) imaging agent	Image-Guided Intraoperative Sentinel Lymph Node Mapping in Head and Neck, Melanoma, Breast and Gynecologic Malignancies	Phase I: recruiting NCT02106598	[53–55]

1.1.4. Current limitations and directions for development of hybrid NPs for cancerology

1.1.4.1. Biocompatibility requirement of hybrid NPs

There is clearly a gap between the number of publications in hybrid nanoparticle research and the number of particles that are really transferred to clinical phase of development. This can be easily understood as due to the concerns regarding to the potential toxicity of inorganic materials which are not usually present in human body. Therefore, the first and foremost criteria for translatable hybrid NPs must be their biocompatibility. That explains why only NPs made from iron oxide, gold, hafnium oxide and silica are among the first to be accepted. Iron is present abundantly in human body and its metabolism is guaranteed by different mechanisms. Meanwhile, silica, gold and hafnium oxide are proven as inert and biocompatible in different studies.[9,21,56] Otherwise, inorganic materials require a biocompatible and stable coating. This can be achieved by the development of novel chelators and surface chemistry. In *in vitro* tests, these solutions have proven to be efficient. Nevertheless, in living animals, the difference in intravenous pharmacokinetics of nanomaterials compared to molecular agents creates another barrier for using NPs in the clinics.

1.1.4.2. Pharmacokinetic requirements of hybrid NPs

Intravenous injection appears to be the first ideal route to introduce a medicine in human body since it allows systemic distribution and deep penetration to most of disease sites. However, it also implies numerous potential interactions between medicines with biological species in human body. Thus, thorough pharmacokinetic studies of intravenous medicine are usually required to understand carefully their behaviors in *in vivo* and in patients before they can be accepted.

It was demonstrated that the pharmacokinetic profiles of nanomaterials are quite different from traditional small molecules. From the 1990s, during the development of very first generation of nanomedicine i.e. liposomal and protein drug carriers such as Doxil or Abraxane, researchers have started to realize the difference in pharmacokinetic behaviors of NPs. Since then, more and more researches have been conducted to further explain the interaction between nanomaterials and biological species in human body. Now, it is well

known that most NPs are highly prone to be captured in liver, spleen, lung, lymph nodes or bone marrows. These NPs will be excreted mainly through liver, then bile and then feces. This situation implies two main disadvantages: 1) the risks of long-term toxicity and 2) the interference with other diagnoses and treatments.[3,10,12]

Long-term toxicity of NPs can appear when the coating layers lose their stability gradually. This is firstly because of longer residence time of the particles in an organ. Secondly, particles will have to go through the intracellular enzymatic degradation inside hepatocytes which can possibly dissolves or fractures their biocompatible coatings or chelators and releases the toxic metals such as Cd, Se in quantum dots; Gd, Mn in MRI nano contrast agents or other lanthanides in luminescent NPs.

Hepatobiliary excretion also possibly affects the results of other biomedical tests or slows down the re-administration of the next dose of NPs. This is because hepatic clearance is a very slow process combining several complicated metabolic sub-processes.

To overcome this problem, it is necessary to design renally excretable NPs since renal clearance seems to be the most efficient mechanism to quickly and completely eliminate NPs from human body. Studies conducted on the physiology of kidney and renal clearance of macromolecules show that glomerular basement membrane in the kidneys only allows molecules under certain size to pass. Molecules with $D_H < 6$ nm might be filtered rapidly without depending on their charges, while molecules with $D_H > 8$ nm have the tendency to remain in the circulation. Finally, molecules with D_H in the range of 6 – 8 nm might also be filtered, but their rates of filtration are dependent on their surface charges. Negative molecules in this size range tend to stay longer compared to positive counterparts due to electrostatic repulsion of glomerular basement membrane (Figure 1-2).[57,58] This is recently confirmed in a study carried out by Choi *et al.* They have shown that quantum dot particles having an average *in vivo* hydrodynamic diameter (D_H) less than 6 nm can be quickly and effectively eliminated via renal clearance.[10] It is worth noting that the diameters of particles in these studies can vary slightly depending on the methods and instruments that have been used to measure them. Besides size threshold, opsonization of serum proteins on the surface of the particles is also an important factor. NPs either too positively or too negatively charged can induce severe serum proteins adsorption which would eventually make the physiological size of the particles well above the threshold of the renal clearance and facilitate the subsequent capture by mononuclear phagocytic system (MPS).[3,59,60]

All of these studies point out the criteria to obtain renal clearable NPs: 1) they should be ultrasmall (the limit of D_H can vary depending on each study but, as a rule of thumb, a $D_H <$ 10 nm is usually accepted) and 2) they should be able to avoid serum protein adsorption. For the latter, even though ultrasmall NPs have been demonstrated as having much less interaction with serum proteins, appropriate coatings are still necessary. Researchers have introduced different types of biocompatible coatings to prevent the opsonization. The two strategies that provide most promising results are to coat NPs by very hydrophilic ligands or zwitterionic ligands. The former has been mostly done by the introduction of medium size polyethylene glycol (PEG) polymer chains to create an adsorbed water layer preventing protein contacts (stealth effect). The zwitterionic coating has been realized by using amino acids or a combination of positive and negative ligands to distribute charges homogenously on

the surface of the particles. This surface design somehow also efficiently prevents the opsonization.[10,12,61–64] Zwitterionic coatings seem to even show more advantages compared to PEGylated coatings since it does not increase significantly the size of the particles and the viscosity of the colloidal solutions. Hence, it allows deeper and more homogeneous tissue penetration.[12,62]

On the other hand, ultrasmall nanoparticles (UNPs) seem to be better choices compared to bigger counterparts for imaging applications. This is due to their fast accumulation in tumor sites; deeper and more homogenous tissue penetration and rapid escape from non-targeted tissues. All of these properties enable a faster imaging time point after the injection of probes and higher signal-to-background ratio.[3]

In the next part, different examples of hybrid UNPs will be introduced. The focus will be on NPs used to improve radiotherapy in cancer treatment.

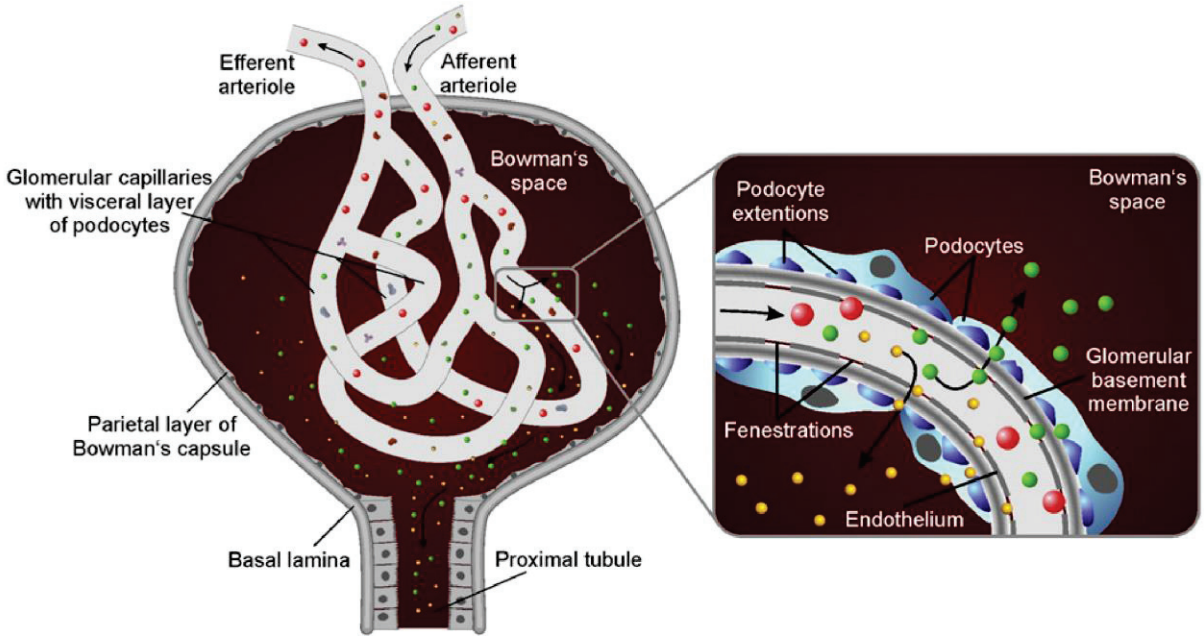

Figure 1-2. Schematic representation of renal clearance of ultrasmall NPs. Yellow spheres are NPs with D_H < 6 nm, green ones are NPs with D_H in 6 – 8 nm and red ones are NPs with D_H > 8 nm.[3]

1.2. Hybrid NPs for improving radiotherapy (RT)

1.2.1. Hybrid NPs as radiosensitizers

1.2.1.1. RT in cancerology

Cancer is one of the most challenging health problems in our time. It accounts for more than 8 million deaths, 14 million new cases globally in 2013 and enormous social and economic burden for modern society. More importantly, the trend is still going up as predicted by many reports.[65–67] Among different treatment options of cancer today, radiotherapy remains a principal modality that is used in 50 – 60% of cancer patients as single treatment or most often in combination with other treatments. Radiotherapy implies the use of ionizing radiations to destroy the cancerous cells in the tumors. However, the irradiation can also damage the normal tissues surrounding the tumors. In recent years, technological advancement has been made in the design of instrumentations to improve beam shaping. The

appearance of 3D conformal RT techniques such as intensity modulated RT (IMRT), image-guided RT (IGRT), stereotactic RT (SRT) or robotic RT allow more and more precise dose delivery. However, side effects still limits the therapeutic windows of RT.[68–70] Two of latest strategies that have been introduced to overcome the side effects include 1) using hadrons i.e. protons, neutrons… or heavy ions e.g. carbon, helium… instead of conventional photons or 2) using radiosensitizers to enhance locally the delivered dose within the tumors.[6,69,71]

In this context, ARGENT, which stands for **A**dvanced **R**adiotherapy **G**enerated by **E**xploiting **N**anoprocesses and **T**echnologies, was initiated as a Marie Curie European project in 2014 to coordinate international efforts in this two research directions (Figure 1-3).[72] The study carried out in this thesis is also part of this consortium. Our laboratory and other members of ARGENT have designed different highly promising UNPs for this application which will be discussed along with other NPs in the next sections.

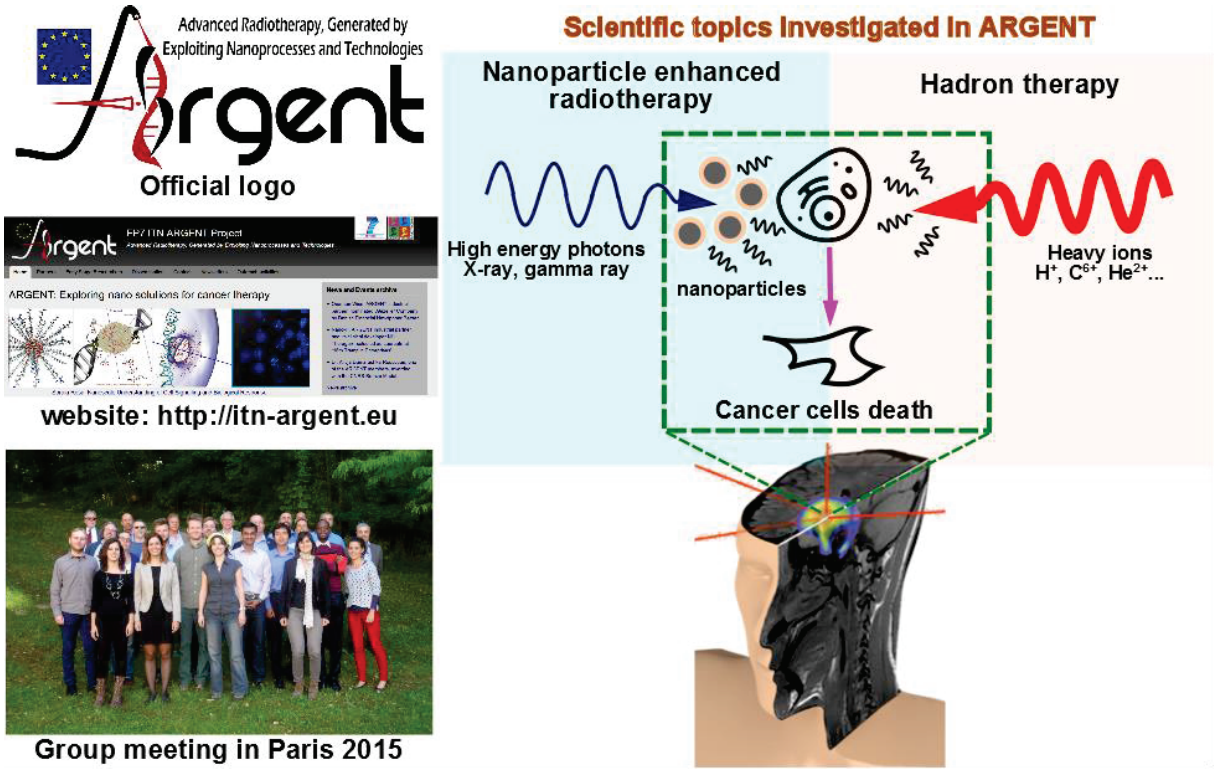

Figure 1-3. Some information about FP7 ITN ARGENT Marie Curie project.

1.2.1.2. Principles of radiosensitization (RS) using heavy metals

Starting from the pioneering work of Hainfeld J.F. *et al.* and Sanche L. *et al.* using gold nanoparticles,[4,5] many researches have reported the enhancement effect of metals with high Z number in nanoparticle form for both conventional X-ray radiotherapy and hadron/heavy ions therapy. The mechanism of action of these high-Z metal based nanomaterials is still not well understood. However, there are at least three main explanations for physical, chemical and biological aspects respectively. In physical point of view, the first attempt to explain the radiosensitization effect of heavy metals focuses on their high attenuation coefficient for ionizing irradiations compared to normal tissues. For example, Figure 1-4 shows the attenuation coefficient for photons of gadolinium and water.[73] Similar graphs can also be found with other high-Z elements. This implies that more energy will be retained by heavy metals after an irradiation compared to normal tissues that contain mainly water.

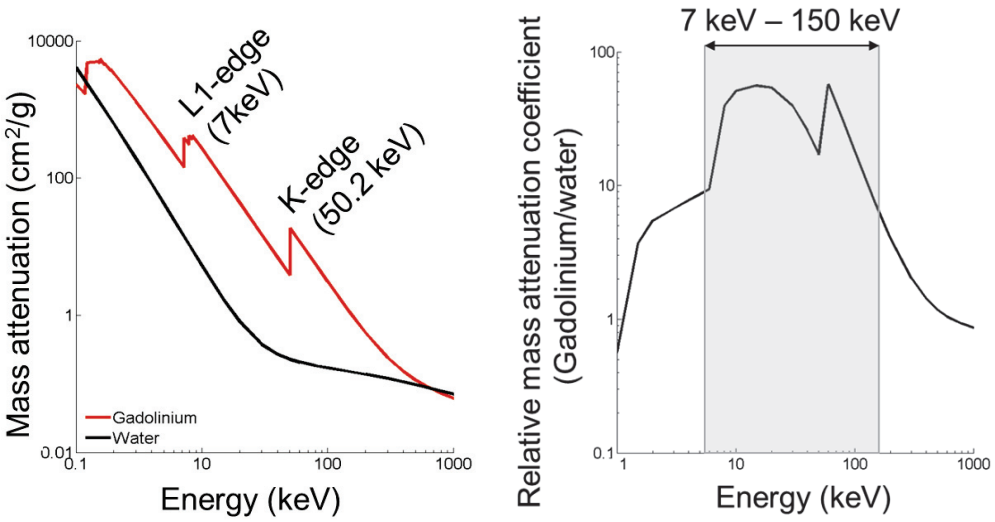

Figure 1-4. Comparison of the photon mass attenuation coefficients of gadolinium and soft tissue. Data taken from Hubbell and Seltzer.[73]

Afterwards, the energy will be released in different forms (Figure 1-5-A) in which the most relevant for the enhancement of ionizing effect are Compton and Auger electrons due to their ionizing power.[6] Nevertheless, this disparity of total absorption can only be observed in the range of few to hundreds keV of energy. So this fails to explain the RS effects of NPs reported sometimes at MeV with clinical accelerators. Hence, Mc Mahon *et al.* came up with another model suggesting a super high local amplification of energy around the NPs created by a cascade of Auger electrons started from the excited NPs (Figure 1-5-B). They reasoned that the ultrasmall size of a NP might be a critical parameter because the very first Auger electrons ejected from an ionizing event cannot travel further than tens of nanometers. Hence, more Auger electrons will be released if the sizes of the particles are smaller.[22,74,75] Furthermore, some authors have also shown that a thick organic coating layer can also absorb more these photoelectrons.[21]

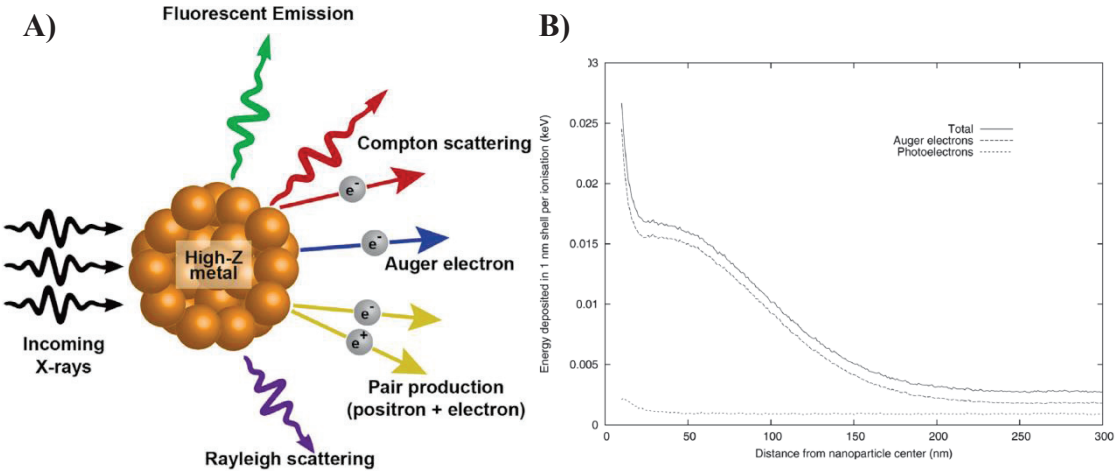

Figure 1-5. A) Different events that can occur after the irradiation of high-Z material nanoparticles by X-ray.[6] B) Simulation of average energy deposit in the vicinity of a 20 nm gold NP after a single ionising event by a 40 keV photon.[22]

In chemical point of view, the formation of reactive oxygen species (ROS) can also play a very important role in killing effect of irradiation. Some studies have shown the significance of this process to the RS efficiency of gadolinium based NPs.[76,77] Meanwhile, in biological point of view, the radiation induced bystander effect (RIBE) could be another explanation.

This is the indirect effects of irradiation to different cellular signaling pathways which somehow lead to cell death in even non-irradiated regions.[78,79] To certain extents, all of these mechanisms may contribute to the observed RS effect of high-Z metal NPs.

1.2.1.3. Some promising hybrid nanosensitizers

Numerous NPs have been studied for RS property in the last couple of decades. The purpose of this section will be only to introduce some of the most high-profile candidates in this field which might be translated to clinical uses in a near future or have a game-changing potential.

1.2.1.3.1. Gold NPs

Owing to many exciting characteristics, gold NPs (AuNPs) always appear as one of the best examples for RS applications. Obviously, Au has a very high Z number (Z = 79) which guarantees a significant enhancement effect upon interacting with ionizing sources. Furthermore, gold has high biocompatibility and AuNPs can be synthesized with the tunable sizes from 2 – 200 nm as well as stably functionalized with a wide variety of commercially available thiolated ligands.[21,80] However, despite the fact that, most of *in vitro* and *in vivo* researches on NP-enhanced radiotherapy were conducted using AuNPs, no clinical test has been carried out or planned for this application.[1] But at least some AuNPs i.e. CYT-6091 (Aurimune) or AuroShell have proceeded to clinical trials as a drug nanocarrier or hyperthermia agent respectively as we have seen previously (Table 1-2). This shows the high potential of clinical translation for AuNPs.[46,81] The main hindrance is still the possible toxicity of AuNPs even though gold was shown to be an inert material. Indeed, some studies have shown toxic behaviors of AuNPs depending on their physical size, coating and interaction with biological objects in the bodies of humans or animals.[21,82] Nevertheless, some promising ultrasmall AuNPs have shown encouraging results in *in vivo* studies. Roux S. *et al.* have developed a series of ultrasmall AuNPs coated by chelators such as thiol derivatives of DTPA or DOTA with average hydrodynamic size (D_H) around 6 – 8 nm. The layers of chelators were used not only to stabilize AuNPs but also to complex with gadolinium or radioisotopes later on for imaging purposes with MRI or radioimaging. These formulations showed quite favorable renal clearance and significant enhancement of radiotherapy which promise their potential use (Figure 1-6-A).[23,83,84] Recently, Grellet S. *et al.* have used AuNP functionalized with different types of sugars and PEG amine (D_H ~ 4 – 7 nm) produced by Midatech Pharma (Oxford, UK) to show selective cytotoxicity and RS effects on a variety of cancer cell lines.[85] *In vivo* experiments have not been done to show their biodistribution or therapeutic properties. The researches conducted with these two above ultrasmall AuNPs were supported in the framework of ARGENT project. In another study done by Xie J. *et al.*, gold nanoclusters coated by glutathione (GSH) were synthesized with a reported average D_H around 3 nm. This formulation was shown to be quickly eliminated via mainly renal clearance and have a high RS effect.[86] Meanwhile, Liu J. et al. have synthesized a targeting-peptide functionalized gold nanocluster with D_H ~ 3 nm to target specifically mitochondria in breast cancer cells MCF7 and demonstrate stronger RS effect compared to control-peptide functionalized cluster.[87] *In vivo* studies have not been reported yet for this NP.

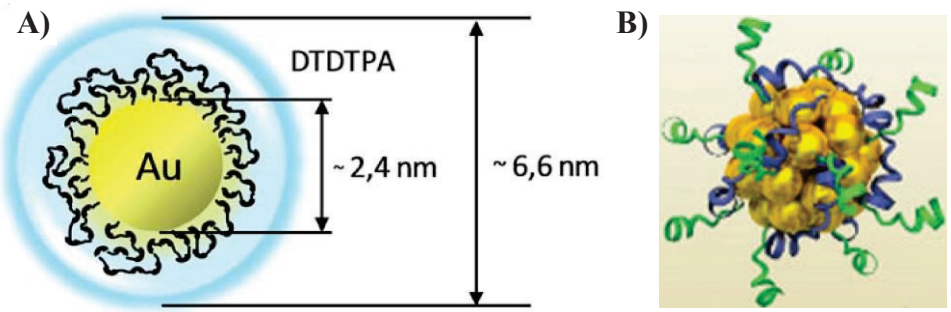

Figure 1-6. Schematic representations of A) ultrasmall AuNP coated by chelators[84] and B) Au nanocluster coated by targeting peptides.[87]

1.2.1.3.2. Hafnium oxide NPs

One of the earliest players in the field of nanosensitizers is actually hafnium oxide (HfO_2) NP. This NP was developed and commercialized by Nanobiotix (Paris, France) under brandname NBTXR3. This is a 50 nm NPs physically coated by trimetaphosphate and injected intratumorally or intra-arterially (Figure 1-7). The strong point of this NP is its biocompatibility, which has been demonstrated by a safe profile in preclinical and clinical studies, and high RS efficiency. NBTXR3 is a rare case of metal-based NPs which is proposed to clinical trials.[9,88] A series of clinical trials of NBTXR3 for different indications in cancer treatment has been currently carried out (Table 1-2). Nevertheless, due to their relatively big size, it is not intended to be used intravenously. The company is currently developing an intravenous formulation of HfO_2 NP, NBTX-IV, in preclinical stage, but no scientific publication has been released to update the progress.

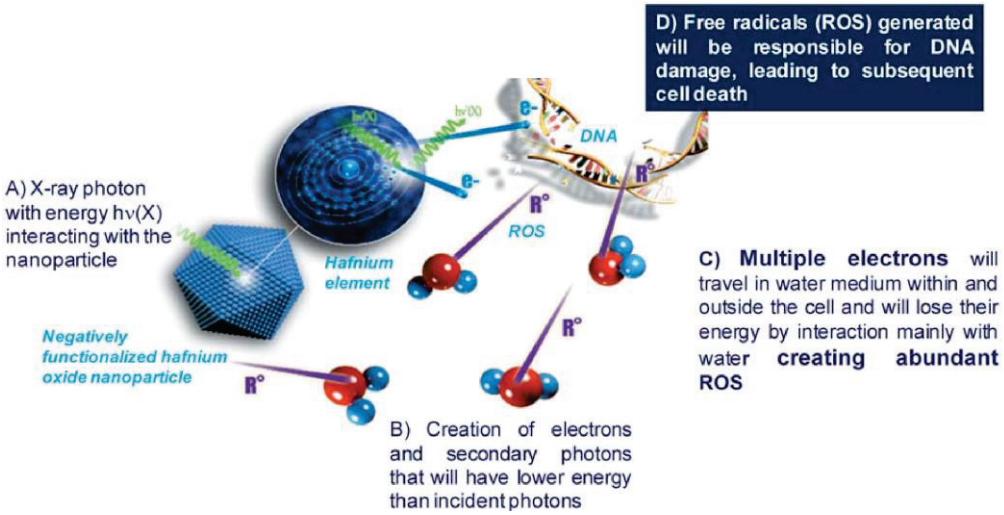

Figure 1-7. Schematic representation of HfO_2 nanoparticle and the proposed radiosensitization mechanism.[51]

1.2.1.3.3. Gadolinium NPs

Gadolinium (Gd) is another attractive element for radiosensitization application. The advantage of Gd does not lie in its Z number (Z = 64), which is usually surpassed by other elements, but in its paramagnetic property which is the most valuable for MRI. Indeed, with seven unpaired electrons in their 4f orbitals, it is the most paramagnetic stable metal ion. In addition, its symmetric S-state ensures a long electronic relaxation time.[89] These features make Gd a very good candidate to realize image-guided and theranostic strategies in cancer treatment which imply the combination of personalized and/or online imaging/diagnostic right

before or at the same time with the irradiation. Furthermore, the increasing use of MRI for anatomical diagnosis and tumor mapping instead of ionizing X-ray CT scan points out the relevance of this combination.[90,91] Hence, many NPs have been designed to contain Gd in chelated form, coated oxide, fluoride or carbonate forms or ionic form doped in other crystals. These particles have been extensively analyzed in a recent review.[91] However, the most difficult aspect in the translation of Gd to clinical application is how to avoid the eventual release of free Gd^{3+} which is known as an inducer of nephrogenic systemic fibrosis (NSF).[92] Some authors coated gadolinium oxide (Gd_2O_3) ultrasmall core with a stable and biocompatible layer.[90,93] Besides, numerous nanoplatforms have been used to graft Gd chelates on. Some structures have indeed ultrasmall hydrodynamic diameters (1 – 10 nm).[94–96] Many of these GdNP have been studied for RS property. For example, Townley H.E. *et al.* have shown that their 65 nm titania NPs which have been doped with rare earth metals including Gd can improve the effect of radiotherapy in killing cancer cells (*in vitro* spheroids model of hepatocellular carcinoma HepG2) and suppressing tumor growth (*in vivo* xenograft model of lung adenocarcinoma A549).[97] The team of Fukumori Y., meanwhile, has shown that their 200 or 400 nm chitosan NPs incorporating Gd-DTPA complexes can enhance the effect of neutron irradiation in suppressing B16F10 melanoma tumors in mice model.[98,99] Recently, Ghaemi B. *et al.* have demonstrated their ZnO NPs doped with Gd (or Eu) as a theranostic agent for enhancing both MRI/CT contrast and X-ray irradiation. Their particles have 9 nm diameter measured by electronic microscopy (TEM) but the D_H should significantly exceed this value and no biodistribution or *in vivo* result has been shown.[100] On the other hand, almost no ultrasmall NP (D_H < 10 nm) of Gd has been demonstrated as effective radiosensitizers. Recently, an interesting study has been reported by Yong Y. *et al.* where they used polytungstate gadolinium nanoclusters (GdW_{10}) coated with bovine serum albumin (BSA) (Figure 1-8) as a theranostic agent to improve the contrast of MRI/CT images and the effect of photothermal and X-ray therapy. D_H of these clusters was reported to be around 3.5 nm and renal excretion has been demonstrated with favorable biodistribution results.[101] However, the reliability of DLS measurement remains under question since the D_H of BSA alone normally is around 7 nm. Besides these candidates, ultrasmall silica gadolinium platform, AGuIX, developed in our laboratory is a highly promising NP for this application. It will be described later in the next part of this chapter.

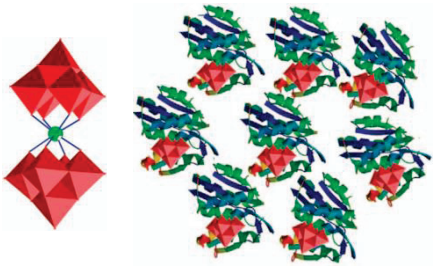

Figure 1-8. Schematic representation of GdW_{10} nanocluster non-coated and coated with BSA[101]

1.2.1.3.4. Bismuth NPs

One interesting element that should be mentioned is bismuth which is also the stable element with highest atomic mass existing in periodic table. NPs containing Bi have been synthesized and studied for enhancing radiotherapy by some groups. Alqathami *et al.* has shown RS effect of Bi_2O_3 NP in *in vitro*. Song *et al.* has demonstrated the use of a core-shell NP

$MnSe@Bi_2Se_3$ as radiosensitizer in *in vivo* experiment after intratumoral injection.[102,103] These studies showed great potential of Bi as sensitizer for radiotherapy. However, these NPs were far bigger than the threshold of renal clearance. This would make their clinical translation as a systemic intravenously injected nanomedicine difficult. Although Bi^{3+} usually shows much lower toxicity compared to other heavy metals, long exposure to this element can still induce severe toxicity.[104] Recently, Bi^{3+} has been added to our ultrasmall silica platform for an *in vivo* study using clinical MeV X-ray source. We will also look through this later in this chapter.

1.2.1.3.5. Platinum NPs

Finally, the list of promising UNP for enhancing radiotherapy might extend to platinum NPs (PtNPs). Due to an almost similar Z number as gold (Z = 78) and less well developed synthesis and functionalization methods, platinum attracts very few attention. Recently, Porcel *et al.* has shown that ultrasmall PtNP with diameter measured by TEM around 3 nm can enhance the DNA double strand breaks caused by proton or C^{6+} ion beam.[105,106] Nevertheless, *in vivo* studies have not been conducted yet with this formulation. Recently, Liu X. *et al.* have used a 30 nm NPs with Au core coated with Pt-PEGylated branches to enhance the contrast in CT imaging and tumor suppression effect of photothermal and/or X-ray radiotherapy. They hypothesized that the combination of two elements in a single NP can give synergistic effects for these therapies. However, no equivalent single-element NP has been tested to compare the effects.[107]

1.2.2. Hybrid NPs as MRI contrast probes

1.2.2.1. The role of medical imaging in cancerology and RT

Another prerequisite in the battle against cancer is to precisely localize the tumors. This is extremely important and realized by modern medical imaging techniques. In fact, imaging has coexisted with radiotherapy (RT) from the very beginning and now has been developed into a so called image-guided radiotherapy (IGRT). This is nothing but the routine practices of physicians to perform target delineation for treatment planning and treatment delivery for real-time readjustment. The role of imaging becomes more and more important in radiotherapy due to the widespread use of intensity modulated radiotherapy (IMRT) and stereotactic body radiotherapy (SBRT) where highly precise treatment planning and delivery need to be done to ensure steep dose gradients of IMRT or multiple-angle irradiation of SBRT will not cause more harm than good.[20] Besides, imaging techniques would be definitely useful tools to monitor the progress of treatment. Finally, the advancement in functional imaging which allows the recognition of genetic biomarkers of tumors is fundamental for realizing the concept of future personalized medicine.[108]

1.2.2.2. Common imaging techniques and their molecular probes for cancerology

Currently, there are several imaging techniques that can be used for diagnosis in cancerology including ultrasonography (US), X-ray computed tomography (CT), magnetic resonance imaging (MRI), modern radioimaging (it is mainly comprised of single photon emission computed tomography (SPECT) and positron emission tomography (PET)) and optical imaging (OI).

1.2.2.2.1. Ultrasonography

This technique is based on the difference between reflected signals of acoustic waves from different tissues and their boundaries. This can be seen as the earliest imaging technique and it is still widely used today in clinics. The advantages of US are high safety, no use of electromagnetic radiation, low-cost operation, speed, well-established know-hows, quite high spatial resolution (< 0.05 mm) and temporal resolution (< 10 ms). However, it implies several limitations such as the use of handheld probe which means high operator dependency, difficulty to perform whole-body scan and quantify, inability to detect disease sites behind bone or air structures. Moreover, the resolution can be significantly reduced for the sake of penetrability if low frequencies need to be used. Finally, the choice of contrast agents is limited to micro-bubbles of air which remain mostly inside the blood circulation. US used to be a common technique in cancerology in the past but it was replaced after the appearance of X-ray CT scan in the 1970s.[18–20]

1.2.2.2.2. X-ray computed tomography

X-ray CT scan uses ionizing X-ray to irradiate the tissues and record the difference in the X-ray absorption of different tissues. The absorption coefficient depends mainly on Z number of elements made up of tissues. Hence, the magnitude of signal increase in the order of air (Z~0) < fatty tissues (Z~6) < normal tissues (Z~8) < bones (Z~15, 20). The advantages of CT include relatively cheap price (compared to MRI), extremely high spatial and temporal resolution (even relatively better than MRI), very high contrast for bone tissues, very fast acquisition time which allows complete elimination of physiologic motion, decent contrast for soft tissues if appropriate contrast agents are used and an ability to be used as quantification tool in some cases. However, CT scan still has several drawbacks such as the use of ionizing radiation, relatively low sensitivity which limits its applications in quantification and biodistribution studies, the need for high doses of contrast agents and the potential toxicities relating to contrast agents since they use heavy elements for this purpose. Nowadays, X-ray CT is the most common technique used for treatment planning and delivery partly due to the compatibility of the equipment used for CT scan and RT. Common contrast agents used in CT are molecules with high-Z elements such as iodine or barium. Gold and other elements e.g. bismuth are also attracting more attention recently.[18–20]

1.2.2.2.3. Magnetic resonance imaging

From its discovery in the 1980s, MRI is gaining more and more popularity in hospitals. MRI shares the same physical principle as NMR used by chemist to elucidate chemical structures (Figure 1-9). Patients were also placed in a giant magnet like chemical samples in NMR. But this magnet is equipped with a sophisticated spatially encoded magnetic field gradient. Most of the time, protons of water are the nuclei to be observed in MRI. Larmor resonating frequency of proton depends on

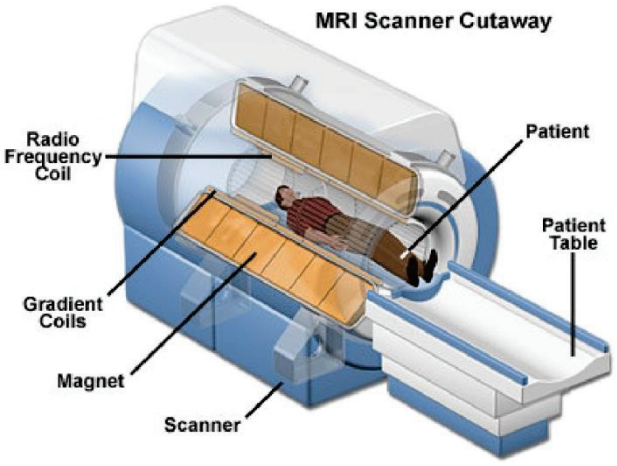

Figure 1-9. Schematic representation of a MRI setup. Image taken from https://pancreaticcanceraction.org/

the magnetic field. So, by creating magnetic field gradient, protons at different positions in the patient will resonate at different frequencies. By applying different exciting magnetic pulses through the radiofrequency coil and record the radiofrequency energy emitted from protons at different positions in the body when they relax to normal stage, MRI can give very informative structural images in very different ways. Numerous of pulse sequences have been developed for MRI to exploit subtle differences in proton density or proton relaxation times relating to structural differences of tissues even if they are very close geometrically or physiologically. First of all, this technique is widely considered as very safe since it uses only low-frequency electromagnetic waves. It usually shows very good spatial resolution and therefore is as suitable for anatomical imaging as CT. Moreover, it is ideal for imaging soft tissues where CT scan can hardly detect any differences since X-ray attenuations are almost the same. Most importantly, it can offer a great variety of contrast mechanisms based on endogenous differences or the introduction of exogenous agents. Nevertheless, MRI has a relatively longer acquisition time compared to CT. Therefore, it is not an ideal solution for imaging regions with rapid physiological motions i.e. heart or lung. MRI also has a relatively low sensitivity and complicated procedure for quantification. To overcome the weakness in sensitivity, MRI images are often superimposed with images from other more sensitive techniques especially radioimaging.[18–20]

Molecular contrast agents used in MRI are mostly comprised of Gd even if Mn complexes have also been developed. Gd complexes are more widely used for clinical imaging because Mn complexes in general have lower relaxivities and stability constants.[109–111] There are at least nine Gd complexes (and one Mn complex whose the production has already been stopped) that have been approved for human uses. Gd^{3+} and Mn^{2+} are used as contrast agent thanks to its paramagnetic property induced by 7 (Gd) or 5 (Mn) unpaired electrons in their 4f (Gd) or 3d (Mn) orbitals and a slow electronic relaxation rate.[110] Gd^{3+} and Mn^{2+} both have very short magnetic longitudinal and transverse relaxation times. So while being in contact with water molecules, they will speed up the relaxation process of protons in surrounding medium during MRI measurements. In this way, they create zones of stronger signals appearing as white spots in T1-weighted MR images. Table 1-3 shows the characteristics of nine commercialized Gd complexes in which the structure of four most common ones are shown in Figure 1-10. As discussed previously, one of the most difficult tasks in developing Gd contrast agents is to prevent the side effect (NSF) associated to free Gd^{3+} ions. Hence, the stability of these complexes *in vivo* has to be very high and the clearance needs to be as quick as possible. To fulfil these criteria, not only their thermodynamic stability constants need to be high but also the dissociation kinetics need to be extremely slow to allow enough time for the clearance.[112] That explains why even though the thermodynamic stability of Gd-DTPA (pKa = 22.1) is not that much lower than Gd-DOTA (pKa = 25.6) or Gd-HP-DO3A (pKa = 23.8) and a bit higher than Gd-BT-DO3A (pKa = 21.8), so far the incidences of NSF were only reported in patients who have used Gd complexes of DTPA and its derivatives. This is due to an extremely slow dissociation kinetics of macrocyclic chelators such as DOTA (dissociation half-life at pH 1, $T_{1/2}$ ~ 338 h) or DO3A ($T_{1/2}$ ~ 3.9 h or 43 h) compared to DTPA ($T_{1/2}$ < 5 s) (Table 1-3).[92,112,113]

Table 1-3. Characteristics of nine approved Gd chelates[113]

	Linear						Macrocyclic		
	Ionic				Nonionic		Ionic	Nonionic	
Acronym Trade name	Gd-DTPA Magnevist	Gd-BOPTA MultiHance	Gd-EOB-DTPA Primovist/Eovist	MS-325 Vasovist/Ablavar	Gd-DTPA-BMA Omniscan	Gd-DTPA-BMEA OptiMARK	Gd-DOTA Dotarem	Gd-HP-DO3A ProHance	Gd-BT-DO3A Gadovist/Gadavist
Excess ligand[a]	0.1%	0%	0.5%	0.1%	5%	10%	0%	0.1%	0.1%
Osmolality (mOsm/kg H_2O, 37°C)	1960	1970	688	825	789	1110	1350	630	1603
Viscosity (mPa.s, 37°C)	2.9	5.3	1.2	2.1	1.4	2.0	2.0	1.3	5.0
Log K_{therm}[b]	22.1	22.6	23.5	22.1	16.9	16.6	25.6	23.8	21.8
Log K_{cond}[c]	17.7	18.4	18.7	18.9	14.9	15.0	19.3	17.1	14.7
$T_{1/2}$[d]	< 5 s	< 5 s	< 5 s	< 5 s	< 5 s	< 5 s	338 h	3.9 h	43h
Relaxivity (r1/r2, 1.5T)[e]	3.9-4.3/3.8-5.4	6.0-6.6/7.8-9.6	6.5-7.3/7.8-9.6	18.0-20.0/32.0-36.0	4.0-4.6/4.2-6.2	4.4-5.0/4.3-6.1	3.4-3.8/3.4-5.2	3.9-4.3/4.2-5.8	4.9-5.5/5.2-7.0
Relaxivity (r1/r2, 3T)[e]	3.5-3.9/4.3-6.1	5.2-5.8/10.0-12.0	5.9-6.5/10.0-12.0	9.4-10.4/56.0-64.0	3.8-4.2/4.7-6.5	4.2-4.8/5.0-6.8	3.3-3.7/4.0-5.8	3.5-3.9/4.8-6.6	4.7-5.3/6.2-8.0
Clearance	Renal	96% renal 4% hepatic	50% renal 50% hepatic	79-94% (mean 84%) renal ~5% hepatic	Renal	Renal	Renal	Renal	Renal

[a]Excess ligand in percentage of the molar concentration of the Gd contrast agent (at pH 7.4) (26).
[b]K_{therm} = Thermodynamic stability constant (10,27).
[c]K_{cond} = Conditional stability constant (10,27).
[d]$T_{1/2}$ = Dissociation half-life at pH 1.0 and 25°C (11).
[e]Values in L $mmol^{-1}$ s^{-1} (plasma, 37°C) (28).

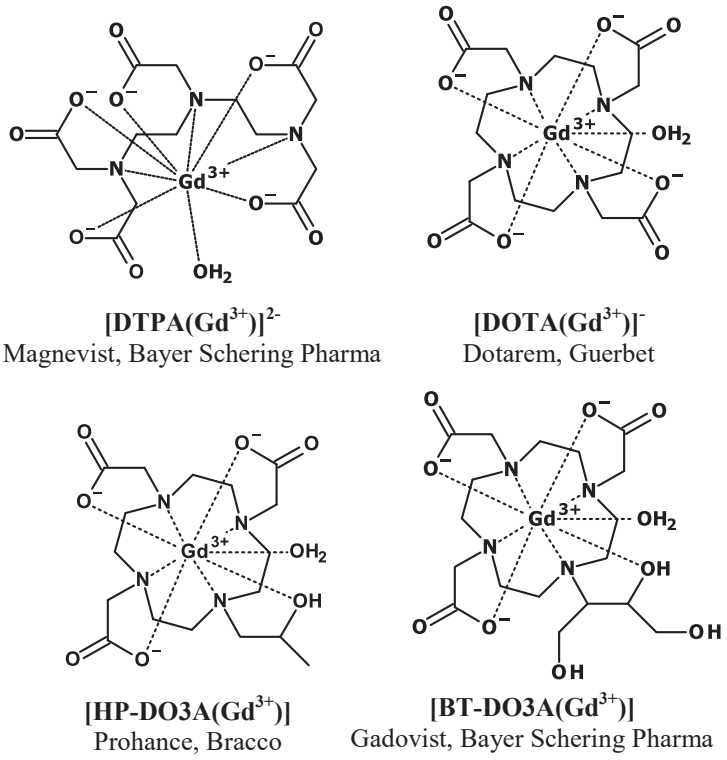

Figure 1-10. Chemical structures of some most common Gd chelates.

1.2.2.2.4. Radioimaging

Two main methods in modern radioimaging are single photon emission computed tomography (SPECT) and positron emission tomography (PET).

1.2.2.2.4.a. SPECT

SPECT requires the administration of a gamma particle emitting radionuclide inside the body. These radioisotopes will emit gamma particles that will be detected by a gamma camera from different angles. 3-D images will be reconstructed by tomographic algorithm just like X-ray CT. One of its advantages over PET is the possible detection of different energies and so of different isotopes allowing multiple tracers imaging. Among different modern imaging modalities, it has the worst spatial resolution. Additionally, compared to PET, its sensitivity is one order of magnitude lower.

Most commonly used radioisotopes in SPECT are ^{99m}Tc ($t_{1/2}$ ~ 6 h), ^{111}In ($t_{1/2}$ ~ 2.8 day) or ^{123}I ($t_{1/2}$ ~ 13 h). The two formers are metals and can be stably complexed in a chelate.

1.2.2.2.4.b. PET

PET is based on the use of positron emitting radionuclides. While traveling in the body, these radioisotopes will emit positron particles which will be almost immediately annihilated by an electron nearby to emit two opposite gamma particles at a precise energy of 511 keV (Figure 1-11). The photons will be detected similarly with gamma cameras. Since the two coincidental photons will arrive at almost the same time to the opposite detectors, algorithms can be applied to remove random noises. The collimator is not needed which means less photons will be wasted in PET. These properties explain its higher sensitivity compared to SPECT. In addition, the fact that two photons created from an event of annihilation separate oppositely allows a more precise localization and therefore increases the resolution of PET compared to SPECT.

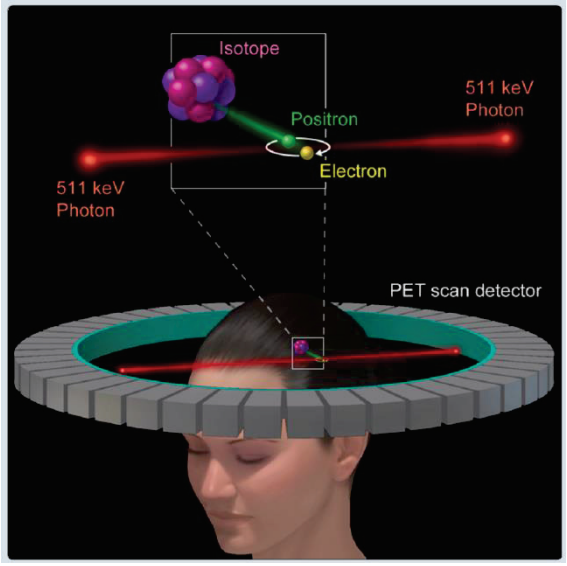

Figure 1-11. Schematic representation of PET mechanism. Image taken from ref [114].

Most commonly used radioisotopes in PET are ^{18}F ($t_{1/2}$ ~ 110 min), ^{64}Cu ($t_{1/2}$ ~ 13 h), ^{68}Ga ($t_{1/2}$ ~ 68 min) or ^{89}Zr ($t_{1/2}$ ~ 78 h). The three latter are metals and can be stably complexed in a chelate.

The advantages of both SPECT and PET are their much higher sensitivity and highly quantitative results compared to CT or MRI and deeper penetration compared to optical imaging. Since they have high sensitivity, they can be used to couple with biomarkers to detect molecular activities and give extremely useful biological and genetic information about the tumors. These characteristics are brought into thanks to the use of radioisotopes and the gamma particles that they emit. However, the use of radioactive materials is also a disadvantage not only because of safety concerns but also due to the scarce availability and short shelf-lives of radiomaterials. The cost of operation is also very high for using these techniques especially in the case of PET. Finally, the resolution of these techniques is generally poor and they require complementary information from images of CT or MRI.[18–20,28,108,114]

1.2.2.2.5. Optical imaging

Optical imaging is another major technique which is increasingly used but most often in preclinical researches. This technique exploits the use of a fluorophore as a probe like the use of a radioisotope in radioimaging. Its strengths are excellent sensitivities and relative stability (much higher than radioisotopes) of fluorescence probes, the ease of use, the possibility for semi-quantification applications and multiple fluorophores for different targets in the same object as well as the suitability for microscopic studies. However, the clinical use of OI is still very limited due to the high absorption, autofluorescence and diffusive scattering of biological tissues. Even though the fluorophores might be chosen to be excited and emit at the physiological window from 650 to 900 nm to avoid as much as possible the absorption of

normal tissues and other biological components such as hemoglobin,[115] these artifacts are still pronounced. These problems also lead to a poor penetrability which limits OI as a technique to detect superficial lesions (< 2 mm from the surface) or requires the use of an optical fiber for endoscopy. As radioimaging, OI generally gives a poor resolution and needs complimentary information from CT or MRI for anatomical construction of the object. Because of these advantages and limitations, OI is rather more useful for studies in small animals.[18,19]

1.2.2.2.6. Multimodal imaging

Since each technique has its own advantages and drawbacks (Table 1-4), the combination of complementary techniques, which is the so called multimodal imaging, to achieve both high resolution and sensitivity is an active research field. More and more commercial apparatus have been designed to allow CT-SPECT, MRI-SPECT, CT-PET or MRI-PET imaging protocols (Figure 1-12).[20,108] Similarly, demand for multimodal imaging probes is also increasing. This opens more opportunities for researchers working on nanoparticles which can potentially combine different imaging probes in the same platform. A tremendous amount of nanoparticles has been proposed in the literature. We will only focus on promising NPs used in MRI and their combinations with other modalities. Furthermore, as shown previously, NPs with high potential for clinical translation need to be totally biocompatible and renally clearable meaning being either ultrasmall and/or completely degradable.

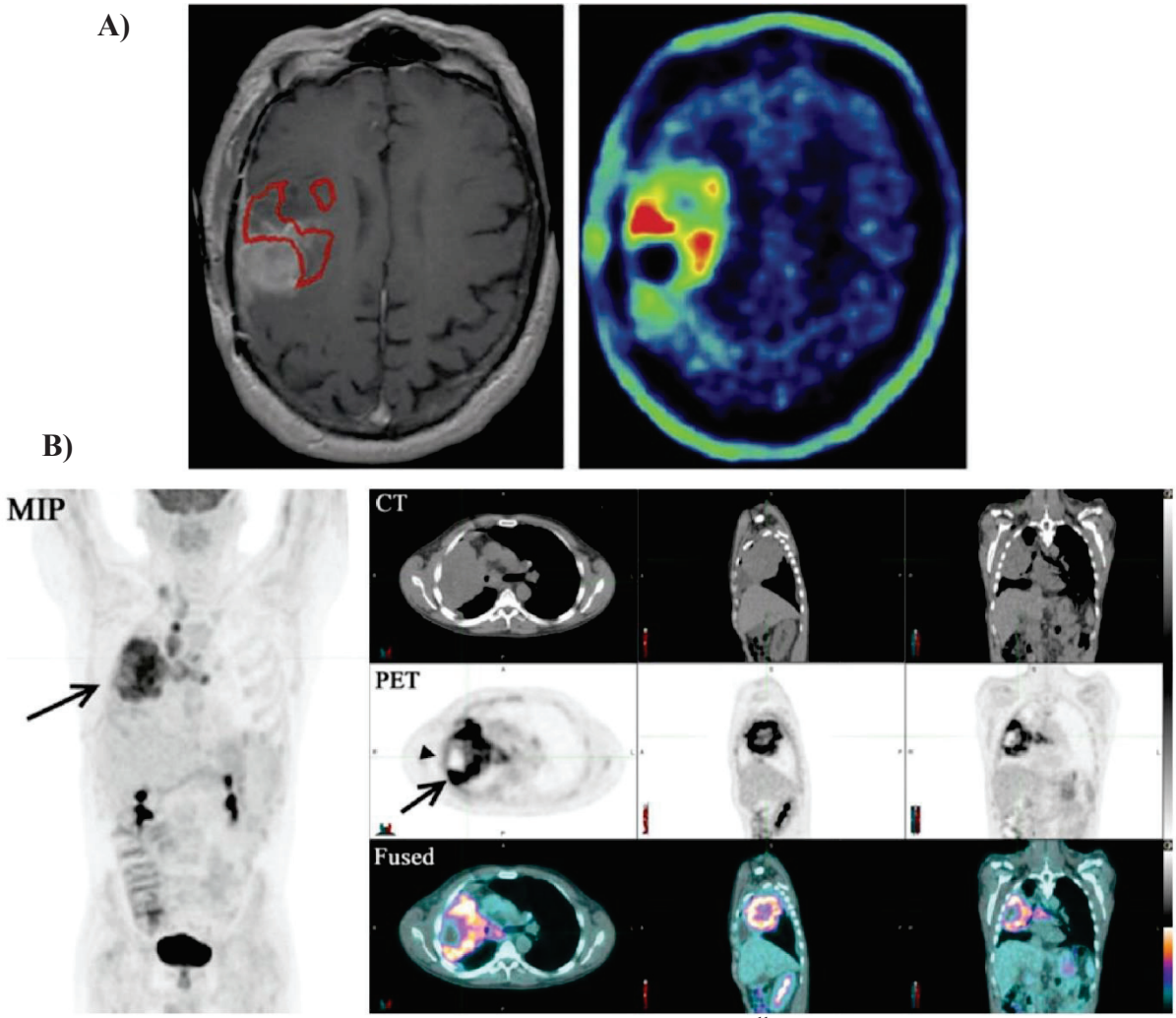

Figure 1-12. Examples of multimodal imaging. A) T1-weighted MRI image (left) and ^{11}C-methionine PET (right) of a patient with brain tumor after resection. Image taken from ref [20]. B) CT/ ^{18}F-FDG-PET in a patient with a recent diagnosis of small cell lung carcinoma. Image taken from ref [108].

Table 1-4. Pros and cons of each imaging technique

Modalities	Advantages	Disadvantages
Ultrasonography	Low cost No ionizing radiation High spatial resolution Fast acquisition	Operator dependency Difficult to do whole body scan Difficult to quantify Shadows close to bone or air structures Limited contrast agents Penetrability limited by resolution
X-ray CT	Relatively low cost Very high spatial resolution Very fast acquisition Elimination of physiologic motions High contrast for bone tissues Relatively quantifiable	Ionizing radiation Low sensitivity High doses of contrast agents Toxicities of contrast agents
MRI	No ionizing radiation Very high spatial resolution Great variety of contrast mechanisms especially for different soft tissues	Relatively expensive Long acquisition time Low sensitivity Difficult to quantify
SPECT	High sensitivity High penetrability Highly quantifiable Multiple probes	Ionizing radiation Low resolution Availability of radioisotopes High cost
PET	Very high sensitivity High penetrability Highly quantifiable	Ionizing radiation Relatively low resolution Availability of radioisotopes Very high cost

Optical imaging	No ionizing radiation Relatively low cost High sensitivity Easy access Semi-quantifiable Multiple probes Suitable for microscopic study	High background signals Poor penetrability Poor resolution Poorly implanted in clinic (Not widely used for deep organs or tissues)

1.2.2.3. Some promising hybrid MRI contrast nanoprobes

1.2.2.3.1. Gadolinium based NPs

As have been shown previously, GdNPs can be designed in the form of oxides, fluorides, carbonates, Gd-doped crystals or Gd^{3+} chelates and until now the chelates seem to show more potential thanks to better toxicity profiles. Roux S. *et al.* have grafted thiolated chelators on an ultrasmall core of AuNP to obtain NPs with total D_H in the range of 6 – 8 nm intended for RS applications. These NPs have been complexed with Gd or radioisotopes i.e. ^{99m}Tc and ^{111}In to study their biodistribution in *in vivo* models using MRI or SPECT. The results show rapid clearance through kidney which justifies further clinical translation of these NPs.[83,84] Besides, some very promising GdNPs have been developed as imaging agents although they have not been tested for radiosensitization property. Moriggi L. *et al.* has synthesized a similar structure with an ultrasmall Au core (~2-3 nm) covered by a layer of thiolated DTNP(Gd) complexes (~1-2 nm). At first sight, this structure seems to fulfil the criteria and show high relaxivities but more efforts need to be done to elucidate their behaviors in animal models. Ferreira M. F. *et al.* continued this line of research and synthesize AuNP functionalized by different type of thiolated Gd chelates. The D_H of these NPs were in the range of 4 – 6 nm which fall very well in the range of renal clearable NPs. However, while AuNP functionalized with monothiolated DOTA(Gd) showed a rapid renal clearance followed by MRI, the radiolabeling biodistribution study carried out with AuNP functionalized with dithiolated DOTA(Gd) showed a high uptake by liver. Though, further optimization needs to be done for these formulations, the results were very promising for clinical translation. In another study, Endres P. J. *et al.* have functionalized DOTA(Gd) on a titan dioxide (TiO_2) UNP (~3-5 nm). Although *in vivo* studies have not been conducted yet, this UNP seems to have a high potential since TiO_2 is also considered as highly biocompatible.[96] Micelle is another nano-object which size can be controlled down to sub 5 nm. Gianolio E. *et al.* have conjugated a new chelator AAZTA with a lipophilic C17 chain which formed a self-assembly micelle system with D_H ~ 6 nm. Due to its highly negative charge, it interacted with albumin and induced a bigger hydrodynamic size D_H ~ 12 nm.[116] With new knowledge about the ability of preventing protein adsorption by neutral and zwitterionic coatings, we might hope to see more optimizations conducted along this line of research. As have been shown in previous part, polytungstate gadolinium nanoclusters synthesized by Yong Y. *et al.* is also an interesting contrast agent for both MRI and CT. Its potential has been demonstrated in *in vitro* and *in vivo* models.[101] In another study, Zhou Z. *et al.* developed a gadolinium iron co-oxide NP coated with zwitterionic dopamine sulfonate as a T1 contrast agent (Figure 1-13). The size of such NP can be tuned from 3 to 5 nm. Although the relaxivity was not highly enhanced (staying from 3 to 8 $mM^{-1}.s^{-1}$), clear contrasted images were still obtained. Renal clearance was demonstrated to be more favorable than hepatobiliary clearance by some preliminary qualitative tests. Zwitterionic coating was proven to be more effective than negative coating

in preventing protein adsorption and eventually liver uptake.[117] These results were very promising for clinical translation but it would be expected to have more quantitative biodistribution data and the evaluation of Gd^{3+} leaking. The latter might be the major hindrance for this type of NP. Among different GdNPs investigated for MRI contrast enhancement, ultrasmall silica NP, AGuIX, is a very successful example. Further details about this NP will be described later in this chapter.

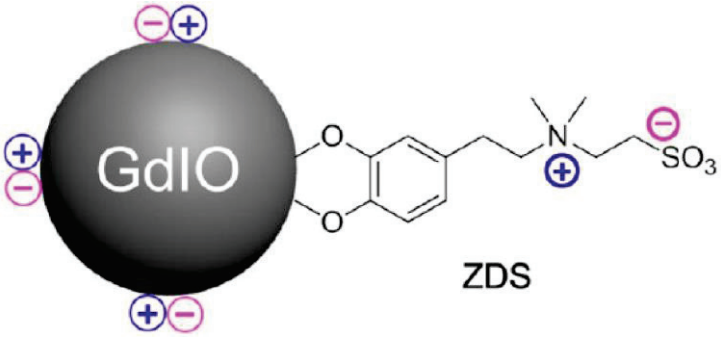

Figure 1-13. Gadolinium iron co-oxide NP coated by zwitterionic dopamine sulfonate (GdIO@ZDS). Image taken from ref[117].

1.2.2.3.2. Manganese based NPs

Manganese (Mn) is the second most studied element as positive contrast agent. The clinical use of Mn salts is also plagued by its neurotoxicity and limited in oral form. Thus, intravenous use of Mn also requires suitable chelators. The only one Mn complex that has been approved so far is Mn-DPDP (Teslascan, GE Healthcare) which more favorably retains in the liver.[110] It was withdrawn from US and European markets for commercial reasons. Ca^{2+} salt of that complex found application in preventing nerve damages in patients suffered from chemotherapy and was commercialized under the name PledOx (Pledpharma). The compound has completed phase II multicenter clinical trial in US and Europe (ClinicalTrials.gov Identifier: NCT01619423). In NP form, an exciting one has been developed and commercialized as SpagoPix by Spago Nanomedical AB. Details of physicochemical characterization were not revealed. However, it was described as having $D_H \sim 5$ nm, almost neutral zeta potential and high relaxivity $r_1 \sim 30$ $mM^{-1}.s^{-1}$.[118] We might hope to see more preclinical and clinical data in the future for this NP.

1.2.2.3.3. Iron oxide based NPs

Besides Gd or Mn, iron oxide nanoparticles (IONPs) have also attracted much attention in the last couple of decades. When IONPs obtain sizes below a critical size, they become one single domain and their magnetic moments will be aligned with an applied magnetic field. They will exhibit superparamagnetism. Their effect in MRI is to shorten mostly the transverse relaxation time (T_2) and to a lesser extent longitudinal relaxation time (T_1). Therefore, MRI images performed with IONPs will give a dark spot at their locations. This is less desirable than T_1 contrast agents since the boundary of targets can be difficult to perceive. However this is still valuable when images are taken in a bright background e.g. in an organ like liver. More importantly, IONPs are appealing because of not only their magnetic property but also their biocompatibility given that iron is present abundantly in human body and their metabolism in liver and spleen is pretty quick.[24,119] That explains why a large number of IONP formulations have been approved and commercialized (Table 1-2). However, most of them are still limited

as gastrointestinal tract or liver targeted agents because of their big sizes. In addition, normal IONPs can be retained in liver or spleen for a long period of time.[119] Although, this might not be lethal, the surplus level of iron could hamper the re-administration of NPs or the results of other diagnostic tests. Some iron oxide NPs have been reported to have smaller D_H and so more probably rapid clearance through kidney. Even though synthesizing ultrasmall renal clearable iron oxide NPs seems to be an appealing strategy, different studies have reported that IONP with diameter less than approximately 5 nm exhibits significant decrease in magnetic moment and surface spin order which lead to higher r_1 but much lower r_2. As a consequence, they are less efficient as a T_2 contrast agent. Many authors suggest using them as T_1 contrast agent, unfortunately, their r_1 values are not really high in most of the cases. For example, very small iron oxide NPs (VSOP) coated by citrate have been developed by Pilgrimm H. with a claimed D_H ~ 7 - 8 nm.[120] Not many physicochemical characterizations have been revealed but preclinical and clinical studies show favorable results.[121–123] However, there were no full biodistribution data to evaluate the clearance pathway. As expected, relaxivities of VSOP at 1.4 T in water were r_1 = 13.97 ($mM^{-1}.s^{-1}$) and r_2/r_1 = 2.39. The same values at 7 T in water were r_1 = 3.48 ($mM^{-1}.s^{-1}$) and r_2/r_1 = 9.82. These values made it difficult to classify VSOP as positive or negative contrast agent. The authors have decided to test it as a T_1 enhanced blood pool contrast agent in these studies. Similarly, Kim B.H. *et al.* have synthesized extremely small iron oxide NPs (ESIONs) with diameter measured by TEM from 2 – 4 nm. The particles were capped with PEG-derivatized phosphine oxide to obtain aqueous colloidal stability. Relaxivities at 3 T in water of ESION with diameter at 2.2 nm and 3 nm and the ones of normal IONP with diameter at 12 nm were r_1 = 4.78, 4.77 and 2.37 ($mM^{-1}.s^{-1}$), and r_2/r_1 = 3.67, 6.12 and 24.8 respectively. ESION was also tested as a T_1 enhanced blood pool contrast agent in rats.[124] Zeng L. *et al.* have fabricated pure, zinc doped and nickel doped IONPs at 4 nm, 4 nm and 5 nm (measured by TEM) repspectively. They had relaxivities at 0.5 T in water as r_1 = 5.99, 7.93 and 6.85 ($mM^{-1}.s^{-1}$), and r_2/r_1 = 15.5, 14.6 and 12.9 respectively. *In vitro* MRI experiment showed their efficiency to enhance the contrast of T_1-weighted images.[125] Shen L. *et al.* showed a facile one-pot synthesis of IONPs in diethylene glycol. This method produced ultrasmall cores from 2 – 14 nm (measured by TEM) in the presence of sodium citrate as reducing and capping agent. Relaxivities of particles at 1.9 nm, 3.1 nm and 4.2 nm at 7 T were r_1 = 1.41, 0.84 and 0.33 ($mM^{-1}.s^{-1}$), and r_2/r_1 = 2.0, 13.6 and 111.6 respectively. Particle with 3.1 nm core had a D_H ~ 8 nm that was stable in a wide range of pH. The ones at 1.9 nm and 3.1 nm appeared to be promising T_1 contrast agents *in vitro*.[124] More *in vivo* and biodistribution data are expected to demonstrate the ability to be rapidly cleared through kidney of these NPs.

Since the hepatobiliary clearance of IONPs is much faster and assured than other particles, other researchers also investigated the combination of renal clearance and hepato clearance of moderately small IONPs. This strategy seems to be more advantageous if a powerful T_2 contrast agent is the goal to be obtained. For example, Bégin-Colin S. *et al.* have functionalized a 10 nm IO core with different phosphonates ranging from linear octaethylenglycol carboxylic acid (OEGCA) to dendrons of 1, 2 and 3 generations of OEGCA to create at the end particles with D_H at around 15, 20, 20 and 30 nm respectively. The dendronized particles seemed to have higher colloidal stability in solutions at high ionic strengths. They also grafted a fluorophore (Alexa647) on these particles and evaluated their bioelimination in mice after IV injection. IONP functionalized with linear phosphonates

seemed to be cleared completely 4 h after injection whereas IONP functionalized with dendrons of generation 1 and especially of generation 2 seems to persistently stay in kidneys, liver and bladder 6 h after injection.[127] In another study, similar IONPs functionalized with biphosphonates of linear OEGCA or monophosphonates of dendrons of OEGCA at D_H = 14 and 16 nm respectively were grafted with Alexa647. They were intravenously injected to mice bearing human hepatocarcinoma tumor (Huh-7-Luc). Rapid renal clearance was observed with IONPs functionalized with bisphosphonates of linear OEGCA while renal clearance and complementary hepatobiliary clearance were observed with IONPs functionalized with monophosphonates of dendrons of OEGCA. Even though no tumor accumulation was observed for both particles, this result represents a promising design of intravenous clearable IONPs.[128] Probably, the combinations of positively charged ligands and/or active targeting ligands might improve the tumor uptake of these particles in future studies.

1.2.3. Promising nanotheranostic agents for RT

An even more advanced idea of designing NP is to combine imaging and therapy in a single platform which is so called theranostics. This is extremely useful in the case of radiotherapy since the combination with imaging is indispensable. In this way, the distribution of nanomedicine can really be monitored. In addition, this concept reduces the cost of development of nanomedicine and the medication burden of cancer patients. Nevertheless, as we have seen, the criterion of being renal clearable really narrows down the playing ground to a couple of highly promising nanomedicine for this purpose. The first candidate can be AuNP functionalized with Gd chelates of Roux's team. This NP can be imaged by CT, MRI and radioimaging as well as shows a remarkable RS effect. Second, GSH-coated AuNP of Xie's group can also be classified in the list as it works as a CT contrast agent and can enhance radiotherapy. Polytungstate-Gd cluster of Zhao's group is another candidate which improves both MRI/CT contrast and photothermal/radiotherapy.

1.2.4. AGuIX nanoparticle

1.2.4.1. Physicochemical properties of AGuIX

As mentioned above, AGuIX is a unique NP with many distinct properties suitable for theranostic application. AGuIX is an ultrasmall NP with a silica core whose surface is covered by aminosilanes. Approximately half of surface aminosilanes were coupled with DOTAGA and > 97% of these DOTAGA was complexed with Gd^{3+} (Figure 1-14).

AGuIX has characteristics that fulfil the requirement of a potential nanomedicine (Table 1-5). First of all, the basic components that made up this particle i.e. silanes and Gd chelates are well accepted clinically. Silane has been intensively used as the core or the coating layer in many types of nanocarriers for metals or other different active compounds due to many of its favorable properties. Silane precursors and silica NPs are normally well tolerated in humans and animals with high biocompatibility.[129] In addition, the chemistry of silanes was quite developed in recent years to meet the demands in different fields i.e. electronics, adhesives, medical devices, optics etc. and so a wide range of different functional groups might be grafted on silica structures.[130] In most of the cases, they are quite inert and do not interfere with the interaction between external stimuli, e.g. irradiation, optical beams etc., and the active compounds/metals.[129]

Regarding its nanostructure, it has an ultrasmall D_H (3 – 5 nm) and a surface zeta potential (0 – 9 mV) balanced by two opposite functional groups i.e. $[-NH_3]^+$ ammoniums and $[-DOTA(Gd^{3+})]^-$ chelates at physiological pH. These properties make AGuIX readily eliminated through kidney while reducing the adsorption of blood proteins and so evade the capture of mononuclear phagocytes system (MPS). The rapid renal excretion of AGuIX was extensively demonstrated in different *in vivo* studies carried out on both rodents and non-human primates.[131,132] Despite its small size, it showed a sufficient retention in tumor by only relying on passive targeting thanks to EPR effect.[133–135] Moreover, it can degrade in physiological condition by the hydrolysis of siloxane bonds to give smaller non-toxic silane fragments.[136]

On the other hand, AGuIX can offer several imaging modalities as well as therapeutic effect based on RS property.

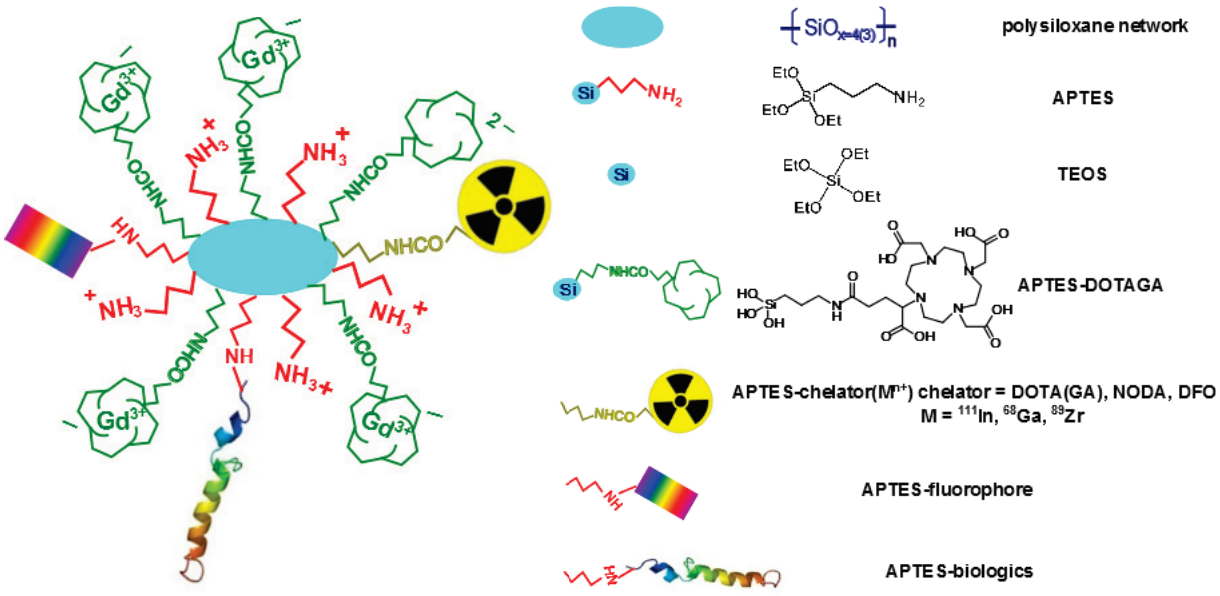

Figure 1-14. Schematic representation of AGuIX nanoparticle with all potential modalities. Radioisotopes, fluorophores and biologics are optionally added after the synthesis to obtain additional functionalities if necessary.

Table 1-5. Main characteristics of AGuIX

Properties	Method(s)	Values
D_H (nm)	DLS, NMR DOSY	3 – 5
Zeta potential (mV)	Zeta potentiometry	0 – 9 (pH 7.4)
Gd : Si : N : C (% mass)	Elemental analysis	14 : 10 : 26.5 : 7.4
Gd : A-D : A : T (molar ratio)		1.0 : 1.0 : 1.0 : 2.0
Molar mass (kDa)	ESI-MS	~ 8 – 10
r_1 ($mM^{-1}.s^{-1}$) (37°C, 60 MHz)	Relaxometry	13 – 14
r_2/r_1 (37°C, 60 MHz)		1.3 – 1.4

**A-D: APTES-DOTAGA, A: APTES, T: TEOS*

1.2.4.2. Imaging properties of AGuIX

Firstly, the presence of $DOTA(Gd^{3+})$ on the surface makes AGuIX a paramagnetic structure. Moreover, nanometric size of AGuIX enhance the longitudinal relaxivity of the system (r_1 ~ 13 – 14 $mM^{-1}.s^{-1}$) to 3 times higher compared to molecular $DOTA(Gd^{3+})$ (r_1 ~ 3.5 $mM^{-1}.s^{-1}$) at

1.4 T, 37°C. Second, thanks to the presence of amine groups, other functions such as different fluorophores (Cyanine5.5, RhodamineB, and Fluorescein) or chelators (DOTA, NODAGA, DFO) can be potentially grafted. With the latter, a wide variety of radioisotopes (^{111}In, ^{68}Ga, ^{89}Zr) can also be complexed on AGuIX to offer different types of radioimaging (Figure 1-14).[131,135,137–139]

The multimodality of AGuIX was exploited, first of all, to evaluate its biodistribution. Some typical images are presented in Figure 1-15. Figure 1-15-A shows MRI images of a mouse injected with AGuIX. Figure 1-15-B shows CT/SPECT images of a mouse injected with ^{111}In radiolabeled AGuIX. Figure 1-15-C shows fluorescence images of a mouse injected with rhodamine conjugated AGuIX.[137] And, Figure 1-15-D shows MRI and CT/PET images of the same mouse treated with AGuIX conjugated to NODAGA and labeled with ^{68}Ga.[138] These examples illustrate a wide variety of imaging modalities that can be introduced on AGuIX. They were used to demonstrate the favorable renal excretion pathway of AGuIX since it was clear that the signals from kidney, bladder and urine are always predominant compared to other organs.

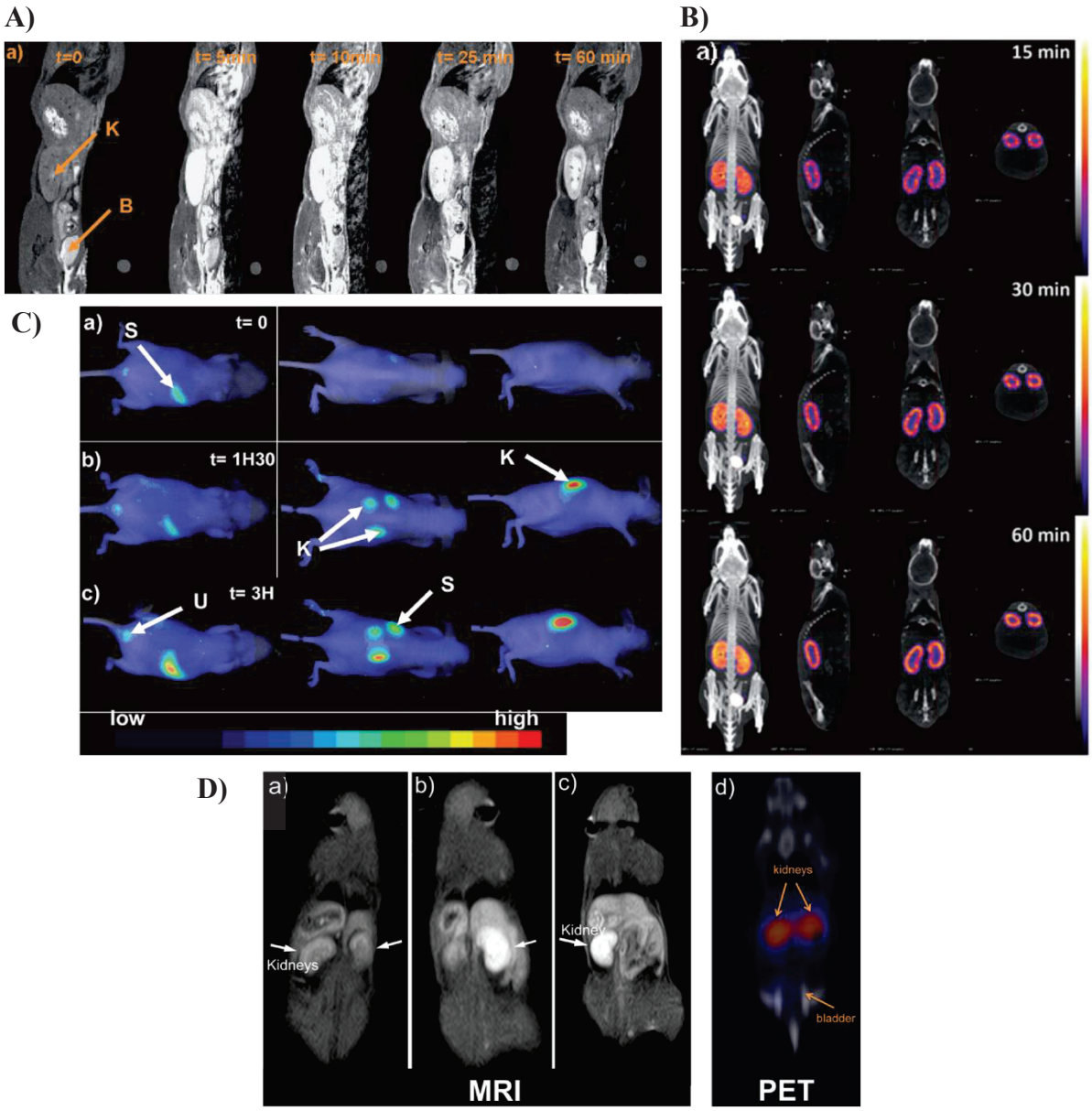

Figure 1-15. Multimodal imaging to evaluate biodistribution of AGuIX.
A) T1-weighted images of a slice including one kidney (K) and the bladder (B) of a mouse before and after iv injection of AGuIX.
B) In vivo SPECT/CT imaging of a mouse after iv injection of AGuIX radiolabeled with ^{111}In.
C) Fluorescence imaging of a mouse after iv injection of AGuIX conjugated to cyanine5.5.
D) MRI image of (a) a non-treated mouse, (b-c) a treated mouse after iv injection of AGuIX@NODAGA-^{68}Ga and CT/PET image (d) of the treated mouse. Images taken from refs [137, 138].

More importantly, AGuIX was a very effective multimodal agent for detecting tumors. Figure 1-16 shows some examples of what have been done with AGuIX for this purpose. Figure 1-16-A shows MRI images taken in the brain of a rat bearing glioblastoma tumor. The clear white region in right hemisphere was the location of the tumor visualized thanks to the presence of AGuIX. The signal reduced over time indicating the wash-out of AGuIX but the retention was still remarkable since the difference with normal tissue was still recognizable.[140] In another study (Figure 1-16-B, C), glioblastoma tumor was subcutaneously inoculated in mice before NODAGA conjugated ^{68}Ga labeled AGuIX was injected. The location of tumor was shown clearly in MRI and CT/PET images. The signals remain strong at least after 1h. This allows a suitable window for carrying out subsequent radiotherapy if necessary.[141]

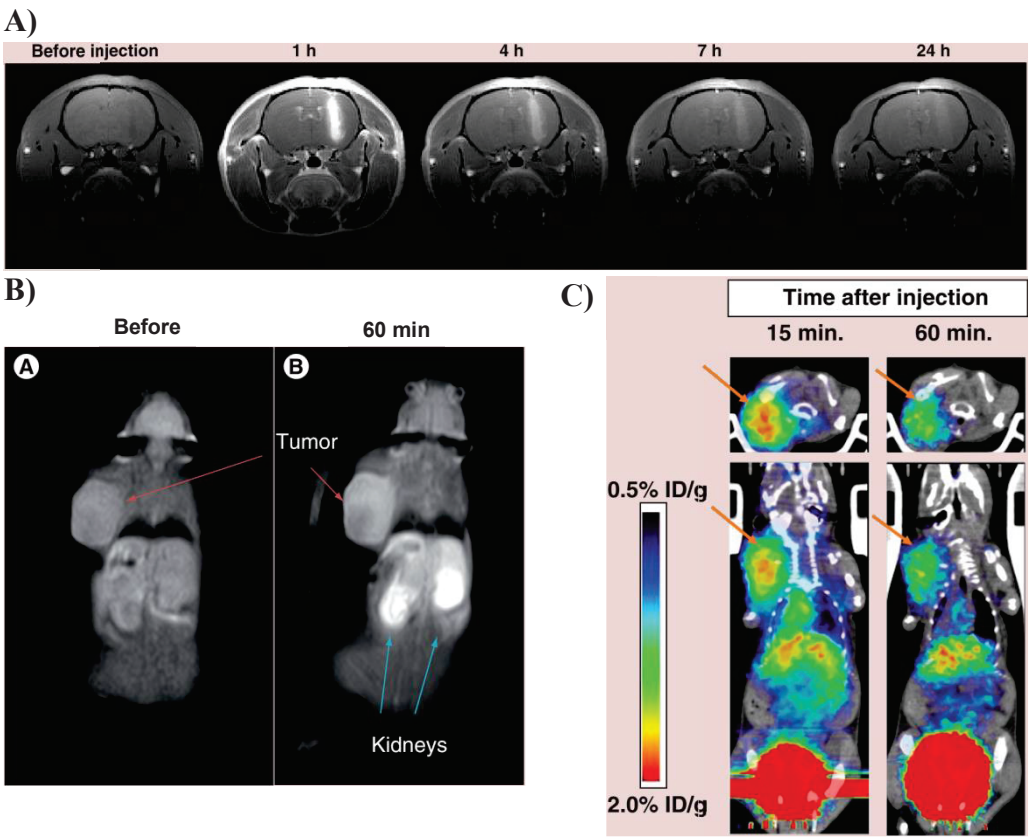

Figure 1-16. Multimodal imaging to localize tumors using AGuIX.
A) T2- and T1-weighted MR images of 9L-ESRF-bearing rats after iv injection of AGuIX.
B) T1-weighted magnetic resonance images and C) PET images of a U87MG tumor-bearing after iv injection of AGuIX@NODAGA-68Ga. Images taken from refs [140, 141].

Besides these macroscopic techniques, fluorophore conjugated AGuIX was indispensable for microscopic observations. Figure 1-17 shows some typical examples of using fluorescence microscopy for investigating AGuIX. In Figure 1-17-A, RhodamineB-AGuIX was used to assess the elimination of AGuIX in kidney tissues of mice.[131] After 4h, the kidney's cells were surrounded by intensive signal from rhodamineB. However, after 2 weeks, almost no fluorescence of rhodamineB could be detected anymore. This indicates an almost complete elimination of AGuIX through renal clearance. In Figure 1-17-B, Fluorescein-AGuIX was used to show the uptake of the particles by cancer cells.[135] The merged image shows that the particles have been well taken into cytoplasm of the cells. These techniques allow precise localization of the particles among microstructures inside tissues and cells.

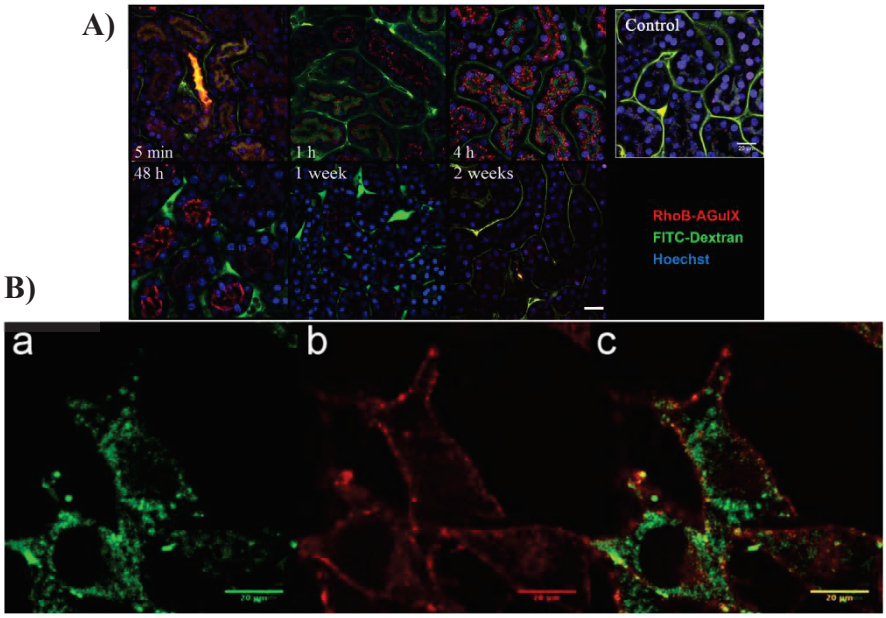

Figure 1-17. Microscopic images of AGuIX grafted with fluorophores.
A) Two-photon microscopy of mice kidneys after a single injection of RhodamineB-AGuIX (red). B) Fluorescence image of B16F10 cells obtained by confocal microscopy 1 hour after the addition of AGuIX-Fluorescein, the plasma membranes were labeled with Alexa Fluor 594 (a) at λex/λem = 499/520 nm (Fluorescein), (b) at λex/λem = 592/620 nm (Alexa Fluor) and (c) the merged image. Images taken from refs [131,135].

1.2.4.3. Radiosensitizing property of AGuIX

AGuIX is one of very rare Gd contained NPs that have been tested for RS property. Its effect has been demonstrated in many studies. A list of *in vitro* experiments that have been conducted is presented in Table 1-6. Briefly, AGuIX has shown the RS effect to different extent in cervical carcinoma (HELA) cells, head and neck carcinoma (SQ20B) cells, glioblastoma (U-87MG), Chinese hamster ovary carcinoma (CHO), pancreatic normal cells (Panc 1) and pancreatic adenocarcinoma cells (Capan-1) using different radiation sources from preclinical to clinical X-ray, heavy ions beam (C^{6+}, He^{2+}) or gamma ray (^{60}Co).

Table 1-6. Radiosensitizing effect of AGuIX in *in vitro* experiments. DEF: dose enhancement factor, SER: sensitizing enhancement ratio, SF: survival fraction, D^{50}: dose corresponding to 50% cell survival, EF: enhancing factor.

Investigator	Radiation energy	Cell line	[NP]/Incubation time	Biological effect
Luchette M. *et al.*[142]	220 kVp X-ray	Cervical carcinoma (HELA)	0.5 mM / 1h	SER_{4Gy} = 1.54 DEF = 1.54
	6 MV	Cervical carcinoma (HELA)	0.5 mM / 1h	SER_{4Gy} = 1.28 DEF = 1.15
Miladi I. *et al*[143].	250 kV	Head and neck carcinoma (SQ20B)	0.4 mM / 1h	SF_{2Gy} = 0.60 vs 0.72 SER_{2Gy} = 1.20
			0.6 mM / 1h	SF_{2Gy} = 0.35 vs 0.72 SER_{2Gy} = 2.0
Rodriguez L. *et al.* (unpublished data)	LET = 33.6 KeV/µm (C^{6+})	Head and neck carcinoma (SQ20B)	0.3 mM/ 1h	SER_{2Gy} = 1.33
			0.6 mM / 1h	SER_{2Gy} = 1.59
Detappe A. *et al.*[144]	220 kVp	Pancreatic normal cell (Panc 1)	0.5 mM / 1h	SER_{4Gy} = 1.41 DEF = 1.46
	6 MV	Pancreatic normal cell (Panc 1)	0.5 mM / 1h	SER_{4Gy} = 1.12 DEF = 1.19
Detappe A. *et al.*[145]	6 MV	Pancreatic adenocarcinoma (Capan-1)	0.43 g/l/15 min	DEF = 1.36 (6 MV-FFF) DEF = 1.22 (6 MV)
Detappe A. *et al.*[146]	6 MV	Pancreatic adenocarcinoma (Capan-1)	0.43 g/l/15 min	DEF = 1.37
Porcel E. *et al.*[76]	LET = 13 KeV/µm (C^{6+}) LET = 2.33 KeV/µm (He^{2+})	Chinese hamster ovary cell (CHO)	1 mM / 6h	D^{50} (Gy) = 1.90 vs 2.33 EF = 18.5 % D^{50} (Gy) = 2.19 vs 2.47 EF = 11.3 %
Stefancikova L. *et al.*[147]	1.25 MeV γ-ray (^{60}Co)	Glioblastoma (U-87 MG)	0.5 mM / 6h	SF_{2Gy} = 0.24 vs 0.31 SER_{2Gy} = 1.29

Stefancikova L. *et al.*[148]	1.25 MeV γ-ray (^{60}Co)	Glioblastoma (U-87 MG)	1 mM/1 h	SF_{1Gy} = 0.55 vs. 0.81 SF_{4Gy} = 0.37 vs 0.42

AGuIX has been tested in several *in vivo* models. Only some studies will be presented here as typical examples. Briefly speaking, AGuIX has shown the RS effect in gliosarcoma brain cancer models[136,140], non-small-cell lung cancer models[149], pancreatic adenocarcinoma models[145,146] and melanoma brain metastases model.[135] Among many types of cancers that have been tested we will only present the results for brain cancer either in glioma primary tumor or metastases form which is the first target of the group. This is one of the most challenging cancers since it is very aggressive and the prognosis of this disease is usually very poor while surgical resection is normally very difficult. In a recent study, our group has shown that AGuIX can improve the survival time of mice bearing orthotopic melanoma brain metastases after a 7 Gy X-ray irradiation compared to control group and irradiated alone group (Figure 1-18-B). In this study, MRI was used to find the peak accumulation time of AGuIX for irradiation planning (Figure 1-18-A).[135]

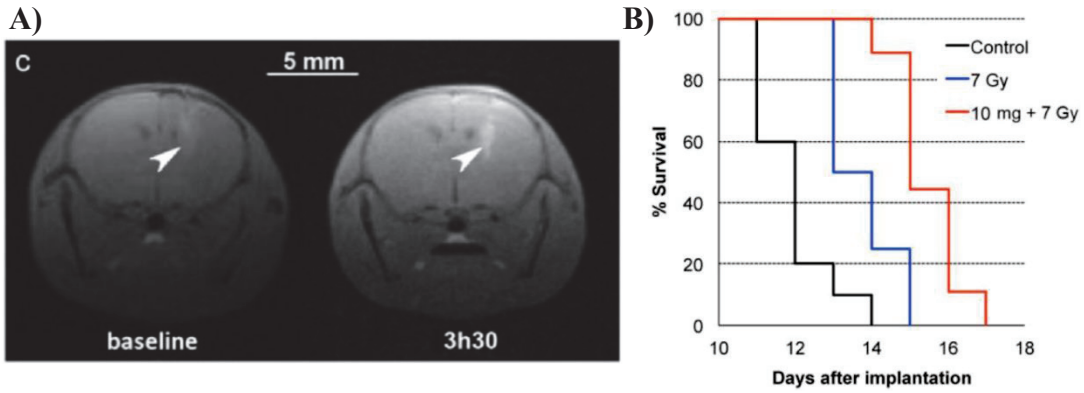

Figure 1-18. *In vivo* radiosensitizing effect of AGuIX in melanoma brain metastases model.
A) T1 -weighted images of the brain of B16F10-bearing mouse after iv injection of AGuIX.
B) Survival curve obtained for brain B16F10 metastases-bearing mice.
Images taken from ref [135].

In another study, AGuIX has been shown to be effective in a rat glioblastoma model with clinical 6 MV beam (Figure 1-19). Average tumor volume measured by MRI was smaller in the case of irradiation after treated with AGuIX indicating that the combination can actually slow down the tumor growth more efficiently compared to irradiation alone.[140] These promising results encourage the launching of on-going phase I clinical trial for the treatment of brain metastases using AGuIX along with whole brain radiation therapy (NANO-RAD; ClinicalTrials.gov Identifier: NCT02820454).

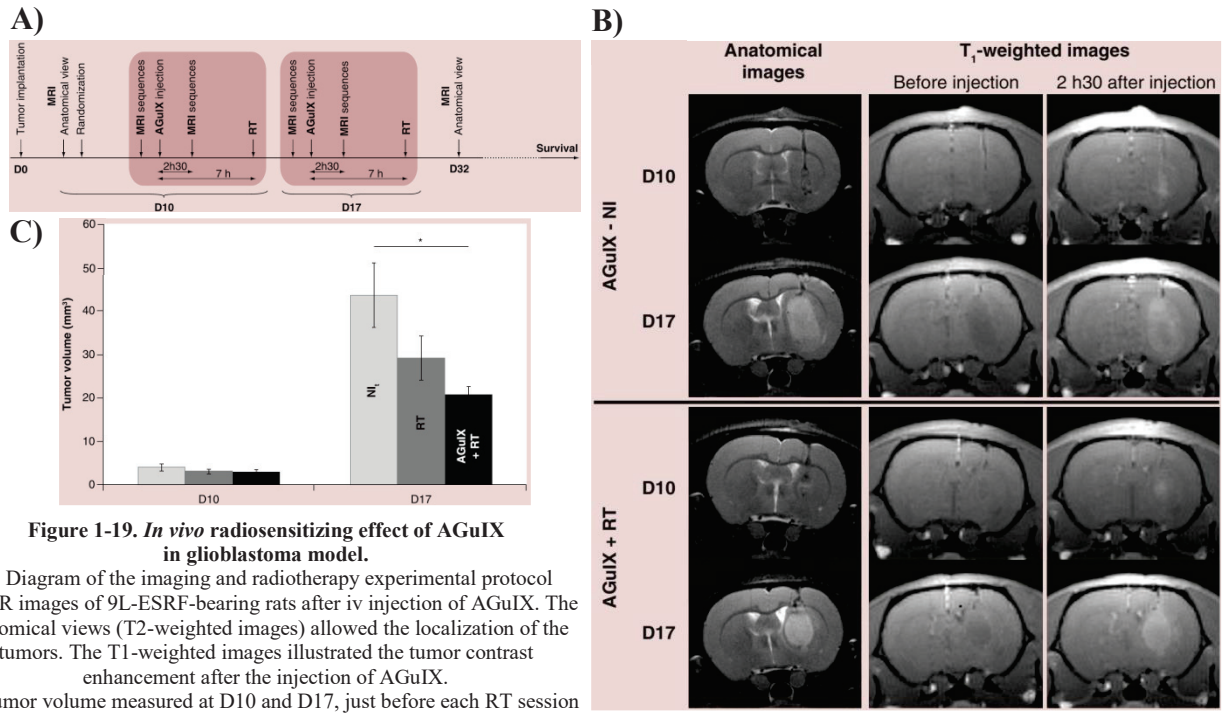

Figure 1-19. *In vivo* radiosensitizing effect of AGuIX in glioblastoma model.
A) Diagram of the imaging and radiotherapy experimental protocol
B) MR images of 9L-ESRF-bearing rats after iv injection of AGuIX. The anatomical views (T2-weighted images) allowed the localization of the tumors. The T1-weighted images illustrated the tumor contrast enhancement after the injection of AGuIX.
C) Tumor volume measured at D10 and D17, just before each RT session for non-irradiated animals, irradiated animals without particle and irradiated animals after NPs' injection.
Images taken from refs [140].

1.2.4.4. Active targeting strategies performed on AGuIX

Besides relying only on EPR effect, AGuIX has also been grafted with different targeting ligands to improve their accumulation in disease sites. These ligands range from small organic molecules to biologics i.e. peptides or antibodies (Figure 1-20). Morlieras J. *et al.* have used quaternary pyridinium to enhance the affinity of AGuIX to proteoglycans abundant in cartilages and chondrosarcoma tumors. This is highly relevant for clinical context since chondrosarcoma is a very stubborn cancer form that is resistant to most of radiotherapy and chemotherapy treatments. The functionalized particle has been shown to effectively accumulate and retain in cartilage and chondrosarcoma tumor longer than the non-functionalized one.[150,151] She and colleagues also used quinoxaline derivative to target melanin which is overexpressed in melanoma tumors.[152] Several peptides have also been conjugated to AGuIX to add more modalities. Morlieras J. et al. has also grafted cyclic form of RGD peptide (cRGDfK) that is well known as having a high affinity to $\alpha_v\beta_3$-integrins overexpressed in a wide range of cancer cell lines. She has shown the effective targeting enhancement of functionalized NP in *in vitro* and *in vivo* models.[153] Dentamaro M. *et al.* has used TLVSSL (E3) peptide which has a high affinity to phosphatidylserine externalized on apoptotic cells. This peptide can be used to monitor the treatment efficiency by quantifying the radiation-induced apoptosis.[154] Apart from cancerology, early detection of Alzheimer's disease is also a recent research topic in our group. Plissonneau M. *et al.* has shown in her papers the ability to conjugate AGuIX with LPFFD and KLVFF peptides, Pittsburgh compound B or nanobody that have high affinity towards β-amyloid fibrils, one of the main established causes of the Alzheimer's disease.[155,156]

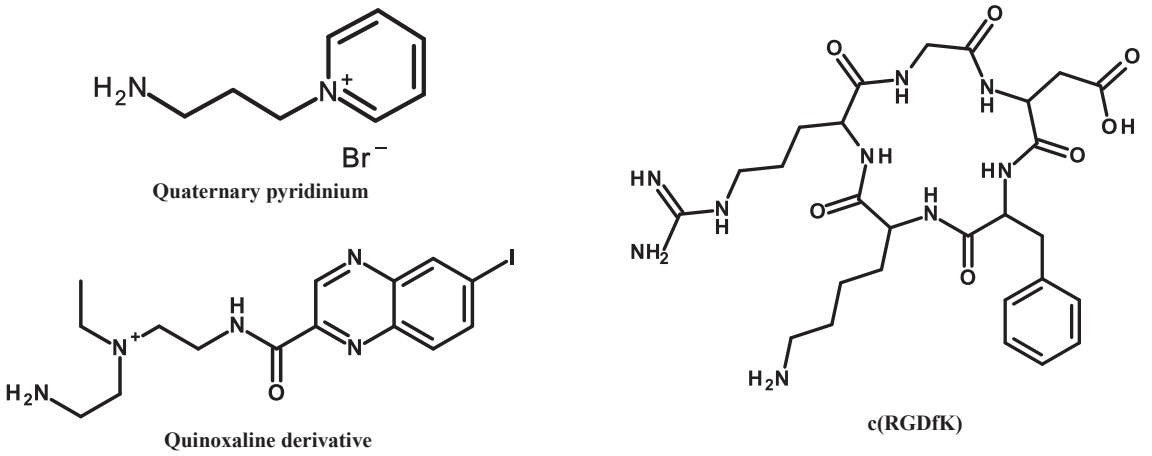

Figure 1-20. Some targeting ligands that have been grafted on AGuIX.

1.2.4.5. Technical difficulty in synthesizing ultrasmall silica NPs

We have seen many of valuable properties of AGuIX NP. However, the synthesis of AGuIX is not straightforward because there are very few or almost no well-documented techniques that allow the fabrication of such small-size silica NPs.

1.2.4.5.1. Classical synthesis methods in the literature

Silica nanoparticle (SNP) can be synthesized by conventional sol-gel method first described by Stöber *et al.* and later optimized by several authors where silane precursors were hydrolyzed and condensed in a mixture of water/ethanol at certain ratio catalyzed by ammonia or amino acids.[157–162] This method can be easily performed at large scale to obtain homogenous particles with the diameter down to tens of nanometres. However, producing homogenous silica NPs with D_H < 10 nm was still challenging.

Recently, Wiesner U. *et al.* modified Stöber method to synthesize ultrasmall silica NP with D_H ~ 7 nm (C dot). This SNP showed a high versatility since it can incorporate various active components i.e. near infra-red dyes, ^{124}I radioisotope, anticancer drugs and targeting peptides. It has obtained the approval from FDA for a phase I clinical trial in human as an intraoperative bimodal (PET/OI) probe for lymph node metastases.[53,54,163–166] Recently, they turned the whole synthesis into completely water-based (C' dot) (Figure 1-21).[167] They were able to tune the size of the final particles in the range of 4 – 8 nm. This synthesis comprises at least 3 steps. First, it relies on the fast hydrolysis and slow condensation in water of methyl orthosilicate, including fluorescent dyes conjugated organosilane i.e. 3-mercaptopropyl trimethoxysilane (MPTMS) and network-forming silane i.e. trimethoxy orthosilicate (TMOS) to form ultrasmall silica cores. Second, another layer of polysiloxane is formed by the slower hydrolysis and condensation of tetraethyl orthosilicate (TEOS) to protect the dyes from the environment. Finally, the growth of the polysiloxane

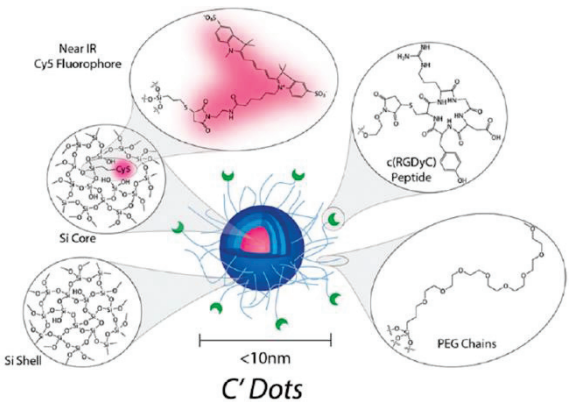

Figure 1-21. C' dot ultrasmall SiNP. Image taken from ref [167].

layer is terminated by methoxy(polyethyleneoxy)propyl-trimethoxysilane (PEG-silane, 0.5 kDa). This layer protects the coalescence between particles and prevents the adsorption of protein when the particles are used *in vivo*.

Another method which allows synthesizing rather small (down to 10 nm) and more homogenous silica NPs is inverse micro emulsion. This method requires using an emulsion system comprising of oil and surfactants to create micro reactors for the hydrolysis and condensation of silanes.[168] Our lab has used this method to coat 5 nm gold cores to obtain total 50 nm core-shell NPs.[169,170] Recently, Wiesner U. *et al.* have filed a patent claiming the synthesis of a mesoporous silica NP with average D_H less than 15 nm.[171] However, the effect of oil and surfactants on other active components in the formula needs to be taken into account. In addition, this implies a more complicated procedure of purification to remove these reactants.

1.2.4.5.2. AGuIX's top-down synthesis

AGuIX was discovered accidentally in an experiment designed to reduce the coating thickness of a more classical ultrasmall Gd_2O_3 core – silica shell structure (Gd_2O_3@SiO_x) (Figure 1-22).[133] The initial Gd_2O_3@SiO_x ultrasmall NP surprisingly fragmented in water to produce a highly colloidally stable ultrasmall structure with silica core on which organosilanes containing amine groups and Gd chelates were exposed. This is how the final structure of AGuIX has been obtained.

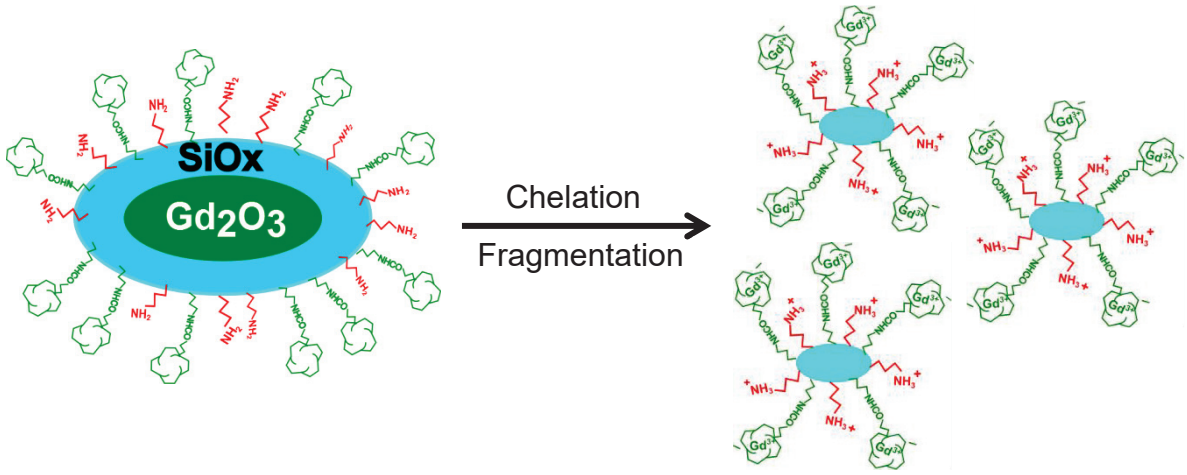

Figure 1-22. Simplistic representation of the innovative fragmentation step during the top-down synthesis.

This top-down method for synthesizing AGuIX is, even though highly innovative, still quite time and material consuming. The construction of classical Gd_2O_3@SiO_x platform before the fragmentation already requires tremendous efforts. The final product also requires a long purification process to remove reagents and the organic solvent used in previous steps. Besides, it implies the difficulty to change or add different metals post-synthetically.

1.3. The aims of my thesis

Therefore, the main aim of this thesis is to explore novel synthetic approach that can overcome the above limitations. Such a method when being realized will allow not only saving production cost of the product but also offering an unprecedented flexibility and gaining substantial knowledge in the fundamental nanochemistry of AGuIX particle. The fact

that different metals can be easily added on the new particle would lead to many more potential applications in diagnostic and therapeutic applications in cancerology. In the second part of the thesis, different functionalization strategies have also been realized on AGuIX for different purposes. Firstly, chelating silanes have been synthesized and grafted on AGuIX through silane chemistry to introduce more free chelators for radioimaging. This strategy presents an unusual but very effective way of functionalization on siloxane particles such as AGuIX without compromising their nanostructures. Second, a multifunctional chelate containing specific chelator for small ions and a tumor-targeting near-infrared (NIR) fluorophore was grafted on AGuIX to potentially give a trimodal targeting nanoprobe combining MRI, radioimaging and optical imaging in a single platform. Finally, a new strategy was realized to graft quaternary ammonium on AGuIX for further *in vivo* experiments demonstrating its active targeting and superior RS effect in chondrosarcoma. All of these projects further strengthen our knowledge in molecular engineering of ultrasmall nanoparticles such as AGuIX.

CHAPTER 2

The development of one-pot bottom up synthesis of ultrasmall silica nanoparticles (USNP)

Chapter 2. The development of one-pot bottom up synthesis of ultrasmall silica nanoparticles (USNP)

2.1. Synthesis and characterization of current USNP (AGuIX)

Before going to the new synthesis protocol, it is necessary to briefly recapitulate in details what have been done so far to synthesize and characterize AGuIX NP. During my thesis, I have participated to the development of different complementary characterization methods to further clarify the structure of AGuIX.

2.1.1. Current top-down synthesis of AGuIX

As have been discussed previously, the current synthesis of AGuIX is done via an original top-down process. A more detailed scheme is presented in Figure 2-1. First, a small, 1 to 3 nm, gadolinium oxide core was synthesized in diethylene glycol (DEG). This process is called polyol method taking advantage of high viscosity and boiling temperature of DEG to produce small oxide particles.[172] Then, this core was coated with a thin layer of polyorganosiloxane by hydrolysis and condensation reaction of alkoxysilanes. Next, this layer was functionalized with DOTAGA anhydride. After that, the nanoparticle was transferred to water for biological application. Unexpectedly, this process dissolved the core and released Gd^{3+} ions, which were chelated gradually by DOTAGA. The polysiloxane coating layer which did not have an internal support anymore collapsed and fragmented to form ultrasmall colloidally stable nanoparticles. These nanostructures are what we called AGuIX.[133,137]

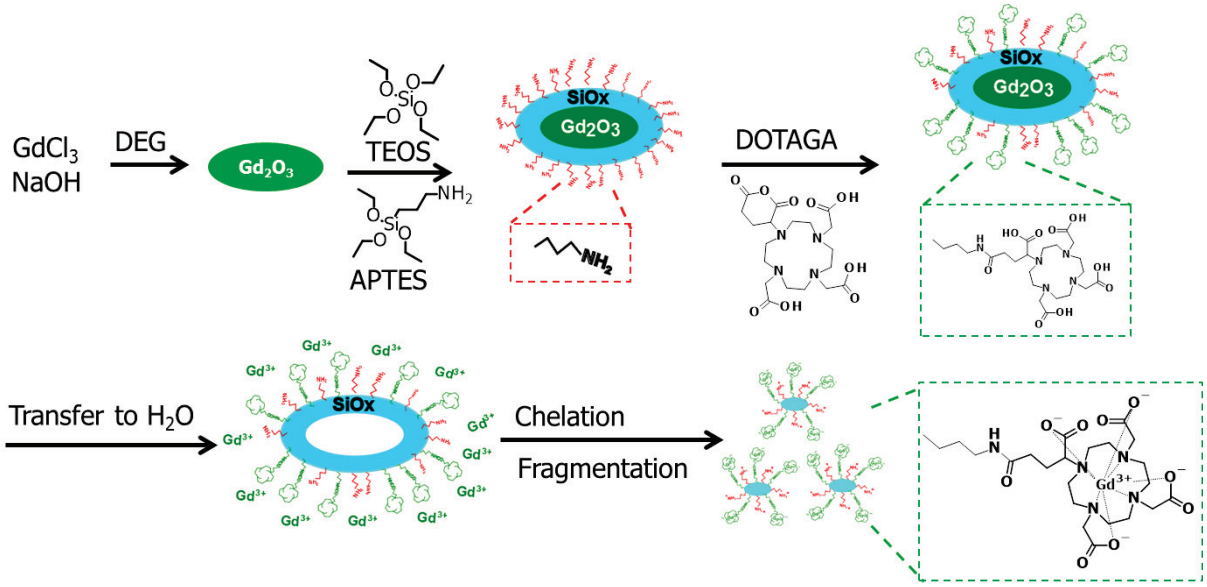

Figure 2-1. Scheme of top-down synthesis of AGuIX

During the development of AGuIX, many physico-chemical studies have been done to characterize this ultrasmall NP. Table 2-1 summarizes the results obtained so far for AGuIX in different studies and the respective references.

Table 2-1. Physico-chemical characterization of AGuIX

Properties	Method(s)	Results	Reference(s)
D_H (nm)	DLS	3 – 5	Quality control (QC) data
	NMR DOSY	3 – 5	Truillet et al.[27,173]
Zeta potential (mV)	Zeta potentiometry	0 – 9 (pH 7.4)	QC data
Retention time (min)	HPLC (295 nm)	13 – 15 (depends on column, solvent program)	QC data
Peak shape	HPLC (295 nm)	Symmetrical	QC data
Purity (%)	HPLC (295 nm)	> 90 %	QC data
Gd : Si : N : C (% mass)	Elemental analysis	14 : 12 : 27.1 : 7.5	QC data
Gd : A-D : A : T (molar ratio)	(Calculation)	1.0 : 1.0 : 1.0 : 3.0	-
Gd content (µmol/mg)	Elemental analysis	0.89	QC data
r_1 ($mM^{-1}.s^{-1}$) (37°C, 60 MHz)	Relaxometry	13 – 14	QC data
r_2/r_1 (37°C, 60 MHz)		1.3 – 1.4	QC data
Gd_2O_3 remnants	SQUID	No	Mignot et al.[133,174]
	EPRS	No	Mignot et al.[133,174]
Gd_2O_3 crystallinity	TEM	No	Mignot et al. [133,174]
Complexation constant ($log\beta_{110}$)	Potentiometry	24.78 ($log\beta_{110\ DOTAREM}$ = 25.58)	Mignot et al. [133,174]
Molar mass (kDa)	ESI-MS	8.5 and 9.7	Truillet et al.[27,173]
Free DOTAGA	Eu titration	1	Thomas et al.[175]
	Xylenol orange titration	1.5	Thomas et al.[175]
	HPLC with Cu^{2+}	2	Thomas et al.[175]
Degradation $t_{1/2}$ (min)	DLS, Relaxometry, HPLC (UV)	18 – 20	Le Duc, Marais, Truillet et al.[27,136,176]

**A-D: APTES-DOTAGA, A: APTES, T: TEOS*

2.1.2. Characterization of the top-down mechanism

First, to prove the dissolution of the initial Gd_2O_3 core, the final particle was carefully verified by SQUID (superconducting quantum interference device), electron paramagnetic resonance spectroscopy (EPRS) and transmission electron microsopy (TEM).

In SQUID, Neel temperature of AGuIX (0.11 K) is comparable to the value of DOTA(Gd) chelates (0.13 K) and significantly lower than the one of Gd_2O_3@PEG NP (1.72 K) and bulk Gd_2O_3 (17-18 K). This showed the absence of magnetic interaction between Gd atoms. In other word, Gd ions are well separated by the chelates.

In EPRS, typical X-band spectrum of Gd^{3+} complex with clear signal at around 3200 G (0.32 T) was obtained instead of nearly zero signal of Gd_2O_3 (Figure 2-2).[174]

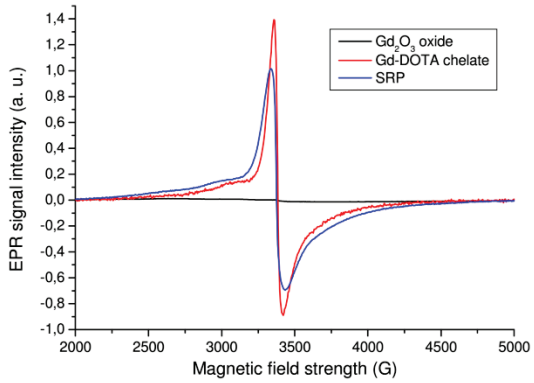

Figure 2-2. EPRS spectra of Gd_2O_3 (black), Gd-DOTA chelate (red) and AGuIX (referred as SRP) (blue) at 2.4 mM in Gd.[174]

Meanwhile, in high resolution TEM, crystallinity pattern of Gd_2O_3 was no longer observed in the sample of AGuIX after DOTAGA was added (Figure 2-3).[174]

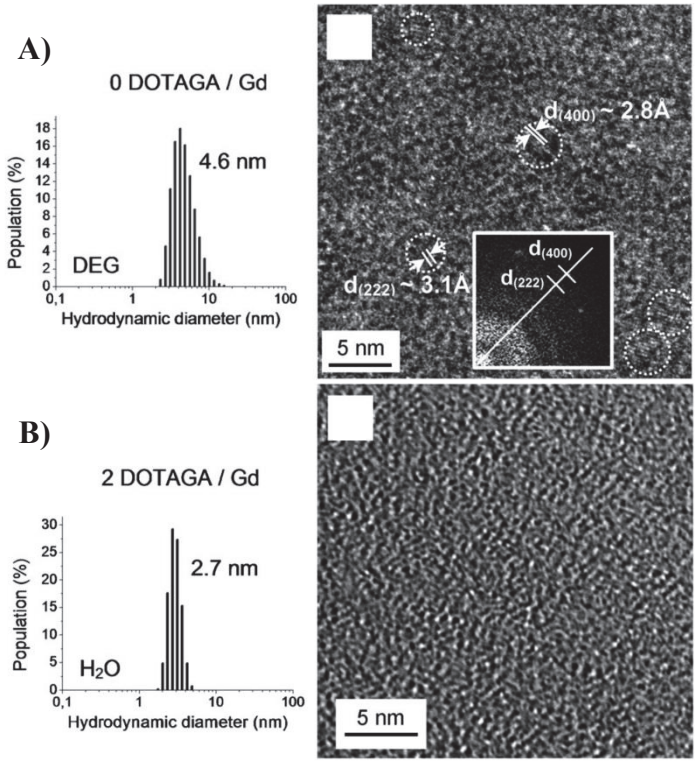

Figure 2-3. DLS measurement (left) and high resolution TEM image (right) of A) the core-shell particle before DOTAGA was added and B) the fragmented particle after DOTAGA was added.[133]

These results proved that Gd_2O_3 no longer remains but all chelated by DOTAGA during the fragmentation. This is also important for safety reason since an uncoated Gd oxide core can act as a reservoir to gradually release toxic free Gd^{3+}.

2.1.3. Characterization of the final product

2.1.3.1. Previous results

As we have seen before, some properties such as D_H, zeta potential, retention time in chromatography, homogeneity and purity, elemental composition and relaxivity have been regularly verified by DLS, zeta potentiometry, HPLC, elemental analysis and relaxometry for

each produced batch as a part of quality control (QC) requirements. Average results have been shown in Table 2-1.

Besides, some complementary characterizations have been done to further elucidate the structure of this NP. For example, complexation constant of DOTAGA on AGuIX towards Gd^{3+} was proven to be equivalent to the value of commercial DOTA ($log\beta_{110(AGuIX)}$ = 24.78 vs. $log\beta_{110(DOTA\text{-}Gd)}$ = 25.58).[133] This ensures the stability of the complex in *in vivo* condition.

Free DOTAGA on the particle has been determined by different assays (Eu titration, Xylenol orange titration or HPLC probed with Cu^{2+}). The results in all cases are from 1 to 2 % of total amount of DOTAGA.

Diffusion ordered spectroscopy using nuclear magnetic resonance (NMR-DOSY) has been carried out to not only confirm ultrasmall D_H (3 – 5 nm) of AGuIX but also to show the presence and integrity of organic groups on the particle (Figure 2-4).

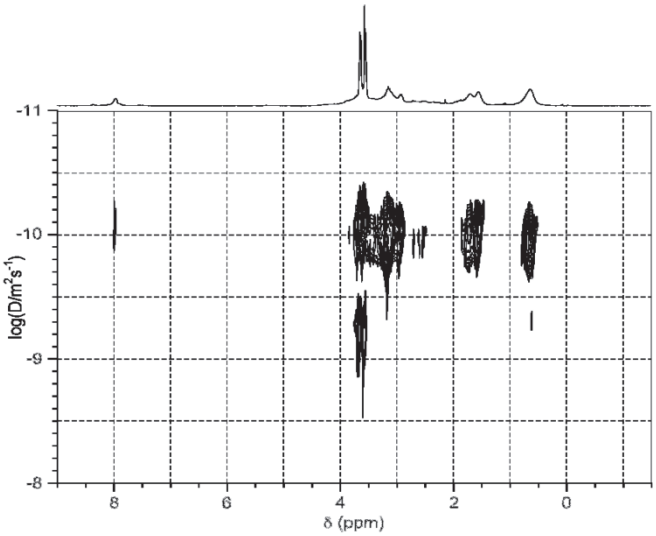

Figure 2-4. 1H NMR-DOSY spectrum of AGuIX in D_2O at 30 g/l (diffusion delay 100 ms, gradient pulse length 2.75 ms)[133]

Molar mass of a single particle was measured by electrospray ionization mass spectrometry (ESI-MS) and deconvoluted by a multiplicative correlation algorithm (MCA) to give a main value around 8.5 kDa and another smaller population at 9.7 kDa (Figure 2-5).

Although these results show a quite extensive level of characterization for this NP, some aspects still need to be clarified in the structure of AGuIX. Therefore, we decided to conduct some complementary studies using small angle X-ray scattering (SAXS), NMR-DOSY (data processed by a more suitable software) and ESI-MS (using a more adapted apparatus).

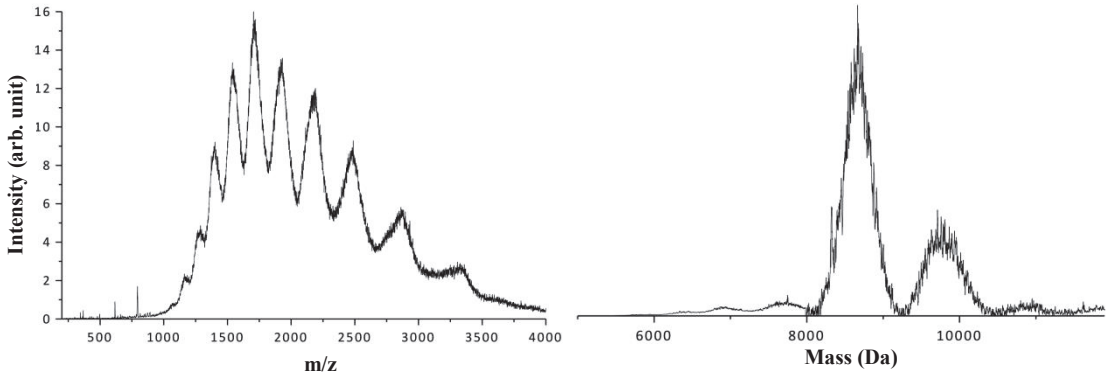

Figure 2-5. ESI-MS spectrum (left) and corresponding deconvoluted spectrum (right) of AGuIX.[27]

2.1.3.2. Complementary characterizations conducted during my thesis

2.1.3.2.1. Radius of gyration of AGuIX by SAXS

As shown above, the size of AGuIX has been determined by different techniques. However, each of them presents some limitations.

Hydrodynamic diameter of the particle has been measured using DLS (photon correlation spectroscopy) and NMR-DOSY. DLS showed values in the range of 3 – 5 nm which is very close to the limit of detection for this method. NMR-DOSY, on the other hand, requires replacing paramagnetic Gd^{3+} with a diamagnetic equivalent (Lutetium or Yttrium).

Physical size of the particle could be determined by electron microscopy. However, the contrast of the silica matrix of AGuIX is not high enough to allow quantitative measurement.

Hence, we propose here to use SAXS to measure the radius of gyration (R_g) of AGuIX. R_g is defined as average of square distances from center-of-mass to every element in the object weighted by the scattering length density which is proportional to the mass of the corresponding element (Equation 2-1). This parameter is similar to the physical size measured by electron microscopy. Given to the poor contrast obtained in our previous experiments with electron microscopy techniques, SAXS can be considered as a good alternative.

$$R_g = \sqrt{\frac{\sum m_i r_i^2}{\sum m_i}} \qquad \textbf{Equation 2-1}$$

Where
m_i: mass of an element i
r_i: distance from element I to the center-of-mass

Another minor strong point of SAXS is wider range of concentration of samples that can be measured. In DLS, AGuIX is normally diluted to a moderate concentration (~ 10 g/l) in order to avoid high absorption and high viscosity of the sample. However, as shown in many studies, polysiloxane backbone of AGuIX might start to degrade at this concentration and give wrong results.[8–10] In SAXS, a synchrotron X-ray was used as the light source. Thus, even if the signal is reduced by the absorption at high concentration, there should be enough scattering light for measuring. In addition, this method is not based on diffusion physics so the result is independent on viscosity of the sample.

2.1.3.2.1.a. Principle of SAXS

In SAXS, X-ray source irradiated a solution sample. Figure 2-6 briefly shows the principle of SAXS. The incident light was collimated to be a monochromatic plane wave with wave vector $k_0 = 2\pi/\lambda$ (λ is the wavelength of the X-ray beam). Atoms in the objects interact with the incident radiation and become secondary wave sources. The scattering light waves from them interfere with each other to create different patterns on a detector. Each pattern represents the resulting scattering wave vector k_1. By applying a Fourier transform, data can be converted from real space of laboratory coordinate (r) to reciprocal space of scattering vector q (or s, depending on the annotation system) = $k_1 - k_0$. The scattering intensity I will be in a function of the scattering vector q. This function has different form depending on the structure of the objects in the solution and their interactions. There are different mathematical models to exploit this scattering function. The most often used is the Guinier's approximation. At very small q, I(q) is proportional to q^2 (Equation 2-2). This parabolic equation can be easily fitted to give radius of gyration (R_g). If we assume the particles are homogeneous spheres, then the hydrodynamic diameter can be easily calculated from R_g (Equation 2-3).[180–182]

$$I(q) \approx I(0)\exp(-\frac{1}{3}R_g^2 q^2) \qquad \textbf{Equation 2-2}$$

Where
I(q): light intensity at wave vector q
I(0): incident light intensity
Rg: radius of gyration

$$D_H = 2\sqrt{\frac{5}{3}R_g^2} \qquad \textbf{Equation 2-3}$$

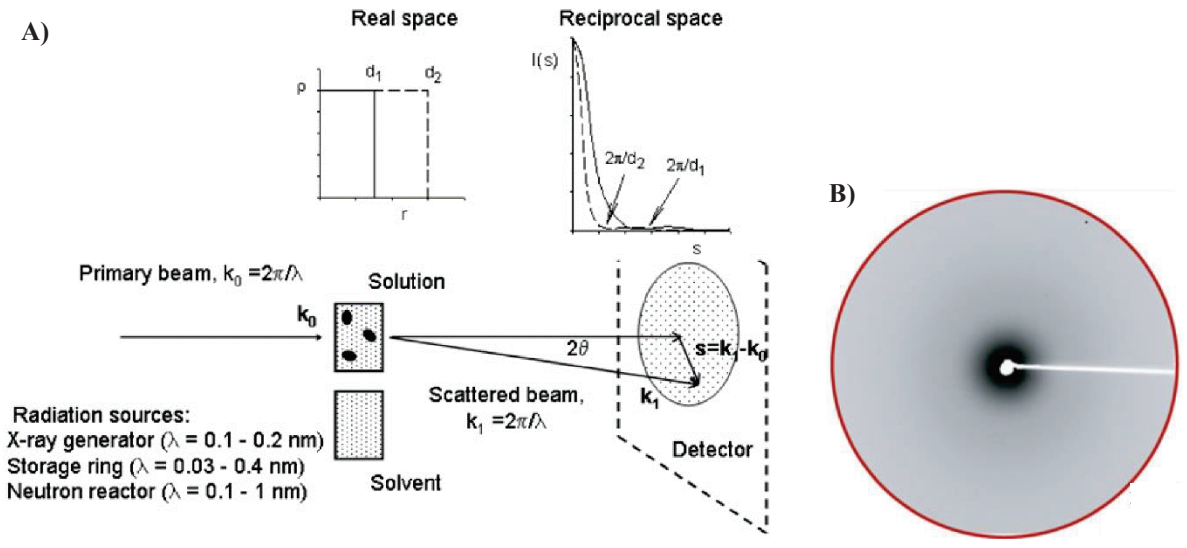

Figure 2-6. A) Schematic representation of the principle of SAXS; B) A real example of scattering patterns obtained on the detector. Image taken from ref [181].

2.1.3.2.1.b. Results

The experiments were conducted at European Synchrotron Radiation Facility (ESRF) in Grenoble under the main instruction of Dr. Guillaume Sudre and Prof. Laurent David (Ingénierie des Matériaux Polymères, UCBL I). Data were treated by Dr. Sudre G. using an

in-house program compiled on IGOR Pro. The measurements for normal AGuIX samples synthesized in the laboratory and clinical AGuIX samples synthesized in a GMP factory were shown in Figure 2-7. The Guinier's equation was nicely fitted with the real data. The D_H values inferred from the radii of gyration of two batches were in accordance with the results obtained directly from DLS. This result confirms the validity of DLS measurement.

A)

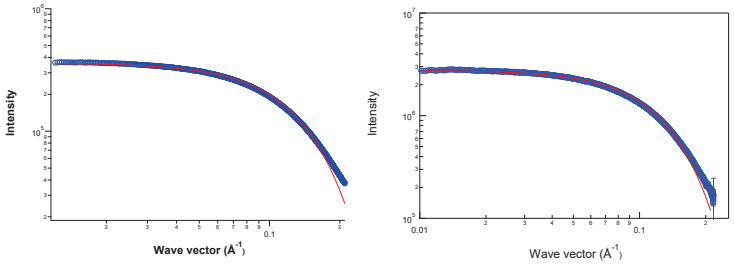

B)

Samples	Rg	$D_{H(cal.)}$	$D_{H(DLS)}$
AGuIX (100mM)	1.36	3.51	3.06
Clinical AGuIX (50mM)	1.46	3.77	3.96

Figure 2-7. A) Real data obtained from normal AGuIX sample (left) and clinical AGuIX sample (right) (blue circles) and respective Guinier's fits (red lines). B) Radiation of gyration (R_g) and hydrodynamic diameters (D_H) calculated from R_g or measured by DLS.

2.1.3.2.2. Hydrodynamic diameter and structure of AGuIX by NMR and NMR-DOSY

The NMR-DOSY measurement carried out previously used a conventional Topspin processing software which might not give a perfect result for samples with several species having very different diffusion coefficients as AGuIX. Therefore, it is necessary to redo the experiment while using a more adapted software, NMRNotebook, developed by NMRTEC.[183] Furthermore, besides diffusion coefficient, more advanced structural information can also be withdrawn from NMR spectra.

But as briefly mentioned above, this technique cannot be used directly on Gd contained particles such as AGuIX. Paramagnetic ions can hardly be studied in NMR since they can shorten the relaxation times and so broaden the peaks in the spectrum.[184] Short relaxation time will also disable the pulse sequence designed for DOSY measurement. Gd^{3+} is the most paramagnetic ion in the periodic table, thus, the NMR spectrum of Gd^{3+} containing species is disastrous with almost only one huge peak of proton residue of solvent. Therefore, to investigate the structure of AGuIX using NMR, it is obligatory to replace Gd^{3+} by a diamagnetic ion. In this thesis, we replaced Gd^{3+} in the synthesis by diamagnetic metals such as Lu^{3+} or Y^{3+} for NMR experiments. Lu is chosen since it is another member of lanthanide group which is well known for similar chemical properties, while Y has the same atomic radius (180 pm) as Gd and has very similar electronic configuration as well as chemical property as lanthanides[185]. For this particular experiment, we used Y^{3+} since the NP obtained after the synthesis showed more similar physicochemical properties to AGuIX NP.

2.1.3.2.2.a. Principle of NMR-DOSY

In 1965, Tanner J. E. and Stejskal E. O. introduced for the first time the use of NMR to distinguish the diffusion coefficients of different molecules in a solution. This discovery opened a new and important branch of NMR technique, diffusion ordered spectroscopy or

DOSY.[186] Simplistically, in a DOSY experiment, pulsed field gradients (G) are applied along the z-axis. Figure 2-8-A shows the pulse sequences normally designed for DOSY experiment. The very first DOSY experiments employed pulsed field gradient (PFG) spin-echo sequence. Nowadays, PFG stimulated-echo sequence is more commonly used. The latter enables longer delay time for measuring macromolecules. Nevertheless, the basic principle remains the same. Basically, the first gradient pulse (G_1) will impose a spatially dependent phase on the magnetization vectors. There will be another 180° pulse (PFG spin-echo) or two 90° pulses (PFG stimulated-echo) which are applied before a second gradient pulse of equal duration and magnitude is sent to refocus the magnetization vectors' phase. However, during this process, molecules in the solution will diffuse away and so the refocusing process will not be completely efficient. Figure 2-8-B shows an example of two molecules (A, B) with two different diffusion rates. They will "feel" different field strengths before the second gradient pulse is applied. This leads to an attenuation in the obtained magnetic signal intensity and the extent of the attenuation depends on the diffusion rate of each molecule. Tanner J. E. and Stejskal E. O. discovered an exponential relation between the observed signal intensity, gradient strength and diffusion coefficient of the molecule (Equation 2-4, Figure 2-8-C). So by measuring the attenuated intensity at different gradient strength and fitting to this equation, we will be able to find out the diffusion coefficient.[187,188]

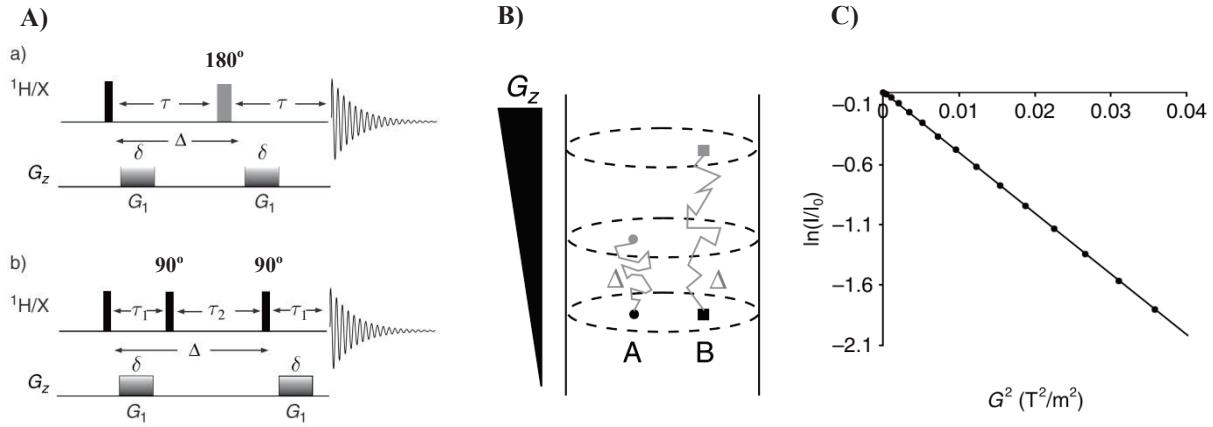

Figure 2-8. Principle of NMR-DOSY. A) Pulse sequences for measuring molecular diffusion based on (a) the PFG spin-echo and (b) the PFG stimulated-echo; B) A schematic representation of signal attenuation through molecular diffusion; C) Regression analysis to obtain the diffusion coefficient by fitting of linear decay ($\ln(I_G/I_{G=0})$ vs G^2). Images taken from ref [187].

$$I = I_0 exp\left[-\gamma^2 G^2 \delta^2 \left(\Delta - \frac{\delta}{3}\right) D\right] \qquad \textbf{Equation 2-4}$$

Where
I: signal intensity at a certain G
I_0: signal intensity in the absence of the gradient
γ: magnetogyric ratio of the observed nuclei
G: gradient strength
δ: gradient pulse duration
Δ: diffusion delay
D: diffusion coefficient

2.1.3.2.2.b. Treatment of DOSY data

So far, we are only able to achieve total diffusion coefficient curve of each chemical shift which might be composed of different diffusion coefficients from different species. Another complicated step is to make a deconvolution from this curve to find out how many species are behind each chemical shift and what their respective diffusion coefficients are. The very first

graphs were obtained using DOSY module integrated in conventional Topspin software (Bruker, Germany). However, the results were not satisfactory with low resolution and strange, unfinished shapes of the peaks (data not shown). The reason might be the incapability of this software to solve the equation of a complex sample containing different species with very different coefficients. Hence, we decided to use DOSY module of NMRNotebook (NMRTEC, France) to treat the data due to its potential higher capacity to deal with complex systems.[183]

2.1.3.2.2.c. Synthesis of diamagnetic ultrasmall silica yttrium nanoparticle USNP(Y)

The particle (Figure 2-9-A) was synthesized according to the top-down protocol of AGuIX with some modifications. First, $YCl_3.6H_2O$ was used instead of $GdCl_3.6H_2O$. Second, as the solubility of YCl_3 in DEG is limited, a small amount of water was added to help dissolve YCl_3. The product was characterized by DLS, HPLC and elemental analysis (Table 2-2 and Figure 2-9-B, C). The HPLC program used for this NP will be repeated for other samples if nothing is specified. The results suggest a highly similar structure to AGuIX. The particles have an average D_H = 5.2 nm with a homogeneous population revealed by HPLC chromatogram. Elemental analysis indicates a very similar composition of USNP(Y) compared to AGuIX with an approximated molecular formula $(TEOS)_{3.9}(APTES)_{0.9}(APTES\text{-}DOTAGA)_{1.0}(Y)_{0.9}$ assuming that APTES-DOTAGA, APTES and TEOS after condensed implies the molecular structure as $SiO_{1.5}(CH_2)_3NH\text{-}DOTAGA^{(2-)}$, $SiO_{1.5}(CH_2)_3NH_3^+$ and SiO_2 respectively.

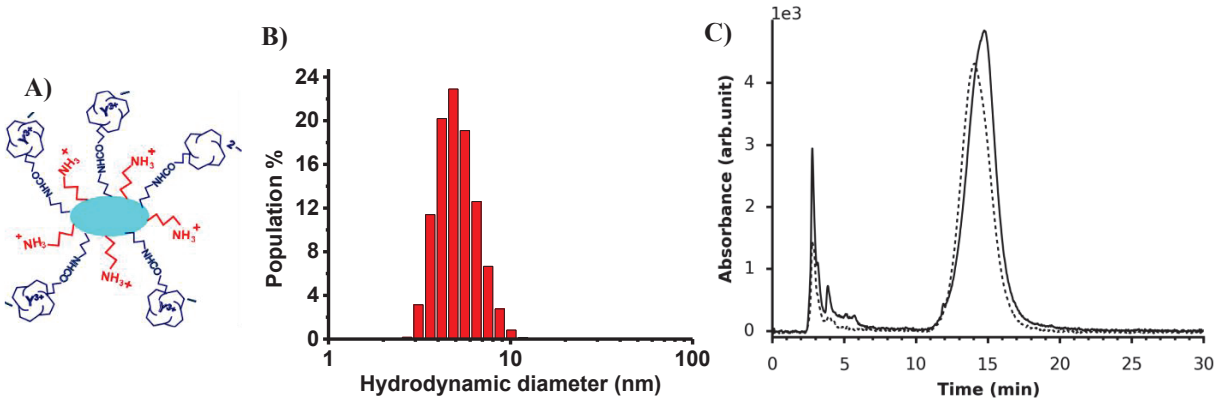

Figure 2-9. Characterization of USNP(Y). A) Schematic representation of USNP(Y); B) DLS diagram at 25 mM in Y; C) Chromatograms at 295 nm of AGuIX at 5 mM in Gd (dashed line) and USNP(Y) after purification diluted 4 times (solid line).
HPLC condition:
Injection volume: 20 µl
Column: Jupiter C4 column (150 mm × 4.60 mm, 5 µm, 300 Å, Phenomenex)
Flow rate: 1 ml/min
Detector: UV at 295 nm
Oven temperature: 30°C
Solventgradient: mixture of A: H2O/TFA (99.9:0.1) and B: Acetonitrile (ACN)/TFA (99.9:0.1)
1 – 7 min: 1% B; 7 – 22 min: to 90% B; 22 – 29 min: 90% B; 29 – 30 min: to 1% B ; 30 – 38 min : 1% B

Table 2-2. Characterization of USNP(Y)

Properties	Method(s)	Results
D_H (nm)	DLS (25 mM)	5.2 ± 1.4
	NMR DOSY (60 mM)	4.3
Retention time (min)	HPLC (295 nm)	14.7 min (vs. 14.0 min for AGuIX)
Purity (%)	HPLC (295 nm)	85.5% (vs. 92.1% for AGuIX)
Y : Si : N : C (% mass)	Elemental analysis	7.4 : 14 : 27.3 : 7.6

Y : A-D : A : T (molar ratio)	(Calculation)	1.0 : 1.1 : 1.0 : 3.9
A/A-D	(Calculation)	0.92
A/A-D	^{1}H NMR	1.54
Y content (µmol/mg)	Elemental analysis	0.83

**A-D: APTES-DOTAGA, A: APTES, T: TEOS*

2.1.3.2.2.d. NMR characterization of USNP(Y)

Measurements were performed by Ms. Baudouin A. and Mr. Fenet B., Common Center for NMR, University Claude Bernard Lyon I. Experiments were carried out at 298 K, without spinning, on a Bruker Avance III 500 MHz spectrometer (Bruker, Germany) equipped with 5 mm PABBI probe. For ^{1}H NMR diffusion experiments, the standard ledbpgp2s sequences were used. The diffusion delay d20 were set to 100 ms, and the bipolar pulses p30 were adjusted to obtain a 95% attenuation at full strength, typically in the range of 2 to 4 ms. 64 points of 32 scans each were acquired in the diffusion dimension, with 5s relaxation delay allowing full relaxation of protons, giving a total experiment time of 3 h..

Figure 2-10 shows the results of NMR characterization for USNP(Y). First, ^{1}H spectrum has been obtained (Figure 2-10-A). Due to faster relaxtion time induced by slower stumbling rate of NPs, all proton peaks have been more or less widened. 2D correlation spectroscopies including heteronuclear single quantum correlation (HSQC) and heteronuclear multiple bond correlation (HMBC) between ^{1}H and ^{13}C nuclei were also performed. HSQC spectroscopy shows the correlation between C and H directly bonded. A simple scheme is presented to show an example of this type of correlation (Figure 2-10-C, top). Meanwhile, HMBC spectroscopy shows the correlation between C and H indirectly bonded. Similarly, a simple scheme (Figure 2-10-D, top) shows an example of HMBC correlation. The results from two techniques show a strong direct correlation between ^{1}H-^{13}C couples at 0.63 – 8.9 ppm, 1.70 – 20.3 ppm and 2.93 – 41.7 ppm respectively and indirect correlations between them (Figure 2-10-C, D). Lehman S. E. *et al.* have shown that, in the structure of APTES, ^{1}H peaks at around 0.6, 1.7 and 2.9 ppm are from protons attached to the first, second and third carbon calculated from the silicon atoms.[188] Furthermore, Brambilla R. *et al.* have shown that ^{13}C peaks at around 9.4, 21.2 and 42.9 ppm are from those carbons respectively.[189] Combining these results, we can undoubtedly assign the peaks at 0.63, 1.70 and 2.93 in the ^{1}H spectrum of USNP(Y) for hydrogens that bind to the first, second and third carbon closest to silicon atom of APTES and APTES-DOTAGA functions grafted on the particles. Fortunately, despite its complicated spectrum, DOTAGA has no ^{1}H peak at higher field than 1 ppm[190] where the protons at carbon 1 (H1) can be found. The area of this peak is the sum of contributions from 2 protons of APTES and 2 protons of APTES-DOTAGA, whereas the total area of all of peaks is the sum of 6 protons of APTES and 33 protons of APTES-DOTAGA (only non-exchangeable protons were counted). Presumably, NP solution was free from other organic impurities. Solving this two-variable linear equation system will give the ratio between the amount of APTES over the amount of APTES-DOTAGA in the sample. In this case, the result was 1.54, while the value deduced from elemental analysis was 0.92.

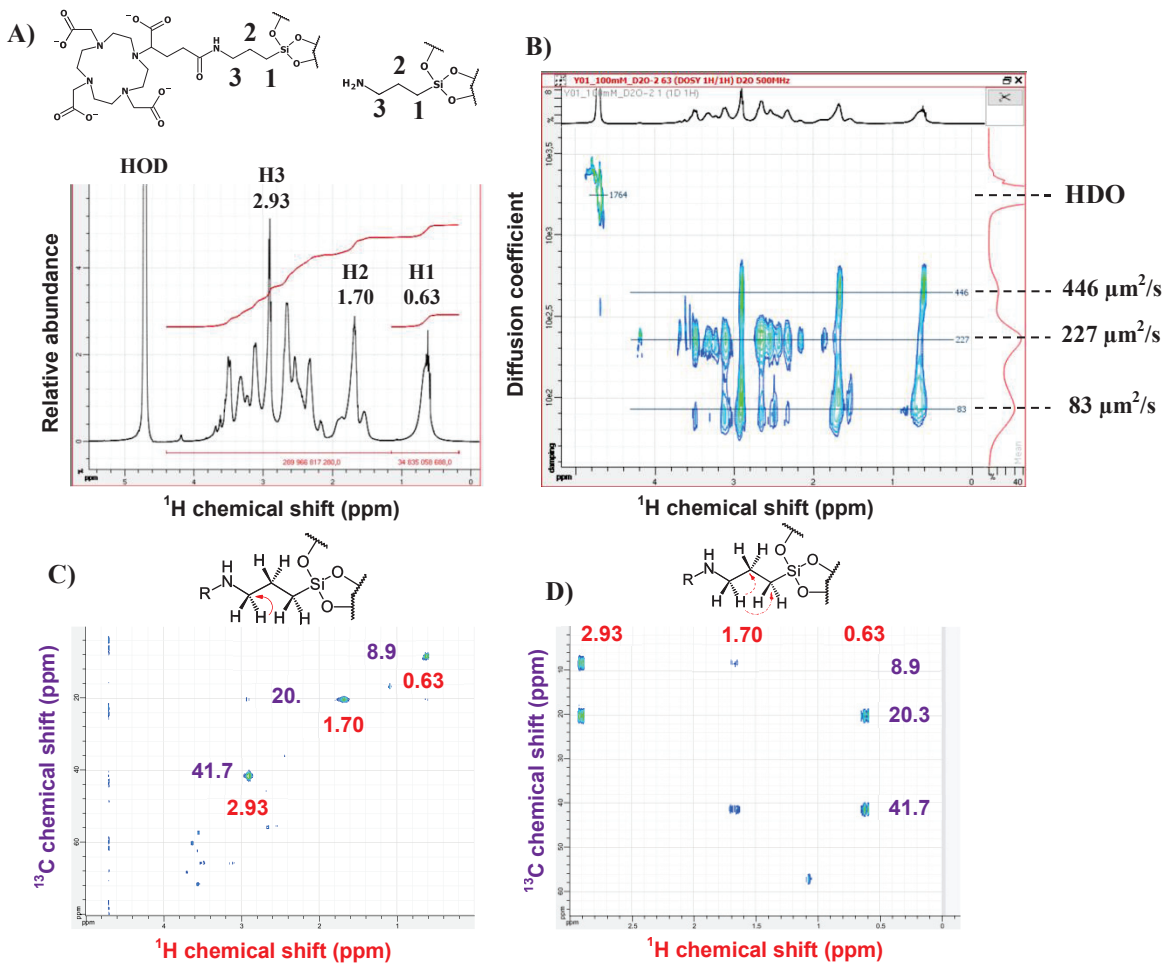

Figure 2-10. NMR results of USNP(Y). A) ^{1}H NMR spectrum, B) NMR-DOSY spectrum, C) HSQC 13C/1H spectrum (with an illustration (on top) of an example of HSQC correlation, the arrow shows the carbon which is in direct correlation with the example proton) and D) HMBC 13C/1H spectrum (with an illustration (on top) of an example of HMBC correlation, the arrow shows the carbons which are in indirect correlation with the example proton) of USNP(Y) at 60 mM in Y.

Then, DOSY experiment has been conducted to obtain the diffusion coefficients (D) of different species in the ^{1}H spectrum (Figure 2-10-B). At least, three populations have been identified with D as 83, 227 and 446 µm^2/s respectively. Obviously, the species with lowest D are the intact NPs, and the two others are smaller fragments issued from the hydrolysis of the particles. The intact particles have spots with all chemical shifts of ^{1}H spectrum indicating the presence of both types of functional groups APTES (-$(CH_2)_3NH_3^+$) and APTES-DOTAGA (-$(CH_2)_3$NH-DOTAGA$^{(2-)}$). The lack of some spots in the chemical shift of protons on DOTAGA in the smallest species (446 µm^2/s) implies fragments without DOTAGA. This explains their smaller size compared to the other fragments (227 µm^2/s). The deconvolution of diffusion coefficient curves with several species is not an easy task so the results can hardly be considered as a precise quantification method. If we assume the particles have spherical shapes, Stokes-Einstein's equation (Equation 2-5) can be applied to speculate the hydrodynamic diameter of the main NP which was 4.3 nm. This result corresponds well with D_H obtained by DLS. These are interesting methods that will be applied to other NMR-friendly samples in the subsequent sections.

$$D_H = \frac{k_B T}{3\pi\eta D}$$ **Equation 2-5**

Where
D_H: hydrodynamic diameter
k_B: Boltzmann constant
T: absolute temperature
η: viscosity
D: diffusion coefficient

2.1.3.2.3. Molar mass of AGuIX by ESI-MS-QTOF

Even though, ESI-MS has been performed previously to estimate the molecular mass of AGuIX[133,173], this technique can still be further improved. In my studies, the experiments were performed with micrOTOF-Q II from Bruker Daltonik, Germany. Compared to the previous system, linear quadrupole ion trap mass spectrometer (LTQ, Thermo Fisher Scientific, USA), this system offers a softer ionization condition and a wider range of value up to 10000 Th (vs. 4000 Th in LTQ). The higher range of m/z also allows tuning to even softer ionization condition without losing data in the high end of the spectrum. These characteristics of the system leads to better preservation of the macrostructure of AGuIX and reflect better its molar mass. The measurements were performed with technical assistance of Ms. Zerbino C.C. and Dr. Antoine. R., team Spectrobio, Institute of Light and Mater, University Claude Bernard Lyon I.

2.1.3.2.3.a. Principle of ESI-QTOF

A micrOTOF-Q-II system consists of electrospray ionization source, ion transfer system, quadrupole system and a time-of-flight (TOF) detector. As other ESI systems, sample solution will be sprayed into a capillary on which a high electric tension is applied to create at the other end of the capillary microdroplets of solution. These droplets are transferred to vacuum chambers. Solvent will be evaporated gradually and the droplets shrink until their charge densities become too high so that they will burst into smaller units. These events continue until only gas-phase ions remain and fly through the quadrupole and collision cell. In our case, only single MS was performed, so quadrupole will only work as an ion transmitter. In collision cell, they can be broken down for fragmentation analysis (MS/MS). In our case, fragmentation was rather minimized to preserve the integrity of the particle. Finally, the ions are analyzed by a reflector TOF analyzer based on their differences in arrival time to a detector which is proportional to their differences in m/z (Equation 2-6).[191–193]

$$t = \frac{s}{\sqrt{2eU}}\sqrt{\frac{m_i}{z_i}}$$ **Equation 2-6**

Where
t: arrival time to detector
s: travelling distance to detector
e: charge of an electron
U: applied voltage
m_i: mass of ion i
z_i: charge of ion i

2.1.3.2.3.b. Deconvolution algorithm

A typical m/z spectrum of a macromolecule generated by an ESI-MS system contains an envelope of peaks due to the multiplicity of charge states. Therefore, it is obligatory to

process the data through a deconvolution algorithm to extract a useful mass-only spectrum. An in-house software was developed based on multiplicative correlation algorithm (MCA)[26,194] to achieve this task. This approach is summarized in Equation 2-7.

$$I_m = \prod_{z=z_0}^{z_1} \frac{I_{m/z}}{I_{rms}}$$ **Equation 2-7**

Where
I_m: calculated intensity in the deconvoluted spectrum
$I_{m/z}$: measured intensities in the original m/z spectrum
z_o: minimum charge state
z_1: maximum charge state
I_{rms}: root-mean-square of the measured intensities

2.1.3.2.3.c. Results

Figure 2-11-A shows the MS spectra of AGuIX particles synthesized in GMP condition. The black one was obtained by LTQ apparatus and the violet one was obtained by micrOTOF-Q II apparatus. They are averaged from different spectra acquired in different ESI-MS conditions to collect all charge states of this NP. As reported previously, this type of NP usually gives a complex and unresolved spectrum due to the presence of multiple ionizable functional groups i.e. carboxylic acids, amines, silanols.[133] Despite this complex appearance, the position of the peaks in the spectrum is quite stable, although the relative abundance of the different peaks is found to be slightly dependent on the ESI-MS conditions.

As we expected, the spectrum obtained with micrOTOF-Q II seems to have lower resolution but contains more species probably due to a softer ionization condition. The QTOF spectrum seems also to contain fewer and lower peaks at the low end of the spectrum which correspond to the small fragments of the particles. Nevertheless, the positions of the peak in both spectra seem not to be significantly different from each other.

These spectra can be deconvoluted by using multiplicative correlation algorithm. The deconvoluted spectrum was shown in Figure 2-11-B. They give at least five broad peaks at around 6.2 kDa, 7.6 kDa, 8.9 kDa, 10.2 kDa and 11.5 kDa for spectrum from micrOTOFQ-II and six peaks at around 6.2 kDa, 7.0 kDa, 7.8 kDa, 8.5 kDa, 9.9 kDA and 11.0 kDa for spectrum from LTQ. It is worth to mention that these results were obtained if the charge states of the species were supposed to be from +4 to +8.

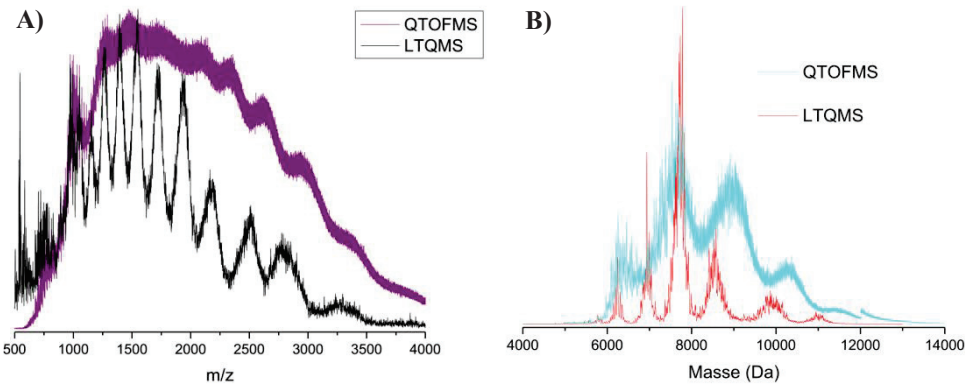

Figure 2-11. A) Mass spectra of AGuIX obtained with LTQ apparatus (black) and micrOTOF-Q II (violet) and B) Deconvoluted spectra from raw spectra obtained with LTQ (red) and micrOTOF-Q II (blue).

2.1.4. The equilibrium between degradation and reconstruction

2.1.4.1. Degradability of AGuIX

In previous studies, it was clearly shown that AGuIX can degrade in aqueous solution in different conditions due to the hydrolysis of the siloxane network.[27,174,176] The half-life of the degradation was once determined by DLS or relaxometry at 2.5 mM in Gd, pH 7.4, 37°C in simulated physiological salt solution or bovine serum as around 18 – 20 minutes.[136] Although, this value can vary according to each synthesis batch however in all studies some common factors such as concentration and pH have been pointed out to affect its degradation. For example, Marais A. has used relaxometry to follow the longitudinal relaxivity (r_1) of AGuIX in pH 7 at different concentration from 50 mM to 0.5 mM in Gd (Figure 2-12-A).[176] As mentioned previously, the r_1 of Gd chelates increases when they are grafted on a nanostructure such as AGuIX's polysiloxane core.[89] Hence, a decrease of r_1 signifies the detachment of Gd chelates through the dissociation of siloxane bonds in the matrix. In other words, the decrease of r_1 reflects the degradation of the particles. From the results, a clear dependence of degradation on concentration was marked. Over time, r_1 of all samples reduce but to different extents depending on the concentration of the sample. Moreover, after sometime, r_1 value of each sample seems to obtain a plateau without further reducing. This implies the existence of a thermodynamic equilibrium between the free degraded silanes and grafted silanes on the particles. The amount of silanes remain grafted seems to be in direct proportion to the total concentration of silanes.

Recently, I have used NMR-DOSY to measure size distribution of yttrium equivalent of AGuIX (USNP(Y)) in aqueous solutions at different concentration 60 mM, 24 mM and 6 mM (Figure 2-12-C). The solutions were diluted from a stocksolution at 100 mM and left at room temperature overnight to obtain equilibria before measurement. As we have discussed above, DOSY measurement gives the distribution of diffusion coefficients (D) over chemical shift of protons. A lower D indicates a slower stumbling rate or a bigger hydrodynamic diameter of an object. As it can be seen from the results, there are at least three populations with different D in each sample. On the right side of the graphs, we have a spectrum reflecting the mean abundance of signal from certain diffusion coefficients over the whole range of chemical shift. When concentration decreases, the population with lower D (~83 $\mu m^2/s$) tends to reduce in its contribution to the signal and then disappear nearly completely. The values of D of the other two populations (~446 and 227 $\mu m^2/s$) also slightly increase (~504 and 292 $\mu m^2/s$). This result might indicate the dissolution of the particles to produce smaller fragments. Unlike relaxometry, the disadvantage of NMR-DOSY is that it needs a long acquisition time, so the real time measurement for kinetics study cannot be reproduced.

Another factor that affects the degradation of AGuIX is pH. To investigate this parameter, samples at 100 mM in different pH from 1 to 7 (adjusted by adding appropriate amounts of HCl or NaOH solutions) was prepared and diluted to 5 mM with aqueous solutions in different pH from 1 to 7 immediately before being measured in relaxometry (Figure 2-12-B). The results show that the rate and extent of the degradation were much lower when pH was decreased.

This property is an advantage of AGuIX compared to other nanoplatforms because the degradation can facilitate the renal elimination of the particles over time.

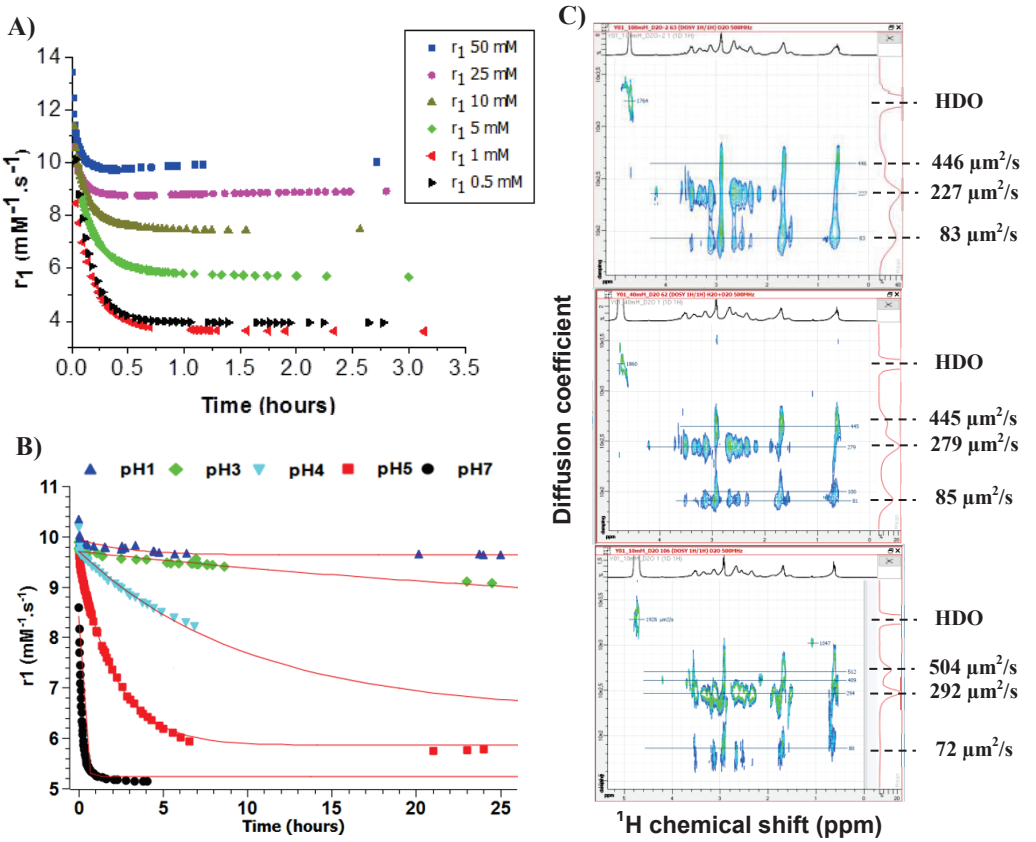

Figure 2-12. Degradation of AGuIX: followed by relaxometry (1.4 T, 37°C) A) at different concentration from 50 to 0.5 mM, pH 7; B) at different pH from 7 to 1, 5 mM and C) NMR-DOSY spectra of USNP(Y) at 60 mM (top), 24 mM (middle) and 6 mM (bottom) (Spectra were obtained with samples prepared overnight from a stock solution at 100 mM).

2.1.4.2. Reconstructability of AGuIX

One peculiar property of AGuIX that we have observed was its ability to reform after being degraded. This phenomenon has been preliminarily described by Marais. A. in his M2 internship report.[176] This property has been re-verified by an experiment carried out with relaxometry and chromatography. A solution of AGuIX has been diluted to 0.5 mM in ultrapure water and left at 37°C overnight to dissolve the particles as much as possible. After that, the solution was evaporated in a rotary evaporator at around 40°C under reduced pressure in four steps to theoretical concentrations at 1.9 mM, 6.3 mM, 9.3 mM and finally 31.4 mM. At each step, sample was taken for analysis by relaxometry and HPLC. In relaxometry, we observed a gradual increase in relaxivity indicating a reformation of nanoobjects containing Gd chelates in the solution (Figure 2-13-A). This is also confirmed by HPLC analysis (Figure 2-13-B). In the chromatograms, the first eluted group of peaks with retention time (t_R) from 2 to 5 min might be assigned to the unreacted precursors and the second wider peak (t_R ~ 13 - 17 min) can be assigned to the produced NPs. This chromatographic behavior has been well studied previously for similar nanoparticles.[173] The area of the particles' peak increases gradually while the concentration increases.

From these experiments, it seems there is an equilibrium between the degraded products (molecules) and the initial NPs depending on the concentration of the particle. This phenomenon is not common among other types of NPs such as polymeric or metallic ones. However, this is well reported for siloxane materials. Since the formation of NPs is based on the condensation of silanol groups to form siloxane bonds by removing water, the hydrolysis

of siloxane bonds to give back free silanols should also occur simultaneously (Equation 2-8). Some reports have shown that the extent of the hydrolysis reaction in this equilibrium depends on (i) the pH of the aqueous solution, (ii) the steric hindrance of the silane and (iii) the number of siloxane bonds the silane can make. The lower pH, the longer and bulkier silanes as well as the more the siloxane bonds, the lesser the hydrolysis.[177,179,195]

$$[\equiv Si - OH\ (silanol) \Leftrightarrow \equiv Si - O - Si \equiv (siloxane) + H_2O] \qquad \textbf{Equation 2-8}$$

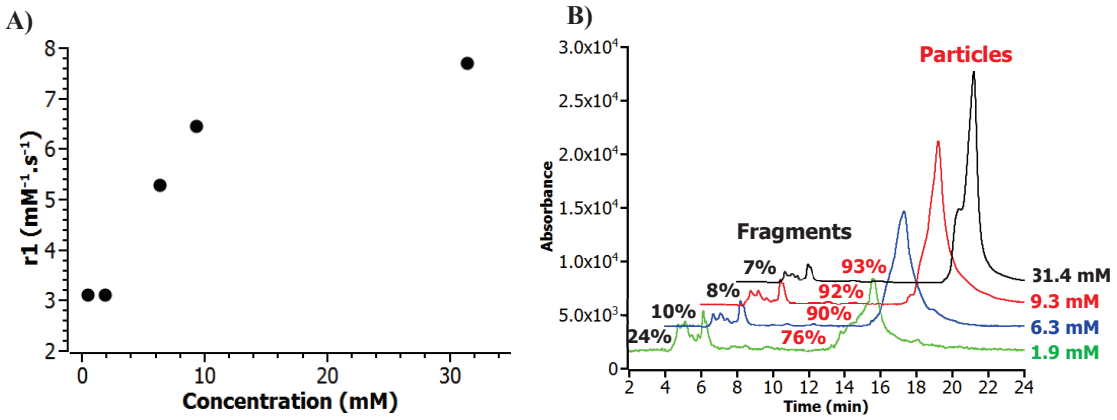

Figure 2-13. Reconstruction of AGuIX. A) Longitudinal relaxivty (1.4 T, 37°C) of reconcentrated solutions of AGuIX at different concentrations; B) Chromatograms of respective solutions at 295 nm normalized to an equivalent to 10 mM of AGuIX.

Another important spin-off idea from this observation is that it should be highly possible to synthesize such ultrasmall nanoparticles following a bottom-up approach which starts directly from molecular precursors rather than the current indirect top-down method. In the next parts, we will see that this idea can turn into a full-fledged applicable synthesis protocol.

2.2. New one-pot synthesis of USNPs and their characterizations

As we have seen before, a bottom-up synthesis would be extremely desirable for the synthesis of multifunctional ultrasmall silica NPs such as AGuIX to increase the yields and reduce the number of synthesis steps. Detailed structural information can be studied by NMR techniques applied on empty intermediate silica NP or diamagnetic metal complexed NP. Finally, a wide variety of metals can be easily complexed to exploit new physical properties such as optical imaging and RS potential of different elements. In this part, we will explore this synthetic strategy using different silane precursors (Figure 2-14).

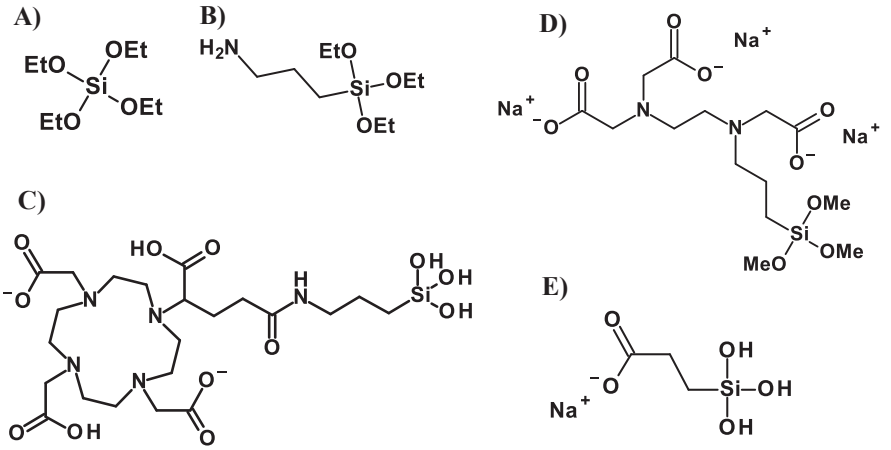

Figure 2-14. Different silanes used in this study: their chemical name (acronym, code used in this study). A) Tetraethyl orthosilicate (TEOS, T); B) Aminopropyltriethoxysilane (APTES, A); C) APTES-DOTAGA conjugate (A-D); D) Sodium salt of triacetic acid N-(trimethoxysilylpropyl)ethylenediamine (TANED, TN); E) Sodium salt of carboxyethylsilanetriol (CEST, C).

The most direct approach would be to start with TEOS and APTES (Figure 2-14-A, B), two silanes that have been used during the top-down synthesis of AGuIX (Figure 2-1). This was carried out in the work of Marais A.[176] However, this system somehow failed to provide stable particles smaller than 10 nm (data not shown). Therefore, during my thesis, we hypothesized that the presence of bulky chelates grafted silanes (APTES-DOTAGA) (Figure 2-14-C), which were created before the formation of ultrasmall particles, might be essential for this process.

We first used a commercialized chelating silane TANED (abcr GmbH, Germany) (Figure 2-14-D) along with APTES and TEOS to explore this synthetic strategy. TANED was chosen due to its similar structure compared to APTES-DOTAGA and its availability. Besides, we also replaced positively charged APTES by a negatively charged silane, CEST (abcr GmbH, Germany) (Figure 2-14-E) to see if the stability can be influenced. The particles synthesized by these silanes will be referred as USNP@TANED.

In the second part, we synthesized APTES-DOTAGA and used it along with APTES and TEOS for synthesizing the polysiloxane particles based on the experience gained from working with TANED. A reliable protocol starting from this ready-to-use powder of APTES-DOTAGA was optimized to produce ultrasmall silica NPs which have very similar characteristics to AGuIX. These particles will be referred as USNP@DOTA. Finally, a protocol where APTES-DOTAGA is formed *in-situ* was proposed to further speed up the procedure. The products of this process will be coded USNP@DOTA$_{IS}$.

2.2.1. Screening conditions with an alternative commercialized organosilane

As mentioned above, we first tested some preliminary formulas using TANED, the available commercialized chelating silane. The synthesis scheme is summarized in Figure 2-15. The formulas that have been tested and their characteristics are summarized in Table 2-3.

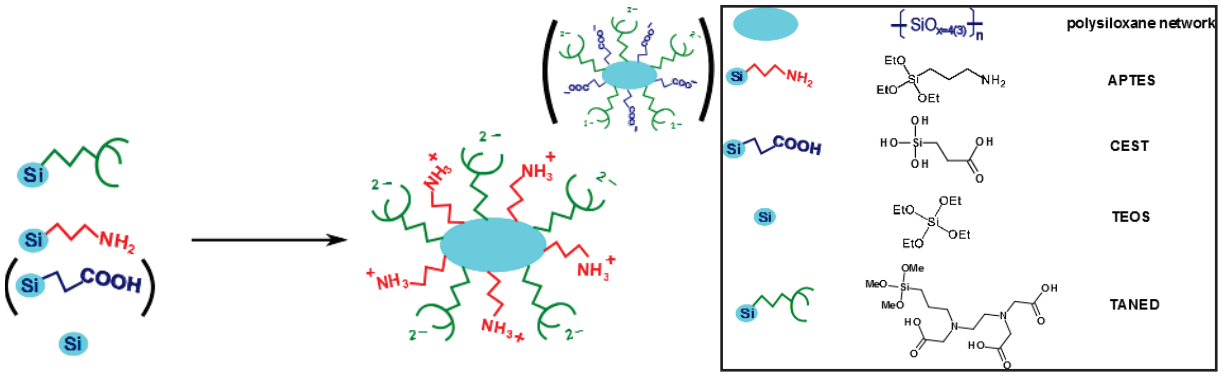

Figure 2-15. The synthesis scheme of USNP@TANED

Table 2-3. Properties of USNPs made from TANED (USNP@TANED)

Properties	Method(s)	USNP@TANED-1	USNP@TANED-2	USNP@TANED-3	USNP@TANED-3^{+}
Starting ratio TN : A/C : T*	-	1 TN : 1 A : 2 T	1 TN : 3 T	1 TN : 1 C : 2 T	1 TN : 1 C : 2 T
Total silane concentration (mM)		400	400	400	400
D_H (nm)	DLS	4.4 ± 1.8	4.6 ± 1.5	3.8 ± 2.0	4.6 ± 1.1
	NMR DOSY	-	-	4.7	5.0
Zeta potential (mV)	Zeta potentiometry	-	-	-	full curve -25.8 (pH 7.0)
Retention time (min)	HPLC (295 nm)	11.4	11.6	12.2	12.1
Peak shape[#]	HPLC (295 nm)	D	D	S	S
FWHM (min)	HPLC (295 nm)	1.3417	1.0667	1.0250	1.0333
Purity (%)	HPLC (295 nm)	-	-	99.8	92.4
Chelator content (µmol/mg)	EBT titration	-	-	-	85.5
C/TN	1H NMR	-	-	1.44	1.30
Si : N : C (% mass)	Elemental analysis	-	-	-	27.0 : 3.7 : 22.6
TN : C : T (molar ratio)	Elemental analysis	-	-	-	1.0 : 1.1 : 5.2
Yield (%) (in TANED)	-	-	-	-	22.6

**TN: TANED, A: APTES, C : CEST, T: TEOS, [#]S: symmetrical, D : distorted,* $^{+}$: scaled up batch

Since previous works have pointed out the degradation of AGuIX through the hydrolysis of siloxane bonds at concentration lower than 50 mM[176], we first tried to keep the concentration of TANED at 100 mM. To resemble the ratio of silanes in AGuIX (APTES-DOTAGA : APTES : TEOS ~ 1 : 1 : 2 – 3), APTES and TEOS were added at 100 mM and 200 mM respectively. The rest of the formula was only water (USNP@TANED-1). TANED, stored as 45 % solution in water, was added first. pH of the solution was around 10.5. APTES and TEOS were added one by one to the solution of TANED. APTES was soluble in water and hydrolyze within minutes. TEOS was not soluble in water but created another oily phase. Therefore, this mixture was left stirring at 25°C overnight until a homogenous solution was obtained. Afterwards, pH of the solution was adjusted to 4.5 by adding hydrochloric acid solutions under vigorous stirring. This pH was chosen because at this pH, 1) silanol groups and carboxyl groups on DOTAGA were (partially) protonated, thereby reducing the electrostatic repulsion between the precursors and facilitating their assembling[130] 2) siloxane bonds seem to be more stable and 3) at this pH, AGuIX was synthesized in the top-down protocol. At this stage, probably, most of precursors especially organosilane precursors i.e.

TANED and APTES were held together by hydrogen bonds between silanol groups. So the solution was stirred during 1 h more before being heated in an oil bath at 80°C for 18 h to complete the condensation. i.e. the formation of covalent bonds between precursors.[130] This process also assured the thermodynamic equilibrium between silanes and particles was reached. Two other syntheses without APTES, one with more TEOS (USNP@TANED-2), the other with CEST instead of APTES (USNP@TANED-3), were also tested following the same protocol.

These solutions were analyzed by DLS and HPLC (Figure 2-16-A). DLS diagrams of three samples were satisfactory with D_H at around ~ 4.4, 4.6 and 3.8 nm respectively. However, in HPLC, they showed different results. It is necessary to mention that, among these silanes, only TANED absorbs significantly at 295 nm. Therefore, the peaks appeared in the chromatograms are more likely from grafted TANED or scattering light of the particles. While USNP@TANED-3 showed a symmetrical and quite intensive peak of NP at 13 min (compared to precursors' peak at the beginning), USNP@TANED-1 and 2 showed a distorted and very weak NP's peak. These solutions were purified by tangential filtration (Vivaspin, 3 kDa) for several cycles using HCl 10^{-4} M to maintain the pH. With USNP@TANED-3, the particles were purified 256 purification factor (purification factor = starting volume/end volume) to make at the end a golden solution. This solution was analyzed by HPLC and showed a high purity (Figure 2-16-B). With USNP@TANED-1 and 2, golden solutions of the particles continuously passed through the membranes. These solutions turned transparent after the purification. These results suggest that the NPs made from TANED are not stable enough at this concentration, and the presence of CEST probably stabilizes the grafting of TANED.

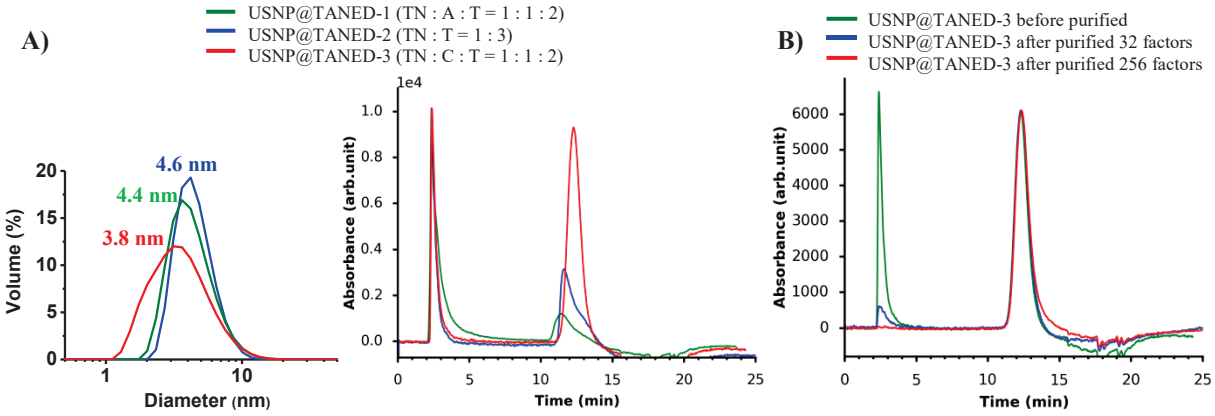

Figure 2-16. Characterization of simulating formulas of ultrasmall silica NP. A) DLS diagrams (left) and chromatograms of USNP@TANED-1 (green), USNP@TANED-2 (blue), USNP@TANED-3 (red) (Note: chromatograms were normalized to the same height of precursor's peak; B) Chromatograms of USNP@TANED-3 before purified (green), after purified 32 factors and after purified 256 factors.

Even though CEST is not a component in AGuIX, since this result is quite interesting, we decided to reproduce this formula in a medium scale (~ 2 grams) and further characterize it with different techniques (Figure 2-17). DLS and HPLC showed similar results with D_H ~ 4.6 nm and a symmetrical peak in chromatogram (Figure 2-17-A, C). Zeta potentials of the particles were well negative as expected (Figure 2-17-B). Proton NMR spectra of CEST, TANED and USNP@TANED-3 were recorded (Figure 2-17-E) along with NMR-DOSY spectrum of USNP@TANED-3 (Figure 2-17-F). ^{1}H spectrum of USNP@TANED-3 contained all the peaks that might come from CEST or TANED. Most of these protons have the same diffusion coefficients at 77 $\mu m^2/s$ corresponding to a D_H ~ 5.0 nm. These results

indicate the presence of both silanes on the particles. Few protons have diffusion coefficients at 479 and 305 $\mu m^2/s$ which correspond to the free silanes presenting in the equilibrium with the particles. ^1H spectrum of CEST showed two main peaks at 2.35 and 0.91 ppm which were not overlapped by any peaks in the spectrum of TANED. By integrating the area of these peaks and comparing with the total area of all protons' peaks, we can determine the ratio CEST/TANED which was, in this case, 1.30.

^{29}Si solid state NMR spectrum was also recorded and deconvoluted by Ms. Lorentz C. at Institut de recherches sur la catalyse et l'environnement (IRCE, Lyon) (Figure 2-17-D and Table 2-4). The interpretation of the spectrum can be found in the previous publication.[133] From this result, we can calculate the percentage of organosiloxane (T2 and T3 species, from CEST and TANED) over pure siloxane (Q2, Q3 and Q4 species, from TEOS) which was 45/55. This is slightly lower than what we have seen in AGuIX ($\sum T/\sum Q$ = 62 / 38).[133] This result is in accordance with the results of the elemental analysis that showed a higher ratio of TEOS in USNP@TANED-3 i.e. TANED : CEST : TEOS ~ 1 : 1 : 5 (Table 2-3) compared to the values in AGuIX i.e. APTES-DOTAGA : APTES : TEOS ~ 1 : 1 : 3 (Table 2-1). The higher ratio of TEOS in USNP@TANED-3 might also explain a slightly bigger hydrodynamic diameter D_H = 4.6 nm vs. $D_{H(AGuIX)}$ ~ 3 nm.

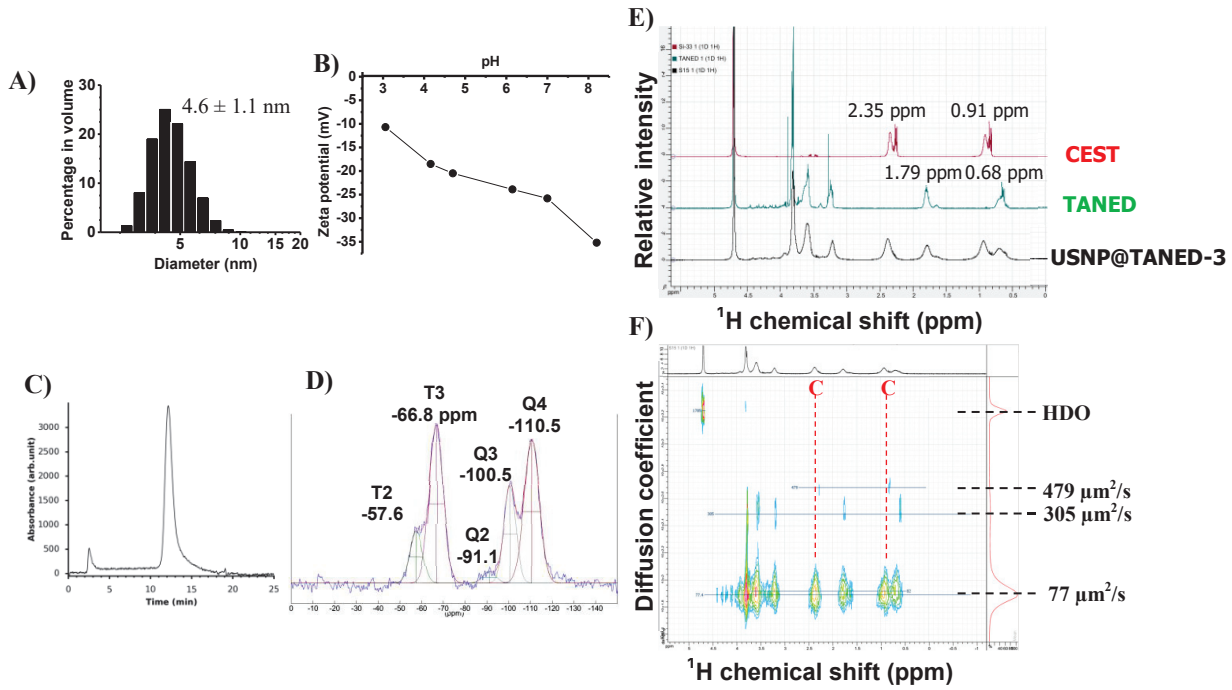

Figure 2-17. Characterization of scaled up USNP@TANED-3. A) DLS diagram; B) Zeta potential curve; C) HPLC chromatogram after purified > 10k factors; D) ^{29}Si solid state NMR; E) 1H NMR spectra of CEST (red), TANED (green) and USNP@TANED-3 (black) solutions; F) NMR-DOSY spectrum of USNP@TANED-3 at 48 g/l, pH 4.5 (red C marks the peaks from functional groups of CEST).

Table 2-4. Deconvolution results of ^{29}Si solid state NMR for USNP@TANED-3

Species	Amplitude	Position (ppm)	Width (Hz)	Peak area (%)	Absolute area
T2	3.66	-57.6	679.7	10.5	2646
T3	11.11	-66.8	740.8	34.7	8764
Q2	0.81	-91.1	693.1	2.4	595
Q3	6.84	-100.5	634.1	18.3	4617
Q4	10.03	-110.5	812.0	34.3	8668

In conclusion, it is possible to use this direct mixing protocol to produce ultrasmall silica nanoparticles. Unfortunately, the simulating silane (TANED) failed to provide enough hydrolytic stability to the polysiloxane system, especially while being combined with APTES. This is not surprising given that APTES was well documented as an intramolecular catalyzer for siloxane hydrolysis[178,179,196] and was used often to speed up the dissolution of polysiloxane network in mesoporous silica NP.[197] Interestingly, carboxylsilanes such as CEST help stabilize TANED on the siloxane surface. It is probably due to the formation of an acidic microenvironment around the surface of the particles which maintains the stability of the siloxane bonds from the hydrolysis of water. Nevertheless, this result should not be necessarily extrapolated to the case of APTES-DOTAGA which is much bulkier and more efficient as a protective layer compared to TANED. Moreover, the replacement of APTES by CEST can compromise the total neutral zeta potential of the particles which is more desirable to prevent protein adsorption. In the next part, we will see the results obtained with APTES-DOTAGA.

2.2.2. One-pot synthesis of USNP@DOTA (AGuIX like particle)

In this part, first of all, APTES-DOTAGA was synthesized and isolated as ready-to-use powder. Then, this powder was utilized to synthesize USNP with a similar protocol to the one used for USNP@TANED. Finally, we further shorten the protocol by combining the synthesis of APTES-DOTAGA within the synthesis of USNP in a single step to speed up and increase the yield of the procedure.

2.2.2.1. The synthesis of APTES-DOTAGA

APTES-DOTAGA can be synthesized from 2 different methods through the reaction between APTES and 1) the activated carboxyl group on butyl protected DOTAGA by HBTU (2-(1H-benzotriazol-1-yl)-1,1,3,3-tetramethyluronium hexafluorophosphate) (Figure 2-18-A) or 2) DOTAGA anhydride (Figure 2-18-B). The former was performed by our collaborator Thakare V. *et al* in Chematech, Dijon while the latter was carried out in our own laboratory. The two types of products can be used interchangeably as APTES-DOTAGA sources. The advantage of scheme A is the specificity of the reaction and the purity of the product. This is thanks to the hydrophobicity of the butyl protected DOTAGA-APTES that allows it to be separated from the butyl protected DOTAGA by liquid extraction at basic pH. Nevertheless, scheme A is limited by the availability of butyl protected DOTAGA produced scarcely in Chematech. Meanwhile, scheme B is simple and straightforward. However, it is difficult to obtain pure APTES-DOTAGA since the main product and by-product hydrolyzed DOTAGA have very close solubility. Therefore, it requires a quantification method to determine the amount of APTES-DOTAGA in the final mixture.

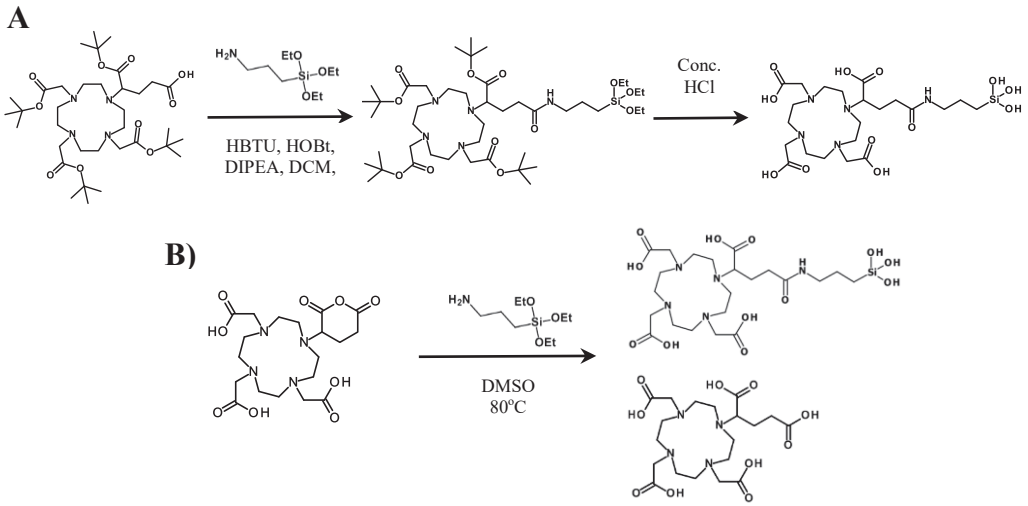

Figure 2-18. The reaction schemes of the synthesis of APTES-DOTAGA A) from DOTAGA anhydride or B) from t-butyl protected DOTAGA.

2.2.2.1.1. Synthesis of APTES-DOTAGA from butyl protected DOTAGA

2.2.2.1.1.a. Synthesis protocol

APTES-DOTAGA can be synthesized starting from the t-butyl protected DOTAGA which was coupled to APTES through peptide coupling. This was followed by the deprotection of the intermediate to get the final compound. The reaction scheme is presented in (Figure 2-18-A).

DOTAGA(tBu)$_4$ (Chematech) (0.9g, 1.284 mmol) was weighed in 100 mL round bottom flask and was dissolved in 20 mL of DCM (dichloromethane, VWR) under the hood with stirring. DIPEA (N, N-diisopropylethylamine, Alfa Aesar) (1.14 mL, 6.55 mmol) was added into above solution followed by coupling agents namely HBTU (0.52 g, 1.37 mmol) and HOBt (Hydroxybenzotriazole, Fluorochem) (0.18 g, 1.37 mmol) and the solution was left for stirring at rt (room temperature) for 15 min. APTES (0.3 g 1.37 mmol) was added to the above solution directly using the 1mL syringe and solution was stirred further at rt for 60 min after which the product formation was confirmed through MS. The above solution was mixed with 50 mL of citric acid solution (pH:2.5-3) in a separating funnel and the organic layer was recovered. The organic layer was further mixed with 50 mL of 5% $NaHCO_3$ in a separating funnel and the organic layer was recovered. The DCM solution was stirred with 5 g of $MgSO_4$ for 10 min and filtered using sintered funnel to receive the dry and clear DCM solution. Organic phase was evaporated under vacuum at 30°C to get a viscous brownish residue, as an intermediate product (1.05 g, 78%). The intermediate formation was verified using HRMS, ^{1}H, ^{13}C NMR and elemental analysis.

DOTAGA(tBu)$_4$-APTES (1 g) was weighed into a 100 mL round bottom flask and was mixed with 5mL of concentrated HCl and stirred for 10min. Later, the acid was evaporated under vacuum at 35°C in 5-15min to get a dried residue. The above dried residue was dissolved in 10mL of water and lyophilized to get a light brown colored powder (850 mg, 81%). The product was verified using HRMS, ^{1}H NMR and elemental analysis.

2.2.2.1.1.b. Characterization

Methods

ESI (Electro Spray Ionisation), High resolution and accurate mass measurements (HRMS) were carried out using a Bruker microTOF-Q™ ESI-TOF mass spectrometer (Germany).

The ^{1}H and ^{13}C NMR spectra were recorded at RT or at 330K. NMR spectra were run on Bruker Avance 300 and/or 500 spectrometers (Germany) using pre-deuterated solvents as internal standard.

Elemental analyses were obtained on EA 1108 CHNS Fisons Instrument.

Characterization of butyl protected APTES-DOTAGA

HRMS: Calculated for $C_{44}H_{85}N_5O_{12}Si$: 926.585 $[M+Na]^+$; Obtained: m/z = 926.584 $[M+Na]^+$ (Figure 2-19)

^{1}H NMR (500 MHz, $CDCl_3$) δ 0.4 – 0.7 (m, 2H), 0.7 – 0.8 (m, 1H), 1.0 (dd, J = 9.0, 6.7 Hz, 1H), 1.1 – 1.2 (m, 9H), 1.3 – 1.5 (m, 32H), 1.5 (p, J = 7.8 Hz, 2H), 1.7 (d, 1H), 1.9 – 2.1 (m, 1H), 2.1 – 2.3 (m, 1H), 2.4 – 3.4 (m, 29H), 3.5 – 3.7 (m, 1H), 3.7 – 3.8 (m, 4H).

^{13}C NMR (126 MHz, $CDCl_3$) δ 7.5, 7.8, 18.3, 20.4, 23.5, 25.9, 26.8, 27.8, 27.8, 27.9, 27.9, 27.9, 28.2, 28.3, 29.7, 33.0, 38.6, 42.1, 47.6, 49.8, 58.4, 63.6, 80.8, 82.3, 171.1, 173.2.

Elemental Analysis: Calculated for $C_{44}H_{85}N_5O_{12}Si$**.** $0.9HPF_6$ (%): C: 51.03, H:8.36, N:6.76. Observed (%): C: 51.86, H: 8.91, N: 8.38.

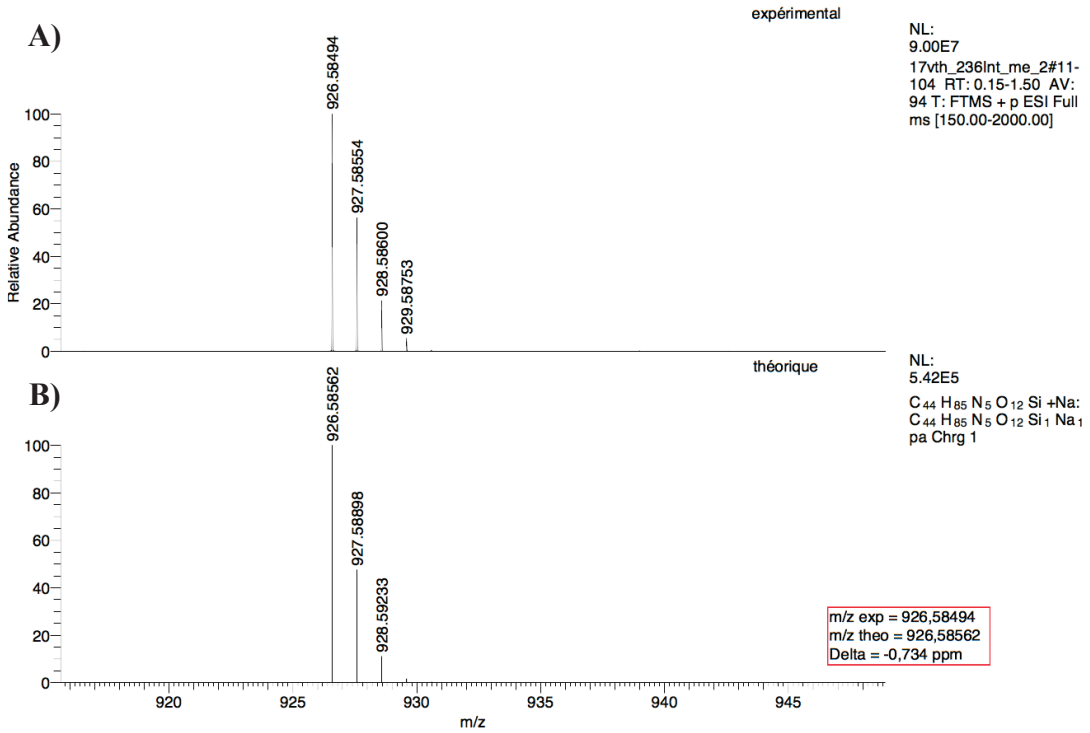

Figure 2-19. Mass spectra of butyl protected APTES-DOTAGA: A) experimental spectrum, B) simulated spectrum

Characterization of deprotected APTES-DOTAGA

HRMS: Calculated for $C_{22}H_{41}N_5O_{12}Si$: 596.259 $[M+H]^+$; Obtained: m/z = 596.261 $[M+H]^+$; 618.242 $[M+Na]^+$ (Figure 2-20).

^1H NMR (500 MHz, Deuterium Oxide) δ 0.5 – 0.8 (m, 2H), 1.2 – 1.3 (m, 1H), 1.4 – 1.6 (m, 1H), 1.6 – 1.8 (m, 1H), 1.8 – 2.2 (m, 1H), 2.3 – 4.5 (m, 26H).

Elemental Analysis:

Calculated for $C_{22}H_{41}N_5O_{12}Si.\ HPF_6.\ 2HCl$ (%): C: 32.44, H:5.44, N:8.60.

Observed (%): C: 32.17, H: 6.54, N: 9.39.

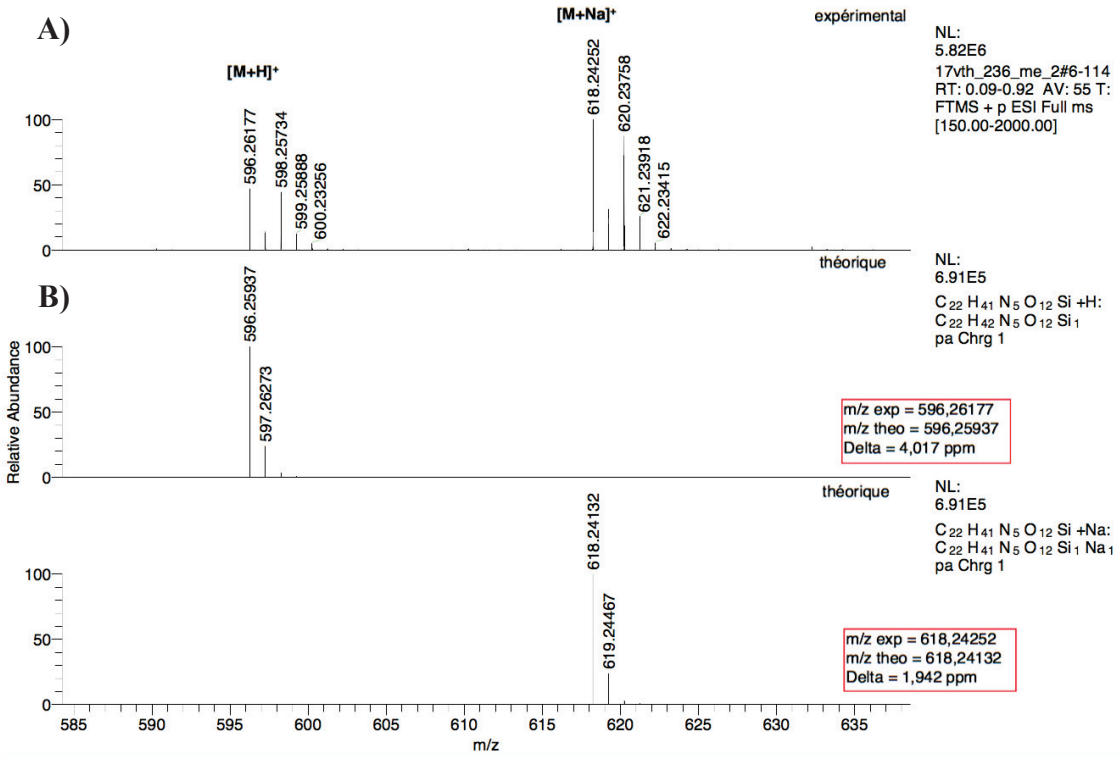

Figure 2-20. Mass spectra of deprotected APTES-DOTAGA: A) experimental spectrum, B) simulated spectrum

2.2.2.1.2. Synthesis of APTES-DOTAGA from DOTAGA anhydride

2.2.2.1.2.a. Synthesis protocol

10.0 g (17.45 mmol) of DOTAGA anhydride (Chematech) was put in a 1 L round flask. Then, 530 ml of anhydrous DMSO (SigmaAldrich) and 2.062 ml (8.72 mmol) of APTES (SigmaAldrich) were added quickly. DOTAGA anhydride was used in excess to make sure all APTES will react (Figure 2-18-B). This allows the precise control of the composition of the final particles in the next step. The reaction was put under Argon atmosphere and heated to 75°C overnight (18 h). The product formed as white precipitate. The product was fully precipitated by transferring to 5 L of acetone and kept at 4°C for 18 h. The precipitate was filtered through filter paper grade 42. Around 2.5 L of acetone was used to wash the precipitate and remove DMSO. The remaining acetone was removed by evaporating at 37°C overnight.

2.2.2.1.2.b. Characterization

IR spectra

DOTAGA and the mixture of APTES-DOTAGA were dissolved in water and adjusted to pH 2 to protonate carboxyl groups. This makes the peak at 1677 cm^{-1} of C=O amide distinguished from the one at 1713 cm^{-1} of C=O carboxyl. The 2 solutions were dried at 80°C for 4 days. IR spectra were acquired with dry powder.

Figure 2-21 shows the IR spectrum of DOTAGA powder and APTES-DOTAGA synthesis mixture. The assignment for some important peaks is shown in the Annexes-4.[98] The appearance of peak at 1677.0 cm^{-1}, and the decrease of peak intensity at 1712.7 cm^{-1} is an indication of the formation of the amide bond.[155]

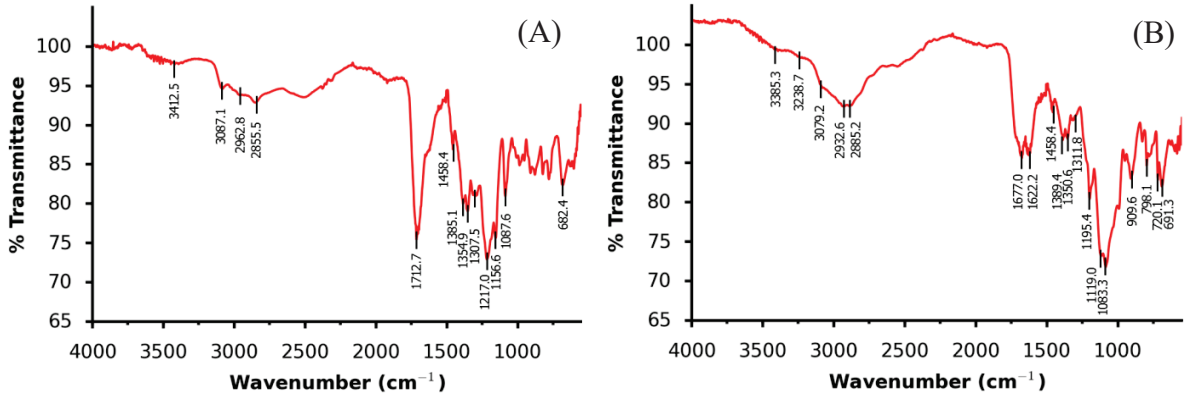

Figure 2-21. Infrared spectra of DOTAGA powder (A) and APTES-DOTAGA synthesis mixture (B)

Mass spectrometry

MS spectrum was obtained in negative mode at the concentration of total DOTAGA around 0.1 mM. Figure 2-22 shows the overall spectrum which has 4 main peaks at 594, 475, 296.5 and 237 m/z. Figure 2-23 to Figure 2-26 show the zoomed region of each of the peak along with the proposed molecular formula and simulated spectrum. The agreement between the real spectra and simulated spectra as well as the co-presence of singly charged ions and doubly charged ions confirm the reliability of the proposed structures.

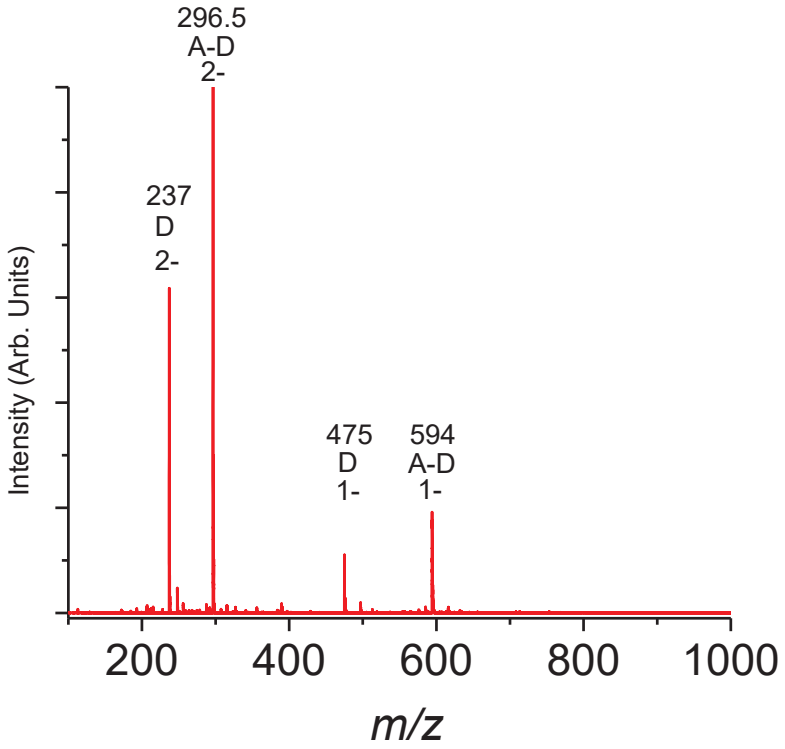

Figure 2-22. ESI-Mass spectrum of APTES-DOTAGA synthesis mixture in negative mode. D : DOTAGA, A-D : APTES-DOGA, 2- : $(M-2H)^{2-}$, 1- : $(M-H)^{-}$

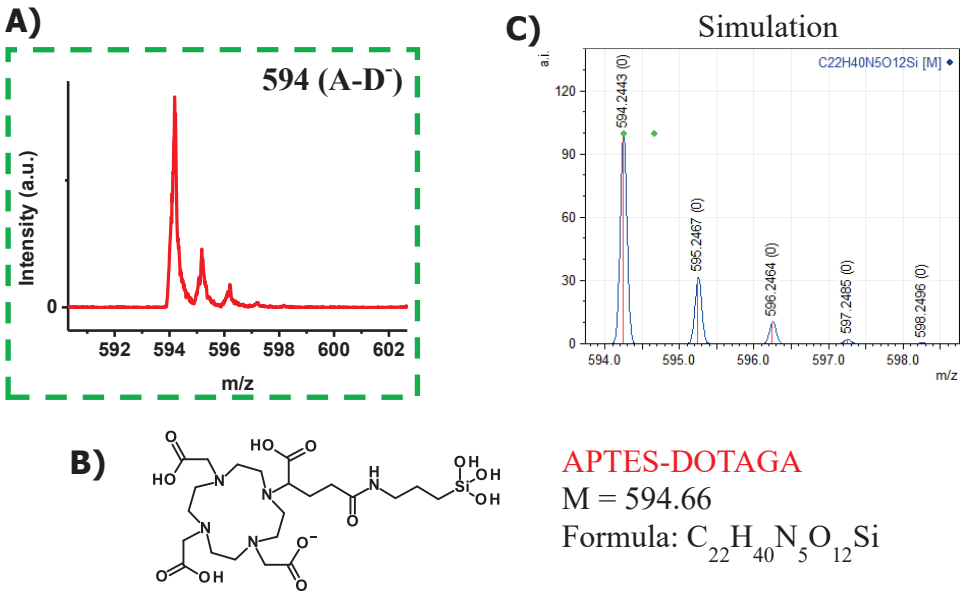

Figure 2-23. (A) Magnified region of peak at 594 m/z, (B) Proposed molecular formula and (C) simulated spectrum.

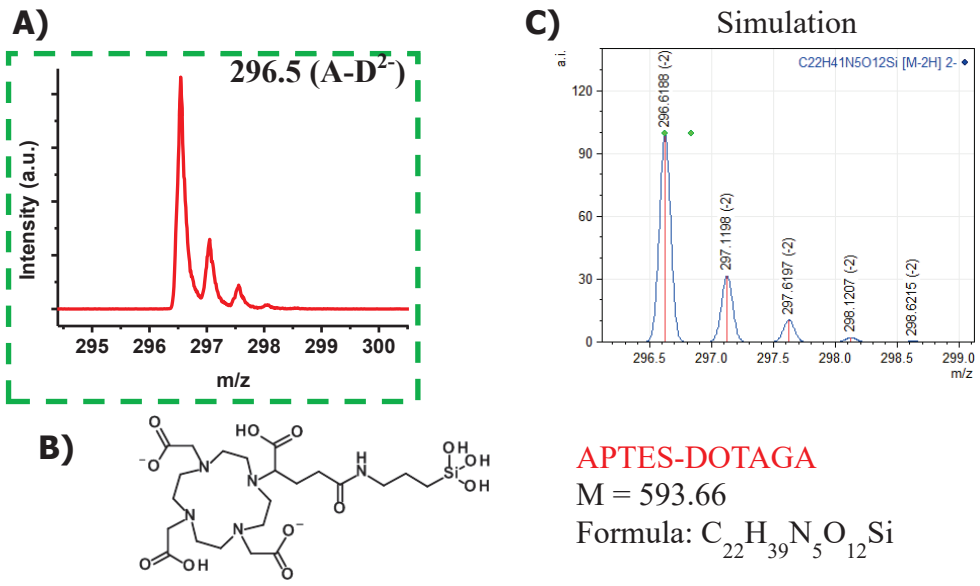

Figure 2-24. (A) Magnified region of peak at 296.5 m/z, (B) Proposed molecular formula and (C) simulated spectrum.

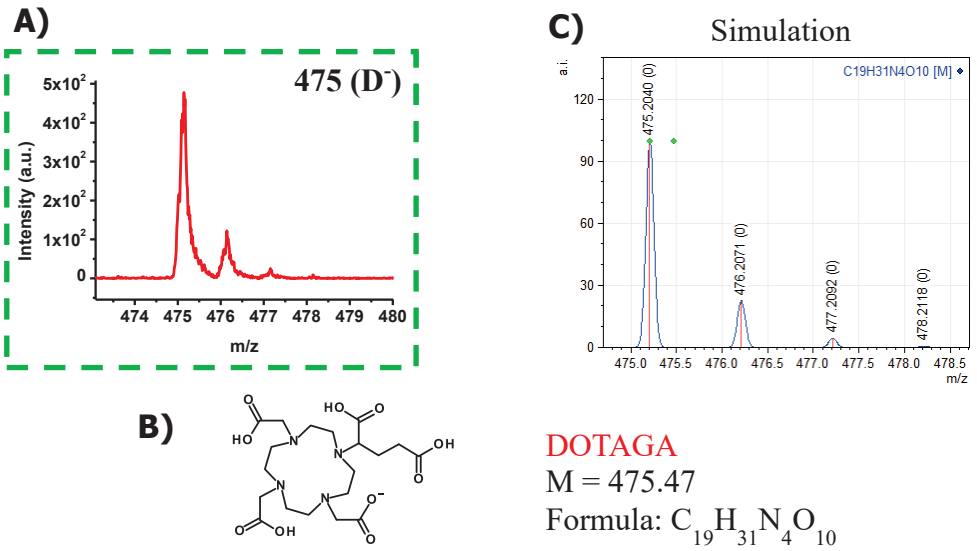

Figure 2-25. (A) Magnified region of peak at 475 m/z, (B) Proposed molecular formula and (C) simulated spectrum.

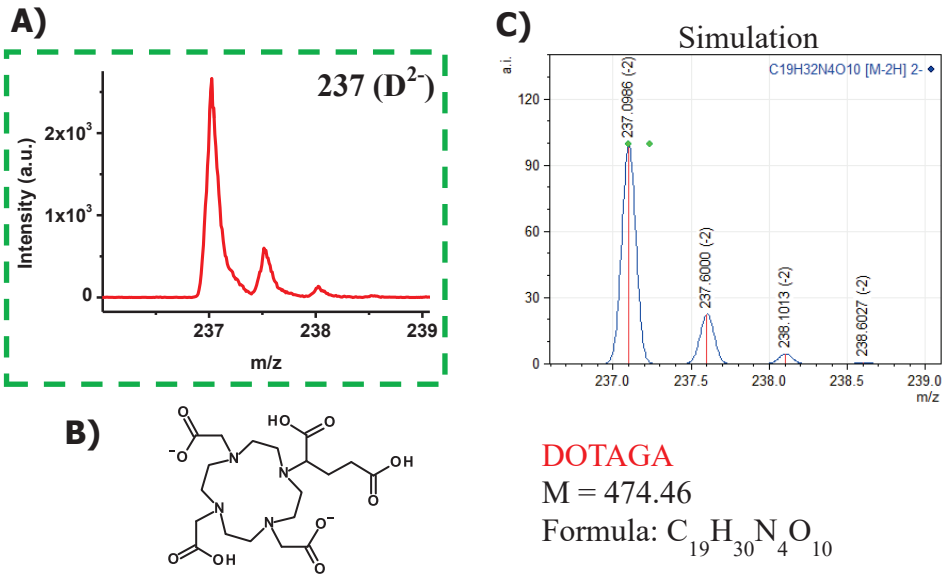

Figure 2-26. (A) Magnified region of peak at 237 m/z, (B) Proposed molecular formula and (C) simulated spectrum.

Determination of the total contents of (reacted and unreacted) DOTAGA

The first method to determine the contents of DOTAGA is colorimetric titration with Ca^{2+} using EBT (Eriochrome® Black T) as color indicator in ammonia buffer solution at pH 10. The test gives a value around 1.70 µmol/mg. This result might be slightly overestimated due to the difficulty of recognizing the equivalent point indicated by the color change from pale blue to violet. However, it gives an approximate idea about the real value (Figure 2-27).

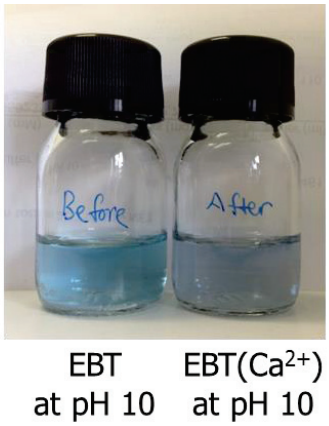

Figure 2-27. Titrating samples of EBT colorimetry before and after the equivalent point.

The second method is complexometric titration with europium salt ($EuCl_3$) (Figure 2-28). A series of samples containing a fixed amount of APTES-DOTAGA powder and an increasing amount of $EuCl_3$ was prepared. Eu^{3+} has two specific phosphorescence emission peaks at 594 nm ($^5D_0 \rightarrow {}^7F_1$) and 616 nm ($^5D_0 \rightarrow {}^7F_2$) when being excited at 395 nm (Figure 2-28-A).[199,200] The intensity of these two peaks can be strongly enhanced when Eu^{3+} was complexed due to the protective effect of DOTAGA ligand from the quenching effect of O-H oscillator of water on Eu^{3+} phosphorescence. Upon the addition of increasing amount of Eu^{3+}, the phosphorescence intensity increases sharply until no DOTAGA is available for chelating. After this point, the intensity obtains a plateau or increases slowly due only to the

phosphorescence of free Eu^{3+}.[138] Figure 2-28-B shows the titration curve of the sample with the equivalent point at around 1.47 ± 0.11 µmol/mg for the content of DOTAGA. This result can be considered more precise and will be used for further calculation.

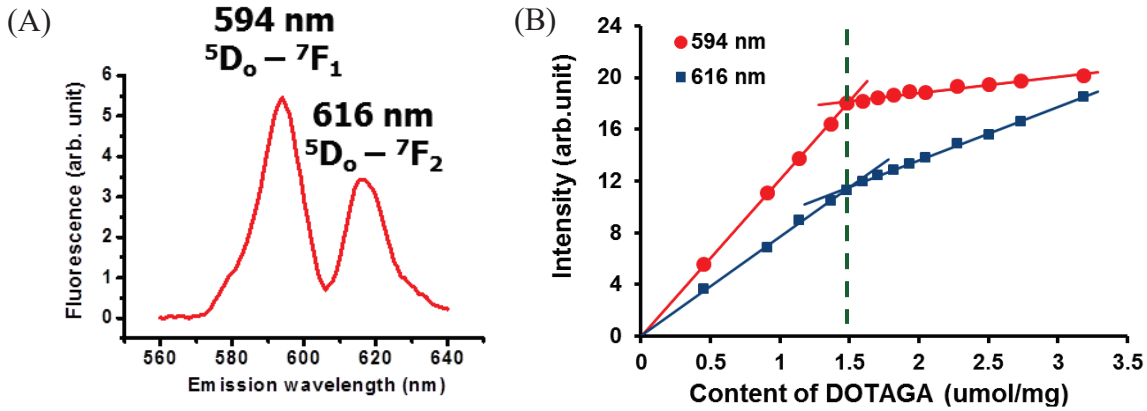

Figure 2-28. (A) Emission spectrum of a mixture of 40 µM $EuCl_3$ and 100 µM DOTAGA excited at 395 nm, (B) Titration curve of APTES-DOTAGA synthesis mixture at 594 nm (red) and 616 nm (blue)

Determination of the content of APTES-DOTAGA

Now, the next task is to determine the content of APTES-DOTAGA. Due to the similarity in chemical properties of DOTAGA and APTES-DOTAGA, it is difficult to determine their contents in a mixture. Therefore, a HPLC method was developed to separate them. Since silanes can react with the residual silanols on the surface of silica chromatographic columns when they are concentrated enough, in order to keep the surface of the column intact, the concentration of silanes should be kept as low as possible. We label DOTAGA with Gd^{3+} and detect the fluorescent emission at 312 nm (λ_{ex} = 274 nm). In our case, the total concentration of silanes was kept lower than 0.2 mM without any observable distortions in peak shape or gradual increase of pressure.

HPLC setup:

The same system was used to analyze this sample with some modification (Figure 2-29). Only isocratic elution was used since no NP is present. A longer C18 column (250 mm) was used to offer higher separation capability. The flow was maintained for 15 min to elute all the expected peaks. After that, acetonitrile was raised to 90 % gradually to clean the column from unexpected organic impurities. Then, the system was re-equilibrated to the initial condition before a new analysis. Before the measurement of each sample, a baseline was obtained in the same manner by injecting Milli-Q water.

Calibration standards preparation: a 10 ml solution of 0.375 µmol $GdCl_3$ and 0.450 µmol DOTAGA was prepared from $GdCl_3.6H_2O$ salt and DOTAGA anhydride. pH was kept below 4 before mixing and adjusted at 5.5 after mixing by addition of NaOH solutions. The solution was incubated at 80°C during 48 h to allow the complexation to complete. Final pH is verified at the end. Solution was filled to 25 ml in a volumetric flask and the final concentrations of $GdCl_3$ and DOTAGA were 15 mM and 18 mM respectively. From this stock solution, a series of samples with DOTAGA(Gd^{3+}) concentration from 0.01 mM to 0.15 mM were prepared by dilution in water. The calibration curve is fitted from the concentrations of DOTAGA(Gd^{3+}) solutions and the areas under the curve of their peaks.

Sample preparation: The dried powder was dissolved in water. This solution was mixed with an excess amount of $GdCl_3$ to achieve final concentration of 57.8 mg/L for the synthesis mixture and 0.2 mM Gd^{3+}. The pH is adjusted to around 5 and incubated at 80°C during 48 h to allow the complexation to complete. Final pH is verified at the end. The area of the DOTAGA(Gd^{3+}) peak was fitted to the calibration curve to give the concentration of unreacted DOTAGA in the sample and the content of APTES-DOTAGA in the powder was then deduced.

Figure 2-29-A shows the chromatograms of the analytes. By superimposing the chromatogram of the synthesis mixture (red) with the one of $GdCl_3$ (black) and DOTAGA(Gd^{3+}) (blue), we can identify the expected peaks. The first peak corresponds to free Gd^{3+}. The third peak should correspond to DOTAGA(Gd^{3+}). Finally, the second peak should correspond to the product of the reaction APTES-DOTAGA(Gd^{3+}). So, the chromatography aided in clearly separating 3 components from each other. Using a calibration curve of the peak area and concentration of DOTAGA(Gd^{3+}) (Figure 2-29-B), we can determine the concentration of DOTAGA(Gd^{3+}) in the sample and then determine its initial contents in the powder which is around 0.74 µmol/mg.

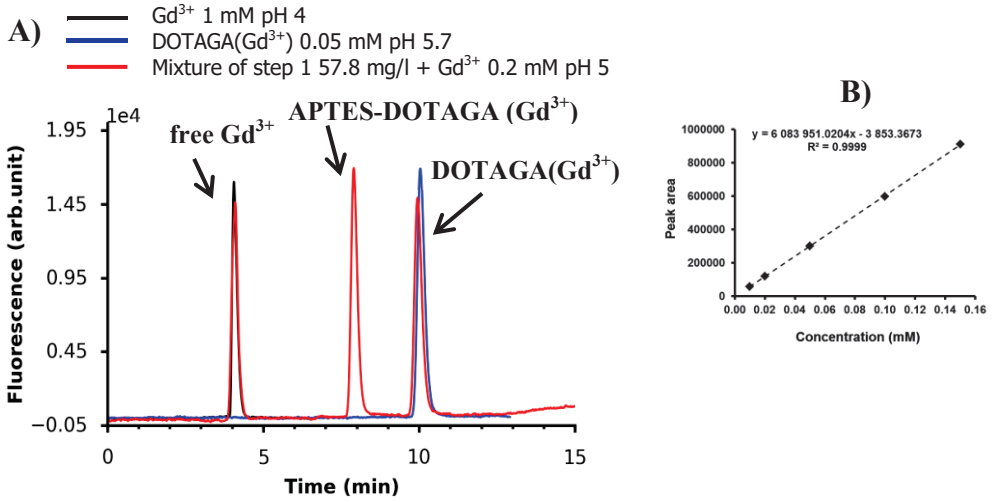

Figure 2-29. A) Chromatograms of the $GdCl_3$ 1mM solution (black), DOTAGA(Gd) 0.05 mM solution (blue) and products after the reaction betwen DOTAGA anhydride and APTES (red)
B) Calibration curve of DOTAGA(Gd^{3+})

HPLC condition:
Injection volume: 20 µl
Column: BDS-HYPERSIL-C18 (250 mm x 4.60 mm, 5 µm, 130 Å, ThermoFisher Scientific)
Flow rate: 1 ml/min
Detector: fluorescence (λ_{ex} = 274 nm, λ_{em} = 312 nm)
Oven temperature: 30°C
Solvent: isocratic mixture of 99% A: H_2O/TFA (99.9:0.1) and 1% B: Acetonitrile (ACN)/TFA (99.9:0.1)

Table 2-5 shows the summary of the above results. IR and MS spectra as well as HPLC chromatograms show that the precursor has been formed after the reaction. The quantifications proved that the reaction was complete and half of the DOTAGA anhydride has reacted with APTES. After the whole process, we obtained the yield of 37 % of APTES-DOTAGA compared to the introduced DOTAGA anhydride or 74 % compared to the expected amount of APTES-DOTAGA. It is worth reminding that, in this case, the starting molar ratio DOTAGA :APTES was 2 : 1.

Table 2-5. Characterizations of APTES-DOTAGA precursor synthesized from DOTAGA anhydride

Features	Method(s)	Result
Amide bond formation	IR	Appearance of C=O amide peak at 1677 cm^{-1}
Molecular weight	Mass spectrometry	Peaks at 594 and 296.5 m/z of APTES-DOTAGA
Content of total DOTAGA	Colorimetry with NET Titration with Eu^{3+}	~ 1.73 µmol/mg 1.47 ± 0.11 µmol/mg
Content of unreacted DOTAGA	HPLC (C18 column, Gd^{3+})	0.74 µmol/mg
Yield APTES-DOTAGA		74.15 %

2.2.2.2. Protocol optimization with APTES-DOTAGA

With the new molecule, APTES-DOTAGA, we tried first to repeat the conditions that we have used with TANED. It means fixed concentrations of APTES-DOTAGA, APTES/CEST and TEOS have been introduced during the synthesis. These syntheses were called USNP@DOTA-pre 1, 2, 3, 4. In USNP@DOTA-pre1, APTES-DOTAGA, APTES and TEOS were introduced at 50 mM, 50 mM and 100 mM respectively. In USNP@DOTA-pre2, APTES was removed when APTES-DOTAGA and TEOS were kept at the same concentrations. In USNP@DOTA-pre3, CEST was used to replace APTES at exactly 50 mM. Finally, in USNP@DOTA-pre4, concentrations of APTES-DOTAGA, APTES and TEOS were increased 4 times to 200 mM, 200 mM and 400 mM respectively to stabilize the particles after the synthesis.

As we have found that the homogeneity of the samples was not satisfactory, we came up with a more non-conventional gradient-silane-concentrations approach where the concentrations of APTES-DOTAGA, APTES and TEOS were kept 5 times lower at 10 mM, 10 mM and 20 mM respectively during the synthesis to produce homogeneous sample. Then, the solution was concentrated to a 5 times higher concentration to stabilize the particles during the purification. This synthesis was cited as USNP@DOTA. For this non-conventional method, another protocol, where APTES-DOTAGA was first complexed with Gd^{3+} before being used in the condensation process, was also tested to produce slightly smaller particle (USNP@DOTAGd*). These strategies were simply presented in Figure 2-30. The formulas and characterization results are summarized in Table 2-6. We will go into details during the next paragraphs.

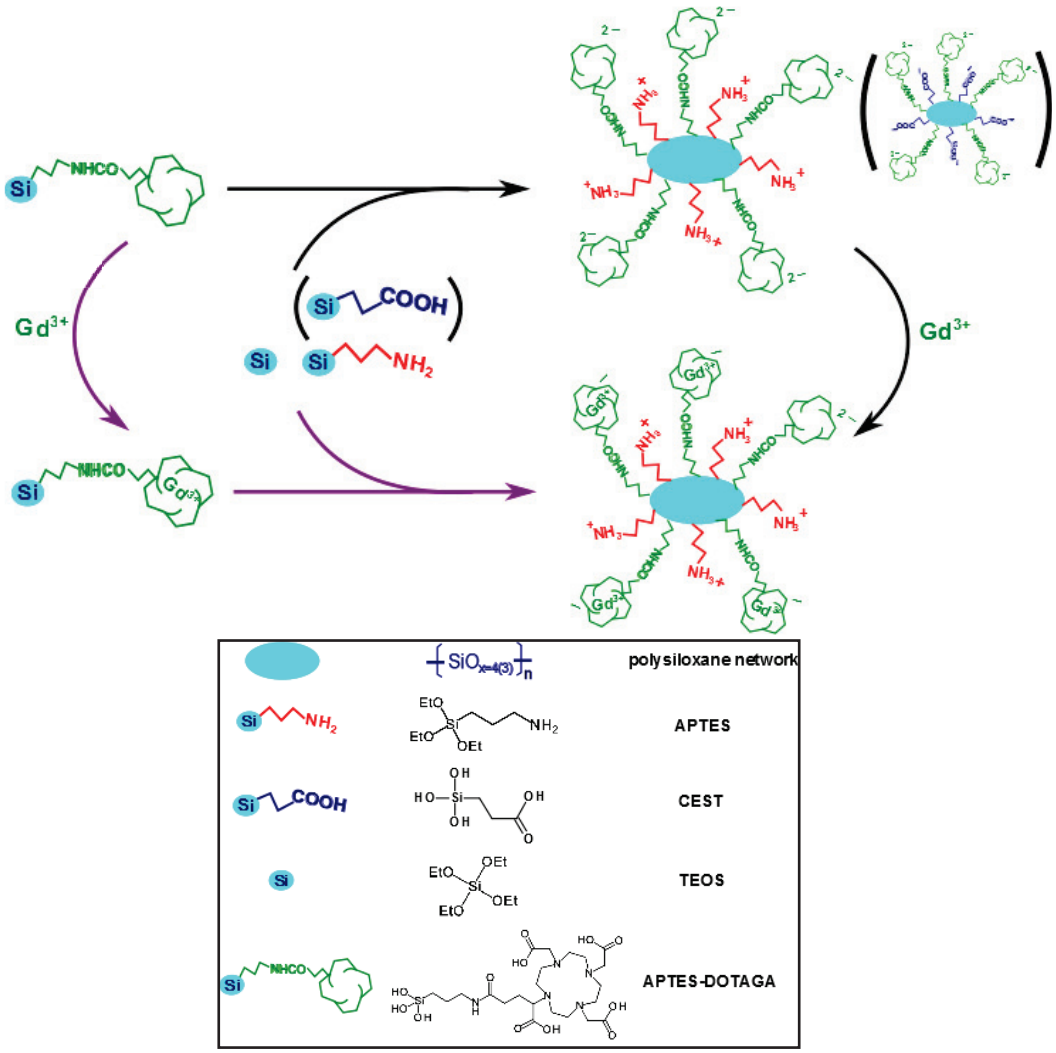

Figure 2-30. The synthesis scheme of USNP@DOTA (black arrows) or USNP@DOTAGd* (violet arrows)

Table 2-6. Properties of formulas of USNP using ready-to-use APTES-DOTAGA (USNP@DOTA)

Properties	Method(s)	USNP@DOTA-pre1	USNP@DOTA-pre2	USNP@DOTA-pre3	USNP@DOTA-pre4	USNP@DOTA	USNP@DOTAGd	USNP@DOTAGd*
Starting ratio A-D : A/C : T (: Gd)*	-	1 A-D : 1 A : 2 T	1 A-D : 2 T	1 A-D : 1 C : 2 T	1 A-D : 1 A : 2 T	1 A-D : 1 A : 2 T	1 A-D : 1 A : 2 T : 0.9 Gd	1 A-D : 1 A : 2 T : 0.9 Gd
Total silane concentration (mM)	-	200	200	200	800	40	-	40
D_H (nm)	DLS	4.9 ± 1.2	6.3 ± 1.6	5.2 ± 1.2	4.9 ± 1.5	4.6 ± 1.6	5.7 ± 1.3	2.8 ± 0.7
	NMR DOSY	-	5.4	5.5	5.5	7.0 ± 2.5 (empty) 6.8 ± 2.4 (Lu^{3+})	-	-
Zeta potential (mV)	Zeta potentiometry	-	-	-	-	-21.4 (pH 6.63) -27.1 (pH 7.37)	- 5.8 (pH 6.65) -8.2 (pH 7.34)	-35.6 (pH 7.38)
Retention time (min)	HPLC (295 nm)	11.9	13.6	13.1	12.7	13.0	15.7	15.2
Peak shape[#]	HPLC (295 nm)	D	S	S	D	S	S	S
FWHM (min)	HPLC (295 nm)	1.1667	0.8583	0.6083	1.6833	1.0250	2.4083	2.6583
Purity (%)	HPLC (295 nm)	92.4	~ 100	94.5	94.7	97.6	~ 100	96.8
	HPLC (Cu^{2+})	-	-	-	-	93.9	-	-
DOTAGA content (µmol/mg)	EBT titration				78.1	-	-	-
	Eu^{3+} titration				-	0.787	-	-
	HPLC (Cu^{2+})				-	0.715	-	-
r_1 ($mM^{-1}.s^{-1}$) (37°C, 60 MHz)	Relaxometry	-	-	-	-	-	21.4	18.5
r_2/r_1 (37°C, 60 MHz)	Relaxometry	-	-	-	-	-	1.59	1.55
A(or C)/A-D	1H NMR	-	-	-	1.13	1.35 (empty) 0.87 (Lu^{3+})	-	-
M content (µmol/mg)	ICP-OES	-	-	-	-	-	0.604	0.630
(Gd :) Si : N : C (% mass)	Elemental analysis	-	-	-	-	19.0 Si : 8.0 N : 28.6 C	9.5 Gd : 18.0 Si : 6.8 N : 24.1 C	9.9 Gd : 17.0 Si : 7.0 N : 25.9 C
A-D : A : T (: Gd) (molar ratio)	Elemental analysis	-	-	-	-	1.0 A-D : 1.0 A : 5.1 T	1.0 A-D : 1.2 A : 6.0 T : 0.8 Gd	1.0 A-D : 0.3 A : 5.1 T: 0.7 Gd
Free DOTAGA (%)	Eu^{3+} titration	-	-	-	-	100	10	24
Free DOTAGA (%)	Elemental analysis	-	-	-	-	100	23.2	33.0
Yield (%) (in DOTAGA)	-	-	-	-	-	9.2	6.9	10.7
Yield (%) (in Gd)	-	-	-	-	-	-	64	10.6

**A-D: APTES-DOTAGA, A: APTES, C : CEST, T: TEOS, [#]S: symmetrical, D : distorted*

2.2.2.2.1. Fixed silane concentration protocols

Three first syntheses i.e. USNP@DOTA-pre1, 2, 3 were designed with the concentration of APTES-DOTAGA (from Chematech) at 50 mM. In the first synthesis, the ratio of APTES-DOTAGA : APTES : TEOS was kept at 1 : 1 : 2 (USNP@DOTA-pre1). Syntheses without APTES (USNP@DOTA-pre2) and with CEST as a replacement of APTES (USNP@DOTA-pre3) were also conducted for comparison. To begin the synthesis, APTES-DOTAGA was dissolved in water and pH of the solution was adjusted to 9 before APTES (or CEST) and TEOS was added. This pH is probably high enough to facilitate the hydrolysis of silanes but low enough not to hydrolyze amide bonds of APTES-DOTAGA. The rest of the protocol was similar to the case of TANED.

All three samples demonstrate satisfactory hydrodynamic diameter i.e. 4.9, 6.3 and 5.2 nm respectively (Figure 2-31-A). The difference was again only revealed with HPLC (Figure 2-31-B). Formula with carboxylsilane, USNP@DOTA-pre3, showed a more intense and symmetrical NP's peak compared to the other two, when samples at the same concentration were injected to HPLC.

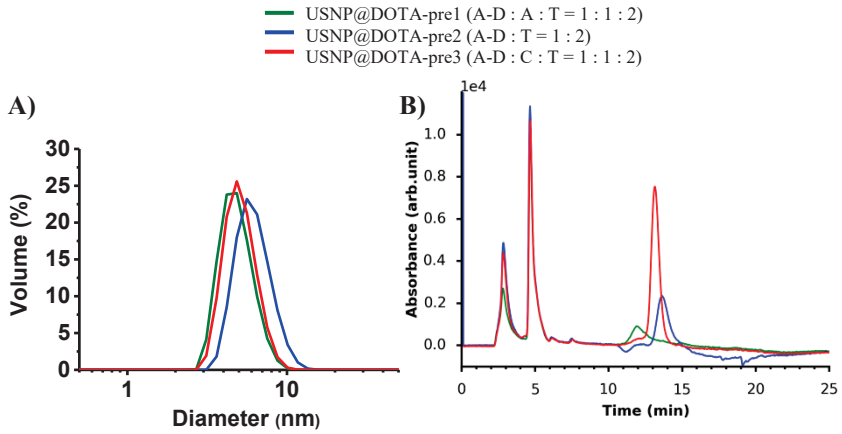

Figure 2-31. The effects of silane composition on three initial formulas of USNP@DOTA (USNP@DOTA-pre1, 2 and 3). A) DLS diagrams; B) HPLC chromatograms before purification.

USNP@DOTA-pre3 was also purified by tangential filtration and re-analyzed by HPLC and NMR-DOSY (Figure 2-32-A, B). As the chromatograms and DOSY spectrum have shown, the purified sample presented a homogeneous and stable population of NP with D ~ 71 $\mu m^2/s$ corresponding to a D_H ~ 5.5 nm. Until now, the tendency was very similar to what happened with TANED. What make APTES-DOTAGA different were the results of USNP@DOTA-pre1 and USNP@DOTA-pre2. These particles actually remain stable during the purification process. The chromatograms and DOSY spectrum of USNP@DOTA-pre2 were actually very similar to the ones of USNP@DOTA-pre3. Another point to be noticed is that these DOSY spectra were recorded at 10 and 15 g/l of USNP@DOTA-pre2 and 3 respectively. These concentrations are quite low compared to the ones that have been used previously. These data show a much higher level of stability of APTES-DOTAGA compared to TANED in the same conditions of synthesis. This might be due to a bulkier structure of APTES-DOTAGA compared to TANED. Hence, APTES-DOTAGA might be more efficient than TANED in protecting the polysiloxane network from being hydrolyzed. The effect of bulkiness of

organosilanes has been used to explain the greater hydrolytic stability of 11-aminoundecyltriethoxysilane (AUTES) or N-(6-aminohexyl)aminomethyltriethoxysilane (AHAMTES) compared to APTES[179,196,201] or the greater hydrolytic stability of long chain C18 functionalized silica HPLC reversed phase column compared to short chain C4 functionalized silica.[202–204]

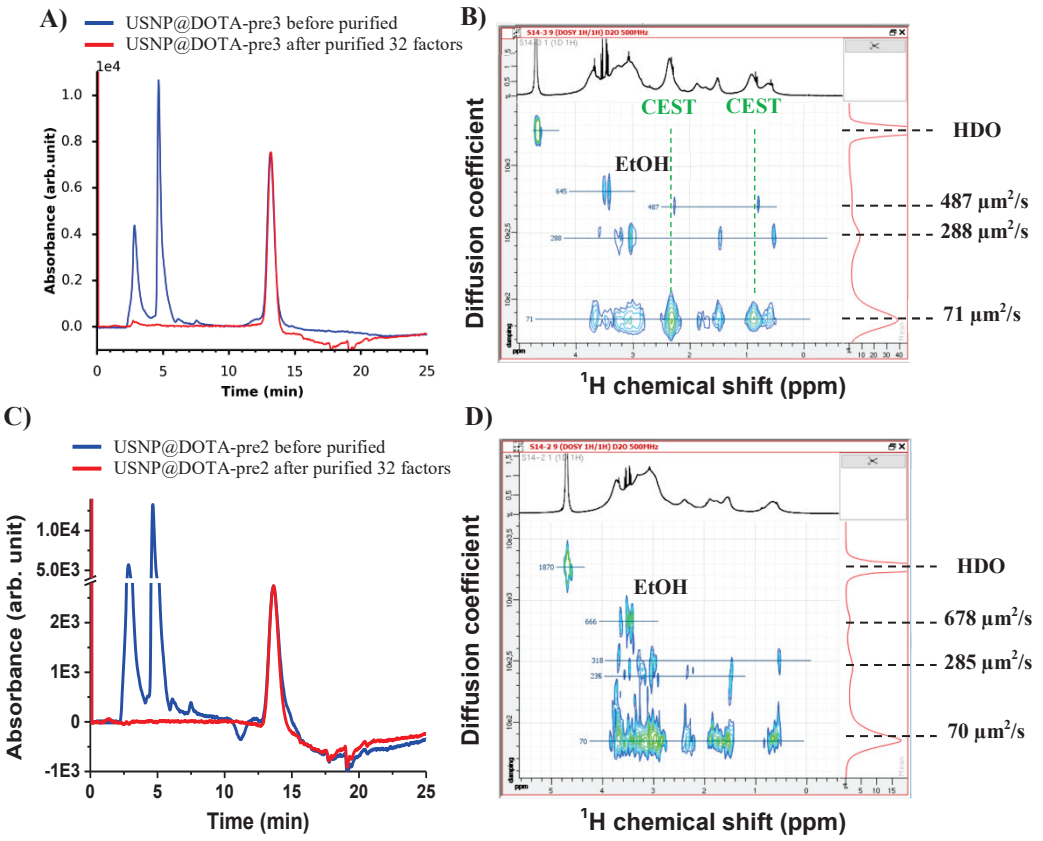

Figure 2-32. A) Chromatograms before and after purified of USNP@DOTA-pre3; B) NMR-DOSY spectrum of USNP@DOTA-pre3 after purified at 15 g/l pH 4.5. C) Chromatograms before and after purified of USNP@DOTA-pre2; B) NMR-DOSY spectrum of USNP@DOTA-pre2 after purified at 10 g/l pH 4.5.

For USNP@DOTA-pre1, the real composition of AGuIX that we would like to achieve, although, the particles were stable during the purification, chromatogram of purified sample showed a distorted NP's peak with at least two populations underneath (Figure 2-33-A). It was speculated that since the efficiency of the reaction was low (probably ~ 20 – 30% based on the mass collected after lyophilization), the concentration of the silane after purification probably reduced to around 10 – 15 mM which might be too low to keep the particles remain intact. Hence, the produced particles might have degraded during the purification to show inhomogeneous population.

The first solution that we proposed to overcome this phenomenon was to increase the silane concentrations in the formula to four times higher than the initial one (800 mM vs. 200 mM) to maintain a high concentration at the end of the process after all the purification steps (Table 2-6). The new formula (USNP@DOTA-pre4) has been prepared with a similar protocol to USNP@DOTA-pre1. Though the symmetry of the particle's peak after purification seemed a bit improved, there were still evidences indicating the presence of two populations (Figure

2-33-B). The peak width of the chromatogram was still too wide ($FWHM_{USNP@DOTA\text{-}pre4}$ = 1.6833 vs. $FWHM_{USNP@DOTA\text{-}pre3}$ = 0.6083). DOSY spectrum also showed a little bit sign of non-symmetrical distribution of diffusion coefficients at the value of the particles (~70 $\mu m^2/s$) (Figure 2-33-C). The most obvious evidence was the chromatogram of the particles after complexed with Cu^{2+} (Figure 2-33-D). The chromatogram was recorded at 700 nm where Cu^{2+} complexes absorb specifically. We can see clearly a shoulder appearing before the main particle peak.

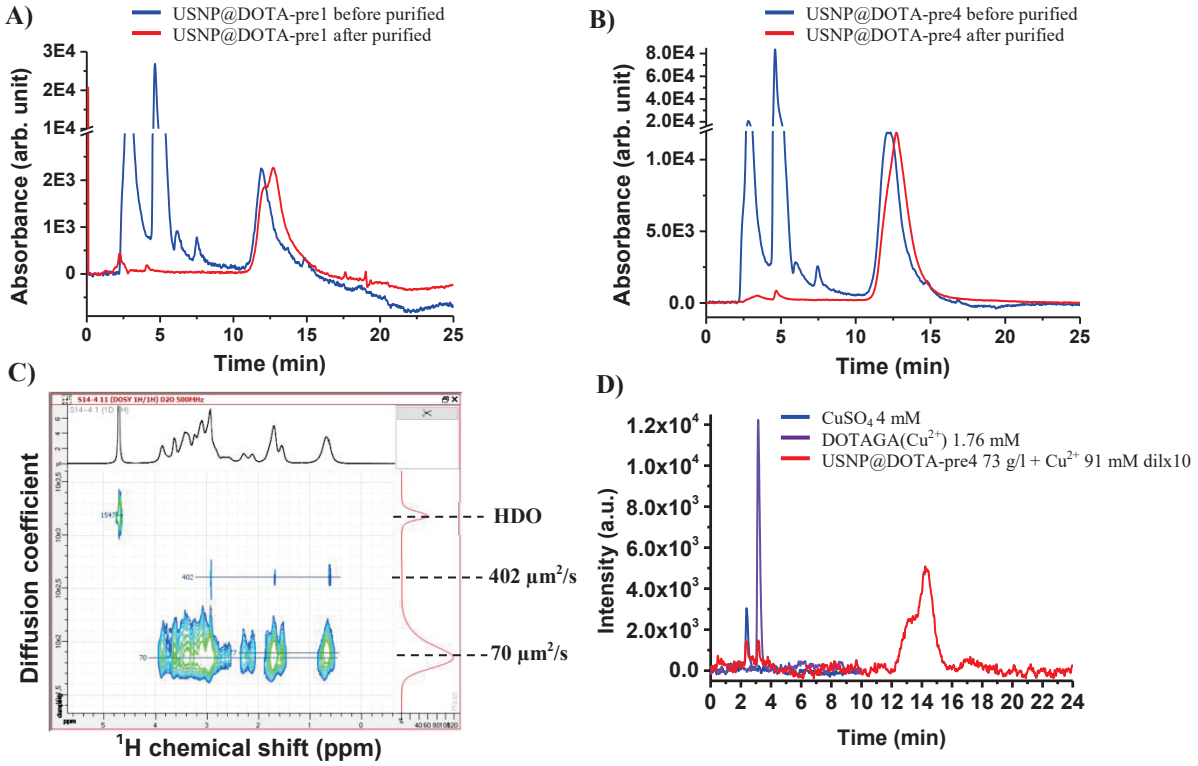

Figure 2-33. The effect of concentration on USNP@DOTA (USNP@DOTA-pre1 vs. USNP@DOTA-pre4). A) Chromatograms of USNP@DOTA-pre1 before and after purified; B) Chromatograms of USNP@DOTA-pre4 before and after purified; C) NMR-DOSY spectrum of USNP@DOTA-pre4 after purified at 80 g/l pH 4.5 and D) Chromatogram at 700 nm of USNP@DOTA-pre4 after complexed with Cu^{2+} (red) (chromatograms of CuSO4 (blue) and DOTAGA(Cu2+) solution (violet) were added for comparison)

Possibly, the reason for this inhomogeneity was not only due to a low final concentration but also a too high initial concentration of silanes. At the beginning of the reaction, too high concentration of silanes might make the reaction happen too quickly. Plus, due to stronger basicity of APTES compared to CEST, APTES condensed and catalyzed the condensation of other silanes more quickly.

Therefore, we decided to propose another solution, gradient silane concentration protocol, where the initial concentration of silanes will be kept as low as 40 mM. After incubated, the solution will be first concentrated to a five times smaller volume and then purified at this concentration to maintain the integrity of the produced particles.

2.2.2.2.2. Gradient silane concentration protocols

2.2.2.2.2.a. Synthesis of USNP@DOTA

200 ml of water was added to an amount of powder containing 2.228 mmol of APTES-DOTAGA. The pH of the solution is adjusted to 9 by adding NaOH solutions. The solution was stirred for 1 – 2 h to to hydrolyze any preformed siloxane bonds between APTES-DOTAGA and homogenize its distribution in the solution. Then TEOS (1015 µl, 4.457 mmol) and APTES (527 µl, 2.228 mmol) were added one by one to the above solution. pH of the solution was readjusted to 9 by adding HCl solutions. Water was added to obtain the final concentrations of APTES-DOTAGA, TEOS and APTES around 10 mM, 20 mM and 10 mM respectively. In this condition including slightly basic pH, relatively low concentrations of silanes and high concentration of water, the hydrolysis of silane precursors happens very rapidly. Meanwhile the condensation, which produces water as a byproduct took place very slowly. This allows them to be in the forms of monomers or small oligomers and distributed evenly.[167] The mixture was stirred at 25°C for 18 h to let the solution become homogeneous which implies that all ethoxysilanes were hydrolyzed. HCl was added gradually under vigorous stirring to bring the pH to 4.5. The solution was stirred during 1 h more before being heated in an oil bath at 80°C for 18 h to complete the condensation and reach thermodynamic equilibrium.

The solution was then concentrated to 10 ml by tangential filtration through Vivaspin™ (MWCO = 3 kDa). Then the solution was further purified with tangential filtration. The pH of the solution should be adjusted to 2 by adding HCl solutions before the purification to reduce the electrostatic affinity of free chelators towards amine groups of NPs. The solution was purified for 1024 purification factor using HCl solution 10^{-2} M as washing solvent. Then, the solution was filtered through 0.2 µm membrane to remove dust and large impurities. Finally, the solution was freeze dried for long term storage. 706 mg of lyophilized powder was obtained.

2.2.2.2.2.b. Characterization of USNP@DOTA

1 ml of solution before being concentrated was filtered through 0.2 µm membrane and analyzed by DLS and HPLC. For HPLC, 2 samples were prepared: 1) The filtered solution was diluted 2 times to reach a theoretical concentration of APTES-DOTAGA equivalent to 5 mM before being injected to the column, The absorption was followed at 295 nm. 2) 200 µl of this solution was mixed with 5 µL of $CuSO_4$ 506 mM, an excess amount compared to the theoretical concentration of chelating agents in the solution at pH 3, 80°C for 2 h. The product was diluted to a theoretical concentration of 5 g/L right before being injected to HPLC system. The absorption was followed at 700 nm. Solutions after concentration and purification were also analyzed similarly by HPLC.

Figure 2-34-G shows the size distribution of the solution after the synthesis measured by DLS with average $D_H = 4.6 \pm 1.6$ nm. The zeta potential of the particle was – 21.4 and – 27.1 mV at pH 6.6 and 7.4 respectively. Figure 2-34-A, B, C show the chromatograms at 295 nm of the solution before concentration, after concentration and after purification. Among compounds present in the synthesis mixture, APTES-DOTAGA and DOTAGA (remaining reactant)

absorb more significantly in UV due to their bulkier structures. Meanwhile, APTES and TEOS are known for their UV transparency. Chromatograms at 700 nm of the NPs after complexed with $CuSO_4$ were also recorded to visualize specifically the eluates containing DOTAGA (Figure 2-34-D, E, F). As discussed previously, the first eluted group of peaks with retention time (t_R) from 2 to 5 min might be assigned to the unreacted precursors and the second wider peak (t_R ~ 13 min) can be assigned to the produced NPs. The results show that by concentrating and purifying, we were able to obtain a homogeneous population of NPs with high purity (> 90%).

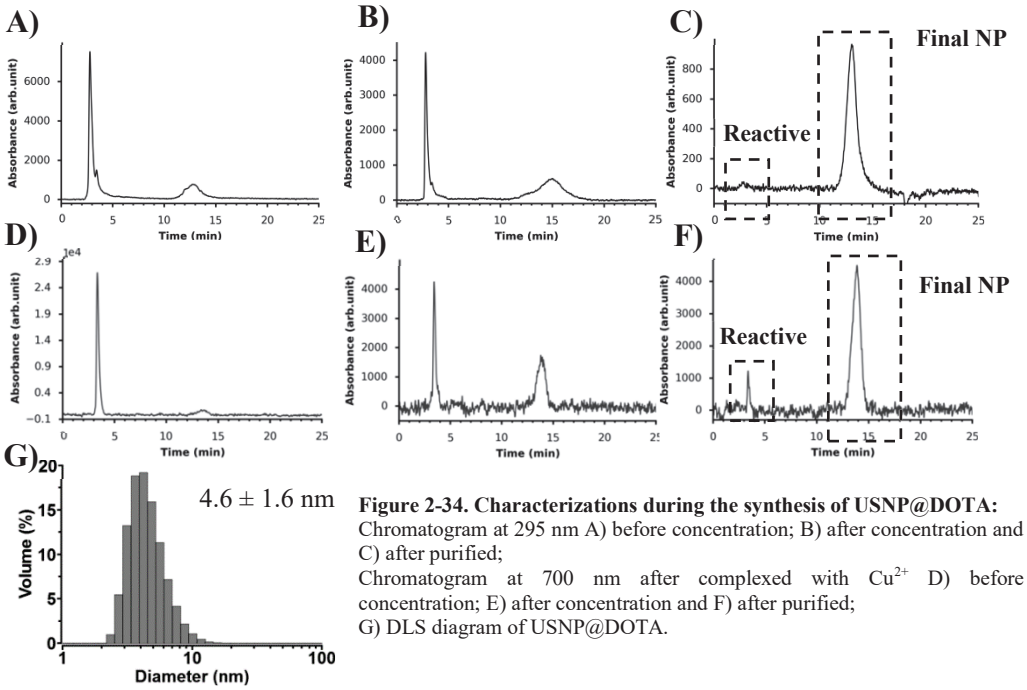

Figure 2-34. Characterizations during the synthesis of USNP@DOTA:
Chromatogram at 295 nm A) before concentration; B) after concentration and C) after purified;
Chromatogram at 700 nm after complexed with Cu^{2+} D) before concentration; E) after concentration and F) after purified;
G) DLS diagram of USNP@DOTA.

To evaluate the diameter of USNP@DOTA, the presence and the ratio of APTES-DOTAGA and APTES on its surface, ^{1}H NMR and NMR DOSY spectra were collected. Figure 2-35-A shows a 2D NMR-DOSY spectrum of USNP@DOTA in D_2O. Most of protons seem to have the same diffusion coefficient (D) at 54.4 $\mu m^2/s$. The result indicates that expected organic groups i.e. APTES-DOTAGA and APTES were grafted on the same particles. Second, there are some free hydrolyzed silanes which have much faster coefficient (194.5 $\mu m^2/s$). Hydrodynamic diameter of the main particles can be calculated from Einstein equation which is around 7.0 ± 2.5 nm. The viscosity of the solution was unknown and might be considerably higher than pure D_2O at this concentration (127 g/l). Therefore, the calculated D_H might be a bit overestimated compared to the value measured from DLS (4.6 ± 1.6 nm, Table 2-6). Nevertheless, it stayed less than 10 nm and was in accordance with the DLS result. Figure 2-35-B shows the peak integration of ^{1}H spectrum of the USNP@DOTA. The ratio APTES over APTES-DOTAGA in the sample was found as 1.35.

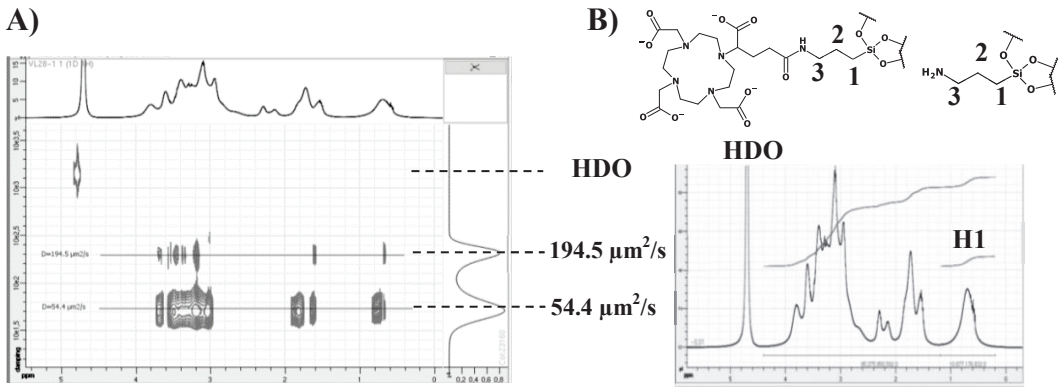

Figure 2-35. NMR study of USNP@DOTA: A) NMR-DOSY spectrum and B) The positions of H1, H2 and H3 on the APTES and APTES-DOTAGA functional groups on the particle and ^{1}H NMR spectrum of USNP@DOTA at 127 g/l in D_2O.

Elemental analysis revealed the contents of USNP@DOTA in Si, C and N (Table 2-8). From these results, we can calculate the contribution of each species i.e. APTES-DOTAGA, APTES and TEOS if we assume that after the condensation, each molecule of APTES-DOTAGA, APTES and TEOS implies the molecular structure as $SiO_{1.5}(CH_2)_3NH$-$DOTAGA^{(2-)}$, $SiO_{1.5}(CH_2)_3NH_3^+$ and SiO_2 respectively. As the results suggest, the ratio of APTES-DOTAGA: APTES : TEOS in USNP@DOTA is 1 : 1 : 5.1.

To obtain the average chemical formula of a single USNP@DOTA, the mass of the particle should be determined. For this purpose, ESI-MS was performed taking its advantage as a soft ionization method which is suitable for studying nano assemblies. Figure 2-36 (left) shows the MS spectrum of USNP@DOTA averaged from 5 different spectra acquired in different ESI-MS conditions to collect all charge states of this NP. The deconvoluted spectrum was shown in Figure 2-36 (right). A main peak at around 12.5 kDa and two other peaks at around 10.9 kDa and 14.3 kDa were observed. Combining with the ratio of species deduced from elemental analysis, this result corresponds with the chemical formula APTES-$DOTAGA_{12.5}APTES_{12.5}TEOS_{64}$ for the main peak and APTES-$DOTAGA_{11}APTES_{11}TEOS_{56}$; APTES-$DOTAGA_{14.5}APTES_{14.5}TEOS_{74}$ for two otherpeaks.

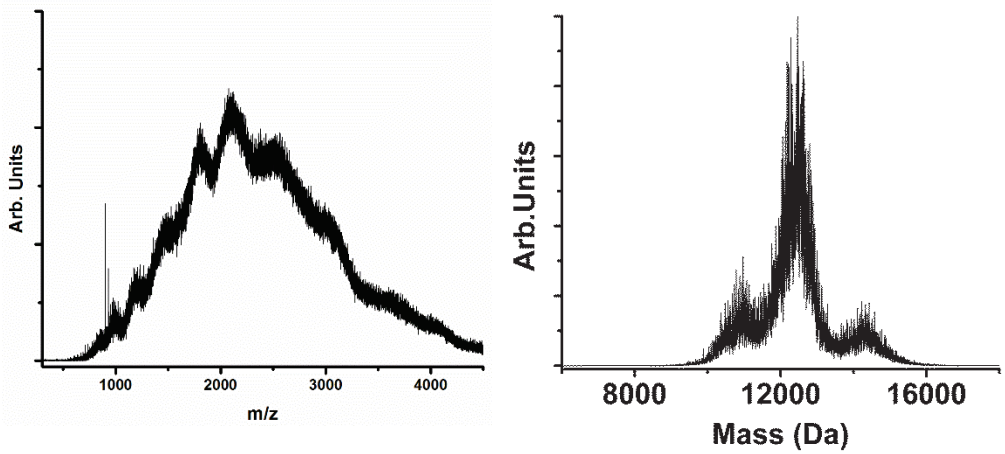

Figure 2-36. ESI-MS spectrum (left) and deconvoluted spectra (right) of USNP@DOTA.

2.2.2.2.2.c. Quantification of DOTAGA on USNP@DOTA

The content of DOTAGA on the particle was also determined by two other methods: 1) HPLC analysis with copper (Cu^{2+}) and 2) titration with Eu^{3+} phosphorescence.

HPLC analysis with Cu^{2+}:

A small amount of USNP@DOTA was complexed with an excess of $CuSO_4$ and analyzed by HPLC (Figure 2-37-A). The chromatograms of the solution at 700 nm was superimposed with the ones of $CuSO_4$ and DOTAGA(Cu^{2+}). The assignment of the peaks in the chromatogram of USNP@DOTA(Cu^{2+}) becomes straightforward. The first peak, the second peak and the third peak correspond to free copper ions, (APTES-)DOTAGA(Cu^{2+}) and USNP@DOTA(Cu^{2+}) respectively. More importantly, the shape of nanoparticles peak shows a homogenous distribution after the complexation. The calibration curves and the detailed results can be found in Figure 2-37-B and Table 2-7. From the results, we can find out the total concentration of DOTAGA in the sample and deduce its content which was about 0.72 µmol/mg.

Phosphorescence titration with Eu^{3+}:

The principle of the titration was exactly the same as described in 2.2.2.1.2.b. Figure 2-37-C shows the titration curve of the sample with the equivalent point at around 0.79 µmol/mg.

In addition, it is also possible to come up with the contents of each species based on the result of the elemental analysis. The content of APTES-DOTAGA was calculated as 0.95 µmol/mg (Table 2-8). The three methods show more or less similar results. However, HPLC analysis using Cu^{2+} is limited by a low level of signal/noise at 700 nm with our detector, the small volume of sample taken and the possible lack of access of some chelators on the particle in a highly concentrated solution. Meanwhile, the results from elemental analysis was based on several indirect calculations that imply accumulating subtle errors. These left Eu^{3+} titration as probably the most precise method. Thus, its result (0.79 µmol/mg) will be used for the next steps.

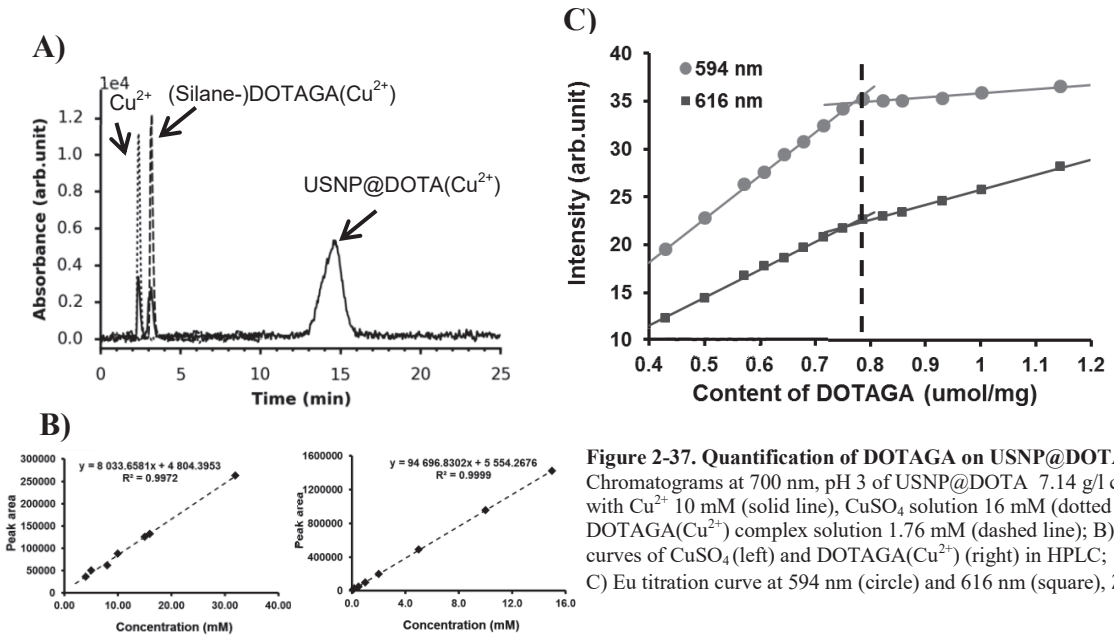

Figure 2-37. Quantification of DOTAGA on USNP@DOTA: A) Chromatograms at 700 nm, pH 3 of USNP@DOTA 7.14 g/l complexed with Cu^{2+} 10 mM (solid line), $CuSO_4$ solution 16 mM (dotted line) and DOTAGA(Cu^{2+}) complex solution 1.76 mM (dashed line); B) Calibration curves of $CuSO_4$ (left) and DOTAGA(Cu^{2+}) (right) in HPLC; C) Eu titration curve at 594 nm (circle) and 616 nm (square), λ_{ex} = 395 nm.

Table 2-7. Summarized table of peak areas in the chromatogram of USNP@DOTA complexed with Cu^{2+}

Peak	Area	Concentration (mM)	%
Cu^{2+}	44342	4.92	
Silane-DOTAGA(Cu^{2+})	53630	0.51	9.94
NP-DOTAGA(Cu^{2+})	441283	4.60	90.06
	Total	10.03	

2.2.2.2.2.d. Synthesis of USNP@DOTAGd*

To verify whether the structural difference between uncomplexed and complexed APTES-DOTAGA can affect the silane chemistry, APTES-DOTAGA was first complexed with Gd^{3+} before being added in the synthesis of the silica particles.

200 ml of water was added to an amount of powder containing 2.333 mmol of APTES-DOTAGA. The pH of the solution is adjusted to 4 by adding NaOH solutions. 1.938 mL of $GdCl_3$ solution at 2.188 M (molar ratio (APTES-DOTAGA+DOTAGA) : Gd = 1 : 0.9) was added in 3 times. Between each time, pH was carefully increased to 4 – 5 by adding NaOH solution with appropriate concentrations before adding the next one. After 3 additions, pH was at 5. This solution was incubated at 80°C. pH was verified and re-adjusted to 5 after each 24 h. After 48 h of incubation, pH stayed at 5 steadily.

The pH of the above solution was adjusted to 9. Then the solution was stirred for 1 h to hydrolyze preformed siloxane bonds between APTES-DOTAGA(Gd^{3+}). Then TEOS (1063 µl, 4.666 mmol) and APTES (551 µl, 2.333 mmol) were added to the above solution. pH of the solution was readjusted to 9 by adding HCl solutions before water was added to obtain the final concentrations of APTES-DOTAGA(Gd^{3+}), APTES-DOTAGA, TEOS and APTES at 9 mM, 1 mM, 20 mM and 10 mM respectively. The rest of the protocol followed the same steps as described for USNP@DOTA. 716 mg of powder of USNP@DOTAGd* was obtained.

2.2.2.2.2.e. Characterization of USNP@DOTAGd*

DLS and HPLC analyses were performed with solution before being concentrated, after being concentrated and after purification in similar manners. For HPLC, the analyses with Cu^{2+}-complexed samples could not be performed, due to the absence of free chelates. Instead, fluorescence detector (λ_{ex} = 274 nm, λ_{em} = 312 nm) was used to qualitatively detect the presence of Gd complexes.

Figure 2-38-G shows the size distribution measured by DLS of the particles after purification with average D_H = 2.8 ± 0.7 nm. This measurement was repeated 2 more times while giving similar values around 3 nm. This result can be explained by a less charged state and/or a more compact configuration of Gd-complexed DOTAGA compared to free DOTAGA. This structural difference might allow a neater assembling of silanes which led to the formation of smaller particles. Figure 2-38-A, B, C shows the chromatograms at 295 nm of solutions at different steps of the synthesis. The same elutions were also followed by fluorescence detector (Figure 2-38-D, E, F). These chromatograms show similar results as observed for USNP@DOTA. Finally after concentrating and purifying, we were also able to obtain a homogeneous population of NPs with high purity (> 90%). Its zeta potential was -35.6 mV at pH 7.4 (Table 2-6).

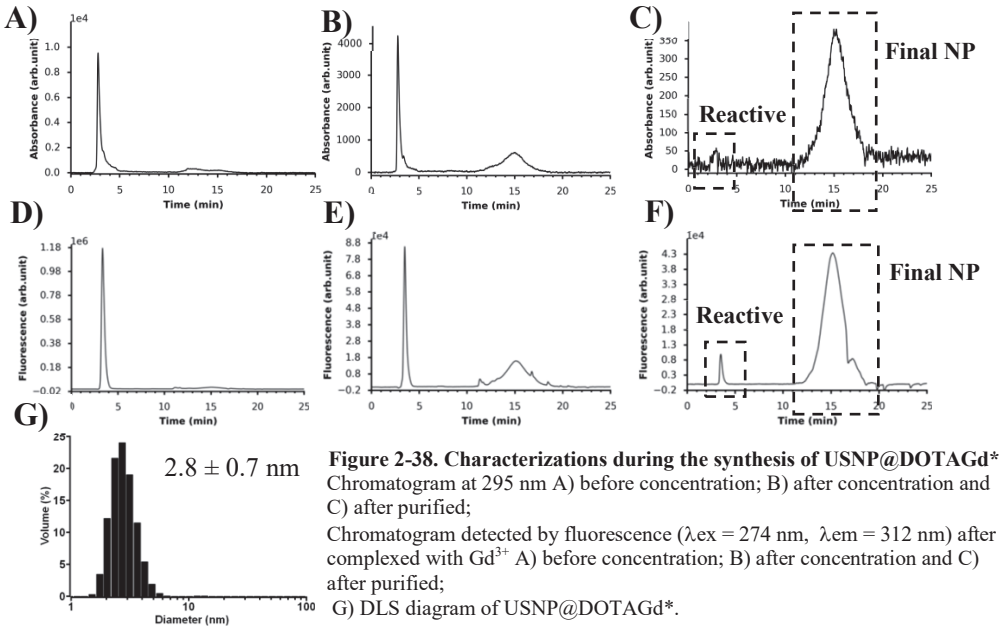

Figure 2-38. Characterizations during the synthesis of USNP@DOTAGd*
Chromatogram at 295 nm A) before concentration; B) after concentration and C) after purified;
Chromatogram detected by fluorescence (λex = 274 nm, λem = 312 nm) after complexed with Gd^{3+} A) before concentration; B) after concentration and C) after purified;
G) DLS diagram of USNP@DOTAGd*.

According to the elemental analysis, the ratio of Gd : APTES-DOTAGA : APTES : TEOS in USNP@DOTAGd* can be estimated as 0.7 : 1 : 0.3 : 5.1 (Table 2-8). USNP@DOTAGd* has less amine (condensed APTES) and slightly more free DOTAGA in its structure which explains a more negative zeta potential compared to USNP@DOTAGd. The reason for the difference between the two particles is totally understood. Probably, the complexed chelating silane (APTES-DOTAGA(Gd^{3+})) somehow affect differently on the condensation and silane distribution compared to the free chelating silane (APTES-DOTAGA). This might be because the former has a fixed charge -1 and a more compact configuration whereas the latter has varied negative charges depending on the pH of the solution and a more flexible configuration.

Table 2-8. Elemental analysis of USNP@DOTA

Batch	USNP@DOTA			USNP@DOTAGd			USNP@DOTAGd*		
%mass Gd	0.0000			9.5000			9.9000		
relative mol Gd	0.0000			1.0000			1.0000		
%mass Si	19.0000			18.0000			17.0000		
relative mol Si	1.1845			10.6069			9.6129		
%mass C	28.6000			24.1000			25.9000		
relative mol C	4.1703			33.2155			34.2541		
%mass N	8.0000			6.8000			7.0000		
relative mol N	1.0000	Ratio	Content (µmol/mg)	8.0341	Ratio	Content (µmol/mg)	7.9363	Ratio	Content (µmol/mg)
relative mol Gd	0.0000		0.0000	1.0000	0.7681	0.6041	1.0000	0.6702	0.6296
relative mol A-D*	0.1672	1.0000	0.9547	1.3019	1.0000	0.7865	1.4922	1.0000	0.9394
relative mol A	0.1640	0.9812	0.9367	1.5247	1.1711	0.9211	0.4753	0.3185	0.2992
relative mol T	0.8533	5.1038	4.8725	7.7803	5.9762	4.7003	7.6454	5.1236	4.8133
free chelators						0.1824			0.3099
% free chelators				23.1883			32.9844		

**A-D: APTES-DOTAGA, A: APTES, T: TEOS*

In conclusion, the synthesis of USNP@DOTA* could interestingly produce slightly smaller particles. On the other hand, the synthesis of USNP@DOTA produced relatively small (< 7 nm), non-metal NPs. This feature makes it possible to thoroughly investigate the structure of the particle using NMR. In addition, this strategy can also prevent a significant waste of Gd during the purification.

2.2.3. One-pot synthesis of USNP using *in situ* formed chelating silanes

In order to propose an even simpler protocol, we combined the reaction of APTES and DOTAGA anhydride with the hydrolysis and condensation to produce the NPs into a single continuous process while reducing the cost and experimental time. In addition, by changing the ratio of silane precursors in the formula, we can control the size of the particles (Figure 2-39). The starting ratio of componentns and characterization results are summarized in Table 2-9. We will go over the details in the next parts.

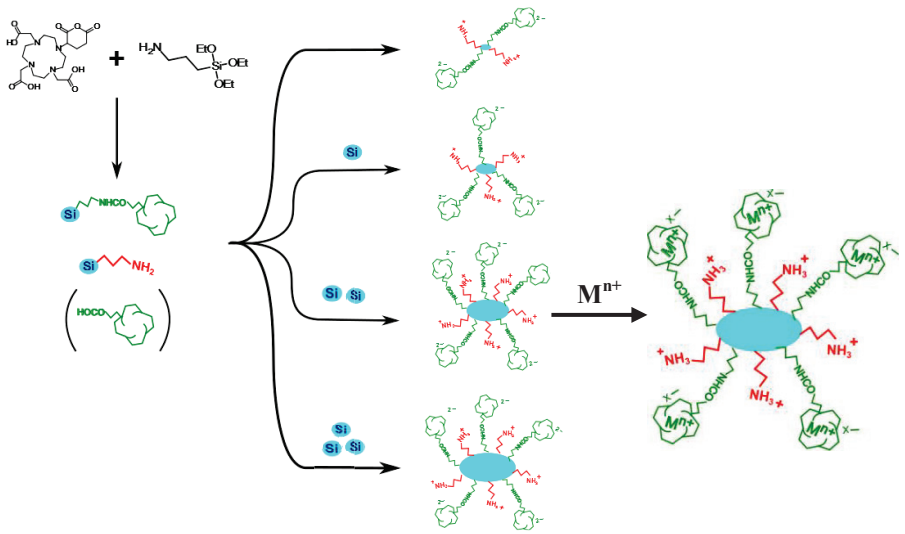

Figure 2-39. The synthesis of USNP using *in situ* formed chelating silane (USNP@DOTA$_{IS}$) and metal complexations (M^{n+} = Gd^{3+}, Lu^{3+}, Eu^{3+} Tb^{3+}, Ho^{3+}, Cu^{2+}, Bi^{3+})

Table 2-9. Properties of formulas of USNP using *in-situ* formed APTES-DOTAGA (USNP@$DOTA_{IS}$)

Properties	Method(s)	USNP@ $DOTA_{IS}$-1	USNP@ $DOTA_{IS}$-2	USNP@ $DOTA_{IS}$-3	USNP@ $DOTA_{IS}$-4	USNP@ $DOTA_{IS}$-5
Starting ratio A-D : A : T*	-	7 A-D : 3 A : 0 T	7 A-D : 3 A : 5 T	7 A-D : 3 A : 10 T	7 A-D : 3 A : 15 T	7 A-D : 8 A : 20 T
Total [silane] (mM)		20	20	20	20	60
Solvent		DMSO/H_2O	DMSO/H_2O	DMSO/H_2O	DMSO/H_2O	DEG/H_2O
D_H after synthesized (nm)	DLS	too weak signal	5.2 ± 1.2	7.5 ± 2.1	13.6 ± 3.9	4.1 ± 1.0
D_H redispersed pH 2 (nm)	DLS	1.9 ± 0.3	3.4 ± 0.6	6.8 ± 1.7	precipitated	-
D_H redispersed pH 7 (nm)	DLS	2.8 ± 0.5	4.3 ± 0.9	7.6 ± 1.9	14.4 ± 7.1	5.2 ± 2.0
D_H (nm)	NMR DOSY	-	-	-	-	7.0 ± 2.5 (empty)
Zeta potential (mV)	Zeta potentiometry	-	-	-	-	Full curve -32.6 (pH 7.27)
Retention time (min)	HPLC (295 nm)	12.4	12.9	13.4	13.5	12.76
Peak shape	HPLC (295 nm)	S	S	S	S	S
FWHM (min)	HPLC (295 nm)	1.1250	0.9917	0.8417	0.4750	0.8583
Purity (%)	HPLC (295 nm)	94.0	97.1	90.1	88.6	98.3
DOTAGA content (µmol/mg)	Eu^{3+} titration	1.1	0.8	0.7	0.7	0.8
r_1 ($mM^{-1}.s^{-1}$) (37°C, 60 MHz)	Relaxometry	-	16.92	19.21	19.79	-
r_2/r_1 (37°C, 60 MHz)	Relaxometry	-	1.53	1.80	2.04	-
A/A-D	1H NMR	-	-	-	-	1.26 (empty)
Si : N : C (molar ratio)	Elemental analysis	-	1.0 : 1.0 : 3.8	1.4 : 1.0 : 3.8	1.8 : 1.0 : 3.9	1.1 : 1.0 : 4.4
A-D : A : T (molar ratio)	Elemental analysis	-	1.0 : 3.4 : 3.6	1.0 : 3.7 : 7.1	1.0 : 2.4 : 10.0	1.0 : 1.0 : 4.7
Yield (%) (in DOTAGA)	-	1.15	7.94	12.20	15.41	24.7

**A-D: APTES-DOTAGA, A: APTES, T: TEOS, #S: symmetrical*

2.2.3.1. Synthesis of USNP@DOTA$_{IS}$ in DMSO/H$_2$O

For the first series of samples (USNP@DOTA$_{IS}$-1, 2, 3, 4), 8 g of DOTAGA anhydride (13.96 mmol) was put in a 100 ml round flask to which 31.6 ml of DMSO anhydrous and 3.300 ml of APTES (13.96 mmol) was quickly added. DMSO was chosen since it is an aprotic solvent and cannot hydrolyze anhydride. This will assure a high yield of this coupling reaction. The reaction was stirred under argon atmosphere and heated to 75^{o}C for 18 h. The product was a golden solution. The mixture was let to cool down to room temperature before 663 ml of ultrapure water was added to dilute DMSO to less than 5% in order not to dissolve the tangential filtration membrane used in the next step.

The pH of the solution was adjusted to 9 by adding NaOH solutions and the mixture was stirred for 1h. Then the solution was separated in 4 volumes. 0, 1.814, 3.466, 5.199 mmol of TEOS and 0.819, 91, 173, 260 ml of water were added to each volume of sample to obtain increasing concentrations of TEOS and keep total silane concentrations in all samples at 20 mM. The samples were named as USNP@DOTA$_{IS}$ -1, 2, 3, 4 accordingly. The ratio of each component can be found in Table 2-9. The pHs of the final solutions were verified and re-adjusted to 9 if necessary. These solutions were stirred at 25^{o}C overnight to completely hydrolyze TEOS.

The day after, pH of the 4 solutions were readjusted to 4.5. The solutions were stirred for another hour before being heated to 40^{o}C overnight.

These solutions were concentrated by Vivaspin (MWCO = 3 kDa) to appropriate volumes in which the theoretical concentration of APTES-DOTAGA reaches 200 mM. Then the pHs of the solutions were adjusted to 2. Solutions were purified at this pH by Vivaspin for 64 purification factors using HCl 10^{-2} M as washing solvent. After the purification, the solutions were filtered through 0.2 µm membrane and freeze-dried for long term storage.

2.2.3.2. Synthesis of USNP@DOTA$_{IS}$ in DEG/H$_2$O

To demonstrate the possibility of scaling up this process, a larger batch has been synthesized (USNP@DOTA$_{IS}$-5). 6.187 ml of APTES (26.17 mmol) was added in a 200 ml glass bottle containing 90 ml of diethylene glycol (DEG). The solution was stirred at rt for 1h before 10 g of DOTAGA anhydride (17.45 mmol) was added.

DEG, previously used in our top-down synthesis, was used as a replacement for DMSO. DEG as other ethylene glycols can be added up to 10% in the aqueous mixture without damaging the filtration membrane used in the purification step. Subsequently, the total silane concentration could be raised to ca. 60 mM. The equilibrium between siloxane bond formation and dissociation depends very much on the concentration.[136,178,179,195] So by increasing moderately the total silane concentration, the yield in DOTAGA of the reaction was expected to significantly increase. A predicted difficulty of this protocol was the solubility of DOTAGA anhydride in DEG which could hamper the coupling reaction with APTES. Unlike the reaction in DMSO, heating, which could increase the solubility of DOTAGA anhydride, was not applied in this case due to the possibility of uncontrolled

reaction of DOTAGA anhydride with alcohol groups of DEG which can probably reduce the yield of the reaction with amine groups. Instead, the mixture was kept stirring at room temperature for a long period of time (5 days).

The starting ratio of APTES and DOTAGA anhydride was increased to 3 : 2 to obtain a more balanced ratio of APTES and APTES-DOTAGA at the end. 7.952 ml of TEOS (34.90 mmol) was added to the suspension. This mixture was stirred for 1h. Then 900 ml of ultrapure water was added. pH during the hydrolysis process was maintained at 4 instead of being adjusted to 9.

Since pH was kept at 4, two processes of hydrolysis and heating to complete the condensation was combined into a single one. The mixture was heated to 50°C and kept stirring for 18 h to allow a complete hydrolysis of TEOS. The solution was concentrated by Vivaflow cassette (MWCO = 5 kDa) to 200 mL. Then the pH of the solution was adjusted to 2. Solution was purified at this pH by Vivaflow for 50 purification factor with water as washing solvent (200 ml – 1 L – 200 ml – 1 L – 100 ml). After the purification, the solution was neutralized to pH 7.4 by adding drops of NaOH 1 M solution, filtered through 0.2 µm membrane and freeze-dried for long term storage.

2.2.3.3. Characterization of USNP@DOTA$_{IS}$

Different samples of USNP@DOTA$_{IS}$-1 (after the reaction between APTES and DOTAGA anhydride and after being exposed at pH 9 overnight) and USNP@DOTA$_{IS}$-5 (after the reaction between APTES and DOTAGA anhydride) were taken to quantify the amount of produced APTES-DOTAGA by the combination of Eu titration and HPLC probed by Gd^{3+}. It is worth to mention that, USNP@DOTA$_{IS}$-2, 3 and 4 were prepared from the same solution of USNP@DOTA$_{IS}$-1 by adding different amounts of TEOS. Hence, there was no interest to repeat these analyses with those samples.

The results for USNP@DOTA$_{IS}$-1 show that the exposure to pH 9 affects neither the DOTAGA structure nor the amide bond of APTES-DOTAGA (Figure 2-40, Table 2-10 (USNP@DOTA$_{IS}$-1)). According to the result, around 70% of DOTAGA anhydride has reacted. Since the same amount of APTES and DOTAGA anhydride was introduced, the ratio between APTES-DOTAGA and APTES before the condensation was 7 : 3. And the ratio of TEOS/(APTES-DOTAGA+APTES) was increased gradually 0 : 1, 0.5 : 1, 1 : 1 to 1.5 : 1 in USNP@DOTA$_{IS}$-1, 2, 3, 4 respectively (Table 2-9).

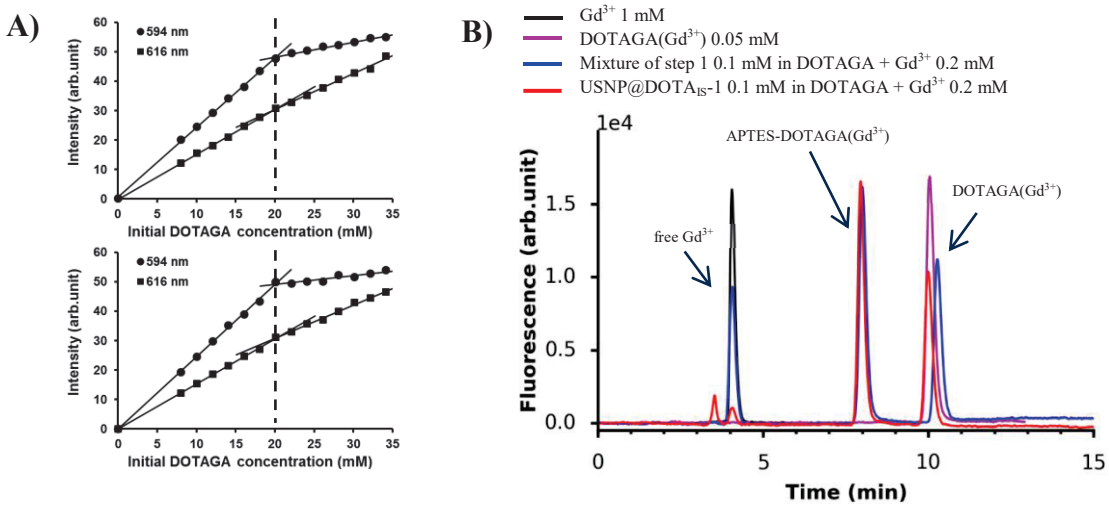

Figure 2-40. Quantification of produced APTES-DOTAGA in one-pot synthesis (USNP@DOTA$_{IS}$-1, 2, 3, 4):
A) Quantification of total DOTAGA by Eu titration: titration curve at 594 nm (circles) and 616 nm (squares) of mixture after the reaction between APTES and DOTAGA anhydride (upper) and the same mixture exposed at pH 9 overnight (lower).
B) Quantification of unreacted DOTAGA by HPLC probed by Gd^{3+}: chromatograms of Gd^{3+} 1 mM solution (black), DOTAGA(Gd^{3+}) solution (violet) and reacted mixture at around 0.1 mM in DOTAGA complexed with 0.2 mM Gd^{3+}(blue) and the same mixture exposed at pH 9 overnight (red).

Sample of USNP@DOTA$_{IS}$-5 was first diluted 10 times in water to obtain a clear solution instead of the initial suspension before being analyzed. Unexpectedly, despite appearing initially as an insoluble suspension after the synthesis, the produced mixture showed a reaction yield effectively equivalent to the one carried out in DMSO in the case of USNP@DOTA$_{IS}$-1 (70%) (Figure 2-41 and Table 2-10 (USNP@DOTA$_{IS}$-5)). Since 70% of DOTAGA anhydride has reacted, the ratio between APTES-DOTAGA, APTES and TEOS before the condensation was 7 : 8 : 20 (Table 2-9).

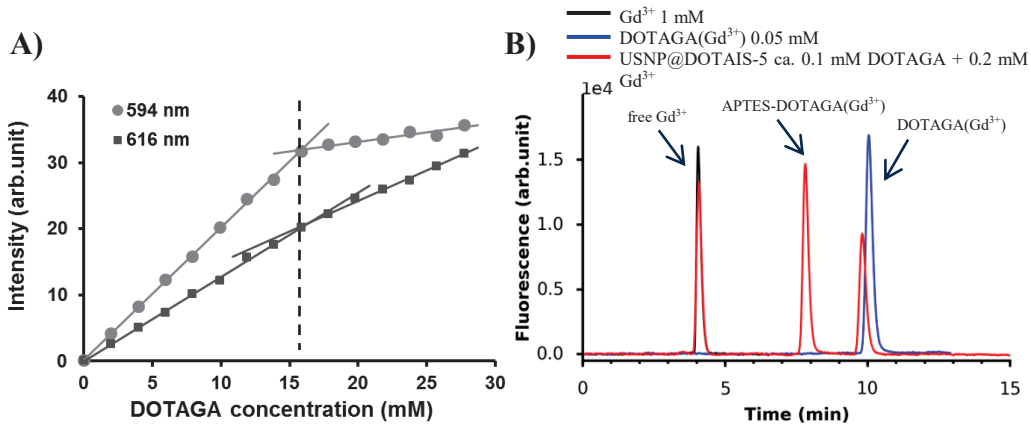

Figure 2-41. Quantification of produced APTES-DOTAGA in scaled up batch USNP@DOTA$_{IS}$-5:
A) Quantification of total DOTAGA by Eu titration: titration curve at 594 nm (circles) and 616 nm (squares)
B) Quantification of unreacted DOTAGA by HPLC probed by Gd^{3+}: chromatograms of Gd^{3+} 1 mM solution (black), DOTAGA(Gd^{3+}) solution (blue) and reacted mixture at around 0.1 mM in DOTAGA complexed with 0.2 mM Gd^{3+}(red)

Table 2-10. Summary of the result of the total DOTAGA and unreacted DOTAGA concentration

Samples	Measured time	[$DOTAGA_{total}$] (mM)	[$DOTAGA_{unreacted}$] (mM)	% $DOTAGA_{unreacted}$
USNP@DOTA-1	After the reaction	20	6.21	30.9
	In pH 9 overnight	20	5.91	29.4
USNP@DOTA-5	After the reaction	16	4.68	29.5

Four samples of USNP@$DOTA_{IS}$-1, 2, 3, 4 after purification and lyophilized were redispersed in water at 100 g/l. These stock solutions were quickly diluted to 10 g/l with HCl 10^{-2} M for DLS measurements. Another series of samples was redispersed at 150 g/L. NaOH solution was added to neutralize samples to pH 7 before water was added to obtain the final concentration around 80 – 100 g/L. Similarly, these stock solutions were quickly diluted to 10 g/L with water before being measured in DLS. Figure 2-42-A, B, C show the diameter diagrams in DLS of samples of the first series (USNP@$DOTA_{IS}$-1, 2, 3, 4) right after the synthesis, after being redispersed at pH 2 and after being redispersed at pH 7. The results showed a clear dependence of NP size and the added amount of TEOS as expected. D_H of USNP@$DOTA_{IS}$-1, 2, 3, 4 at pH 7 were 2.8, 4.3, 7.6 and 14.4 nm respectively. Similar tendency was observed with the same samples after the synthesis and after being redispersed at pH 2. Except the weak signal from USNP@$DOTA_{IS}$-1 after the synthesis and the precipitation of USNP@$DOTA_{IS}$-4 at pH 2, the other measurements reflect similar results. In the first exception, signal was too weak to have a reliable value implying the creation of very small nanoparticles and/or a diluted concentration of NPs. In the second case, the fact that USNP@$DOTA_{IS}$-4 could not be redispersed at pH 2 might be due to its lower colloidal stability explained by a bigger size, higher ratio of TEOS and lower density of protective layer of APTES-DOTAGA and APTES around it.

Chromatography was also performed with these four particles and confirmed the DLS results (Figure 2-42-D). A small sample of each purified solution was diluted 40 times in HCl 10^{-2} M right before being injected to HPLC for analysis at 295 nm. The more TEOS added in the formula, the slower the retention time of NPs. This indirectly shows the dependence of NP size on the amount of TEOS since a higher t_R usually implies a bigger NP.

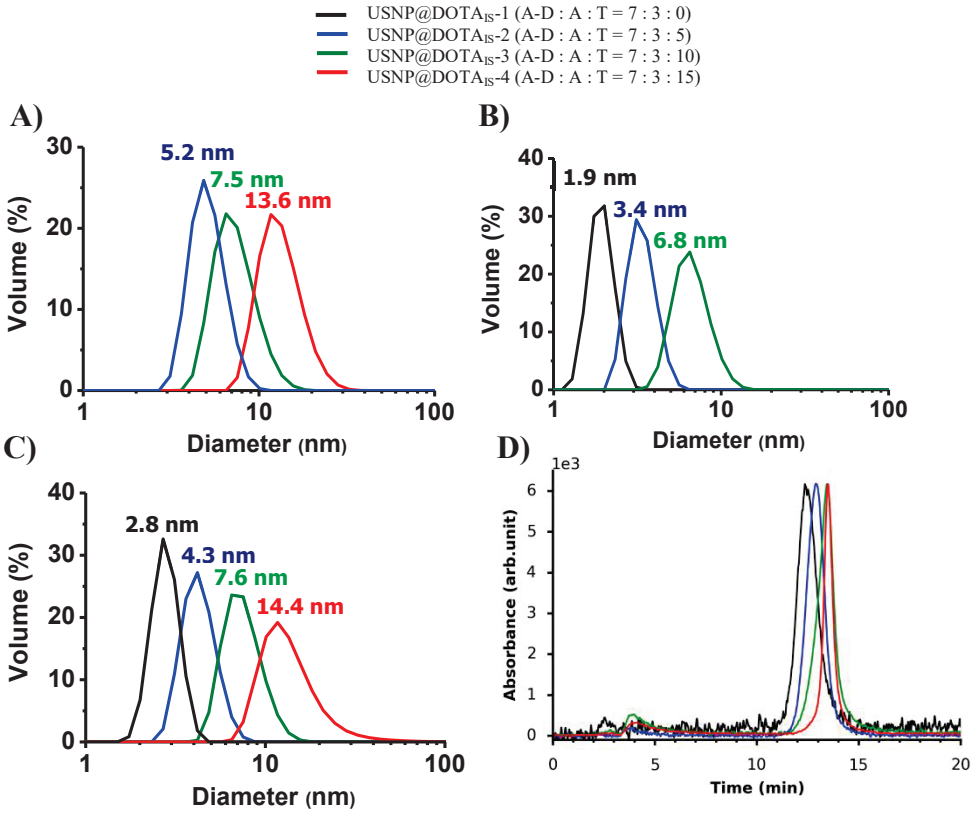

Figure 2-42. Size evolution of USNP@DOTA$_{IS}$: A) DLS diagrams of USNP@DOTA$_{IS}$-1 (black), USNP@DOTA$_{IS}$-2 (blue), USNP@DOTA$_{IS}$-3 (green), USNP@DOTA$_{IS}$-4 (red) A) right after the synthesis, B)) after being lyophilized and being redispersed at pH 2 C) being redispersed at pH 7; D) Chromatograms at 295 nm (normalized to the same height) of the same samples with respective color code (A-D: APTES-DOTAGA, A: APTES, T: TEOS).

Another indirect method to evaluate the size of the particles is to look at their relaxivities after being complexed with Gd. The bigger the particles are, the lower their rotational correlation times and so the higher their relaxivities are.[89] For this experiment, a small quantity of 3 samples was redispersed in water at 150 - 200 g/l or 120 – 150 mM in DOTAGA according to the results found by Eu titration. Their pHs were adjusted to 5.5. Then a small amount of $GdCl_3$ 50 mM in HCl 0.1 mM (molar ratio DOTAGA : Gd = 10 : 1) was added to have a quick and complete complexation without the need of purification. Their pHs were readjusted to 5.5 before being incubated at 80°C for 2 nights. Water was filled to achieve 50 mM in DOTAGA, 5 mM in Gd for each sample right before their relaxation times were measured. The amount of Gd in the samples were quantified precisely again with ICP-OES. Their relaxivities were calculated from relaxation time and Gd concentration and shown in Table 2-11. As expected, r_1 (and also r_2/r_1) increases in the order of USNP@DOTA$_{IS}$-2 (r_1 = 16.9 $mM^{-1}.s^{-1}$, r_2/r_1 = 1.53) < USNP@DOTA$_{IS}$-3 (r_1 = 19.2 $mM^{-1}.s^{-1}$, r_2/r_1 = 1.80) <USNP@DOTA$_{IS}$-4 (r_1 = 19.8 $mM^{-1}.s^{-1}$, r_2/r_1 = 2.04) (Table 2-11). (Due to insufficient reaction yield, USNP@DOTA$_{IS}$-1 could not be extensively characterized)

In short, these results show that by varying the starting ratio of siloxane network creating precursor, TEOS, and organosilanes, APTES-DOTAGA and APTES, the size of the NPs can be tuned.

Table 2-11. Relaxivities of USNP@DOTA$_{IS}$-2, 3, 4

	r_1 ($mM^{-1}.s^{-1}$)	r_2/r_1
USNP@DOTAIS-2 (10% Gd)	16.92	1.53
USNP@DOTAIS-3 (10% Gd)	19.21	1.80
USNP@DOTAIS-4 (10% Gd)	19.79	2.04

The elemental analyses also showed an increase of the molar ratio of Si over N or C in the order of USNP@DOTA$_{IS}$-2<USNP@DOTA$_{IS}$-3<USNP@DOTA$_{IS}$-4 in accordance with the amount of added TEOS (Table 2-14).

For the scaled up batch (USNP@DOTA$_{IS}$-5), the DLS diagrams at different steps during the synthesis show that before H_2O was added, no stable particle was created yet indicating by small values of D_H (~ 1 nm). After the hydrolysis and condensation of silanes, stable particles started to form. The final particle after lyophilized has D_H around 5.2 nm (Figure 2-43 and Table 2-12). Chromatography was also performed to verify the purity of the particle after the purification process (Figure 2-44 and Table 2-12). Its chromatogram showed a symmetrical peak demonstrating a homogenous NP distribution.

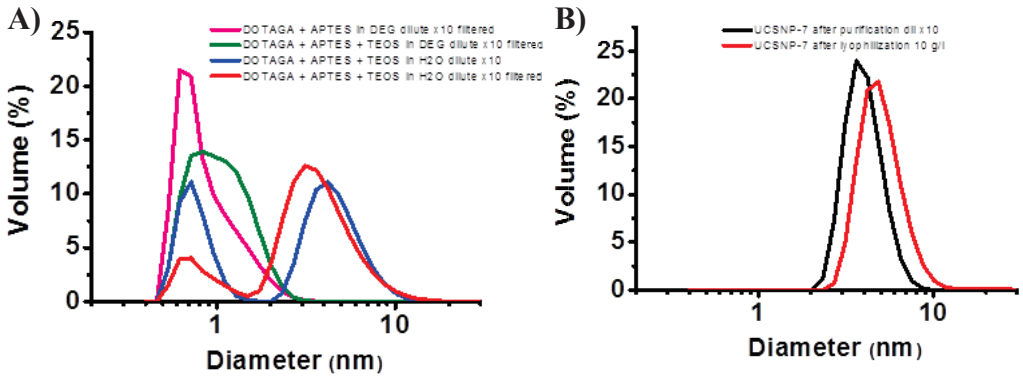

Figure 2-43. DLS diagrams of USNP@DOTA$_{IS}$-5: A) at different step during the synthesis: APTES + DOTAGA anhydride in DEG (pink), APTES + DOTAGA anhydride + TEOS in DEG (green), APTES + DOTAGA + TEOS in H_2O (blue), APTES + DOTAGA + TEOS in H_2O filtered through 0.2 µm membrane (red); **B) After being purified (black) and lyophilized (red).**

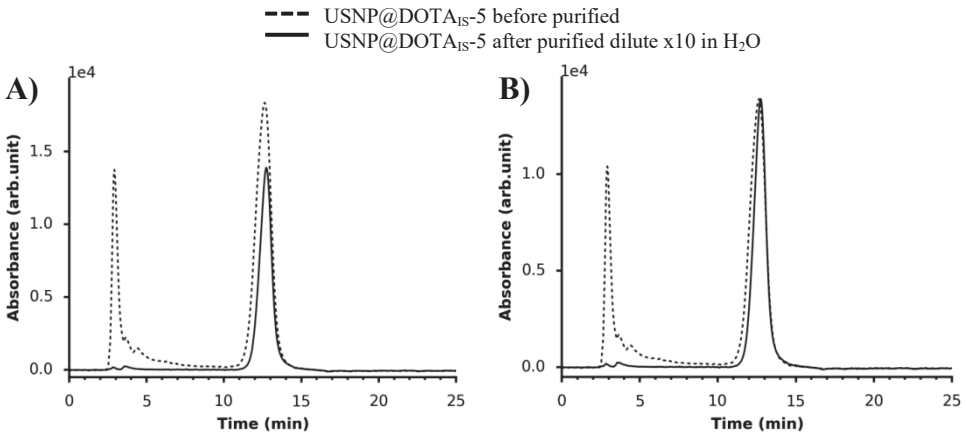

Figure 2-44. Chromatograms of USNP@DOTA$_{IS}$-5 at 295 nm: as A) originally acquired or B) normalized to the same height (dashed line: before purified, solide line: after purified)

Table 2-12. Summary of DLS and HPLC results of USNP@DOTA$_{IS}$-5 in different step during the synthesis

Samples	D_H (nm)	t_R (min)	FWHM (min)	Purity (%)
DOTAGA + APTES in DEG	0.9 ± 0.4	-	-	-
DOTAGA + APTES + TEOS in DEG	1.1 ± 0.4	-	-	-
DOTAGA + APTES + TEOS in H_2O	4.7 ± 1.7 & 0.8 ± 0.2	-	-	-
DOTAGA + APTES + TEOS in H_2O filtered	4.1 ± 1.9 & 0.8 ± 0.2	12.63	1.1333	68.6
USNP@DOTA$_{IS}$-5 after purification	4.1 ± 1.0	12.76	0.8583	98.3
USNP@DOTA$_{IS}$-5 redispersed after lyophilized	5.2 ± 2.0			

Since the amount of material in this batch is more sufficient. More elaborate experiments were performed to further investigate the structure of USNP@DOTA$_{IS}$-5. Zeta potential of the particle at pH 7.3 was -32.6 mV. The isoelectric point (pI) of the particle was around 4.24 (Figure 2-45 and Table 2-13) which seems reasonable given that at this pH DOTA predominantly has minus one or two charge (second and third protonation constants, pK_{H2L} and pK_{H3L}, of DOTA are 9.67 and 4.68 respectively[205]) and the starting ratio of APTES-DOTAGA/APTES was almost 1 : 1.

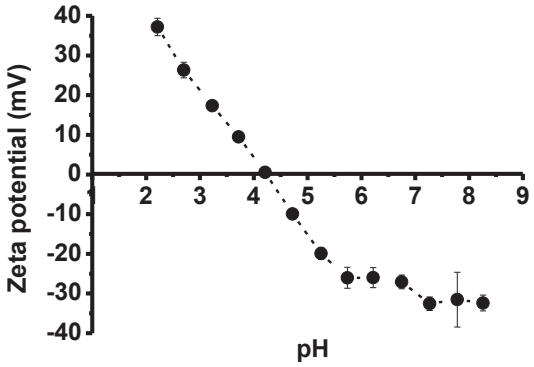

Figure 2-45. Zeta potentials of USNP@DOTAIS-5 at different pHs. (Each point was measured 3 times)

Table 2-13. Zeta potential of empty USNP@DOTA$_{IS}$-5 at different pHs

pH	Zeta potential (mV)
2.21	37.2
3.23	17.3
4.21	0.558
5.25	-19.9
6.22	-26
6.75	-27.1
7.27	-32.6
7.78	-31.5
8.26	-32.4

USNP@DOTA$_{IS}$-5 lyophilized powder was redispersed in D_2O for NMR analysis. DOSY spectrum shows that the diffusion coefficient of USNP@DOTA$_{IS}$-5 was around 55 $\mu m^2/s$ (Figure 2-46-A). D_H of USNP@DOTA$_{IS}$-5 calculated from Einstein equation was 7.0 ± 2.5 nm. This result was very similar to the value of USNP@DOTA. Except two multiplets at 3.52 and 3.62 indicating a small remaining amount of DEG, the ^1H spectrum of USNP@DOTA$_{IS}$-5

was also very similar to that of USNP@DOTA (Figure 2-46-B and Figure 2-35-B). The integration of ^{1}H peaks excluding the ones from DEG showed that the ratio APTES/APTES-DOTAGA in this case was 1.26. The ratio of DEG/APTES-DOTAGA can also be calculated by this technique as 0.33.

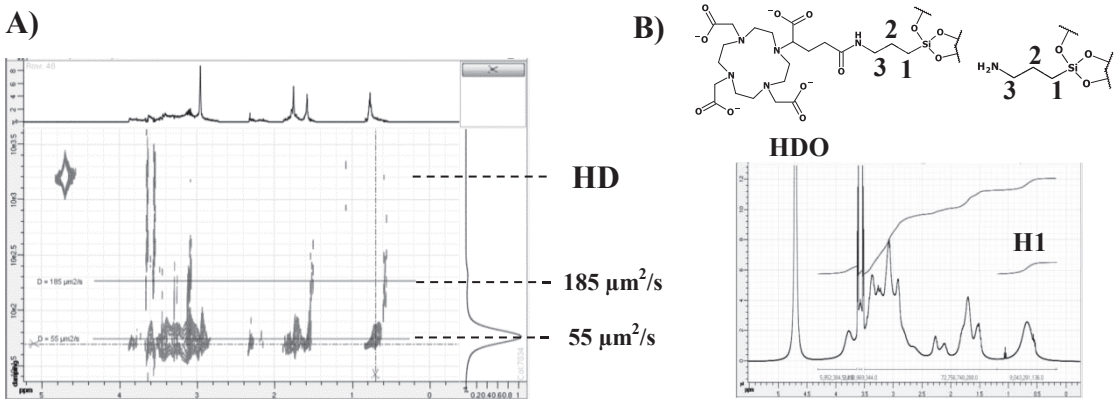

Figure 2-46. NMR spectra of USNP@DOTA$_{IS}$-5 at 100 g/l: A) NMR-DOSY spectrum; B) ^{1}H NMR spectrum.

From elemental anlysis, the ratio of APTES-DOTAGA : APTES : TEOS was calculated as 1.0 : 1.0 : 4.7 taking into account the amount of DEG calculated from NMR experiment (Table 2-14).

Finally, Figure 2-47 shows the original MS spectrum and the deconvoluted spectrum of USNP@DOTA$_{IS}$-5. They were very similar to USNP@DOTA with a main peak at around 11.5 kDa and two minor peaks at around 10.2 kDa and 13.5 kDa. This result was combined with the ratio of species inferred from elemental analysis to give the chemical formula of the main peak as APTES-DOTAGA$_{12}$APTES$_{12}$TEOS$_{56}$ and the ones of two minor peaks as APTES-DOTAGA$_{10.5}$APTES$_{10.5}$TEOS$_{50}$ and APTES-DOTAGA$_{14}$APTES$_{14}$TEOS$_{66}$.

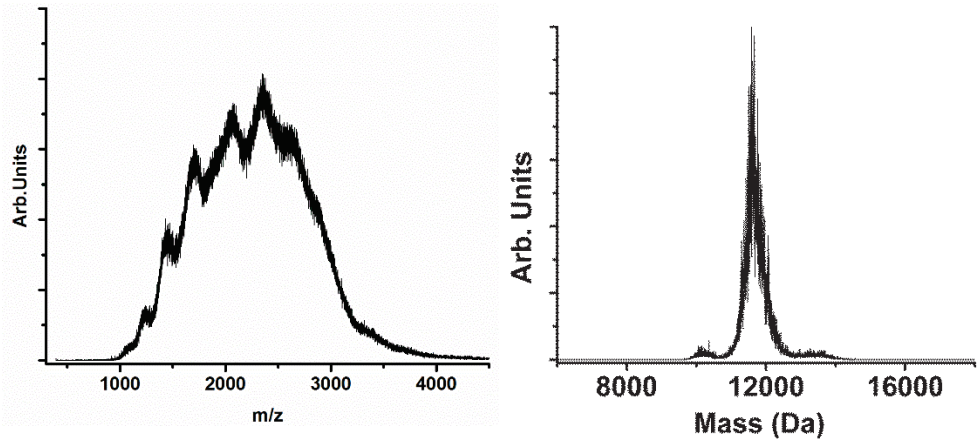

Figure 2-47. ESI-MS spectrum (left) and deconvoluted spectra (right) of USNP@DOTAIS-5.

2.2.3.4. Quantification of DOTAGA on USNP@DOTA$_{IS}$

The DOTAGA content of each sample was determined by Eu titration. For the first series of samples, USNP@DOTA$_{IS}$-1, 2, 3, 4, we see clearly a decrease of DOTAGA content from 1.1 µmol/mg to 0.7 µmol/mg when TEOS was increased in the formula as expected (Figure 2-48).

Combining this result with the total weight of produced particle, the yield of the process can be determined. Interestingly, the more TEOS we put, the higher the yield of APTES-DOTAGA at the end from 1.15% to 15.41% (Table 2-9). Presumably, the siloxane bond between silicic acid and organosilanol might be stronger than the siloxane bond between the organosilanols themselves. In addition, aminosilanes, especially the ones with short carbon chain such as APTES, are known as having quite low hydrolytic stability.[177,178,196] Another possible explanation might be due to the presence of flatter surface curvature on bigger particles which allow the formation of all three siloxane bonds per each organosilane i.e. APTES-DOTAGA and APTES. This feature makes organosilanes stick more stably on the surface of the particles and have higher resistance to water hydrolysis. On the contrary, smaller particles might have higher surface curvature which imposes more steric constraint on the formation of all three siloxane bonds per each organosilane. The relationship between surface curvature and particle stability has been studied before in the case of thiol ligands functionalized on gold NPs. Mei B.C. *et al.* have shown that 15 nm AuNP functionalized with thiol terminated PEGs has higher resistance to the digestion assay induced by sodium cyanide compared to the 5 nm counterpart.[206] It seems the thermodynamic equilibrium was driven more and more towards the creation and maintaining of the particle when more TEOS was added, while the mixture of APTES and APTES-DOTAGA alone cannot make up stable particles. This is the reason why pH was not necessarily adjusted to 9 before adding TEOS anymore in the case of USNP@DOTA$_{IS}$-5 to simplify the protocol. In fact, pH 4 was shown in some studies is where the condensation happens the most slowly.[207] Hence, this would actually facilitate the equilibrium towards keeping the NPs at ultrasmall size.

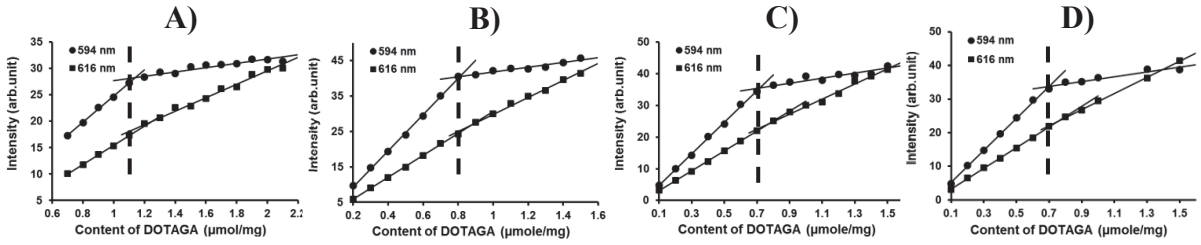

Figure 2-48. Eu titration curves of A) USNP@DOTA$_{IS}$-1, B) USNP@DOTA$_{IS}$-2, C) USNP@DOTA$_{IS}$-3 and D) USNP@DOTA$_{IS}$-4

The DOTAGA content of USNP@DOTA$_{IS}$-5 was determined as ~ 0.8 µmol/mg (Figure 2-49). The yield was 24.7% compared to the introduced quantity of DOTAGA (Table 2-9). This result was 3 times higher than the yield obtained in DMSO/H_2O system for the NP with an equivalent D_H (e.g. 7.9% for USNP@DOTA$_{IS}$-3).

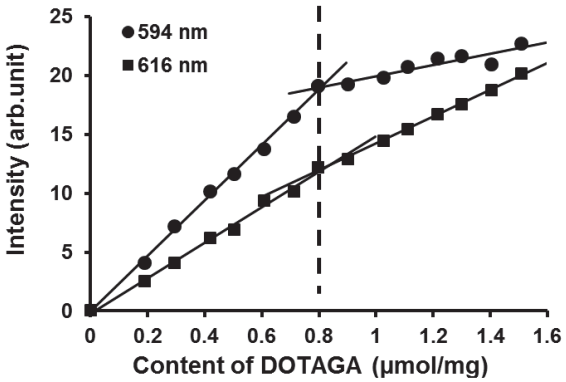

Figure 2-49. Eu titration curve of USNP@DOTA$_{IS}$-5

Table 2-14. Elemental analysis of USNP@DOTA$_{IS}$

Batch	USNP@DOTA$_{IS}$-2			USNP@DOTA$_{IS}$-3			USNP@DOTA$_{IS}$-4			USNP@DOTA$_{IS}$-5		
%mass Gd	0.0000			0.0000			0.0000			0.0000		
relative mol Gd	0.0000			0.0000			0.0000			0.0000		
%mass Si	15.900			19.900			23.700			16.700		
relative mol Si	0.9554			1.3596			1.8185			1.1256		
%mass C	27.300			23.800			22.000			27.900		
relative mol C	3.8369			3.8032			3.9482			4.3981		
%mass N	8.3000			7.3000			6.5000			7.4000		
relative mol N	1.0000	Ratio	Content (µmol/mg)	1.0000	Ratio	Content (µmol/mg)	1.0000	Ratio	Content (µmol/mg)	1.0000	Ratio	Content (µmol/mg)
relative mol Gd	0.0000		0.0000	0.0000		0.0000	0.0000		0.0000	0.0000		0.0000
relative mol A-D*	0.1196	1.0000	0.7083	0.1147	1.0000	0.6798	0.1355	1.0000	0.8025	0.1683	1.0000	0.8889
relative mol A	0.4022	3.3643	2.3829	0.4263	3.7151	2.5255	0.3227	2.3820	1.9117	0.1586	0.9422	0.8375
relative mol T	0.4337	3.6273	2.5692	0.8186	7.1341	4.8496	1.3604	10.0424	8.0594	0.7987	4.7461	4.2188
relative mol DEG free chelators										0.0550	0.3270	0.2907
% free chelators												

**A-D: APTES-DOTAGA, A: APTES, T: TEOS*

2.2.4. USNP as a flexible platform for complexing different metals

Different metals were used to complex with USNP@DOTA or USNP@DOTA$_{IS}$ to demonstrate their flexibility and help study their nanostructures. First of all, as we have seen above, Eu^{3+} was introduced on every particle and Cu^{2+} was complexed with USNP@DOTA to quantify the amount of free DOTAGA. This implies the possibility of using USNP for optical imaging while exploiting luminescence property of Eu^{3+} and/or radioimaging using radioactivity of ^{64}Cu isotope.[25,208] On the other hand, samples were complexed with Gd^{3+} to exploit its magnetic property as positive contrast agent in MRI. For example, USNP@DOTA and USNP@DOTA$_{IS}$-5 were complexed with Gd^{3+} to produce USNP@DOTAGd and USNP@DOTA$_{IS}$-5-Gd respectively. USNP@DOTA was also complexed with a diamagnetic lanthanide ion i.e. Lu^{3+} (USNP@DOTALu) for NMR experiments. Besides, USNP@DOTA$_{IS}$-5 was complexed with Tb^{3+}, Ho^{3+} and Bi^{3+} to give respective complexed particles i.e. USNP@DOTA$_{IS}$-5-Tb/Ho/Bi. These metals have potentials for different biomedical applications. Tb^{3+} as Eu^{3+} has been used frequently as a luminescence probe.[209] Natural isotope of Bi^{3+} has been reported recently along with our previously developed USNP as a promising RS agent.[210] On the other hand, the chelation of Lu, Tb, Ho and Bi here can

imply the potential of USNP as a nanocarrier for ^{177}Lu, ^{161}Tb, ^{166}Ho radioisotopes as beta-particle-emitters and/or ^{213}Bi, ^{212}Bi as alpha-particle-emitters for therapeutic applications.[28] In all cases, the amounts of metals were kept at 90% to 95% compared to the amount of DOTAGA to make sure no free metal was left in the solution.

Table 2-15 summarized the compositions and properties of USNP@DOTA$_{IS}$-5 after being complexed with different metals.

Table 2-15. Properties of metals complexed USNP using *in-situ* formed APTES-DOTAGA (USNP@$DOTA_{IS}$)

Properties	Method(s)	USNP@ $DOTA_{IS}$-5-Gd	USNP@ $DOTA_{IS}$-5-Tb	USNP@ $DOTA_{IS}$-5-Ho	USNP@ $DOTA_{IS}$-5-Bi
Starting ratio A-D : A : T (: M)*	-	7 A-D : 8 A : 20 T : 6.6 Gd	7 A-D : 8 A : 20 T : 6.6 Tb	7 A-D : 8 A : 20 T : 6.6 Ho	7 A-D : 8 A : 20 T : 6.3 Bi
D_H (nm)	DLS	6.3 ± 1.7	6.1 ± 1.7	5.8 ± 1.6	6.0 ± 1.6
Zeta potential (mV)	Zeta potentiometry	-6.9 (pH 6.65) -21.8 (pH 7.36)	-7.9 (pH 6.64) -19.3 (pH 7.39)	-12.0 (pH 6.65) -19.8 (pH 7.42)	2.3 (pH 6.67) -3.4 (pH 7.35)
Retention time (min)	HPLC (295 nm)	15.96	15.96	16.05	15.74
Peak shape	HPLC (295 nm)	S	S	S	S
FWHM (min)	HPLC (295 nm)	3.0333	3.0333	3.1083	2.7417
Purity (%)	HPLC (295 nm)	96.6	98.3	97.3	97.4
r_1 ($mM^{-1}.s^{-1}$) (37°C, 60 MHz)	Relaxometry	23.23	-	-	-
r_2/r_1 (37°C, 60 MHz)	Relaxometry	1.65	-	-	-
M content (μmol/mg)	ICP-OES	0.654	0.558	0.625	0.442
A-D : A : T : M	Assumption	1.0 A-D : 1.0 A : 4.7 T : 0.7 Gd	1.0 A-D : 1.0 A : 4.7 T : 0.6 Tb	1.0 A-D : 1.0 A : 4.7 T : 0.7 Ho	1.0 A-D : 1.0 A : 4.7 T : 0.5 Bi
Yield (%) (in metal)	-	69.2	62.7	68.2	51.2

**A-D: APTES-DOTAGA, A: APTES, T: TEOS, M: metal (Gd, Tb, Ho or Bi), #S: symmetrical*

2.2.4.1. Complexation of Gd on USNP@DOTA to create USNP@DOTAGd

333 mg of USNP lyophilized powder was redispersed in ultrapure water to obtain a solution of 200 g/l. 36 µl of $GdCl_3$ 2.2 M solution at pH 4 (molar ratio DOTAGA : Gd = 1 : 0.9) was added slowly to the solution of USNP in three times. The pH of the solution was adjusted to around 4 during each addition of $GdCl_3$ solution by adding NaOH solutions. The solution was incubated at 80°C. Each 6 h (or 18h), pH was verified and readjusted to around 5. After 48 h, pH of the solution was stable at around 5. Water was added to obtain a final concentration of 127 g/l or 100 mM in DOTAGA of USNP@DOTA and 90 mM in Gd^{3+}. The solution was further purified through Vivaspin™ 3 kDa for 32 purification factor in case some free Gd^{3+} might remain. The pH of the solution was adjusted to 7.4 by adding NaOH solutions. Then, the solution was filtered through 0.2 µm membrane and freeze-dried for long term storage.

2.2.4.2. Complexation of USNP@$DOTA_{IS}$-5 with different metals (Gd, Ho, Tb and Bi)

283 mg of lyophilized powder of USNP@$DOTA_{IS}$-5 containing 227 µmol DOTAGA, was redispersed in water to have a concentration around 200 mM of DOTAGA. pH of the solution was adjusted to 5.5 by adding NaOH solutions. To produce Gd particle, 98.5 µl of $GdCl_3$ solution at 2.188 M (molar ratio DOTAGA : Gd = 1 : 0.95) was added slowly in 3 times while the solution was heated and stirred on a heat plate at 70°C to speed up the complexation. Between each time, pH was carefully increased to 5.5 by adding slowly NaOH solutions before adding the next one. After 3 additions, water was added to obtain a concentration of 100 mM of DOTAGA and a pH around 5.5. This solution was stirred in an oil bath at 80°C for 18 h. After the incubation, pH stayed at around 5.5. This solution was purified with water as solvent by tangential filtration (MWCO = 3kDa) with 16 purification factor to get rid of any free Gd^{3+}. Finally, the solution was neutralized to pH 7 by adding few drops of NaOH solutions and filtered through 0.2 µm membrane and freeze-dried for long term storage. Small samples of purified solution were analyzed by DLS.

Similar protocols were applied using 431 µl of $HoCl_3$ or $TbCl_3$ solutions at 500 mM instead to produce Ho and Tb particles respectively.

For Bi particles, due to a very limited solubility of bismuth hydroxide, 817 µl of $BiCl_3$ solutions at 250 mM in HCl 6 M was used. The nanoparticles solution had to be heated at 70°C before any addition was carried out. Otherwise, bismuth hydroxide would form as white precipitates. NaOH solution at 10 M was needed to neutralize the solution to pH 5.5 and solution was heated in an oil bath at 80°C for 1 h between each step of addition. The molar ratio DOTAGA : Bi = 1 : 0.9 was used. The rest of the protocol was similar.

2.2.4.3. Characterization of complexed USNP@$DOTA_{(IS)}$

Hydrodynamic diameters measured by DLS of USNP@DOTA-Gd, USNP@$DOTA_{IS}$-5-Gd, USNP@$DOTA_{IS}$-5-Tb/Ho/Bi were 5.7 nm, 6.3 nm, 6.1 nm, 5.8 nm and 6.0 nm respectively (Figure 2-52-A, Figure 2-53-A and Table 2-15). These results show a high level of the colloidal stability of USNP platform and the repetitiveness of the protocol.

Zeta potentials of these samples at pH 6.6 were - 5.8, - 6.9, - 7.9, - 12.0 and 2.3 mV (Figure 2-50) and at pH 7.4 were -8.2, -21.8, -19.3, -19.8, -3.4 mV respectively. Though, we were not afford enough materials to run more pH points for establishing the isoelectric point (pI) of

every sample, these values suggest decreases of zeta potential values. This indicates the presence of metals in the chelators which reduces the negative charges of chelators at neutral pH (Table 2-9 and Table 2-15). Bi complexed particle had higher zeta potentials compared to other lanthanides complexed particles at respective pH. This might be due to different chemical properties and lower signals in ICP-OES of Bi compared to lanthanides. The former might influence the silane distribution and activity which probably change the species ratio after the purification while the latter might lead to an underestimation of Bi content.

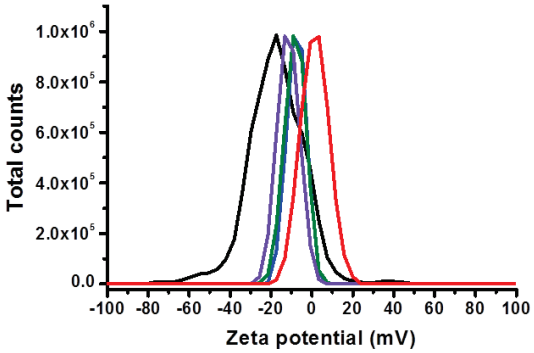

Figure 2-50. Zeta potential graphs at pH 6.6 of empty USNP@DOTAIS-5 (black) and the same NP after complexed with metals: Gd (blue), Tb (green), Ho (violet), Bi (red)

The presence of metals was further confirmed by their IR spectra (Figure 2-51). Solutions after DLS measurement were adjusted to pH 2 (to reveal the typical C=O stretching vibration band of free carboxylic acid at 1720 cm^{-1} from the overlapping bands of amides)[210,211] before being lyophilized for FTIR measurements. The disappearance/decrease of the peak at 1720 cm^{-1} indicated the complexation of metals in DOTA.

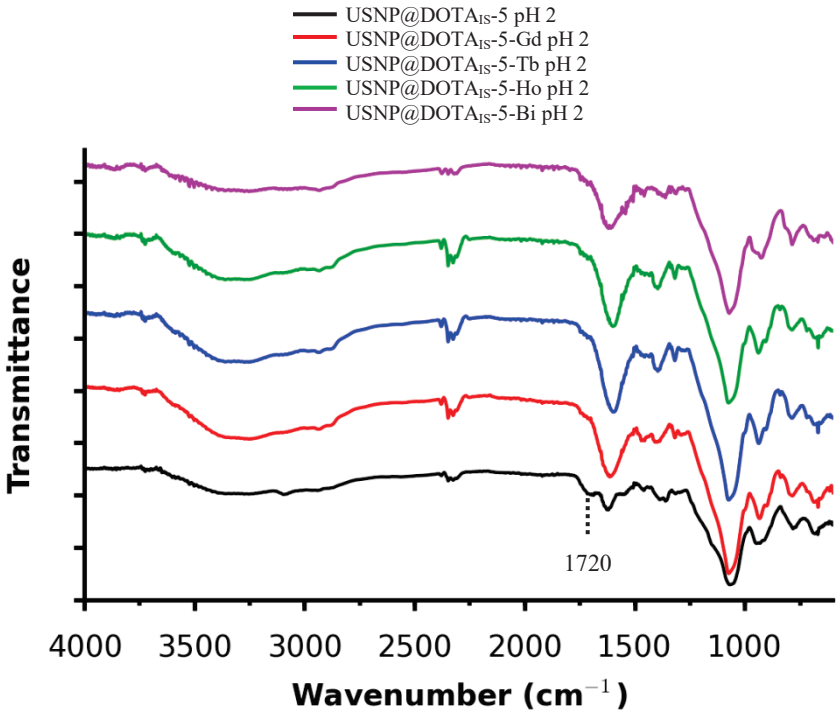

Figure 2-51. Infrared spectra of empty and metals-complexed USNP@DOTAIS-5

The purity and homogeneity of the particles were determined by HPLC analysis. The lyophilized powders of these NPs was redispersed in water and diluted to 5 g/l in aqueous solution of TFA 0.1% right before being injected to the column. Chromatograms of these

samples indicated homogeneous populations of particles with high purities (> 90%). All samples have a very similar t_R at around 16 min (Figure 2-52-B, C, Figure 2-53-B and Table 2-15).

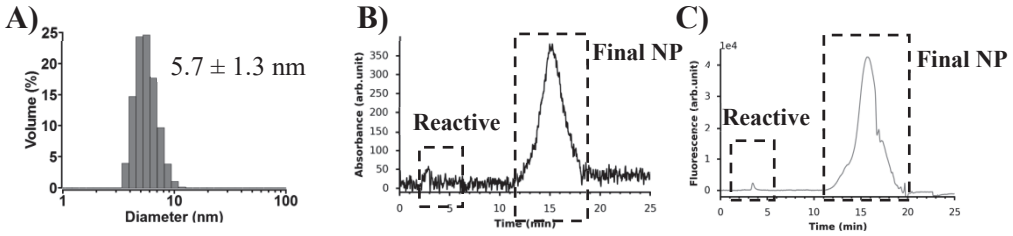

Figure 2-52. Characterizations of USNP@DOTAGd: A) DLS diagram of USNP@DOTAGd and Chromatograms after complexed with Gd^{3+} B) at 295 nm C) detected by fluorescence (λex = 274 nm, λem = 312 nm).

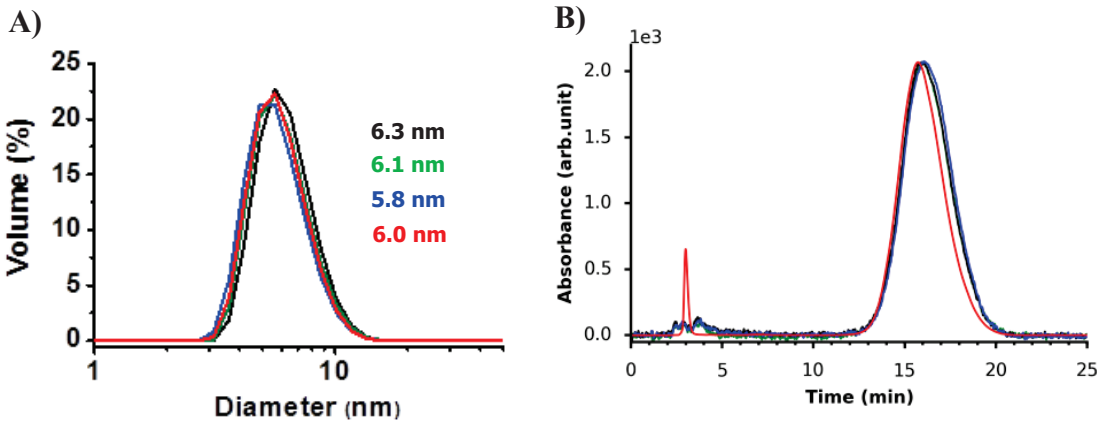

Figure 2-53. A) DLS diagrams of USNP@$DOTA_{IS}$-5 complexed with: Gd (black), Tb (green), Ho (blue), Bi (red); B) Chromatograms at 295 nm (normalized to the same height) of the same samples with respective color code.

The relaxivities of USNP@DOTAGd, USNP@DOTAGd* and USNP@$DOTA_{IS}$-5-Gd were shown in Table 2-16. High longitudinal relaxivity (r_1) (21.4 $mM^{-1}.s^{-1}$, 18.5 $mM^{-1}.s^{-1}$ and 23.2 $mM^{-1}.s^{-1}$) combining with a low ratio r_2/r_1 (1.59, 1.55 and 1.65) indicating their potential as good positive contrast agents for MRI.

Table 2-16. Relaxivities of USNP@DOTA@Gd and USNP@$DOTA_{IS}$-5-Gd

Sample	r_1 ($mM^{-1}.s^{-1}$)	r_2/r_1
USNP@DOTAGd	21.40	1.59
USNP@DOTAGd*	18.51	1.55
USNP@$DOTA_{IS}$-5-Gd	23.23	1.65

To futher investigate the structure of metal complexed particles by NMR, Lu was introduced in USNP@DOTA (molar ratio DOTAGA : Lu = 1 : 0.9) with similar protocol used for USNP@DOTAGd. After complexation, particle was lyophilized and redispersed in D_2O for the measurement. Lu was chosen for NMR studies because of its diamagnetic nature and its similarities in terms of chemical properties to other lanthanides. Other paramagnetic lanthanides i.e. Gd, Eu, Tb, Ho will detrimentally broaden the peaks in NMR spectra and unable the signal acquisition process of DOSY technique. Bi as a diamagnetic element can also be used for NMR experiments. However, since this study focuses more on lanthanides, Lu represents as the best candidate. In the future, different diamagnetic metals can also be

tested to verify their structural differences. NMR-DOSY spectrum of USNP@DOTALu is shown in Figure 2-54-A. It shows a similar result to that of USNP@DOTA. The main products still had D around 56 $\mu m^2/s$. They coexisted with some other smaller species which have faster D (410 and 214 $\mu m^2/s$). D_H of the main particles calculated from Einstein equation was 6.8 ± 2.4 nm. ^1H spectrum of USNP@DOTALu (Figure 2-54-B) was not exactly similar to the one of USNP@DOTA (Figure 2-35-B) since the complexation changed significantly the configuration of DOTAGA.[190] However, still no ^1H of DOTAGA showed a peak at the region smaller than 1 ppm. So the integration method described above for USNP@DOTA can still be applied and give the ratio APTES/APTES-DOTAGA as 0.87. Hence, the size and the ratio of functional groups were rather maintained during the complexation.

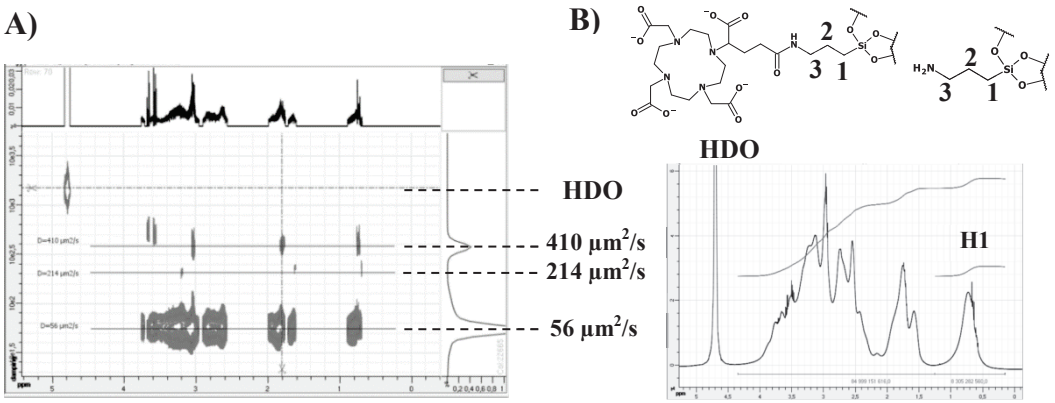

Figure 2-54. NMR study of USNP@DOTALu: A) NMR-DOSY spectrum and B) The positions of H1, H2 and H3 on the APTES and APTES-DOTAGA functional groups on the particle and ^1H NMR spectrum at 127 g/ in D_2O.

To determine specifically the presence and the contents of metals in USNP@DOTAGd, USNP@$DOTA_{IS}$-5-Gd/Tb/Ho/Bi, ICP-OES measurements were conducted. This is a reliable method to specifically demonstrate the presence of metals. Signals were detected at typical atomic emission wavelengths of each metal i.e. 342.246, 335.048, 336.224 nm for Gd; 350.914, 367.636, 387.417 nm for Tb; 345.600, 339.895, 341.644 nm for Ho and 223.061 nm for Bi. The results were 0.604, 0.654, 0.558, 0.625 and 0.442 µmol/mg for USNP@DOTAGd and USNP@$DOTA_{IS}$-5-Gd/Tb/Ho/Bi respectively (Table 2-15).

The ratio of each species in USNP@DOTAGd was calculated from the elemental ratio of Gd, Si, C and N as $(Gd_{0.8}APTES\text{-}DOTAGA_1APTES_{1.2}TEOS_6)_x$ (Table 2-8) which is in accordance with non-complexed USNP@DOTA. Si, C and N in metal-complexed USNP@$DOTA_{IS}$-5 were not analyzed. However, if we assume, after the complexation and purification, the ratio of elements remain the same, DEG have been washed completely and each molecule of APTES-DOTAGA, APTES and TEOS still implies the molecular structure as $SiO_{1.5}(CH_2)_3NH\text{-}DOTAGA^{(2-)}$, $SiO_{1.5}(CH_2)_3NH_3^+$ and SiO_2 respectively, then we can propose the molecular structures of USNP@$DOTA_{IS}$-5-Gd/Tb/Ho/Bi as $(Gd_{0.70}APTES\text{-}DOTAGA_{1.00}APTES_{0.95}TEOS_{4.75})_x$, $(Tb_{0.59}APTES\text{-}DOTAGA_{1.00}APTES_{0.95}TEOS_{4.75})_x$, $(Ho_{0.67}APTES\text{-}DOTAGA_{1.00}APTES_{0.95}TEOS_{4.75})_x$ and $(Bi_{0.47}APTES\text{-}DOTAGA_{1.00}APTES_{0.95}TEOS_{4.75})_x$ respectively (Table 2-15). It is worth noting that the ratio of elements remain unchanged is a strong assumption because the purification process can predominantly remove less-stable, smaller particles compared to other ones and modify this ratio.

To complement the results of ICP-OES, UV-vis and phosphorescence spectra of metals complexed USNP were recorded to show the photophysical imprints of respective metals. The UV-vis spectra of USNP@DOTA$_{IS}$-5 and different metals-complexed particles were recorded at the same concentration. Sample of USNP@DOTA$_{IS}$-5-Bi showed an intense peak at 309 nm which is typical for DOTA(Bi^{3+}) complex (Figure 2-55-A).[212] This result was also demonstrated by a more intense NP peak of the chromatogram of USNP@DOTA$_{IS}$-5-Bi (Figure 2-55-B).

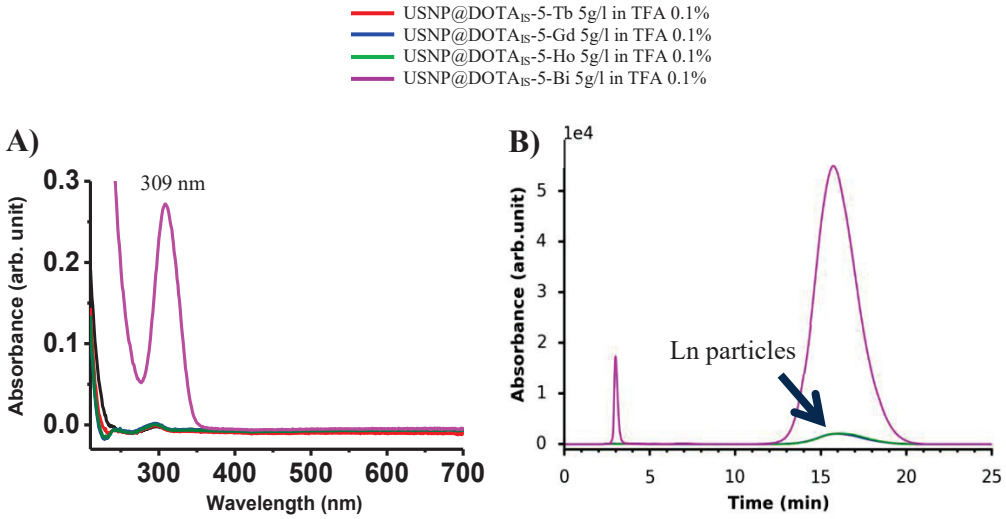

Figure 2-55. The presence of Bi in USNP@DOTA$_{IS}$-5-Bi:
A) Absorption spectra of empty (black), Gd (blue), Tb (red), Ho (green), Bi (violet) NP at 0.06 g/l
B) Chromatograms at 295 nm as originally acquired of USNP@DOTA$_{IS}$-5 complexed with metals: Tb, Gd, Ho, Bi with the same color code at 5 g/l. Spectra and chromatograms of Gd, Tb, Ho complexed particles were put for comparison.

Meanwhile, UV-vis spectrum of USNP@DOTA$_{IS}$-5-Ho shows several absorption peaks of Ho^{3+} (Figure 2-56). Figure 2-57-A shows the excitation and emission spectra of USNP@DOTA$_{IS}$-5-Gd with typical excitation peak and emission peak for Gd at 273 nm and 313 nm respectively.[213] Figure 2-57-B shows those spectra of USNP@DOTA$_{IS}$-5-Tb with typical emission peaks at 489, 546, 586, 622 nm for Tb.[209]

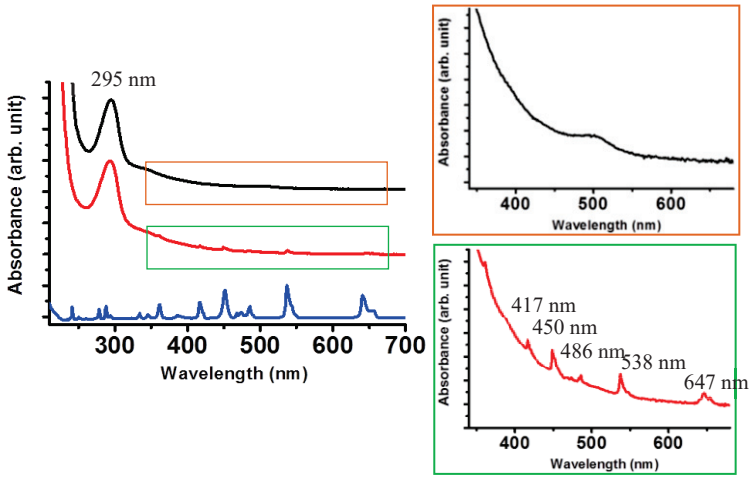

Figure 2-56. Absorption spectra of empty (black) and Ho (red) NP at 5 g/l as well as solution of $HoCl_3$ 50 mM in HCl 0.1 mM (blue). Insets: zoomed ROI of the spectrum of the empty (orange) and Ho complexed NP (green)

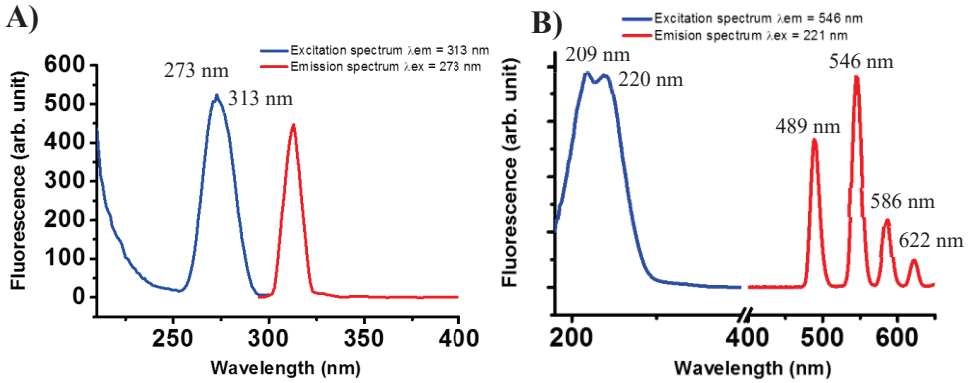

Figure 2-57. A) Excitation spectrum (blue, λem = 313 nm) and emission spectrum (red, λex = 273 nm) of USNP@DOTAIS-5-Gd at 0.06 g/l; B) Excitation spectrum (blue, λem = 546 nm) and emission spectrum (red, λex = 221 nm) of USNP@DOTAIS-5-Tb at 0.06 g/l.

2.2.5. Behaviors of USNP in human serum

The non-specific adsorption of protein on NPs is an important aspect for evaluating a nanomedicine. Physical, chemical and biological properties of NPs can be greatly affected if they have strong interactions with blood proteins. Such interactions can increase the hydrodynamic diameter and prevent renal clearance of ultrasmall NPs. In some cases, the recognition of targeting ligands on the surface of the particle can also be affected by the steric hindrance created by protein adsorption.[12,62]

The interactions between blood proteins and ultrasmall NPs are attracting more and more interests. Different analytical techniques have been developed to investigate these interactions such as circular dichroism, gel electrophoresis, size exclusion chromatography etc.[10,214,215] The choice of methods depends on the properties of the NPs. In the case of Gd-containing NPs, relaxometry is a simple method that might be used to assess strong bindings of proteins on particles. Several authors have reported the increase of longitudinal relaxivity of Gd complexes when being electrostatically attached or covalently bound to a protein. Giardiello M. *et al.* have reported an increase of relaxivity from 7.6 $mM^{-1}.s^{-1}$ to 11.7 $mM^{-1}.s^{-1}$ or from 7.3 $mM^{-1}.s^{-1}$ to 16.0 $mM^{-1}.s^{-1}$ (at pH 7.4, 298 K, 20 MHz) of their DOTA derivatives Gd complexes in the presence of human serum albumin (HSA).[216] Gianolio E. *et al.* have shown that their Gd complexes based micelle can possess a two times higher relaxivity (30 $mM^{-1}.s^{-1}$ vs. 84 $mM^{-1}.s^{-1}$ at 298 K, 20 MHz) while being interacted by HSA.[116] Vandesquille M. *et al.* have observed an increase of 10 times both longitudinal (3.0 $mM^{-1}.s^{-1}$ vs. 29.7 $mM^{-1}.s^{-1}$) and transverse relaxivity (3.5 $mM^{-1}.s^{-1}$ vs. 33.9 $mM^{-1}.s^{-1}$) (in water, 298 K, 60 MHz) of DOTA(Gd) grafted on a single-domain antibody-fragment having a very small hydrodynamic diameter ($D_H \sim 4 – 5$ nm).[217]

As a preliminary attempt to evaluate the interaction between USNP and blood proteins, we measured the relaxation times of concentrated solutions of Gd complexed USNP@$DOTA_{IS}$-5 in water and human serum. Then, we also follow the degradation of diluted samples reflected by the relaxation times in respective media.

For this experiment, Gd was complexed with USNP@$DOTA_{IS}$-5 to produce a second batch of USNP@$DOTA_{IS}$-5-Gd with exactly the same parameters used previously. The characterization of this batch is shown in more details in the Annex-5. D_H of the particle and the retention time in chromatogram was maintained at 5.5 ± 1.3 nm and 16.4 min which were

similar to the first batch. The ratio of particle peak over fragment peaks was 87.5% which was lower than the first batch (96.6%). Phosphorescence emission spectra of filtrates have been recorded and they prove that, after 150 purification factor, the particle solution has reached the maximum purity at the equilibrium of that concentration (140 g/l) and could not be further purified. But this detail should not significantly affect the measurement.

2.2.5.1. Evaluation of non-specific protein adsorption on USNP

Experimental protocol:

Two lyophilized samples of USNP@$DOTA_{IS}$-5-Gd were dispersed in water at 94 g/l (or 56.3 mM, or 56.3 mmol in Gd/100 g of water, pH 7.3) and in human serum (H4522, SigmaAldrich) at 88 g/l (or 56.5 mmol in Gd of NP/100 g of water, pH 7.7). Samples were left at room temperature for 30 min to completely disperse. Relaxation times (at 37°C, 1.4 T/60 MHz) were measured at this point. Then samples were incubated at 37°C for 1 h before relaxation times were measured again to verify if any changes could happen.

Results and discussion:

There are two reasons for using the mass concentration of water in serum rather than using volume concentration of the whole serum. First, Toth E. *et al.* have shown that the linear relationship between relaxation time and concentration is more precise when the relaxivity was normalized with the mass of solvent instead of the volume of solution especially in concentrated solutions.[89] Second, 1 L of human serum contains approximately 45 g to 99 g solutes i.e. proteins, lipids, glucoses, salts which is a considerable amount especially at low concentrations. Relaxation times of serum sample prepared by volume concentration were also recorded but the values during the kinetics measurement were not reasonable with much higher plateau values at the end of the curve than the ones of the sample in water (Annex-5). Probably, the equilibrium of grafted silanes and free silanes depends more precisely on the ratio water/silane in the sample than on the volume concentrations of silanes. Therefore, we choose to present the data of the solutions prepared in the same mass of water for the sake of consistency. We used an average value of 72 g solutes in 1 L of serum to estimate the amount of water.

Table 2-17 shows the relaxation velocities normalized by the amount of NP and the amount of water (100 g of water is equivalent to 1 L in the presentation of conventional molar relaxivity) of USNP@$DOTA_{IS}$-5-Gd in water and human serum at the concentration 94 g particle (56.3 mmol in Gd) per 100 g water. The longitudinal and transverse relaxation velocities in this case are referred to as r_1* and r_2* to distinguish with the conventional molar relaxivity. The results show that r_1* and r_2* of sample in water and in human serum are similar even after 1 h of incubation at 37°C. This preliminary result might indicate that no strong binding ("hard" corona) of biological macromolecules especially proteins happened to USNP@$DOTA_{IS}$-5-Gd.

Table 2-17. Longitudinal (r_1*) and transverse (r_2*) relaxation velocities normalized by the amount of Gd in NP and water in the sample of the second batch of USNP@$DOTA_{IS}$-5-Gd in water (56.3 mmol in Gd /100 g of water) and in human serum (56.5 mmol in Gd g/ 108 ml of human serum containing ~ 100 g of water) (37°C, 60 MHz).

	r_1* ((mmol/100 g water)$^{-1}$.s^{-1})	r_2*/r_1*
USNP@$DOTA_{IS}$-5-Gd in water	20.7	1.69
USNP@$DOTA_{IS}$-5-Gd (37°C, 1 h)	320.4	1.70
USNP@$DOTA_{IS}$-5-Gd in human serum	19.8	1.68
USNP@$DOTA_{IS}$-5-Gd in human serum (37°C, 1 h)	19.6	1.67

2.2.5.2. Degradation of USNP in human serum

Experimental protocol:

The two samples above were quickly diluted in water and in human serum respectively to a concentration of 1 g particle (0.60 mmol in Gd) per 100 g of water. This concentration was chosen since it corresponds with the dose used in clinical trials (ca. 100 g/kg) and the blood volume of an average human (5 – 6 L). The relaxation times (37°C, 1.4 T/60 MHz) were followed during one day to find out the degradation kinetics in two different media.

Results and discussion:

The results are shown in Figure 2-58 and Table 2-18. The relaxation velocity gradually decreased in both water and human serum to almost the same plateau values. It might justify the use of mass concentration of water in serum for calculation. This indicates that the equilibrium of grafted silanes and free silanes is actually in correlation with the ratio of silane/water in the sample rather than volume concentration of silanes. These curves were fitted to a single exponential decay function to give the half-life ($t_{1/2}$) in water and in human serum in terms of r_1* as 94 min and 53 min respectively and in terms of r_2* as 83 min and 49 min respectively. These decreases in relaxation velocities might reflect the detachment of Silane-DOTAGA(Gd) from the polysiloxane network due to water hydrolysis as we have seen previously in the case of AGuIX. The degradation happened more slowly in water since after being diluted pH of particle solution in water went to 6.6, whereas human serum acted as a buffer to keep the pH always at 7.7 for the other sample. Hence, similar to AGuIX particle, whether in intact state or during the degradation, USNP@$DOTA_{IS}$-5-Gd did not show any significant increase in relaxation velocity which may be the indication of the lack of strong interactions with blood proteins. The degradability of such polysiloxane system as USNP is also considered as an advantage for a renal clearable NP.

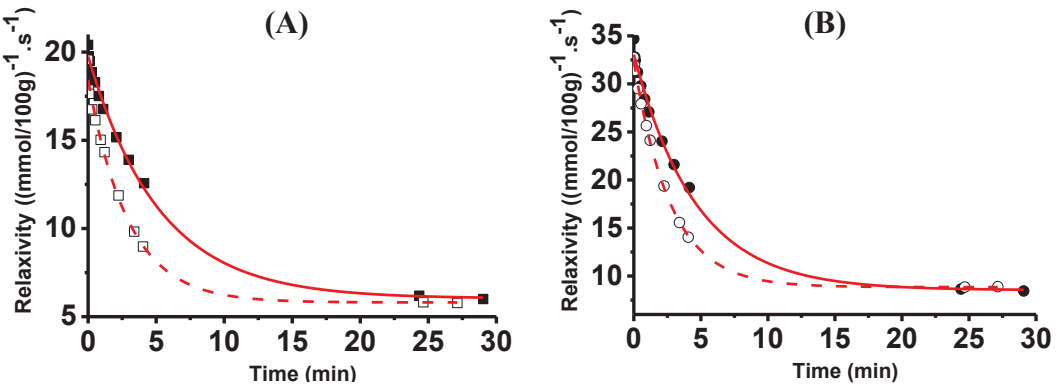

Figure 2-58. Kinetics of degradation measured by relaxometry of the second batch of USNP@DOTA$_{IS}$-5-Gd in water (solid symbols) and in human serum (open symbols) at 1 g particle (0.60 mmol in Gd)/100 g water (37°C, 60 MHz): A) longitudinal and B) transverse relaxation velocities over time. The results were normalized with mmol of Gd in NP and the mass of water in the samples.

Table 2-18. Half-life of longitudinal (r_1*) and transverse (r_2*) relaxation velocities normalized by the amount of NP and water in the samples of the second batch of USNP@DOTA$_{IS}$-5-Gd in water (0.60 mmol in Gd/100 g of water) and in human serum (0.60 mmol in Gd/ 108 ml of human serum containing ~ 100 g of water) (37°C, 60 MHz).

	$t_{1/2}$ (min) of r_1*	$t_{1/2}$ (min) of r_2*
USNP@DOTA$_{IS}$-5-Gd in water	53	49
USNP@DOTA$_{IS}$-5-Gd in human serum	94	83

2.2.6. Cytotoxicity of USNP@DOTAGd

The toxicity of USNP@DOTAGd on prostate cancer cells (PC3) was evaluated rapidly with XCelligence apparatus (ACEA Biosciences, USA). This experiment was conducted with the technical assistance of our collaborator Rosa S., Centre for Cancer Research and Cell Biology Queen's University, Belfast, Northern Ireland.

2.2.6.1. Working principle of XCelligence

XCelligence is an apparatus that allows evaluating the proliferation of cells on a gold electrode (Figure 2-59). The electrodes are located at the bottom of cell culture wells. Normally, there is always a current running through the electrode. When we perform cell culture in these wells, the cells will start to stick on, grow and cover the whole surface. This creates impedance preventing the electric current. Depending on the extent of cell proliferation on the electrode, the impedance will increase correspondingly. The apparatus will show the cell index (CI) value which is the difference between the impedance at a certain time point after cells are cultured and the impedance at the beginning where only medium but no cell is present normalized by the impedance of the electrode alone (Equation 2-9). If the cells are exposed to a toxic compound, they will lose their normal capacity to adhere and spread on the surface of the well. The impedance of poisoned cells will, therefore, decrease compared to normal cells.[218]

$$Cell\ index\ (CI) = \frac{Z_{t1} - Z_0}{Z_{nominal}} \qquad \textbf{Equation 2-9}$$

Where
Z_{t1}: impedance at a certain time point t_1 (in the presence of cells)
Z_0: impedance at t_0 (only medium, absence of cells)
$Z_{nominal}$: impedance of the electrode alone (no medium or cells)

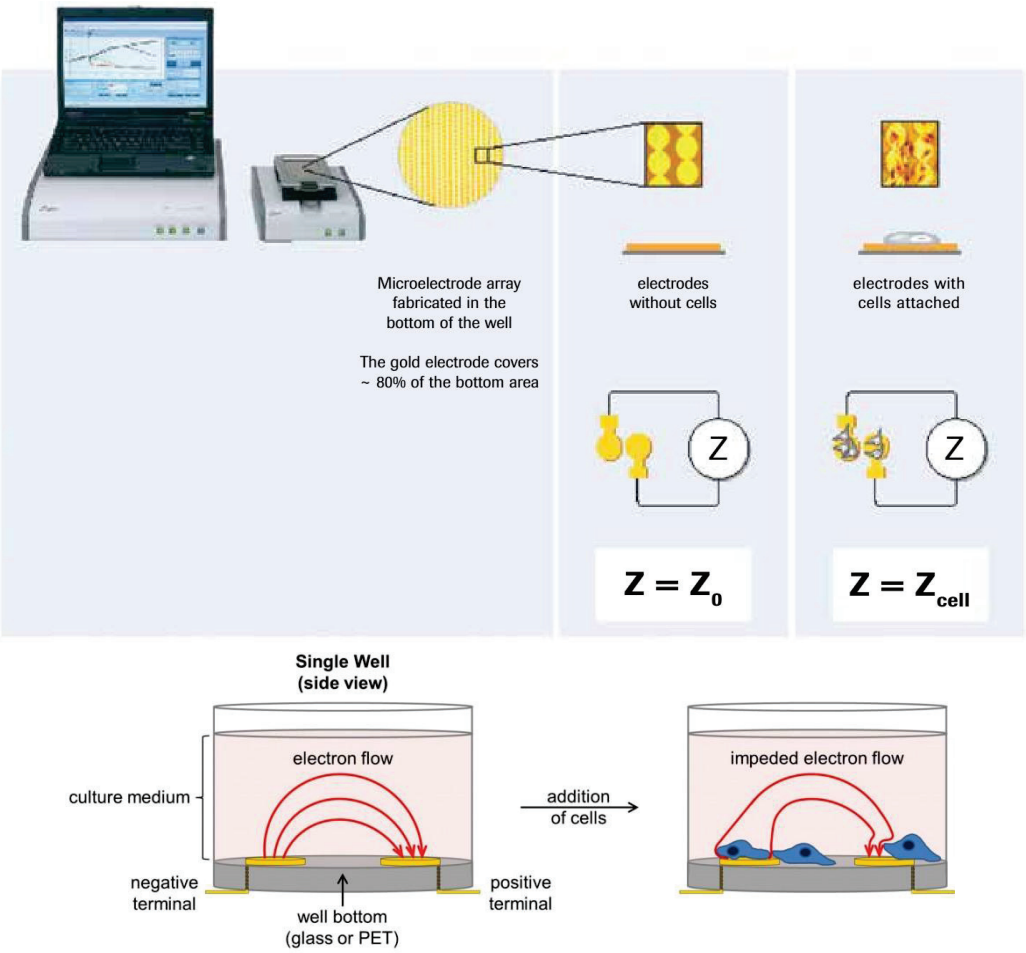

Figure 2-59. XCelligence set up and working mechanism.[218]

2.2.6.2. Results

0.2 ml of prostate cancer cells (PC3) medium containing approximately 3000 cells was cultured on 4 wells of XCelligence setup. These cells were allowed to grow overnight. After 24h, media in 4 wells were aspirated to add 0.2 ml of fresh medium, or solutions at 0.5 mM in Gd of USNP@DOTAGd, AGuIX synthesized in the lab or AGuIX synthesized in GMP condition respectively. These wells were let untouched and the impedance were followed by XCelligence during 7 days (Figure 2-60). As the results have shown, there is almost no difference in the impedance of PC3 cells alone or cells in the presence of USNP@DOTAGd or AGuIX. In conclusion, similar to AGuIX, USNP@DOTAGd seems to have no inherent effect on the proliferation of PC3 cancer cells.

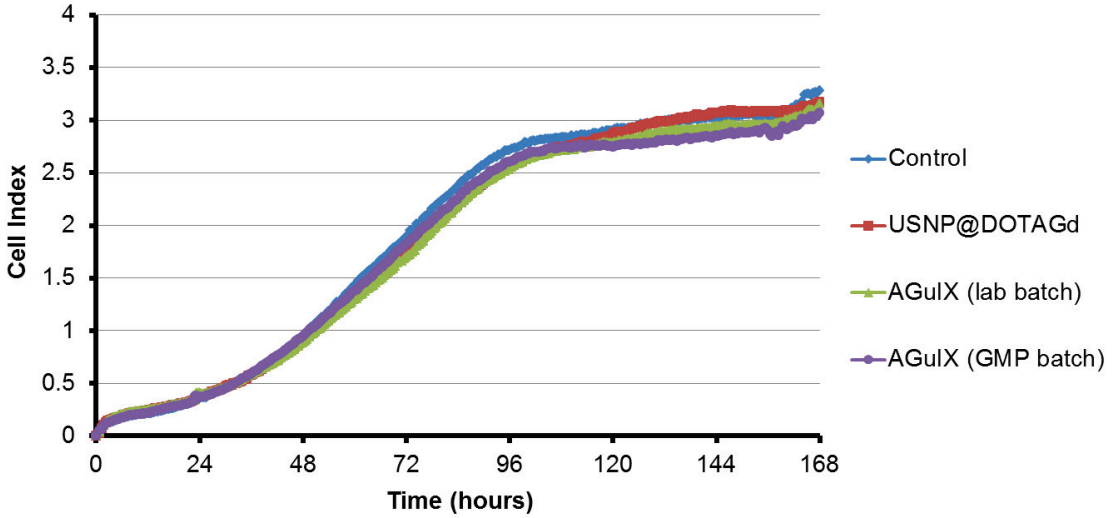

Figure 2-60. Cell index measured by XCelligence during 7 days of PC3 cells alone (blue) or in the presence of 0.5 mM in Gd of USNP@DOTAGd (red), AGuIX synthesized in the lab (green) or AGuIX synthesized in GMP condition (violet).

2.2.7. The application of USNP@DOTAGd* in *in vivo* MRI imaging

As an illustration of the potential for biomedical applications of these ultrasmall NPs, USNP@DOTAGd* was chosen for studying the contrast-enhancing property in MRI of new Gd complexed particles. The solution of particle was intravenously injected in mice bearing ectopically induced colorectal tumors. MRI images over time were acquired to observe the circulation of the particle.

This work has been carried out by Dr. Grégory Ramniceanu and Dr. Bich-Thuy Doan (Team "Synthèse, Electrochimie, Imagerie et Systèmes Analytiques pour le Diagnostic" (SEISAD)) and Dr. Nathalie Mignet (Team "Vecteurs pour l'Imagerie moléculaire et le Ciblage Thérapeutique" (VICT)) from University Paris Descartes.

2.2.7.1. Experimental protocol

Three BALB/c mice were inoculated subcutaneously with colon carcinoma (CT26) cells on both flanks.

USNP@DOTAGd* lyophilized powder was dispersed in physiological serum at 100 mM (in Gd). Solution was diluted to 20 mM in serum before being injected intravenously to three mice at the dose of 200 µmol (in Gd) per kg.

Images were acquired before (pre-contrast) and after injection (post-contrast) using a 7 T MRI system 300WB micro imaging spectrometer, with a 1H 40 mm coil, Paravision 5.11 software (Bruker, Germany). The respiratory rate was continuously monitored by adjusting isoflurane concentration (1.5 %). Dynamic contrast enhanced (DCE) sequence was recorded using Intragate Flash multislices for motion free artifacts with TR = 100 ms, TE = 4 ms, flip angle = 80°. The repetition number was set to 15 and a number of time frames to reconstruct was 1. A field-of-view (FOV) of 3 cm x 3 cm and a matrix of 256 x 256, 4 slices with a thickness of 1 mm were chosen, giving a spatial resolution of 117 µm x 117 µm in plane. The total scan time was in the order of 3 min 14 sec. Finally, an elongated version of the Intragate Flash multislices sequence was used for the dynamic follow-up to obtain the same temporal

resolution in a scan time of 40 min. 2 – 3 min scans were perfomed 3 – 6 hours post-contrast as follow up.

Several regions of interest (ROI) in tumors and liver were monitored and the MRI intensities of ROIs were plotted pre- and post-injection of the particle. Tissue enhancement level of the signal in each tissue area was calculated as $(S_t - S_0)/S_0$, where S_t was the signal intensity measured at each time point after injection, and S_0 was the signal intensity before injection.

Of three mice injected with USNP@DOTAGd*, only one showed clear enough images for assessing hepatic accumulation and clearance due to the difficulty in positioning the animals. In fact, they were positioned rather to reveal better the tumors than the other organs.

The data obtained with USNP@DOTAGd* was compared relatively with the one obtained previously with classical AGuIX particle. AGuIX was also prepared and injected similarly at the same concentration and dose of Gd in three healthy female BALB/c mice. These mice were positioned to reveal better the livers and allow obtaining full data for hepatic clearance.

2.2.7.2. Results

Figure 2-61-A shows MRI cross-sections before and after injection of USNP@DOTAGd* where the tumor regions are highlighted as expected. Comparison of the pre- and post-contrast images clearly reveals the higher brightness at the tumor regions caused by the particle. Contrast enhancement was expressed as percentage of enhancement compared to the pre-contrast image. In the tumor tissue, USNP@DOTAGd* showed an intake phase with a maximal enhancement 30 minutes post injection (35 % of signal increase) and a prolonged clearance phase, with a half-time of 3 hours, demonstrating the EPR effect (Figure 2-61-B). In the liver, peak of enhancement (90 % increase of signal) was observed at 6 minutes post-injection of USNP@DOTAGd* followed by a clearance phase (Figure 2-61-C, triangles curve). After 40 min post-injection, the signal was at half of maximal intensity, indicating a hepatic half-time of 30 minutes. The data obtained previously with AGuIX show relatively comparable hepatic clearance kinetics (Figure 2-61-C, circles curve). After bloodstream circulation with a complementary transitory visualization through the vascular network in the liver, particles were excreted from the kidney cortex to the bladder as previously shown with AGuIX.[131]

This imaging study evidences that USNP@DOTAGd* displays contrast enhancement in both the tumors and hepatic tissues over the full observation period, without the typical liver accumulation observed for macromolecular agents.[219] Thus, they improve the imaging properties without undesired liver uptake. Meanwhile, the relatively long retention time in the tumors opens the perspective for vectorization towards tumor tissues.

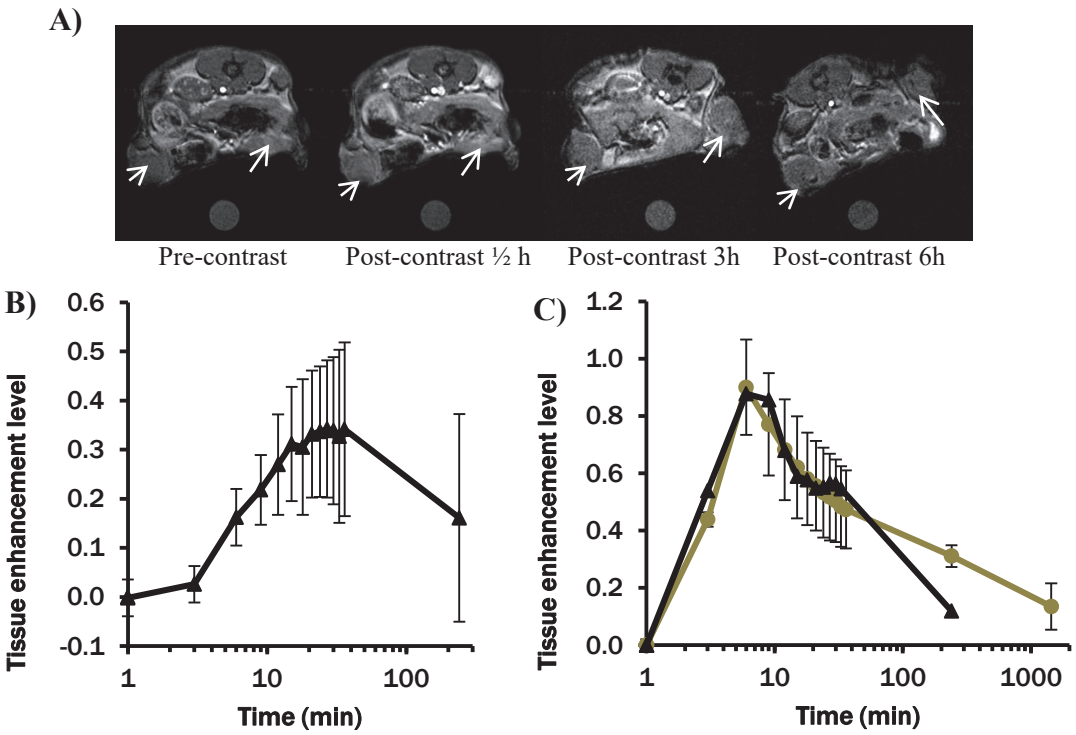

Figure 2-61. ***In vivo*** **MRI contrast enhancement of USNP@DOTAGd*:** A) MRI cross-sections of the tumor tissues (white arrows) pre- (left) and post-injection (right, up to 6 h) of USNP@DOTAGd*; B) Dynamic MRI signal enhancement in tumor tissues after injection of USNP@DOTAGd* and C) Dynamic MRI signal enhancement in the liver after injection of USNP@DOTAGd* (black curve, triangles) (The data obtained previously with AGuIX is presented for relative comparison (gray curve, circles)).

2.3. Conclusion and perspectives

In this chapter, we have 1) revised the synthesis, structure and properties of standard AGuIX nanoparticle; 2) explored the nanochemistry of polysiloxane structures; 3) established a straightforward protocol for synthesizing ultrasmall silica nanoparticles displaying metal chelates as well as 4) characterized them in terms of physicochemical properties, interaction with biomolecules and pharmacokinetic behaviors in mice bearing tumors. Indeed, new products showed promising results in these aspects. This new synthesis pathway will allow easy tailoring of USNP structure and composition for different applications in the future.

CHAPTER 3

Functionalization of AGuIX nanoparticle

Chapter 3. Functionalization of AGuIX nanoparticle

3.1. Functionalization of AGuIX with chelating silanes for bimodal imaging

3.1.1. Introduction

As we have seen previously, each medical imaging technique has different drawbacks alongside with advantages. Among them, MRI is gaining more and more popularity in hospitals for precise imaging thanks to the easy access, high spatial resolution and non-radiative nature. Nevertheless, MRI is plagued by its low sensitivity and contrast which makes it not ideal for quantification purposes. On the other hand, radioimaging, more specifically, single photon emission computed tomography (SPECT) or positron emission tomography (PET), offers precise quantification without being limited by penetrability issue as optical imaging. Hence, more and more researches have been dedicated to the combination of MRI contrast agents and radioisotopes in one single object to correlate the images obtained by MRI and the ones acquired by radioimaging.[18] In this context, a bimodal probe which allows the localization of disease sites by both techniques should be highly desirable. AGuIX nanoparticle or its derivatives can be one of such multifunctional nanoprobes. While being an effective contrast agent for MRI, they can also complex different isotopes e.g. ^{111}In, ^{68}Ga, ^{89}Zr used for radioimaging thanks to the free chelators that existed on its surface from the beginning or being added post-synthetically.[138,139,151]

Common methods for adding free chelators on AGuIX were to use NHS (*N*-hydroxysuccinimide) esters[138,210] or SCN (isothiocyanate) derivatives[139] of chelators to react with amine groups on the surface of the particles. The materials required for these strategies have been well developed and commercialized. Moreover, these reactions are quite fast, straightforward and well known. Nevertheless, there are still some limitations for these strategies. First of all, NHS esters and SCN are prone to be deactivated by hydrolysis. Hence, they cannot be stored for a long period of time even at low temperature in desiccated condition. Second, these activated species can cross-react with amines present in targeting ligands that we want to functionalize, for example, amines of positively charged amino acids i.e. lysine, arginine or histidine of a peptide. This implies complicated protecting/unprotecting strategies such as using tert-butyloxycarbonyl (Boc) or 9H-fluoren-9-ylmethoxycarbonyl (Fmoc) protecting groups.[220] In this part, a new functionalization strategy based on silane chemistry was proposed. DOTAGA (1,4,7,10-tetraazacyclododecane-1-glutaric acid-4,7,10-triacetic acid) and NODAGA (1,4,7-triazacyclononane,1-glutaric acid-4,7-diacetic acid) were coupled with APTES (Figure 3-1-A). These species were then used to functionalize AGuIX by reacting specifically with available silanol groups, Si-OH, on the surface of the particle in a single step without the presence of any other reactants (Figure 3-1-B). This strategy has been used by Ciccione *et al.* to successfully graft precisely certain ratios of fluorophores and different targeting peptides on a 80 nm silica nanoparticle to actively increase the internalization of particles in cancer cells.[221] The activities of silanes are not affected by hydrolysis. Hence, it can be stored and used for a long period of time. In addition, the unreacted silanes are highly soluble so that they should be removed easily by filtration. The functionalized particles were characterized with different analytical methods to prove the presence of free chelators on the particles. By increasing the introduced quantity of chelating silane precursors, the amount of free chelators can be increased proportionally. Finally,

bimodal MRI/PET imaging experiments were performed on mice to demonstrate the potential of this type of NPs. ^{64}Cu was chosen as positron emitters for PET imaging. This radioisotope has a reasonable half-life (13 h) for pharmacokinetic study of AGuIX which has a 1 h half-life in patients' blood (phase I trial NANO-RAD; ClinicalTrials.gov Identifier: NCT02820454). Regarding the choice of chelator, although the thermodynamic stability constant of NOTA (original structure of NODAGA) is comparable to the one of DOTA ($\log K_{NOTA}$ = 21.6 vs. $\log K_{DOTA}$ = 22.2)[222], different studies have shown higher *in vivo* stability of copper complexes of NOTA, NODAGA and their derivatives compared to the ones of DOTAGA and their derivatives.[223–226] Therefore, NODAGA functionalized particle was chosen to be radiolabeled with ^{64}Cu for biodistribution study.

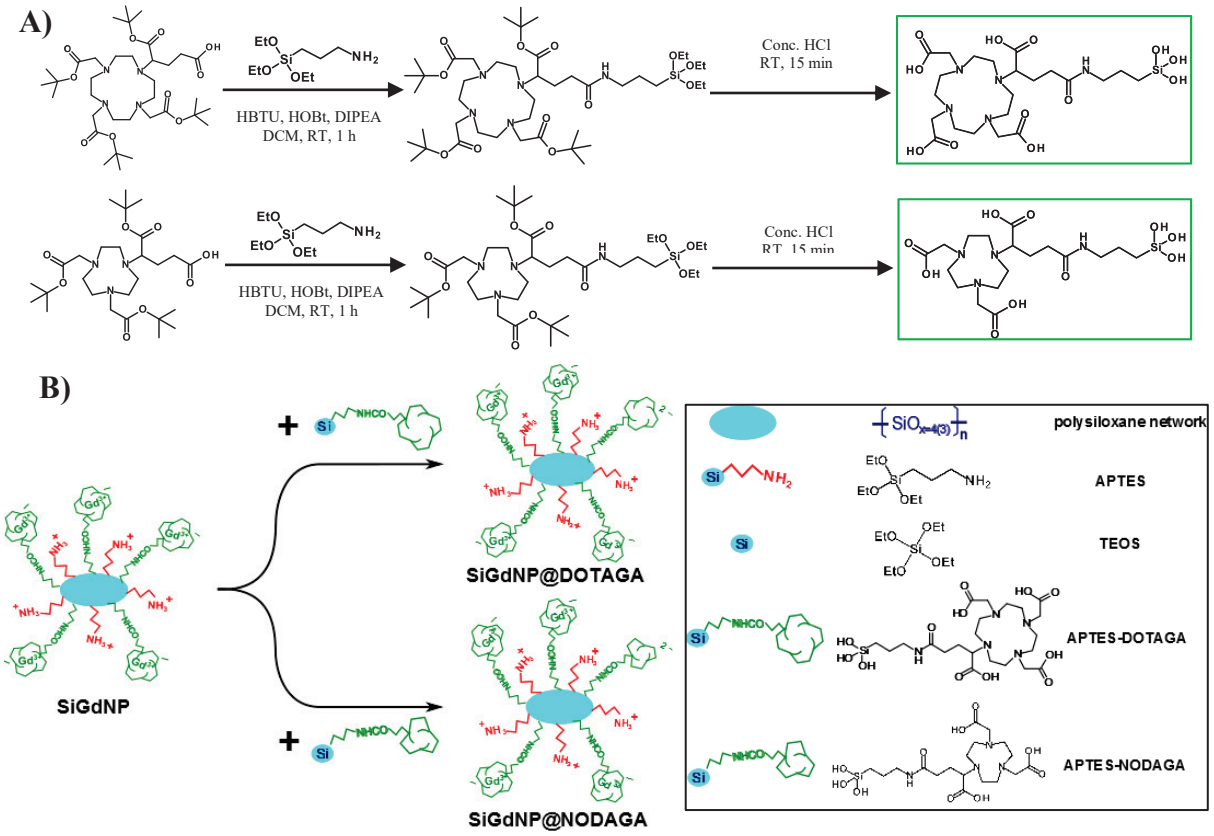

Figure 3-1. A) The reaction scheme of the synthesis of APTES-DOTAGA (upper) and APTES-NODAGA (lower); B) The reaction scheme of the functionalization of APTES-DOTAGA and APTES-NODAGA on AGuIX.

3.1.2. Experimental protocol

3.1.2.1. Synthesis of chelating silanes

Two types of chelating silanes i.e. APTES-DOTAGA and APTES-NODAGA were synthesized from the reaction between APTES and either t-butyl protected DOTAGA ((t-bu)$_4$DOTAGA) or t-butyl protected NODAGA ((t-bu)$_3$NODAGA) (Figure 3-1-A). The peptide bond was formed by using HBTU ((2-(1*H*-benzotriazol-1-yl)-1,1,3,3-tetramethyluronium hexafluorophosphate) as coupling agent. After purification, APTES-(t-bu)$_4$DOTAGA and APTES-(t-bu)$_3$NODAGA were deprotected by concentrated hydrochloric acid to obtain final products. The excess of acid was removed by evaporation. Solutions were lyophilized for storage.

3.1.2.1.1. Synthesis of APTES-DOTAGA

See Chapter 2.

3.1.2.1.2. Synthesis of APTES-NODAGA

This work was carried out by Thakare V. in Chematech, Dijon.

NODAGA(tBu)$_3$ (1.0 g, 1.84 mmol) was weighed in 100 mL round bottom flask and was dissolved in 20 mL of DCM under the hood with stirring. DIPEA (1.3 mL, 7.5 mmol) was added into above solution followed by coupling agents viz. HBTU (1.0 g, 1.95 mmol) and HOBt (1.0 g, 1.95 mmol) and the solution was left for stirring at rt for 15 min. APTES (0.43 g, 1.95 mmol) was added to the above solution directly using the 1 mL syringe and solution was stirred further at rt for 60 min after which the product formation was confirmed through MS. The above solution was mixed with 50 mL of citric acid solution (pH 2.5 - 3) in a separating funnel and the organic layer was recovered. The organic layer was further mixed with 50 mL of 5% $NaHCO_3$ in a separating funnel and the organic layer was recovered. The DCM solution was stirred with 5 g of $MgSO_4$ for 10 min and filtered using sintered funnel to receive the dry and clear DCM solution. Organic phase was evaporated under vacuum at 30°C to get a viscous brownish residue, as an intermediate product (1.5 g, 99%). The intermediate formation was verified using HRMS, ^{1}H, ^{13}C NMR and elemental analysis.

NODAGA(tBu)$_3$-APTES was weighed into a 100 mL round bottom flask and was mixed with 5 mL of conc. HCl and stirred for 10 min. Later, the acid was evaporated under vacuum at 35°C in 5-15 min to get a dried residue. The above dried residue was dissolved in 10 mL of water and lyophilized to get a light brown colored powder (1.2 g, 96%). The product was verified using HRMS, ^{1}H NMR and elemental analysis.

3.1.2.2. Characterization of the intermediate product and APTES-NODAGA

3.1.2.2.1. Methods

See Chapter 2 (methods for characterizing APTES-DOTAGA synthesized from (tBu)$_4$DOTAGA).

3.1.2.2.2. The results for intermediate product (NODAGA(tBu)$_4$-APTES)

HRMS: Calculated for $C_{36}H_{70}N_4O_{10}Si$: 747.493 $[M+H]^+$; Obtained: m/z = 747.493 $[M+Na]^+$ (Figure 3-2)

^{1}H NMR (500 MHz, $CDCl_3$) δ 0.5 – 0.6 (m, 2H), 1.0 – 1.1 (m, 1H), 1.1 – 1.2 (m, 7H), 1.4 (d, *J* = 7.2 Hz, 25H), 1.5 – 1.6 (m, 2H), 1.8 (d, *J* = 8.8 Hz, 1H), 1.9 – 2.1 (m, 1H), 2.2 – 2.5 (m, 2H), 2.6 – 3.3 (m, 22H), 3.7 – 3.8 (m, 4H), 6.2 (d, 1H).

^{13}C NMR (126 MHz, $CDCl_3$) δ 7.8, 18.3, 18.4, 23.1, 26.2, 28.1, 28.2, 28.3, 29.7, 33.4, 38.6, 42.0, 53.7, 55.9, 58.4, 80.8, 165.7, 171.7, 172.8.

Elemental Analysis: Calculated for $C_{36}H_{70}N_4O_{10}Si.0.6HPF_6$ (%): C: 51.81, H: 8.53, N: 6.71. Observed (%): C: 52.58, H: 9.13, N: 8.85.

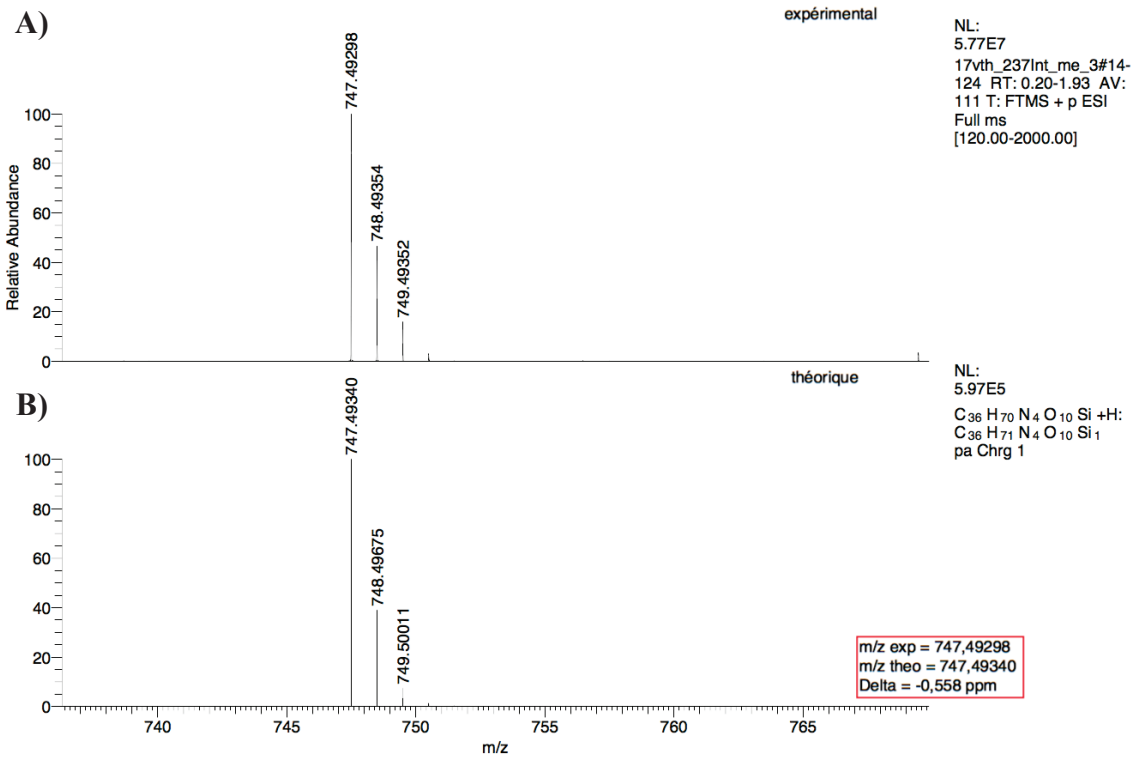

Figure 3-2. Mass spectra of butyl protected APTES-NODAGA: A) experimental spectrum, B) simulated spectrum

3.1.2.2.3. The results for APTES-NODAGA

HRMS: Calculated for $C_{18}H_{34}N_4O_{10}Si$: 495.211 $[M+H]^+$; Obtained: m/z = 495.212 $[M+H]^+$; 517.191 $[M+Na]^+$ (Figure 3-3).

^1H NMR (500 MHz, D_2O) δ 0.41 – 0.80 (m, 2H), 0.93 – 1.28 (m, 2H), 1.39 – 1.59 (m, 2H), 1.84 – 2.18 (m, 2H), 2.27 – 2.46 (m, 2H), 2.73 (s, 5H), 2.97 – 3.18 (m, 5H), 3.19 – 3.45 (m, 7H), 3.48 – 3.75 (m, 1H), 3.79 – 4.10 (m, 4H).

Elemental Analysis:

Calculated for $C_{18}H_{34}N_4O_{10}Si.HPF_6.HCl$ (%): C: 31.93, H: 5.36, N: 8.28.

Observed (%): C: 31.74, H: 6.64, N: 8.81.

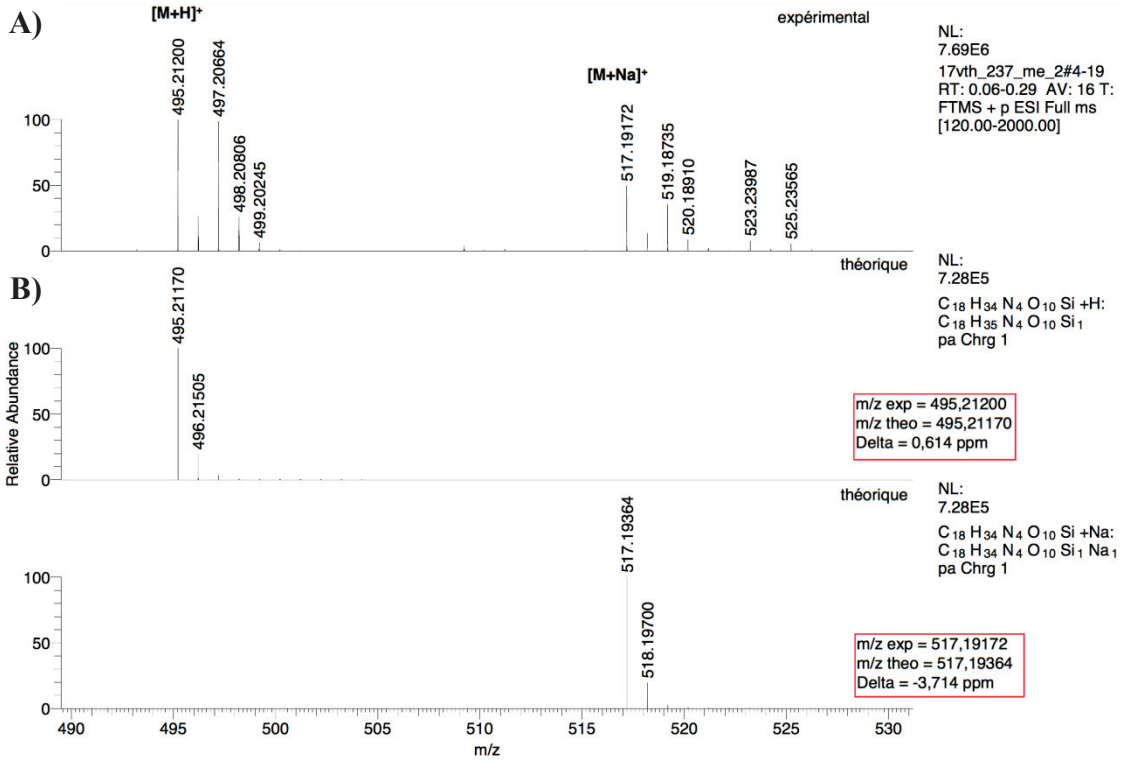

Figure 3-3. Mass spectra of deprotected APTES-NODAGA: A) experimental spectrum, B) simulated spectrum

3.1.2.3. Grafting of APTES-DOTAGA or APTES-NODAGA on AGuIX

First, each type of silanes was mixed with NP in molar ratio Gd : chelator = 10 : 1.5 (AGuIX@D-1 (for DOTAGA functionalized particle) and AGuIX@N-1 (for NODAGA functionalized particle). 250 µmol in Gd of AGuIX were dispersed in water to obtain [Gd^{3+}] = 200 mM for 1 h. pH of the solution was 7.4. 29.8 mg (40 µmol) of APTES-DOTAGA or 24.7 mg (40 µmol) of APTES-NODAGA was dissolved in water. pH of the solution was adjusted to 9 by adding NaOH solutions with appropriate concentrations. This solution was left under stirring for 1 h before water was filled to obtain [chelating silane] = 100 mM. It was then gradually added to the AGuIX solution under stirring at room temperature before water was added to obtain [Gd^{3+}] = 100 mM and [chelating silane] = 15 mM. The mixture was left stirring for 1 h before pH was adjusted to 4.5. It was heated at 80°C and left under stirring overnight.

Secondly, lower temperature (40°C instead of 80°C) and lower total silane concentration (ca. 58 mM instead of ca. 115 mM) were applied to see the effects on the homogeneity of the final NPs (AGuIX@D-2 and AGuIX@N-2). A series of samples with increasing amount of APTES-DOTAGA (Gd/chelator = 10/1.5, 10/2 and 10/4 respectively) (AGuIX@D-2, 3, 4) was prepared to test the possibility of tailoring the amount of free chelators at the surface of the nanoparticle. Similar protocol was applied for these formulas with some modifications: [Gd^{3+}] was decreased to 100 mM. 29.8 mg (40 µmol) or 37.2 mg (50 µmol) or 74.5 mg (100 µmol) of APTES-DOTAGA or 24.7 mg (40 µmol) of APTES-NODAGA was used for AGuIX@D-2, AGuIX@D-3, AGuIX@D-4 and AGuIX@N-2, respectively. The concentration of chelating silane solutions before being added in NP solutions was decreased to 50 mM. At the end, they were heated at 40°C overnight.

Then each solution was purified with tangential filtration through Vivaspin membranes (MWCO = 3 kDa). The pH of the solution should be adjusted to 2 by adding HCl solutions before the purification. The solution was centrifuged until half of the volume remains. This step was repeated by filling the tubes with hydrochloric acid (HCl) solution 10^{-2} M and centrifuging again for at least 50 purification factor (purification factor = starting volume/end volume). Then, the solution was filtered through 0.2 µm membrane to remove dust and large impurities. Finally, the solution was freeze dried for long term storage.

Different syntheses with their respective experimental conditions were summarized in Table 3-1.

Table 3-1. Summary of functionalizing conditions and characterizations of different formulas

Properties	Method(s)	AGuIX	AGuIX@D-1	AGuIX@D-2	AGuIX@D-3	AGuIX@D-4	AGuIX@N-1	AGuIX@N-2
Type of silane	-	-	A-D	A-D	A-D	A-D	A-N	A-N
[AGuIX]initial (mM)	-	-	100	50	50	50	100	50
[Silane]initial (mM)	-	-	15	8	10	20	15	8
Incubation temperature (°C)	-	-	80	40	40	40	80	40
D_H (nm)	DLS	4.2 ± 0.8	4.5 ± 0.9	4.0 ± 0.9	3.8 ± 1.0	3.4 ± 1.0	4.5 ± 0.9	4.0 ± 0.9
Zeta potential (mV)	Zeta potentiometry	+ 8.2 (pH 7.0)	- 8.3 (pH 7.0)	0.07 (pH 6.8)	- 16.7 (pH 6.9)	- 18.8 (pH 6.9)	- 13.7 (pH 7.0)	- 12.1 (pH 6.8)
Free COOH band	IR	No	Yes	-	-	-	Yes	-
Retention time (min)	HPLC (295 nm)	13.6	15.3	14.7	14.8	14.9	14.7	14.6
FWHM (min)	HPLC (295 nm)	2.0333	2.9917	2.4917	2.4500	2.2500	3.3833	2.5250
Purity (%)	HPLC (295 nm)	85.1	95.1	91.7	91.7	92.1	96.4	91.6
Free DOTAGA content (µmol/mg)	Eu^{3+} titration	0.025	0.1	0.09	0.16	0.20	0.1	0.13
% chelator added		-	15	15	20	40	15	15
% chelator grafted	Eu^{3+} titration	-	11	12	20	28	11	17
Gd content (µmol/mg)	ICP-OES	0.890	0.763	0.643	0.640	0.515	0.763	0.650
r_1 ($mM^{-1}.s^{-1}$) (37°C, 60 MHz)	Relaxometry	14.3	18.0	16.1	17.3	17.2	18.2	17.0
r_2/r_1 (37°C, 60 MHz)	Relaxometry	1.36	1.42	1.38	1.45	1.37	1.42	1.42
Gd : Si : N : C (molar ratio)	Elemental analysis	1.0 : 4.8 : 6.0 : 25.3	1.0 : 6.5 : 7.3 : 30.7	-	-	-	1.0 : 6.1 : 7.2 : 30.8	-
Gd : A-D : A-N : A : T* (molar ratio)	Elemental analysis	1.0 : 1.0 : 0.0 : 0.8 : 3.0	1.0 : 1.3 : 0.0 : 1.0 : 4.2	-	-	-	1.0 : 1.0 : 0.3 : 0.7 : 4.0	-
Yield (%) (in chelator)		-	24.0	41.6	46.3	33.8	26.9	48.6
Yield (%) (in Gd)		-	28.6	47.5	37.0	34.8	32.0	38.9

**A-D: APTES-DOTAGA, A-N : APTES-NODAGA, A: APTES, T: TEOS*

3.1.3. Characterization of the functionalized particles

Table 3-1 also shows different characterization results of the NP before and after functionalization by chelating silanes.

First attempts were to functionalize AGuIX with 15% of DOTAGA (AGuIX@D-1) and NODAGA (AGuIX@N-1) using 80°C incubation. D_H of the particles which only slightly increased from 4.2 ± 0.8 nm for AGuIX to 4.5 ± 0.9 nm for AGuIX@D-1 and AGuIX@N-1 indicated that the size was maintained ultrasmall (Figure 3-4 and Table 3-1).

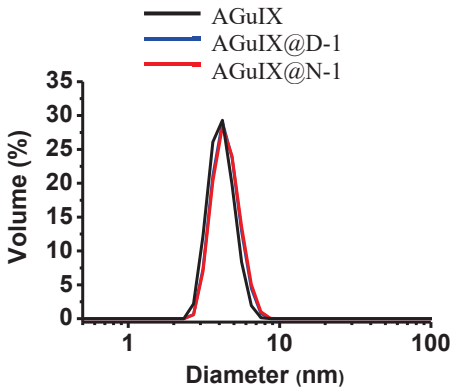

Figure 3-4. DLS diagrams of:
AGuIX (black), AGuIX@D-1 (DOTAGA, 80°C) (blue) and AGuIX@N-1 (NODAGA, 80°C) (red)

In addition, many features proved the presence of free chelators on the particles after the reaction. First of all, the zeta potentials at pH 7.0 decreased from + 8.2 mV for AGuIX to - 8.3 mV for AGuIX@D-1 or - 13.7 mV for AGuIX@N-1 (Table 3-1). Vibration band at 1730 cm^{-1} in IR spectra, corresponding to C=O stretching vibration band of free carboxylic acid, was detected (Figure 3-5). The retention time (t_R) in chromatograms increased from 13.6 min for AGuIX to 15.3 min for AGuIX@D-1 or 14.7 min for AGuIX@N-1 (Figure 3-6-A, B). The content of free chelators quantified by Eu titration increased from 0.025 µmol/mg for AGuIX to 0.1 µmol/mg for AGuIX@D-1 and AGuIX@N-1 (Figure 3-7-A, B, C). The content of Gd measured by ICP-OES decreased from 0.89 µmol/mg for AGuIX to 0.76 µmol/mg for AGuIX@D-1 and AGuIX@N-1. The longitudinal relaxivity (r_1) increased from 14.3 for AGuIX to 18.0 $mM^{-1}.s^{-1}$ for AGuIX@D-1 or 18.2 $mM^{-1}.s^{-1}$ for AGuIX@N-1 (Table 3-1). This might be due to an increase in rotational correlation time resulting from the grafting of a ligand and/or simply the removal of small fragments in the starting material. Meanwhile the ratio r_2/r_1 slightly increased but stayed around 1.4 indicating that the efficiency of the NPs as positive contrast agents was maintained. Results from elemental analysis also confirmed the increases of other elements i.e. Si, N and C compared to Gd (Table 3-1).

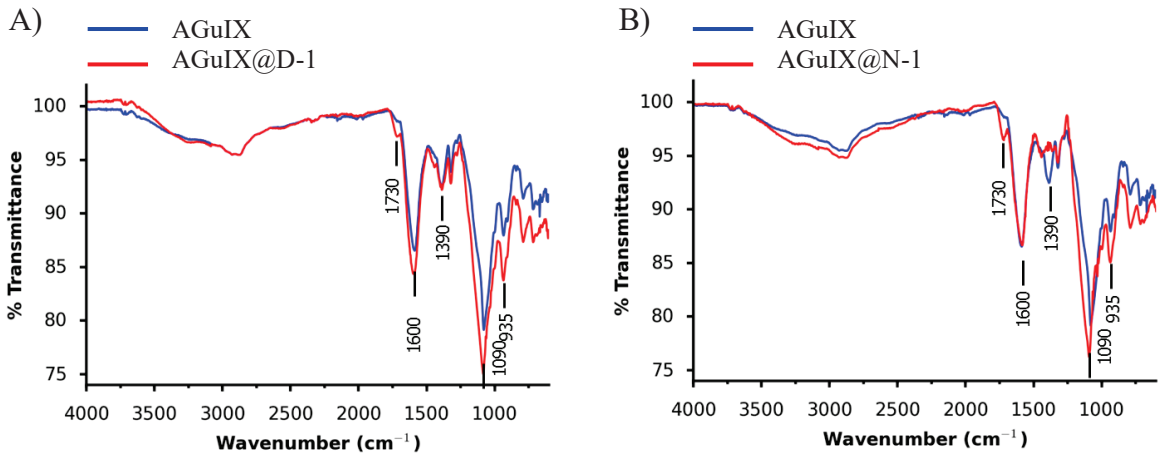

Figure 3-5. Infrared spectra of:
A) AGuIX before functionalized (blue) and AGuIX@D-1 (after functionalized with DOTAGA) (red);
B) AGuIX before functionalized (blue) and AGuIX@N-1 (after functionalized with NODAGA) (red).

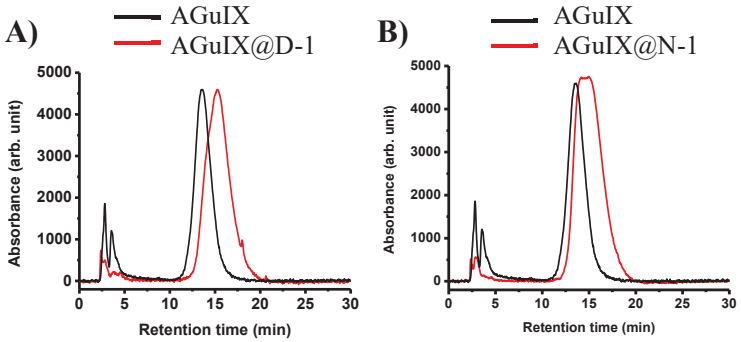

Figure 3-6. HPLC chromatograms of:
A) AGuIX (black); AGuIX@D-1 (DOTAGA, 80°C) (red);
B) AGuIX (black); AGuIX@N-1 (NODAGA, 80°C) (red).

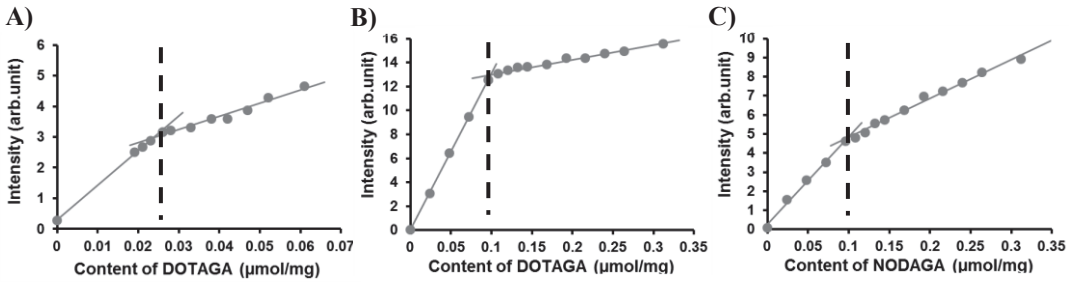

Figure 3-7. Eu titration curves λ_{ex} = 395 nm, λ_{em} = 594 nm of: A) AGuIX; B) AGuIX@D-1; C) AGuIX@N-1.

Two other formulas (AGuIX@D-2, AGuIX@N-2) with the same ratio of NP and free silanes were conducted at lower initial concentrations of reactants (50 mM in Gd of AGuIX and 8 mM of chelating silanes) and lower incubating temperature (40°C). All characteristics were more or less similar to the previous formulas (Figure 3-8, Figure 3-9, Figure 3-10 and Table 3-1) except the homogeneities of the particles which were improved as indicated by full width at half maximum (FWHM) of NP peaks on chromatograms. This was especially true for NODAGA functionalized particles where FWHM of AGuIX@N-1 and AGuIX@N-2 were 3.3833 min and 2.5250 min respectively (Table 3-1 and Figure 3-9-B). But these subtle differences are not anticipated to change significantly the properties of the particles.

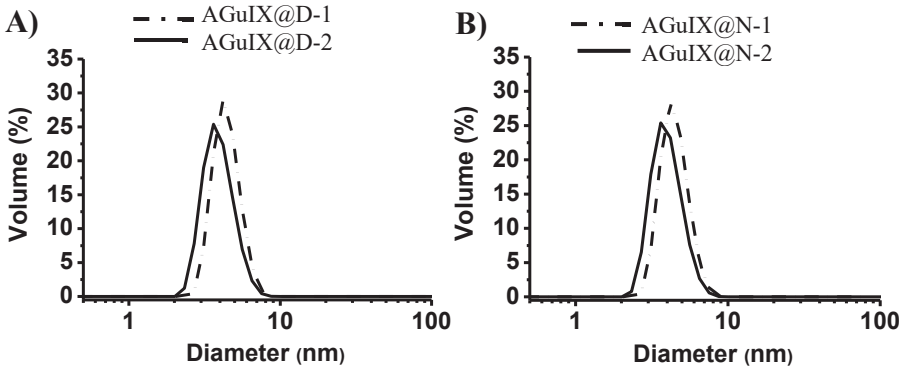

Figure 3-8. DLS diagrams of:
A) AGuIX@D-1 (DOTAGA, 80°C) (dash-dotted line) and AGuIX@D-2 (DOTAGA, 40°C) (solid line);
B) AGuIX@N-1 (NODAGA, 80°C) (dash-dotted line) and AGuIX@N-2 (NODAGA, 40°C) (solid line);

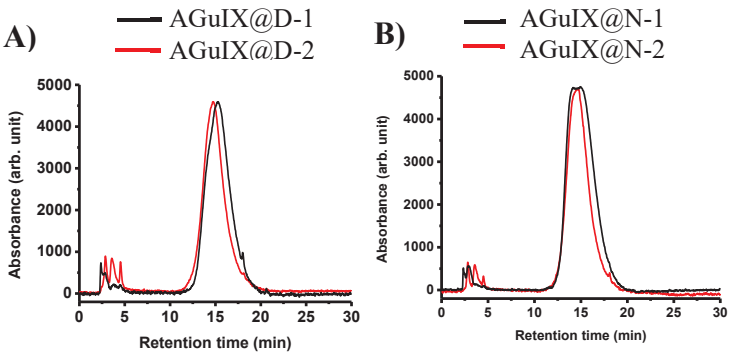

Figure 3-9. HPLC chromatograms of:
A) SiGdNP@D-2 (DOTAGA : Gd = 1.5 : 10, 40°C) (red) vs. SiGdNP@D-1 (DOTAGA : Gd = 1.5 : 10, 80°C) (black);
B) SiGdNP@N-2 (NODAGA : Gd = 1.5 : 10, 40°C) (red) vs. SiGdNP@N-1 (NODAGA : Gd = 1.5 : 10, 80°C) (black).

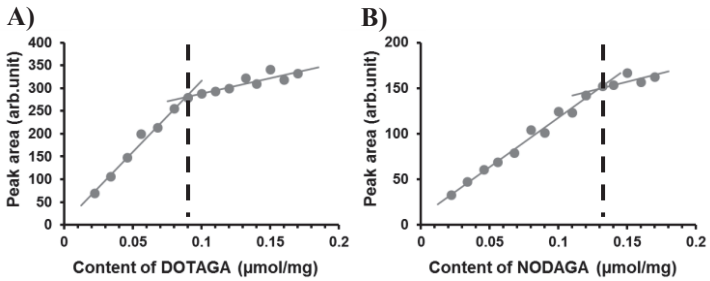

Figure 3-10. Eu titration curves λ_{ex} = 395 nm, λ_{em} = 594 nm of: A) AGuIX@N-1 and B) AGuIX@N-2.

Two more other formulas with higher ratio of APTES-DOTAGA (AGuIX@D-3 and AGuIX@D-4) were tested. The result of Eu titration showed that the amount of grafted free chelators was increased as more chelating silanes were added (Figure 3-11). The chromatograms of these samples do not show any changes in the NP peaks indicating the preservation of homogeneous populations of NPs (Figure 3-12). The relaxivities of these samples were very similar to each other and similar to other samples (r_1 ~ 16 – 17 $mM^{-1}.s^{-1}$ r_2/r_1 ~ 1.4) (Table 3-1).

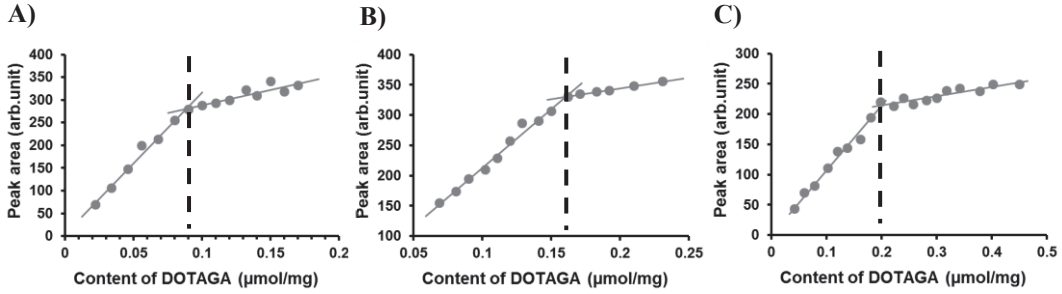

Figure 3-11. Eu titration curves λ_{ex} = 395 nm, λ_{em} = 594 nm of: A) AGuIX@D-2, B) AGuIX@D-3 and C) AGuIX@D-4.

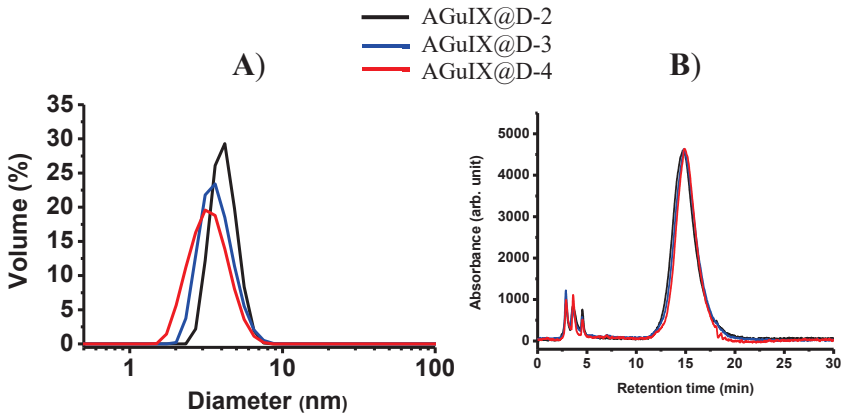

Figure 3-12. A) DLS diagrams and B) HPLC chromatograms of: AGuIX@D-2 (DOTAGA, 40°C, DOTAGA:Gd = 1.5 :10) (black), AGuIX@D-3 (DOTAGA, 40°C, DOTAGA:Gd = 2 :10) (blue), AGuIX@D-4 (DOTAGA, 40°C, DOTAGA:Gd = 4 :10) (red).

3.1.4. Conclusion and perspectives

We have described a straightforward and simple approach to functionalize AGuIX along with the physico-chemical characterization of the products. Macrocyclic chelating silane precursors have been synthesized by peptide coupling. They can be simply redispersed and grafted on AGuIX through siloxane bonds formation. The amount of free chelators can be tailored according to the starting ratio of precursors. The influence of reaction conditions i.e. temperature and initial silane concentration on the homogeneity of the particle was studied.

NODAGA functionalized particle, AGuIX@N-1, will be used for bimodal MRI/PET imaging experiments due to the presence of NODAGA on its surface which can complex ^{64}Cu more efficiently. The radiolabeling, *in vivo* imaging and biodistribution studies in mice bearing TSA breast cancer tumors are being conducted in Dijon by our collaborator Thakare V.

3.2. Functionalization of AGuIX with a multifunctional chelate

3.2.1. Introduction

As we have seen above, multimodal imaging probes are highly demanded and AGuIX can offer a versatile platform on which different modalities can be easily added. As an illustrating example, we have tried to functionalize AGuIX with an innovating bimodal probe 17VTh031 synthesized by Thakare V. (Chematech, Dijon) (Figure 3-13-A). This probe contains both NODAGA and a derivative of IR783, a novel near infra-red fluorophore which possesses both excellent photophysical and tumor targeting properties.

IR783 belongs to a heptamethyl carbocyanine family of fluorophore commercialized by Sigma-Aldrich. The chemical structure of IR783 resembles a more conventional fluorophore, cyanine 5.5. However, it has a seven-carbon methine chain, a cyclohexenyl ring and a central chlorine atom located in the middle of the chain (Figure 3-13-B). These modifications shift the excitation and emission peak of IR783 further to near infra-red (NIR) region ($\lambda ex/em_{IR783}$ = 783/840 nm vs. $\lambda ex/em_{Cy5.5}$ = 675/694 nm) which is more desirable for *in vivo* imaging applications. Besides its photophysical characteristics, it has been discovered to be actively taken up by cancer cells in the laboratory of Prof. Chung L. W. K. in Cedars-Sinai Medical Center, USA.[227] The range of cancer cells and tumors that have affinity to IR783 and its derivatives covers kidney, prostate, breast, lung etc.[228–231] Most recently, IR783 has been demonstrated as having a potential to penetrate blood-brain barrier and blood-tumor barrier to target specifically primary and metastasis brain tumors.[232] Its cellular uptake is possibly mediated by organic anion-transporting polypeptides (OATPs), a family of solute carrier transporter, and induced by tumor hypoxia.

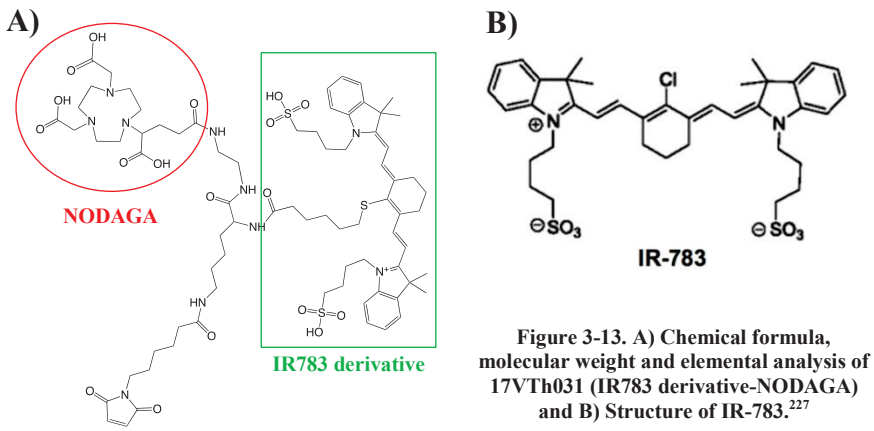

Chemical Formula: $C_{77}H_{111}N_{10}O_{18}S_3^+$
Exact Mass: 1559.72
Molecular Weight: 1560.97
Elemental Analysis: C, 59.25; H, 7.17; N, 8.97; O, 18.45; S, 6.16

Figure 3-13. A) Chemical formula, molecular weight and elemental analysis of 17VTh031 (IR783 derivative-NODAGA) and B) Structure of IR-783.[227]

By combining 17VTh031 into AGuIX, we hope to obtain a trimodal imaging nanoparticle that works as both a contrast agent for MRI, radio probe for PET and NIR fluorophore for optical imaging thanks to the presence of Gd chelates, free NODAGA (for grafting small radioisotopes such as ^{64}Cu, ^{68}Ga) and IR783 respectively. The combination of a NIR fluorophore i.e. IR783 derivative makes it possible to use AGuIX platform as a real-time intraoperative probe for mapping lesions, for example, tumors or sentinel lymph nodes metastates during surgeries.[166] This might allow a complimentary combination of pre-operative precise diagnosis and tumor mapping by sophisticated MRI/PET imaging and image-guidance during operation thanks to optical imaging. In addition, this NP might

actively target cancer tumors thanks to the affinity of IR783 derivative and improve the tumor retention as well as cellular internationalization of AGuIX.

3.2.2. Characterization of bimodal probe

17VTh031 was characterized by Thakare V. (Chematech, Dijon) using high resolution ESI-MS, elemental analysis and fluorescence spectroscopy. Its mother ion M+ (m/z = 1560) and daughter ion [M-H+Na]+ (m/z = 1582) were well detected in ESI-HRMS (Figure 3-14). The results of elemental analysis correspond very well with proposed chemical formula (Table 3-2). Absorption and emission spectra of 17VTh031 showed absorption peak at 780 nm and emission peak at 820 nm (Figure 3-15-A) with high molar attenuation coefficient ε = 178500 $M^{-1}.cm^{-1}$ at 785 nm (Figure 3-15-B). Hence, the photophysical properties of IR783 were well preserved in 17VTh031.

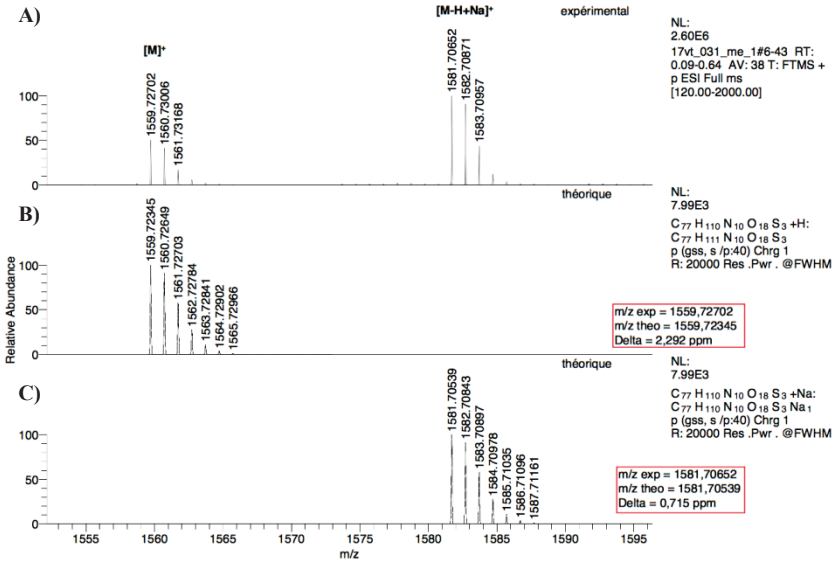

Figure 3-14. Mass spectra of 17VTh031: A) experimental spectrum, B) simulated spectrum of mother ion M^+ and C) simulated spectrum of $[M-H+Na]^+$

Table 3-2. Result of elemental analysis of 17VTh031

Element	C	H	N	O	S
Theoretical relative mol	77	111	10	18	3
% mass	59.25	7.17	8.97	18.45	6.16
Calculated relative mol	77.03	111.95	10.00	18.00	3.00

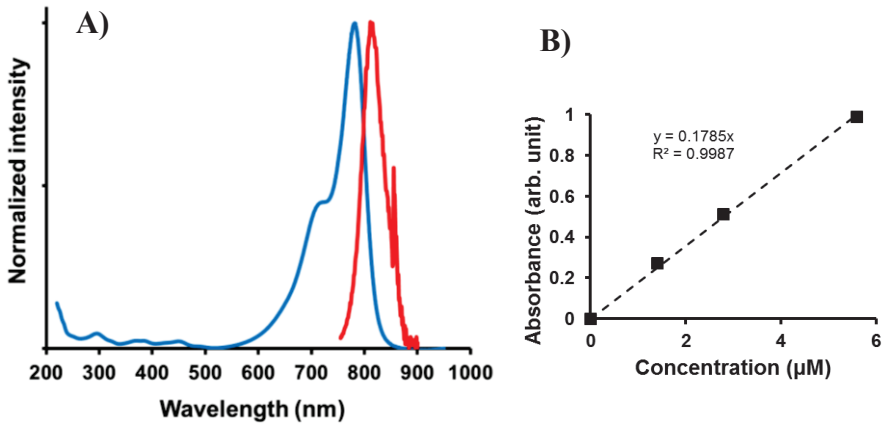

Figure 3-15. A) Absorption spectrum (blue) and fluorescence emission spectrum (red) (λ_{ex} = 780 nm) and B) Calibration curve at 785 nm of 17VTh031.

3.2.3. Functionalization strategy and protocol

For conjugation purposes, 17VTh031 contains a maleimide group which can readily react with thiols. We will simply introduce thiol groups on AGuIX by using the Traut's reagent. Thiolated AGuIX will be quantified for the ratio of thiols/Gd and mixed immediately with 17VTh031 to create a new nanoconstruct, AGuIX-I-N (AGuIX-IR783-NODAGA) (Figure 3-16).

Experimental protocol:

Step 1: thiolation of AGuIX

100 µmol in Gd of AGuIX was redispersed in PBS buffer pH 8 at 200 mM. T_1, T_2 and hydrodynamic diameter of the sample were measured by relaxometry and DLS. Small sample was taken for HPLC analysis. 100 µmol of 2-iminothiolane (Traut's reagent) was dissolved in PBS buffer pH 8 at 300 g/l. 2-iminothiolane solution was added gradually under vigorous stirring to AGuIX solution to produce a transparent solution. 100 µl PBS was added to have enough volume for pH measurement. pH of the mixture was around 6.4 due to acidic nature of Traut's reagent. pH was adjusted rapidly to 8 where the reaction happens the most efficiently[233] by adding NaOH solutions. Solution was stirred 1 h at room temperature. PBS buffer was added to have a mixture of AGuIX and Traut's reagent both at 100 mM. pH did not change after the reaction. pH was adjusted to 7.3 by adding HCl solutions. Thiolated AGuIX (AGuIX-SH) was purified by tangential filtration for 64 purification factor using PBS pH 7 as washing solvent to remove unreacted 2-iminothiolane and its hydrolyzed product. T_1, T_2 and D_H of the sample were again measured. Concentration of purified sample in Gd was re-adjusted using the result of T_1 while assuming longitudinal relaxivity did not change during the thiolation. Sample was quickly titrated with Ellman's reagent to quantify the amount of grafted thiols.

Step 2: conjugation of 17VTh031 to AGuIX-SH

266 µl of AGuIX-SH purified solution (approx. 45 µmol in Gd) was taken to a bottle. 9 mg of 17VTh031 (4.5 µmol) was dissolved in 50 µl PBS pH 7. Few drops of NaOH 1M was added to adjust pH to 6.5 to fully dissolve the fluorophore. Solution of fluorophore was transferred to AGuIX-SH solution gradually under vigorous stirring. 50 µl PBS was used to rinse the fluorophore's container. pH of the solution was verified and stayed at 7.2. The mixture was

left stirring for 2 h at room temperature. Final concentrations of AGuIX-SH and 17VTh031 were 58.5 mM and 5.85 mM respectively. pH was not changed after the reaction. Solution was purified by tangential filtration for 256 purification factors to remove unreacted fluorophores. Absorption of filtrates was measured to verify the efficiency of purification process. T_1, T_2 and D_H of the sample were again measured. Small sample of purified particle was taken for UV-vis spectroscopy and HPLC analysis.

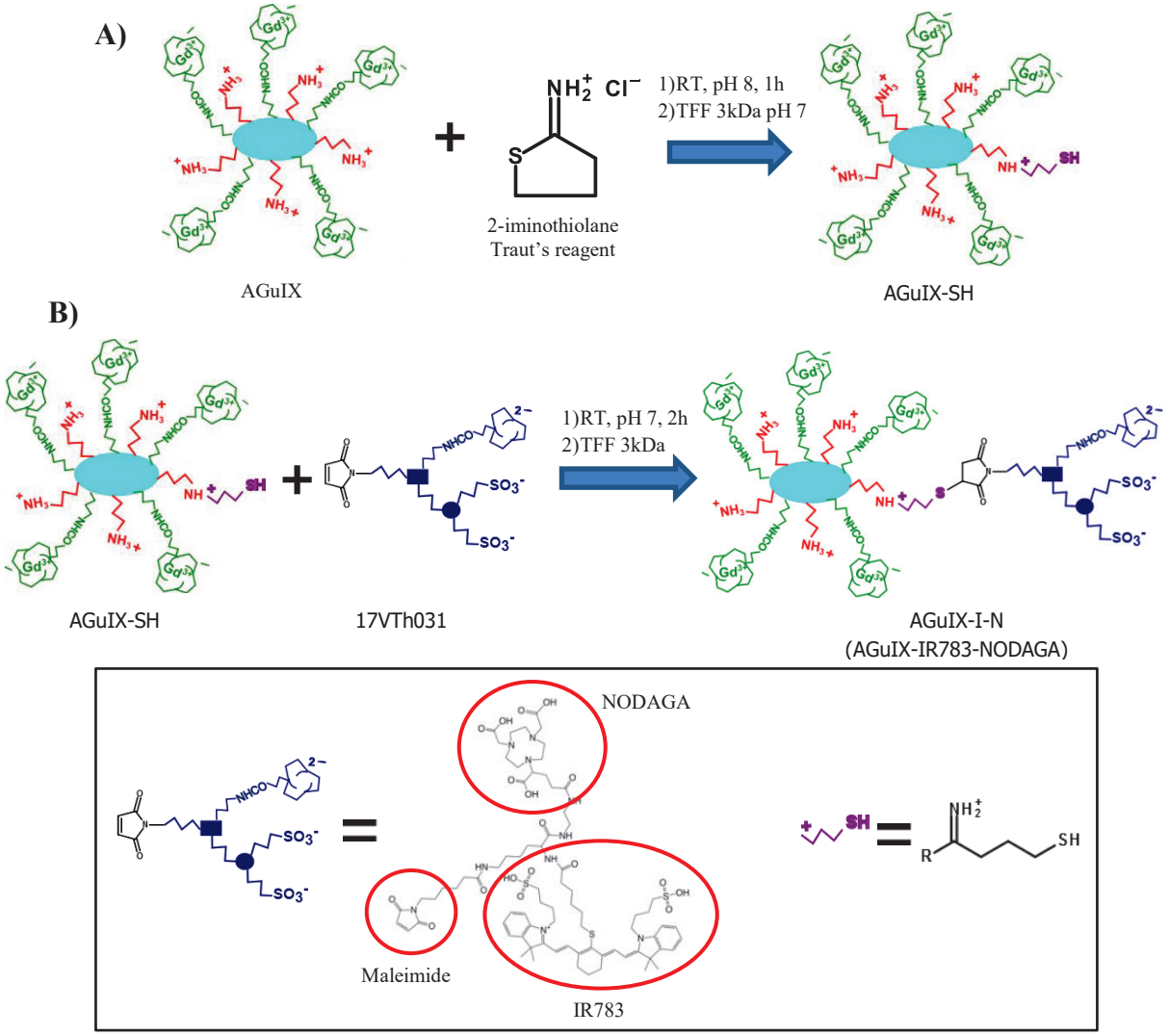

Figure 3-16. Reaction scheme of trimodal MRI/PET/OI AGuIX (AGuIX-I-N): A) step 1: thiolation of AGuIX; B) step 2: functionalization with bimodal probe 17VTh031 (IR783-NODAGA).

3.2.4. Characterization of the functionalized particle

The results from different characterizations during this synthesis were summarized in Table 3-3.

Table 3-3. Characterization of AGuIX-I-N in comparison with non-functionalized AGuIX

Features	Methods	AGuIX	AGuIX-SH	AGuIX-I-N
D_H (nm)	DLS	4.6 ± 0.9	4.5 ± 0.9	12.1 ± 3.0
Relative quantification of SH	Ellman's assay	-	Gd : SH ~ 10 : 2.5	-
r_1 ($mM^{-1}.s^{-1}$)	Relaxometry	13.5	16.8	16.9
r_2/r_1		1.35	1.39	1.83
Retention time (min)	HPLC	13.4	-	17.7
Purity (%)		80.2		95.7

Gd : 17VTh031	UV spectroscopy	-	-	10 : 0.8
Content of Gd (µmol/mg)	ICP-OES	0.8903	-	0.3185
Yield in Gd (%)		-	-	51.6
Yield in 17VTh031 (%)		-	-	24.5

After the thiolation step, Ellman's assay[233] and ICP-OES were performed to determine the ratio of SH and Gd in the solution (Figure 3-17). In Ellman's assay, DTNB (5,5's-dithiobis-(2-nitro benzoic acid), which absorbs at 330 nm, will react with thiol groups to release TNB (5-thio-2-nitro benzoic acid), which absorbs at 412 nm.[234] Hence, a saturated absorption at 412 nm and a sudden increase of absorption at 330 nm indicate the equivalent point of the titration. By correlating the result of Ellman's assay, which gave the amount of thiols in the solution, and the result of ICP-OES, which gave the amount of Gd in the solution, we were able to determine the ratio SH : Gd (equivalent to DTNB : Gd) as 0.25 : 1.0. Assuming there are approximately 10 Gd chelates on each particle[133,173], there would be 2.5 thiol groups on each thiolated particle.

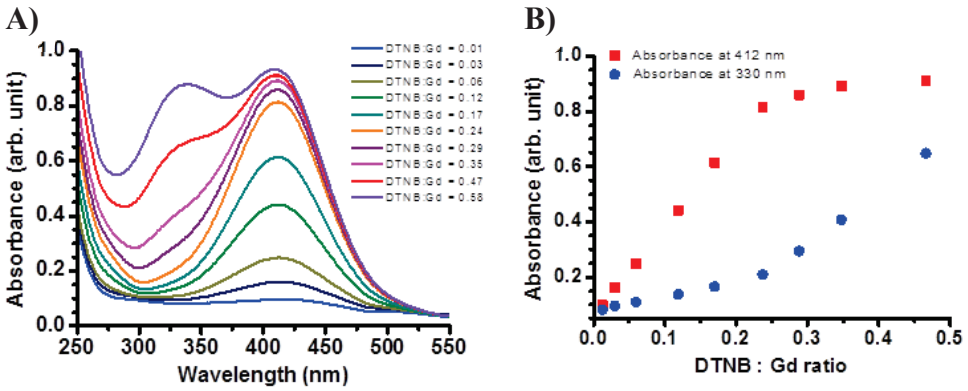

Figure 3-17. Result of Ellman's assay for AGuIX-SH: A) UV spectra of samples; B) Titration curves at 412 nm (red) and 330nm (blue).

Meanwhile, the D_H of AGuIX-SH remained the same (4.5 ± 0.9 nm) as non-functionalized particle (4.6 ± 0.9 nm) (Figure 3-18). Longitudinal relaxivity r_1, however, increased from 13.5 to 16.8 $mM^{-1}.s^{-1}$ while the ratio r_2/r_1 did not change significantly (1.35 vs. 1.39). This was probably only due to the removal by tangential filtration of smaller, less stable particles and free Gd chelates fragments which were already present in AGuIX solution or degraded from the initial particles during the reaction and purification processes. After grafting 17VTh031 on AGuIX-SH, D_H of the particle increased to 12.1 nm due to the bulkiness of the bimodal probe (Figure 3-18). Both DLS apparatuses with different laser sources i.e. 633 nm (red) and 532 nm (green) gave the same value. HPLC chromatograms confirm DLS results since the retention time of AGuIX-I-N was much higher (17.7 min) compared to the initial AGuIX (13.4 min) (Figure 3-19). Surprisingly, r_1 did not increase significantly (16.9 $mM^{-1}.s^{-1}$ vs. 16.8 $mM^{-1}.s^{-1}$) while r_2 seems to enhance substantially (r_2/r_1 = 1.83 vs. 1.39).

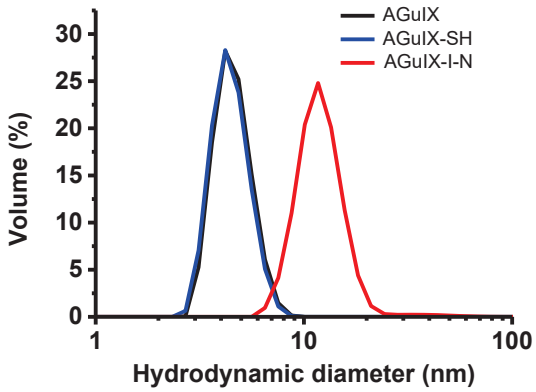

Figure 3-18. DLS diagrams of AGuIX (black), AGuIX-SH (blue) and AGuIX-I-N (red)

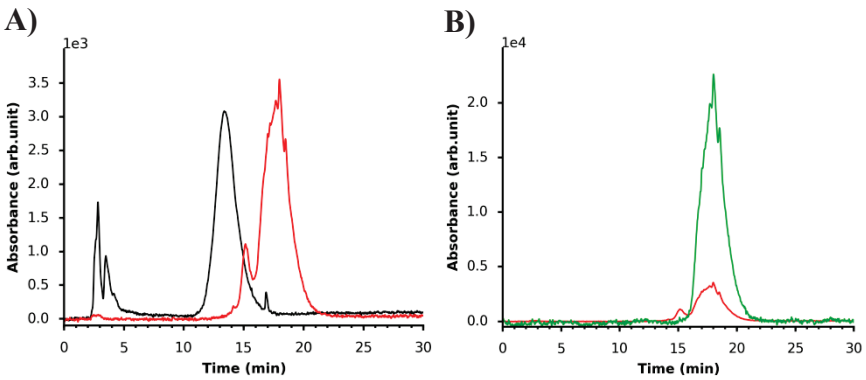

Figure 3-19. A) Comparison of chromatograms at 295 nm of AGuIX (black) and AGuIX-I-N (red); B) Comparison of chromatograms of AGuIX-I-N at 295 nm (red) and 700 nm (green).

The absorption spectra of filtrates and chromatogram at 700 nm demonstrated that most of free fluorophores have been removed (Figure 3-19-B, Figure 3-20), although, some strange peaks have appeared at 295 nm or 700 nm. They might be some unknown impurities that stuck stubbornly on the particle or populations of ungrafted AGuIX. Nevertheless, for a preliminary test, this result was quite satisfying. The content of Gd determined by ICP-OES decreased from 0.8903 µmol/mg (AGuIX) to 0.3185 µmol/mg (AGuIX-I-N) indicating a higher percentage of organic groups in functionalized particle. By combining the Gd concentration determined by ICP-OES and 17VTh031 concentration determined by UV absorption, we can find out the ratio 17VTh031 : Gd as 0.8 : 10.

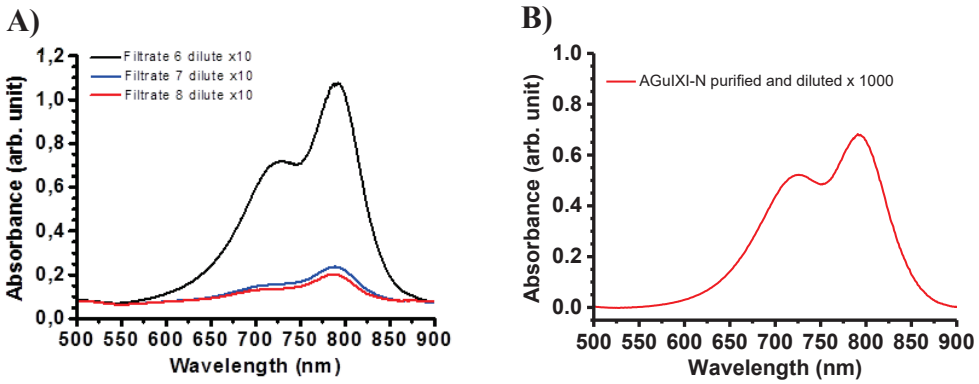

Figure 3-20. UV spectra of A) filtrates of AGuIX-I-N during the purification; B) purified AGuIX-I-N (subtracted to pure water).

3.2.5. Conclusion and perspectives

A new probe has been grafted on AGuIX to produce a trimodal imaging (MRI/PET/OI) nanoagent. We have characterized the product by different analytical techniques to prove the grafting of new species on AGuIX. This new NP will be tested in *in vitro* and *in vivo* models in Dijon to evaluate its efficiency to increase cellular uptake and selectively target cancer tumors.

For further development, it would be interesting to develop a silane of IR783 separately for grafting on AGuIX. Combining this silane-IR783 with APTES-NODAGA introduced in the previous section, we can easily graft the two probes on AGuIX, instead of a cumbersome IR783-NODAGA conjugate, without compromising too much the ultrasmall diameter of the particle. It will also simplify the conjugation protocol and storage condition. Depending on the preliminary biological results, larger-scale production and more thorough studies should also be designed to optimize this NP.

3.3. Functionalization of AGuIX with quaternary ammonium for targeting the proteoglycans (PGs)

3.3.1. Introduction

3.3.1.1. Molecular structure and location of PGs

Proteoglycans are the hybrid molecules of glycosaminoglycans (GAG) and certain proteins. Many types of proteoglycans exist. They are classified by their locations i.e. intracellular PGs, cell surface PGs, extracellular PGs. The targeting strategy developed in this section aims at the extracellular PGs. These types of PGs are one of main structural components in tissue organization. They made up most of the extracellular matrix (ECM) of the tissues. The two most common extracellular PGs are hyalectans and small leucine rich PGs (SLRPs).[235,236] Figure 3-21 shows a simple schematic representation of the structures of hyalectans. Figure 3-22 shows the macroscopic structure of an example of hyalectan and its location in ECM. The common GAG found in both hyalectans and SLRPs include hyaluronan/hyaluronic acid, chondroitin sulfate, keratan sulfate and dermatan sulfate. Figure 3-23 shows the molecular structures of these GAGs. Hyaluronan is made of several units (up to ~ 50000) of disaccharides combining D-glucuronic acid (GlcA) and N-acetylglucosamine (GlcNAc). The other three are much shorter with less than hundreds of disaccharides units. Chondroitin sulfate contains units of GlcA linked to N-acetylgalactosamine sulfate (GalNAcS). Meanwhile, keratan sulfate is made from units of galactose (Gal) and GlcNAc sulfate (GlcNAcS). The structure of dermatan sulfate is very similar to chondroitin sulfate but many glucoronate units are replaced by α-L-iduronate (IdoA). These molecules contain numerous carboxylate and sulfonate groups that make them highly negatively charged. Extracellular PGs are abundantly present in lubricants in the synovial fluid of joints, vitreous humor of eyes and ECM-rich tissues such as cartilages, tendons, ligaments, walls of aorta, skin, blood vessels, heart valves, cornea, bones, hairs and nails.[237]

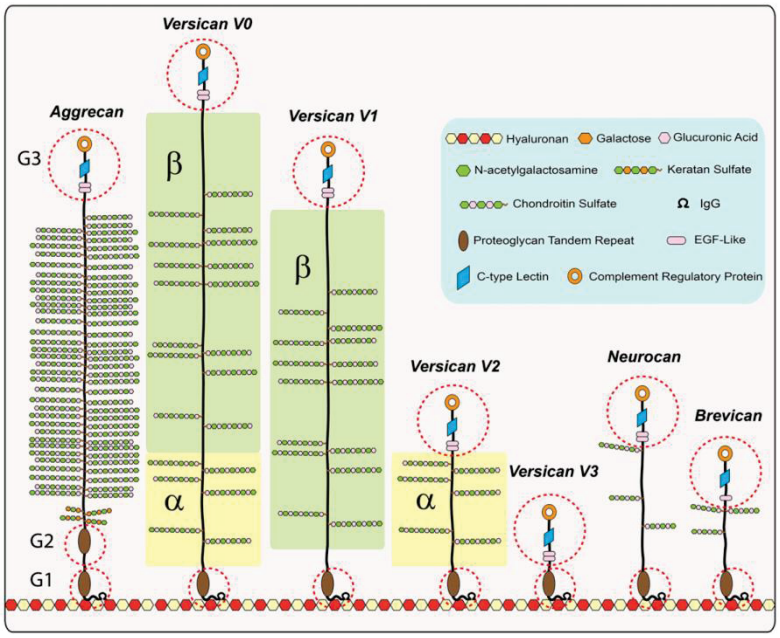

Figure 3-21. Schematic representation of the hyalectans, the PGs acting as key structural components of ECM of many tissues especially cartillages.[236]

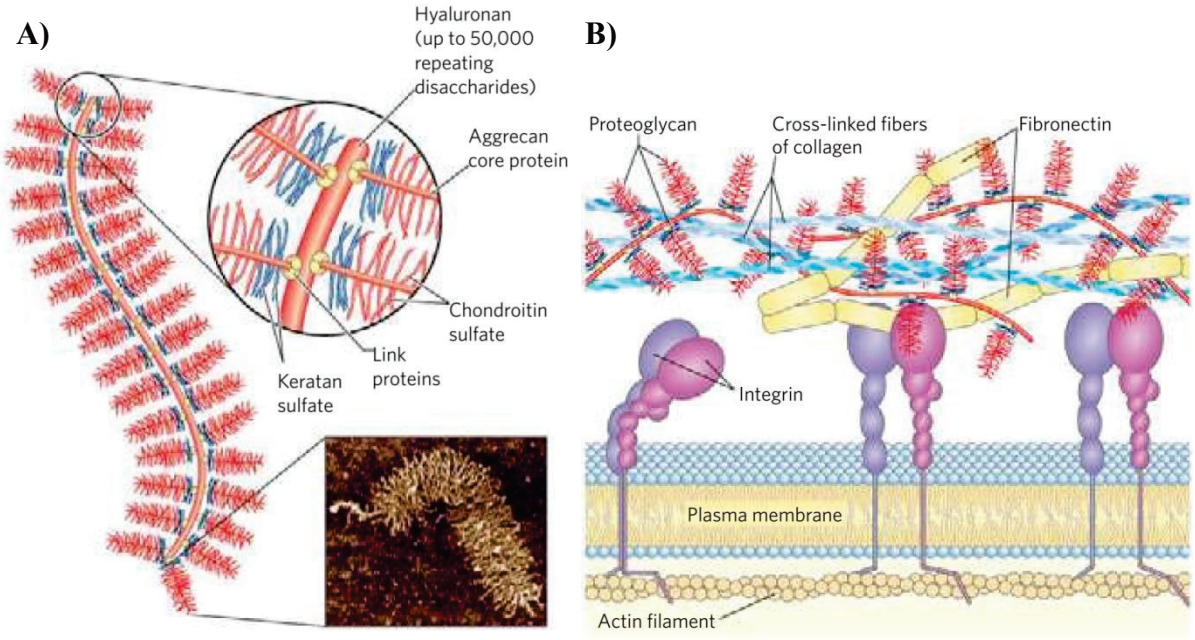

Figure 3-22. Macrostructure and location of proteoglycans: A) schematic representation of a proteoglycan with many aggrecan molecules; B) Proteoglycans in the extracellular matrix.[237]

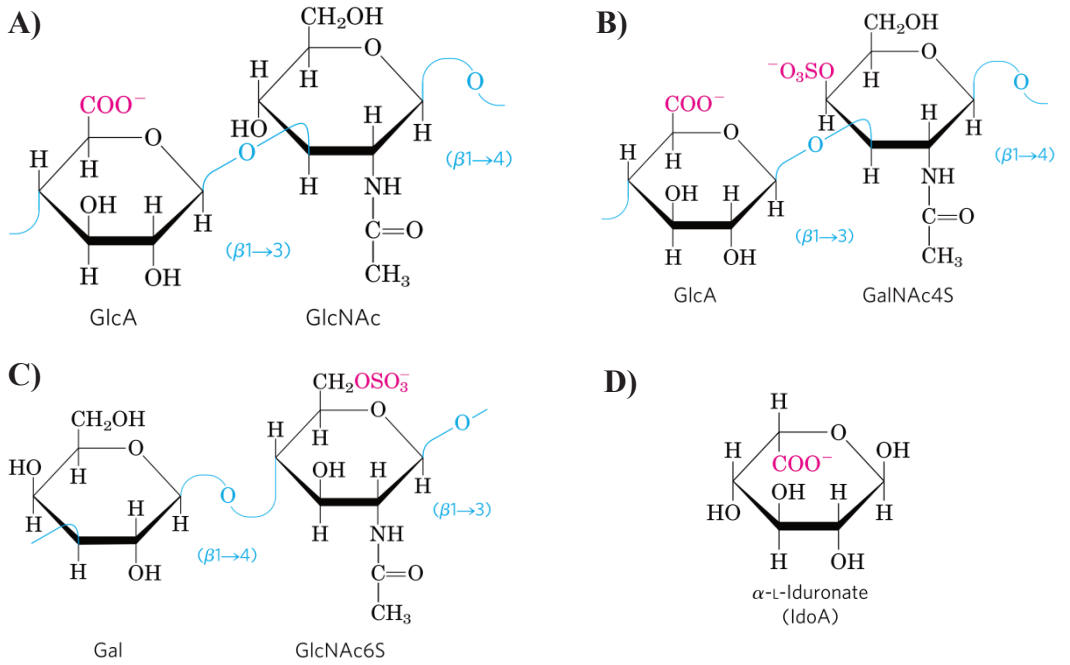

Figure 3-23. Molecular components of proteoglycan: A) 1 unit of hyaluronan; B) 1 unit of chondroitin-4-sulfate; C) 1 unit of keratan-sulfate and D) IdoA, one saccharide in the repeating units of dermatan sulfate.[237]

3.3.1.2. The use of quaternary ammonium as a targeting ligand for cartilaginous tissues and chondrosarcoma

Since 2000, aromatic (pyridinium) and aliphatic ammonium (triethylammonium), due to their positive charges, have been proven to have a strong affinity to PGs, more specifically speaking, carbonates and sulfonates groups on their structures.[238,239] Based on this result, the research team led by Prof. Chezal J-M. and Dr. Miot-Noirault E. in Clermont-Ferrand has developed different molecular probes for nuclear imaging and therapy targeting cartilaginous

tissues where ECM and more specifically PGs make up a large proportion. Agents that have been incorporated with ammonium expanded from radionuclides, inflammatory drugs, metalloproteinase inhibitors and cytotoxic drugs.[240,241] This targeting strategy is especially interesting for developing alternative treatments for chondrosarcoma. The latter is the second most common primary cancer of the skeleton characterized by a high production of ECM by the tumors in cartilage, low percentage of dividing cells, poor vascularity, low pH and high interstitial pressure. These features make chondrosarcoma tumors highly resistant to radiotherapy or chemotherapy. This left surgery as the main option despite the fact that, in many serious cases, the removal of a large part of the body can even decrease the survival chance, cripple the patients or require another large reconstruction surgery. Furthermore, in some cases, tumors can be found in some inoperable locations where vital organs or principal bones are located. In the last few decades, although significant progresses have been obtained for other sarcomas, the prognosis for patients with high grade chondrosarcoma remains almost unchanged.[242,243] These facts point out the need for an innovative treatment to overcome this form of cancer. In the framework of French national project CHONDRAD (http://www.agence-nationale-recherche.fr/?Projet=ANR-14-CE16-0021), we have collaborated with the teams of Prof. Chezal J-M. and Dr. Miot-Noirault E. as well as other scientists in Lyon and Clermont-Ferrand to conjugate quaternary pyridinium on AGuIX platform in the hope of improving the effect of radiotherapy for the treatment of chondrosarcoma. This type of functionalized particle has been shown to have a superior accumulation in cartilage and chondrosarcoma in *in vivo* models.[150,151] These promising results call for further experiments to evaluate the RS effect of the platform. During my thesis, we have modified the functionalization strategy to adapt with the structure of current AGuIX.

3.3.2. Strategy and protocol

New strategy:

Previously, quaternary ammonium (QA) or pyridinium, more precisely, was grafted on AGuIX by forming a peptide bond with a carboxyl group on free DOTAGA (Figure 3-24-B).[150] However, this method reduces the complexing constant of grafted free DOTAGAs and makes their metal complexes less stable, especially for *in vivo* and clinical applications. Moreover, the current generation of AGuIX developed in the lab contains very little amount of free DOTAGA (1 – 3 % compared to total DOTAGA) to increase the loading ratio of Gd. Therefore, it is necessary to develop a new strategy to introduce QA on AGuIX for further experiments. In this study, the amine group of QA was converted to carboxyl group and activated by NHS. This work was carried out by the team of Prof. Chezal J-M. This NHS ester of QA was simply mixed with AGuIX to react with amine groups present on the particles (Figure 3-24-A). The product was purified by tangential filtration and characterized by DLS, HPLC and UV spectroscopy.

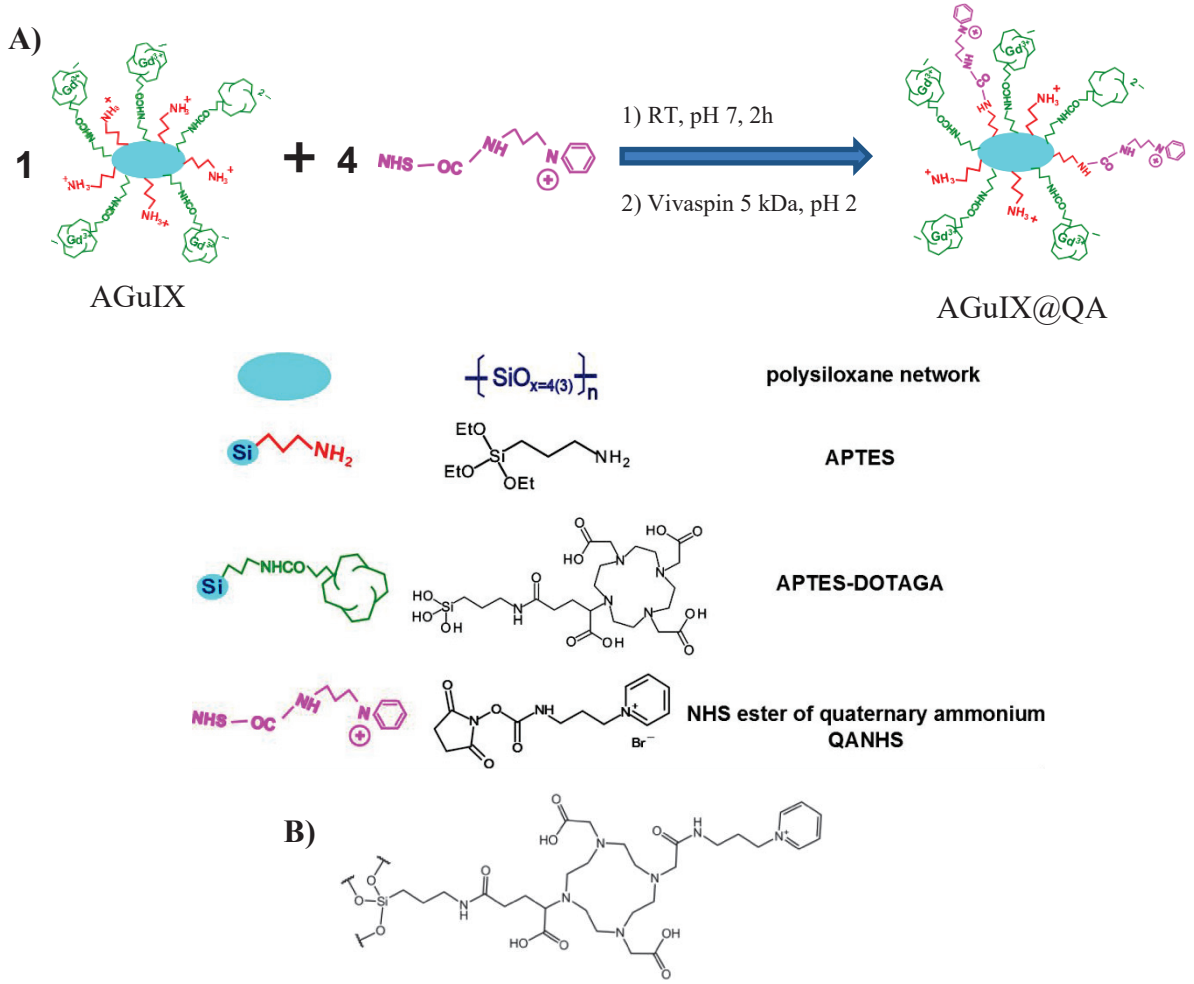

Figure 3-24. A) Functionalization protocol for QA on AGuIX; B) Position of grafted QA in previous studies.

Experimental protocol:

347 µmol in Gd of AGuIX was dispersed in water to have a solution of 200 mM [Gd^{3+}]. Solution was left at rt for 30 min to allow a complete dispersion of NPs. 52.2 mg of NHS ester of QA (QA-NHS) (molar ratio Gd : QA = 10 : 4) was dissolved in 500 µl of water and transferred drop by drop to AGuIX solution under stirring. The container of QA-NHS was rinsed 2 times with 250 µl of water. Water was filled to obtain final concentrations of AGuIX and QA-NHS as 100 mM (in Gd) and 40 mM respectively. pH of the solution was maintained in the range of 7.0 – 7.4 by constantly adding NaOH 1M solution. The solution was stirred for 2h at RT. At the end of the reaction, the solution was purified by tangential filtration through Vivaspin (MWCO = 5 kDa). pH of the solution was adjusted to 2 by adding HCl solutions before the purification. The solution was purified for 1000 purification factor, using HCl 10^{-2} M as washing solvent. At the end, pH of the final product was adjusted to 7. Then, the solution was filtered through 0.2 µm membrane to remove the large impurities. Finally, the solution was freeze dried for long term storage.

3.3.3. Characterization of the functionalized particle

The characterization results are summarized in Table 3-4. Hydrodynamic diameter (D_H) of functionalized particles (AGuIX@QA) only slightly increases to around 3.9 nm compared to 3.4 nm of the initial particles (Figure 3-25-A). This was confirmed by a minor increase in retention time in HPLC chromatogram i.e. 14.0 min (AGuIX@QA) vs. 13.6 min (AGuIX)

(Figure 3-26). The zeta potential curves of AGuIX and AGuIX@QA are presented in Figure 3-25-B. The isoelectric point of AGuIX@QA is very similar to the non-functionalized AGuIX (around 8.5) indicating very similar proportions between positively charged groups i.e. primary amine, pyridinium and negatively charged groups i.e. DOTAGA(Gd) chelates of functionalized and non-functionalized particles. This is reasonable since the reaction only converted a positive amine into another positive pyridinium. The differences in the absolute values of potentials between two particles might be due to different numbers of particles in solutions. The measured samples were prepared at the same molar concentration (10 mM in Gd) but the content of Gd in functionalized particles were lower than the one in non-functionalized particles and led to higher numbers of particles in AGuIX@QA sample. This made the ionic strengths in AGuIX@QA samples higher and slightly decreased the absolute values of zeta potentials. This phenomenon was reported before in literature for protein samples at different ionic strengths.[244,245]

Table 3-4. Characterization of AGuIX@QA in comparison with non-functionalized AGuIX

Features	Method(s)	AGuIX	AGuIX@QA
D_H (nm)	DLS	3.4 ± 0.8	3.9 ± 0.9
Zeta potential (mV)	Zeta potentiometry	+ 8.7 (pH 7.43)	+ 6.3 (pH 7.34)
Retention time, t_R (min)	HPLC (295 nm)	13.6	14.0
Purity (%)		85.1	97.8
r_1 ($mM^{-1}.s^{-1}$)	Relaxometry	14.3	19.2
r_2/r_1		1.36	1.37
Gd : QA	UV-vis spectroscopy	-	10 : 4.6
Content of Gd (µmol/mg)	ICP-OES	0.890	0.627
Yield in Gd (%)		-	35.1
Yield in QA (%)		-	40.7

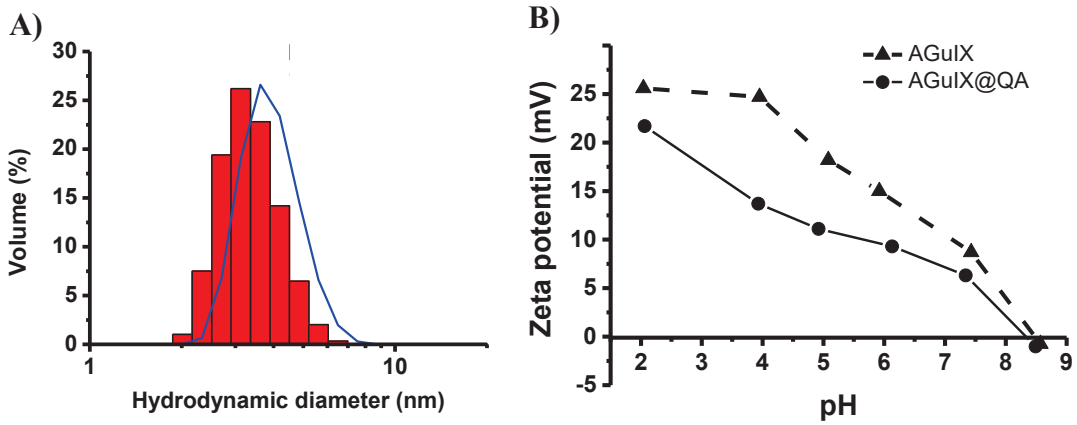

Figure 3-25. A) DLS diagram of AGuIX (red column) and AGuIX@QA (blue line); B) Zeta potential curves of non-functionalized AGuIX (dashed line, triangles) and functionalized AGuIX@QA (straight line, circles). All samples were measured at 10 mM in Gd.

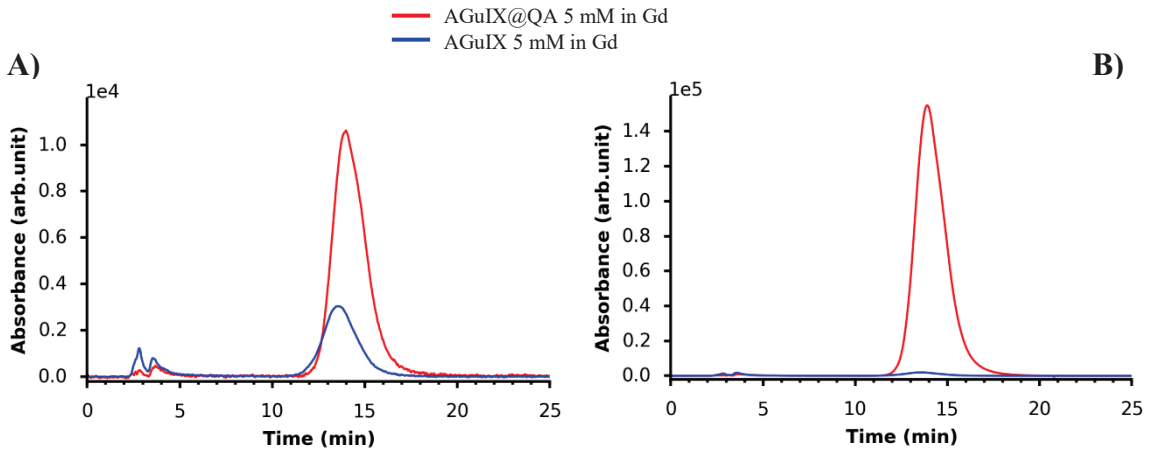

Figure 3-26. Chromatograms of AGuIX (blue) and AGuIX@QA (red) detected at A) 295 nm or B) 259 nm

Longitudinal relaxivity (r_1) increases from 14.3 to 19.2 $mM^{-1}.s^{-1}$ but r_2/r_1 remains similar. It might be because fragments and smaller, unstable particles have been washed out during the purification leaving behind whole intact, slightly bigger particles. Those results show that the functionalization took place without affecting significantly the ultrasmall size and magnetic property of the particle.

The presence of QA on the particle was proven and quantified by its strong UV absorption due to the $\pi - \pi^*$ transition of the pyridine which was reported previously.[150,246] Even though the structure has been changed, UV spectrum of QA remains very similar with a prominent peak at 259 nm (molar attenuation coefficient ε = 4000 $M^{-1}.cm^{-1}$). By subtracting the contribution from AGuIX (a peak at ~ 295 nm) and comparing with a reference solution of QA-NHS ester, the concentration of QA in AGuIX@QA solution can be determined (Figure 3-27).

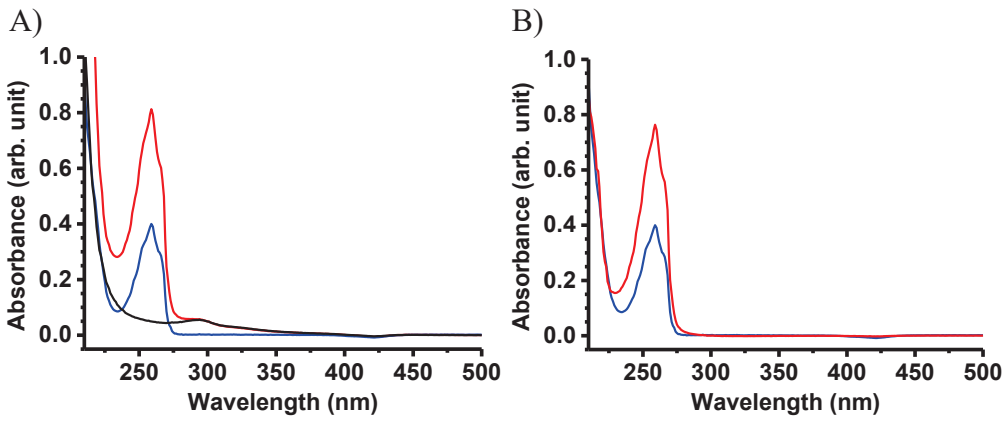

Figure 3-27. UV-vis spectra of AGuIX@QA solution after purified dilute 200 times (red), reference solution of QANHS at 0.1 mM (blue) and AGuIX solution at 0.87 mM in Gd (black): A) before the subtraction; B) after the subtraction.

Combining this result with the precise concentration of Gd determined by ICP-OES, the ratio Gd : QA can be calculated as 10 : 4.6. This is in accordance with the starting ratio in the formula and indicates a high yield of the reaction between QA-NHS and amine groups. The final ratio Gd : QA is even slightly higher than the starting ratio due probably to the fact that the purity of the starting particles was only 85%. The grafting of QA on the particles was also proven by the chromatograms of functionalized particles (Figure 3-26). At the same

concentration of Gd, the NP peak (t_R ~ 14.0 min) was much more intense after functionalized especially at 259 nm.

3.3.4. Biodistribution study by radiolabeling

3.3.4.1. Experimental protocols

Heterotopic tumors were induced on rats by inoculating SWARM chondrosarcoma cells.

AGuIX and AGuIX@QA were radiolabeld with ^{111}In (Figure 3-28-A). AGuIX or AGuIX@QA was dissolved in citrate buffer 50 mM, pH 5. Then the solution was mixed with $^{111}InCl_3$ (in the ratio Gd : ^{111}In ~ 1 µmol : 10 MBq) and incubated at 38 °C for 30 min. The radiochemical purities of the labeled particles were verified by Thin Layer Chromatography (TLC) (Figure 3-28-B). Free ^{111}In isotope was eluted by citrate buffer and migrated to the top of the silica layer, whereas the labeled particles remained at the introduced position. The amounts of free ^{111}In and grafted ^{111}In were measured by gamma counter. The radiochemical purity was determined as % of free ^{111}In/(free ^{111}In + grafted ^{111}In). In case the purity was lower than 95 %, free $^{111}In^{3+}$ would be removed by size exclusion chromatography (SEC) through a PD-10 Sephadex^{TM} column. Otherwise, labeled particles would be used directly without purification.

Radiolabeled particles were injected intratumorally (IT) or intravenously (IV) into tumor bearing rats. Each treated groups contained 20 to 24 rats. After a certain period of time (5 min – 20 or 30 min – 1 h – 2 h (– 4 h) – 24 h), 4 rats were sacrificed and their organs were collected, weighed and measured for radioactivity in a gamma counter. The results were corrected by radioactive decay of ^{111}In and expressed as the percentage of the total injected dose per organ (% ID/organ) and per gram of organ (% ID/g).

The radiolabeling experiment and biodistribution study after IT injection were conducted in Lyon by the team of Dr. Kryza D., Dr. Sidi-Boumedine J. and Prof. Janier M. while the ones for IV injection were carried out in Clermont-Ferrand by the team of Prof. Chezal J.M. and Dr. Miot-Noirault E.

3.3.4.2. Results

Regarding the radiolabeling procedure, the radiochemical purities of (purified) particles before being injected were ≥ 99 % (Figure 3-28-B).

Figure 3-29 and Figure 3-30 show the total radioactivity and radioactivity normalized by mass of different organs after certain periods of time post IT injection of AGuIX and AGuIX@QA. Figure 3-31-A-D shows zooms at the data for kidneys and tumors. From as early as 5 min after IT injection, both particles appeared to clear from the animals through kidneys and showed no or very low retention in other organs especially in liver and spleen. This was demonstrated by much higher radioactivities per gram in kidneys compared to other tissues (Figure 3-29 and Figure 3-30). More importantly, the functionalized particle seemed to retain longer in the tumor compared to the non-functionalized particle (Figure 3-31-C vs. Figure 3-31-A). After 1 h post-injection (pi), the radioactivity at the tumor treated with AGuIX@QA (~ 13 % ID/g) were still two times higher than the one treated with the original AGuIX (~ 5 % ID/g.

The full data after IV injection of AGuIX and AGuIX@QA are still under investigation. However, we have received some preliminary data especially for kidneys and tumors after injection of AGuIX@QA (Figure 3-31-E, F). The results were also interesting but less promising. The particles were still cleared mainly from kidneys and avoided the entrapment in liver and spleen. Starting from 4 h, particles seemed to be completely removed through urine (Figure 3-31-F). Nevertheless, only maximum less than 0.12 % of ID/g could penetrate and accumulate in the tumor 1 h pi (Figure 3-31-E). This poor result can be explained by the resistant physiology of chondrosarcoma tumor characterized by a dense ECM and high interstitial pressure.

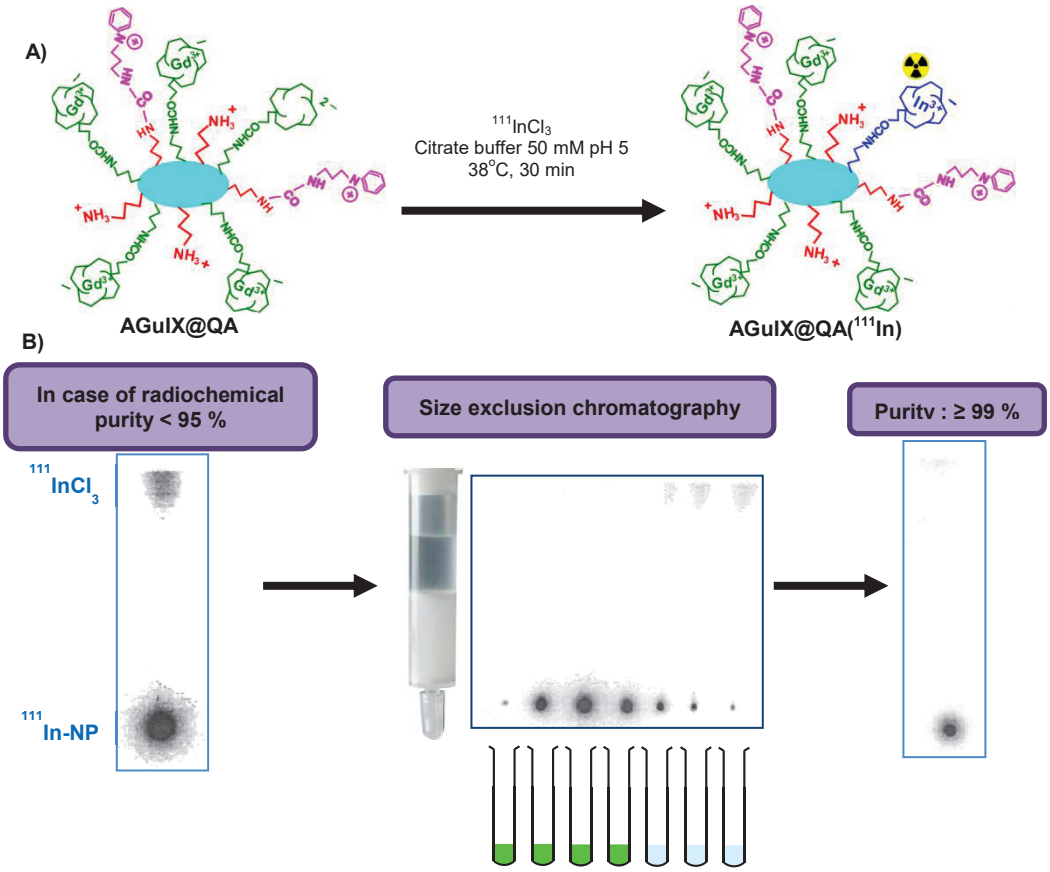

Figure 3-28. Scheme of radiolabeling procedure of AGuIX/AGuIX@QA with $^{111}InCl_3$:
A) Radiolabeling condition and B) Purification by SEC (scheme taken from Prof. Chezal JM).

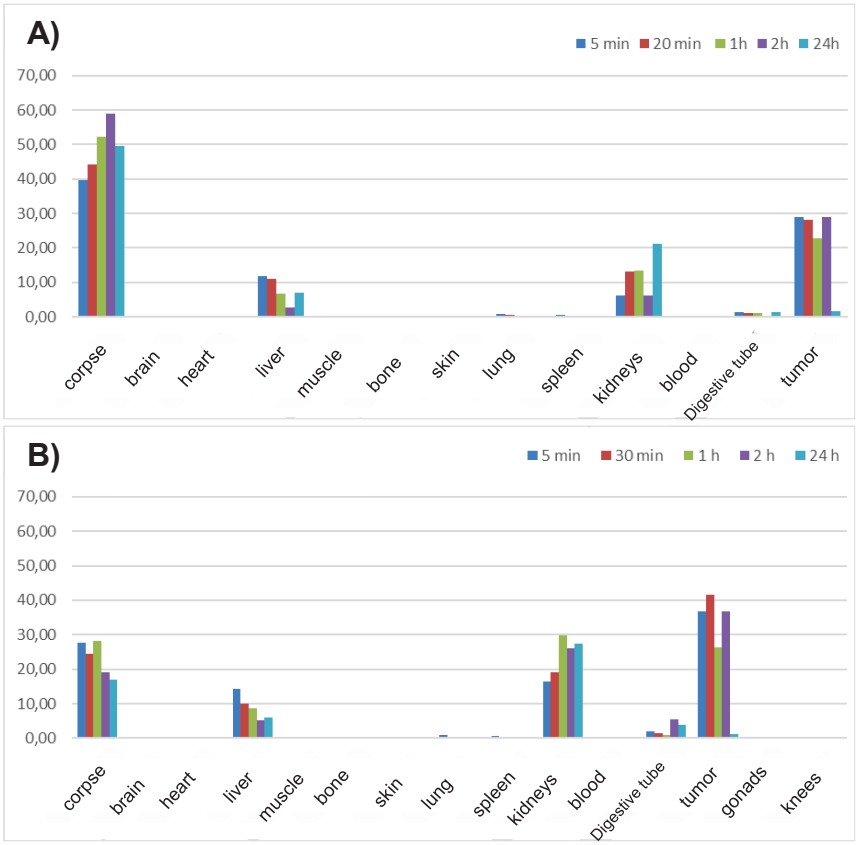

Figure 3-29. Global biodistribution data in mice **in %ID/organ** after IT injection of A) AGuIX and B) AGuIX@QA.

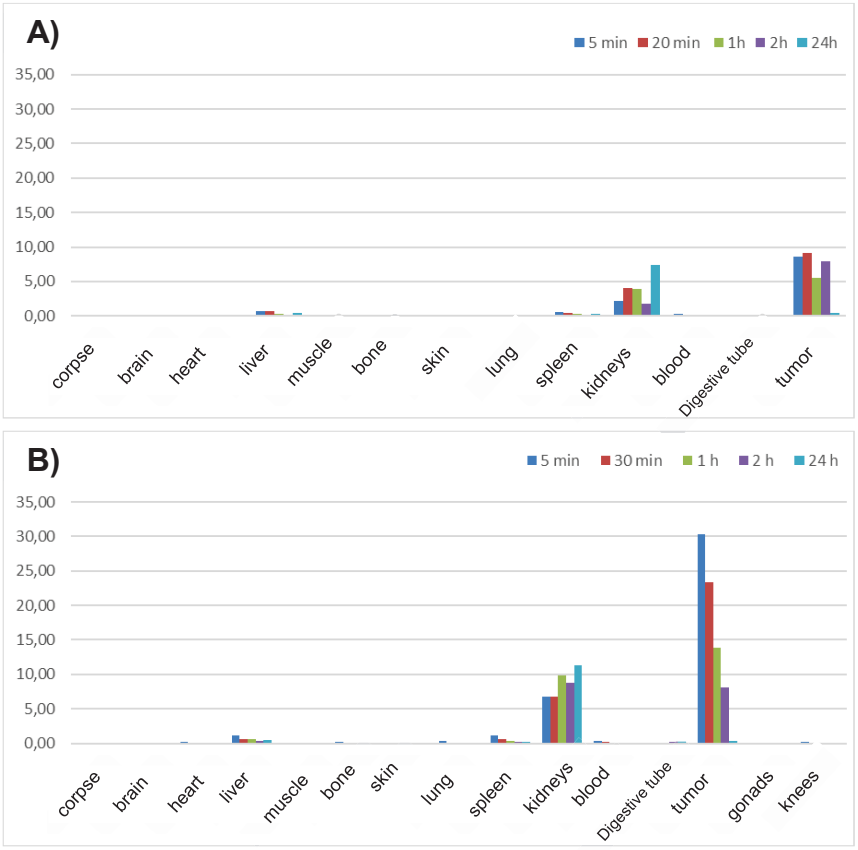

Figure 3-30. Global biodistribution data in mice in **%ID/g of organ** after IT injection of A) AGuIX and B) AGuIX@QA.

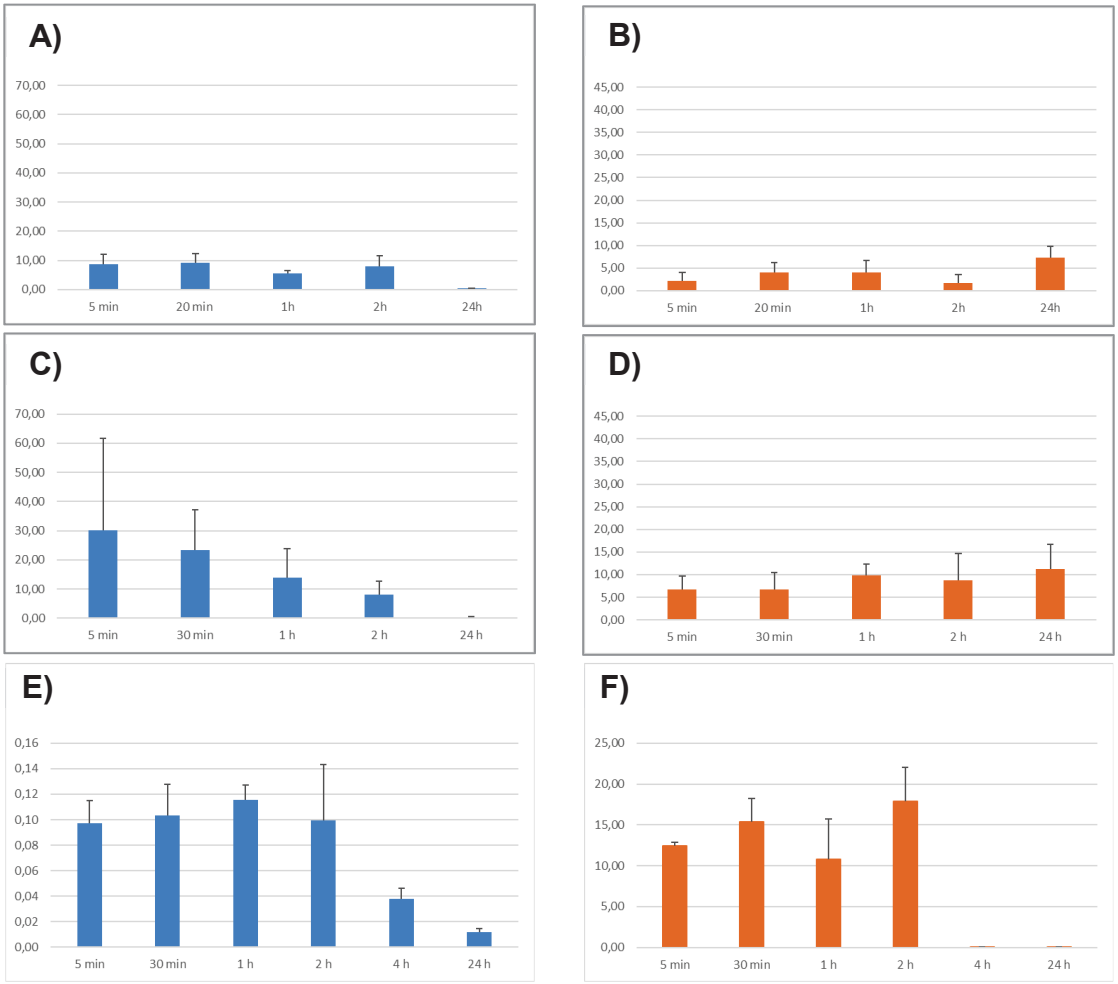

Figure 3-31. Closer look at biodistribution data in %ID/g of organ in tumors (blue columns) and kidneys (orange columns) after IT injection of A-B) AGuIX; C-D) AGuIX@QA and E-F) data after IV injection of AGuIX@QA.

3.3.5. Conclusion and perspectives

Quaternary pyridinium ligand has been successfully grafted on AGuIX using a straightforward strategy without compromising the favorable physical properties of the original particle i.e. ultrasmall size and nearly neutral surface charge. The functionalized particle has been thoroughly characterized to show the presence of pyridinium and quantify its amount in the sample. Biodistribution studies carried out with ^{111}In labeled AGuIX and AGuIX@QA have been conducted. After IT injection, both functionalized and non-functionalized particles seemed to show renal clearability. In addition, AGuIX@QA appeared to show longer retention in the tumor than the normal AGuIX. However, if being IV injected, it seems, functionalized particle still could not improve substantially the delivery of radioisotopes in the chondrosarcoma tumor which is notorious as a very challenging form of cancer. Besides biodistribution study, functionalized and non-functionalized particles are also being tested *in vitro* and *in vivo* to evaluate their radiosensitizing properties. The full dataset will be released in the coming months. A publication highlighting the achievements of this work will be submitted at the end of the project.

GENERAL CONCLUSION AND PERSPECTIVES

GENERAL CONCLUSION AND PERSPECTIVES

This thesis investigated the synthesis, characterization and functionalization of ultrasmall silica nanoparticles displaying chelators for complexation of different metals. These NPs can be used for detecting disease sites i.e. cancer tumors by complementary imaging techniques, delivering radiopharmaceuticals or enhancing locally the effect of radiotherapy.

In the first part, different analytical techniques have been used to further elucidate the peculiar structure and properties of precedent ultrasmall silica based NP, AGuIX, which was already developed in the lab. SAXS results confirmed the ultrasmall diameter of AGuIX which has radius of gyration around 1.4 nm and inferred average hydrodynamic diameter around 3 – 4 nm. NMR-DOSY studies performed on a diamagnetic yttrium equivalent of AGuIX proved the presence of expected organic groups i.e. DOTAGA and amines functionalized on the particle. The hydrodynamic diameter of the particle was estimated from the diffusion coefficients and gave ultrasmall value (4 – 5 nm). 2D $^{13}C/^{1}H$ NMR also provided unambiguous assignment of three proton peaks from aminosilanes which paved the way to an estimation of APTES-DOTAGA/APTES ratio (i.e ~ 1 – 1.5) from peaks integration. ESI-MS was performed in a highly adapted instrument for macromolecules to show a more complete m/z spectrum. Deconvolution algorithm was applied to give an estimation of mass distribution of the particle which was around 6 to 12 kDa. The equilibrium between functionalized silanes and free silanes during the degradation was studied using relaxometry, NMR-DOSY and HPLC. The results showed that the equilibrium directly depends on the concentration of silanes and pH of the solution.

In the second part, we have explored a new strategy to synthesize ultrasmall silica NPs from the molecular silane precursors. Using a commercialized chelating silane, we have shown the possibility of constructing such ultrasmall nanostructures by a simple one-pot bottom-up approach. The stability of USNP has also been demonstrated to depend on the structure of functionalized organosilanes. The carboxysilane (CEST) seems to give higher stability to the particle compared to aminosilane (APTES). This type of USNP has been thoroughly analyzed using different analytical methods to confirm its structure. Next, we have synthesized and characterized a non-commercially-available chelating silane, APTES-DOTAGA, to investigate the bottom-up synthesis of AGuIX-like USNP. The one-pot bottom-up synthesis has been successfully adapted to the new chelating silane to produce stable USNPs even in the presence of aminosilane. The bulkiness of APTES-DOTAGA seems to be the key parameter to provide a high stability to USNP. The difference between the configuration of complexed and non-complexed chelating silanes might also slightly affect the size of produced USNP. We have also succeeded to control the size of the particle from 3 to 14 nm by changing the ratio between TEOS, the polysiloxane network creating precursor, and the organosilanes i.e. APTES-DOTAGA and APTES. Last, we have modified the synthesis into a simple continuous process that would facilitate the scale-up synthesis in the future. Different analytical techniques have been used to confirm the structure of new USNPs. Besides proposing a novel simple synthesis of USNP, these studies also provided clearer understandings of nanochemistry behind polysiloxane structures. This type of NP has been shown to be a flexible platform to incorporate different metals at will. To illustrate the potential use of metal complexed USNP in biomedical applications, one of new Gd

complexed particles was injected in mice bearing colorectal tumors (CT26) and followed by MRI. It effectively showed sufficient retention in tumor tissues, no accumulation in liver and rapid clearance through kidney.

In the third part of this work, different functionalizations have been realized on AGuIX particle to provide additional functionalities. First, two types of chelating silanes (APTES-DOTAGA and APTES-NODAGA) have been synthesized and functionalized on AGuIX using a simple protocol without adding any other reactants. The NODAGA-functionalized AGuIX will be used for radiolabeling with ^{64}Cu for PET/MRI bimodal imaging application. Interestingly, silanes are more stable and easier to use compared to other conjugation reactants. Secondly, a new bimodal probe combining NODAGA and a tumor targeting NIR fluorophore (IR783 derivative) has been grafted on AGuIX. This new hybrid structure will be tested for its use as a trimodal imaging probe (MRI/PET/OI) probably in the field of intraoperative detection with the possibility of improving cancer cellular internationalization of AGuIX. Last but not least, a new strategy has been used to introduce quaternary pyridinium on current AGuIX. This functionalized NP is being tested for its ability to target chondrosarcoma tumors and improve efficacy of radiotherapy towards this resistant type of tumor. Preliminary biodistribution results showed that AGuIX@QA was also mainly eliminated through kidneys while avoiding being trapped in liver or spleen. Ammonium functionalized particle seemed to be retained longer in tumor after IT injection than normal AGuIX. Biodistribution results after IV injection and the radiosensitization effect of the functionalized particle are still under investigation.

For future perspectives, first of all, efforts should be made to investigate the scaling-up of this new one-pot protocol. Even though, the strategy is quite straightforward, every detail should be considered to successfully translate it to industrial scale. Regarding the nanostructure designing, a systematic study could be considered to correlate the size of USNPs, which determines the surface curvature and ligand density, with their hydrolytic stability to find out an optimal size of USNP. Similarly, a systematic comparison between the degradability of conventional top-down AGuIX and the one of bottom-up USNPs should be designed. Another possibility to tailor the degradability of USNP for the applications in which higher stability is required is to use long chain aminosilanes e.g. aminoundecyltriethoxysilane (AUTES) or N-(6-aminohexyl)aminomethyltriethoxysilane (AHAMTES) to replace APTES. In this way, the small size and low viscosity of the particle will not be compromised (compared to the use of PEG chains) and the particle can still avoid non-specific protein adsorption.

Since intermediate non-chelated USNPs can be produced by new synthesis protocol, different metallic compositions can be tested to provide different potential applications ranging from in vitro/in vivo imaging (MRI, radioimaging, luminescence) to therapeutics (radiopharmaceuticals, radiosensitizers). Novel physical properties could also be discovered by combining different elements in a nanosystem.

For further characterizing AGuIX, a more direct method based on either MALDI (matrix assisted laser desorption ionization) mass spectrometry, size exclusion chromatography or gel electrophoresis should be developed for AGuIX to verify the mass of particle obtained by ESI-MS which utilizes mathematical treatments. A new ICP-MS detector coupled with a HPLC system will soon arrive in our laboratory and analyzing methods will be developed.

This new detector will allow observing specifically the presence of different elements such as Gd, Si, C, N during the chromatographic elution of AGuIX particles. Signals from this detector can be correlated with signals from conventional UV detector to precisely identify and quantify different peaks in the chromatogram.

In terms of particle functionalization, silane chemistry can be further exploited to develop facile functionalization strategy for AGuIX. Different ligands can be silanized for long-term preservation. In particular, targeting and therapeutic peptides or other ligands containing amine groups can be synthesized by conventional solid-phase method and silanized later on for functionalizing AGuIX. In this way, harsh deprotection strategy would not be required to be performed in the presence of the particle and exclude the possibility of compromising nanostructure of AGuIX.

ANNEXES

ANNEXES

A1. Principle of NMR

NMR shares fundamental principle with MRI. Figure A1-A shows the setup of a classical NMR spectrometer. The sample tube was put in the center of an electric magnet with a magnetic field B_o. The magnetic field can be adjusted by a sweep generator. Another essential component is a coil surrounding the sample holder that transmits the radio frequency generated to excite the sample. The magnetic signal generated from the sample will be measured by a receiver and transferred to a computer to generate the spectrum. Figure A1-B shows the principle of excitation and relaxation in NMR which is essential for signal generation. Simplistically, when the sample was put in the magnet, the spins of all atoms in the sample will be aligned parallel or antiparallel to vector B_o. The sum will be a vector M_o which always heads to the direction of B_o. It should be mentioned that the summed spin vector is not totally parallel to B_o but make a slight precessional motion around the B_o direction with a certain frequency depending on the type of nucleus (e.g. ^{1}H, ^{13}C). This frequency is called Larmor frequency. Each nucleus of a certain type in a molecule will have a slight shift of Larmor frequency compared to the general value depending on their surrounding chemical environments. To excite a certain nucleus in the sample, a short radio frequency pulse will be sent through the coil. This pulse contains a wide range of frequencies that cover the whole range of Larmor frequencies of the targeted nucleus type. If one frequency in the pulse corresponds exactly to a Larmor frequency of a nucleus, it will excite that nucleus to give the signal for that specific nucleus. It flips its magnetization vector out of z-axis to a certain angle depending on the strength and duration of the sent radio frequency pulse. In a typical example, let us say the pulse is 90^0 which means the magnetization will be flipped to align with y-axis (M_{rf}). This vector will relax to normal state (M_0) by making a spiral movement around z-axis. If we introduce a rotating coordinate system (x', y', z) spinning around z-axis with the same speed as the rotating speed of the magnetization vector (Larmor frequency), we will only have a normal exponential decay of M_{rf}. The signal decays in y-axis and z-axis are described by two similar but different exponential equations (Equation A 1). In these equations, T_1 is called longitudinal relaxation time and T_2 is called transverse relaxation time. These parameters are similar to what we mentioned in MRI. Back to NMR experiment, as we can see in Figure A1-C, the decay along y-axis creates a sinusoidal-exponential signal dependent on time which is called free induction decay (FID). By applying Fourier's transform on this spectrum (Equation A 2), the computer will release a spectrum which is only dependent on frequency. Before the experiment, a standard molecule will be analyzed to establish a zero-point frequency. Then signals from the sample will be normalized relatively to this frequency to give what we usually see on x-axis of a modern NMR spectrum: chemical shift in ppm unit.[184]

$$M_{y'(t)} = M_{y'(0)} exp^{(-t/T_2)} \; ; \; M_{z'(t)} = M_{z'(0)}(1 - exp^{\left(-\frac{t}{T_1}\right)}) \qquad \textbf{Equation A 1}$$

$$F(\omega_0) = \int f(t) e^{-i\omega t} dt \qquad \textbf{Equation A 2}$$

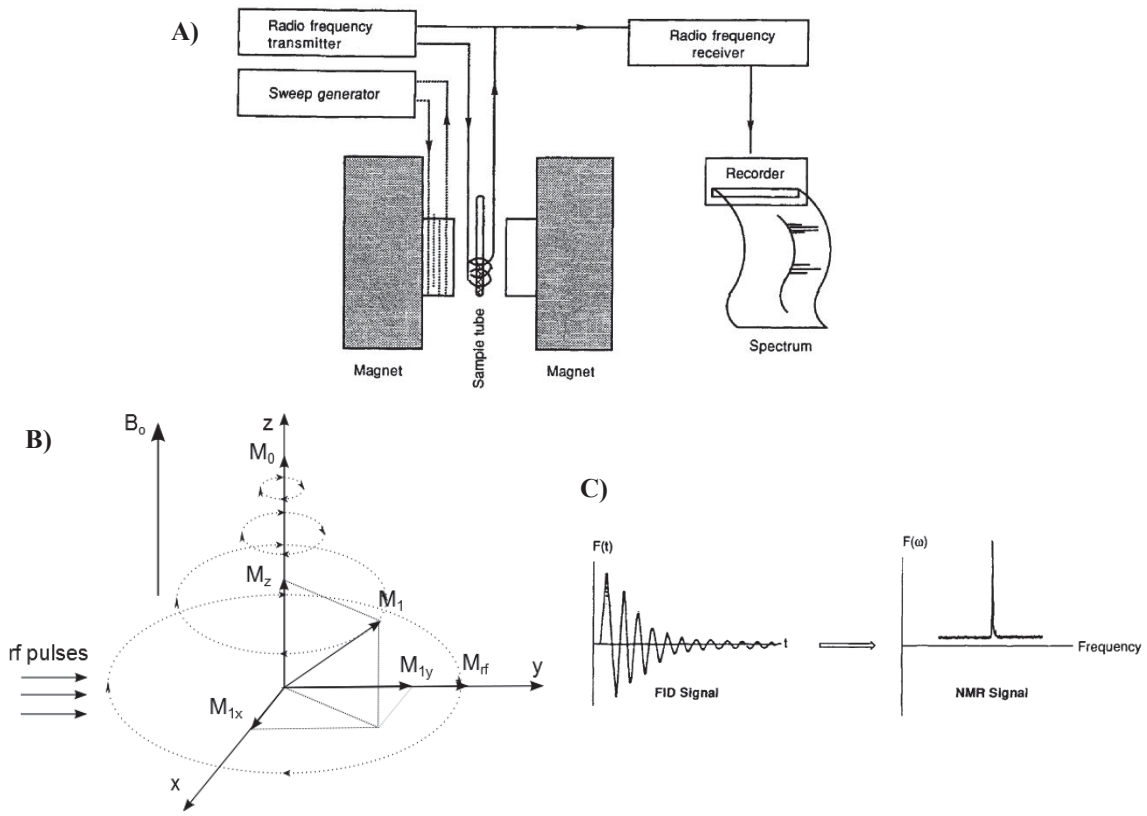

Figure A1. Basic principle of NMR. A) Schematic diagram of a NMR spectrometer; B) Diagram of relaxation process; C) Fourier's transformation from a FID time dependent spectrum to a chemical shift frequency dependent spectrum. Images A and C taken from ref [184].

A2. Schematic diagram of micrOTOF-Q-II

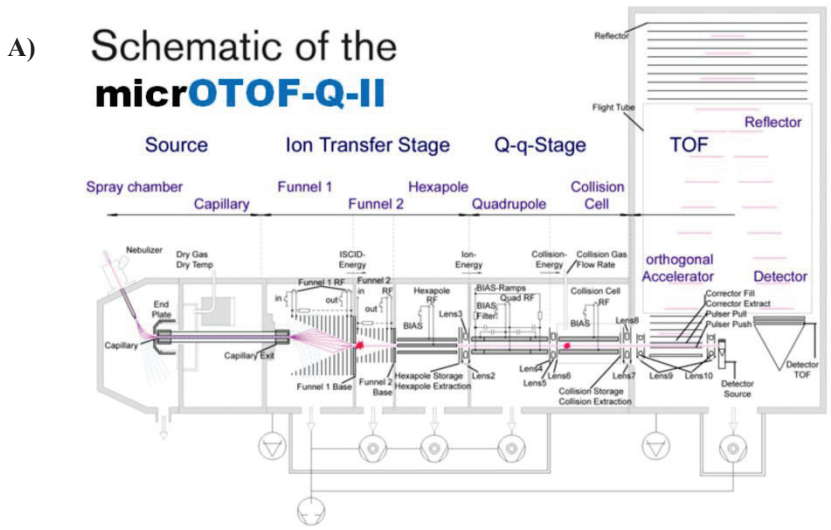

Figure A2. Schematic diagram of micrOTOF-Q II

A3. USNPPt(IV): a new nanocarrier for Pt(IV) anticancer agents

A3.1. Introduction

One spin-off idea came out from the development of one-pot synthesis of USNP was to apply the same protocol for other existing organosilanes. This new structure can also be used as a nanocarrier for small anticancer agents. Among different cytotoxic drugs used in the clinics, Pt complexes were widely used as potent treatments for many types of cancers. Their working mechanism is well studied. Pt complexes normally consist of Pt(II) coordinated by 2 amine groups which are stable during the process and 2 others "leaving groups" that will be hydrolyzed before binding to N7 atoms of purine residues in DNA to form cross-links inside or between DNA molecules. These cross-links distort permanently the structure of DNAs and lead to cell death (Figure A3-B).[247] However, Pt complexes like other classical non-specific cytotoxic agents usually come along with several serious side effects. For example, cisplatin causes nephrotoxicity, nausea, neurotoxicity and ototoxicity, while carboplatin causes myelosuppression and nausea with lower nephrotoxicity and ototoxicity.[248] Many synthetic strategies have been applied to improve the activity and toxicology of platinum complexes. The main modifications that are currently being pursued are 1) to modify the leaving ligands with slower leaving kinetics such as dicarboxylato groups and/or 2) convert Pt(II) into Pt(IV) and modify the axial groups by different structures. The latter creates another barrier to delay the cytotoxic activity of the complexes: Pt(IV) needs to be reduced to Pt(II) before the latter can take action. This process can only be done intracellularly by endogenous reducing agents like ascorbic acid, glutathione or cysteine (Figure A3-B).[247,249] The rate of reduction depends on the nature of the axial groups. Recently, Pichler V. et al. reported that the most simple dihydroxo Pt(IV) has the longest reduction half-life (> 15h).[250] In fact, at least two other research groups have used polysiloxane structures to conjugate Pt(IV) complexes. However, the size of their particles were > 40 nm and the conjugate strategies were quite complicated.[251,252] Hence, the idea of this part is to introduce a simple one-pot protocol to create USNPs that can be complexed covalently with Pt(IV). Thanks to the favorable biodistribution of ultrasmall particles, Pt(IV) will be delivered specifically to the tumors and eliminated through urine without staying long in other organs. Due to the kinetic inertness of Pt(IV) and the covalent links between them and the particles, only the ones that remain in the tumor during a certain time after the injection will be activated inside the cancer cells. This will increase the specificity of the treatment and limit the side effects.

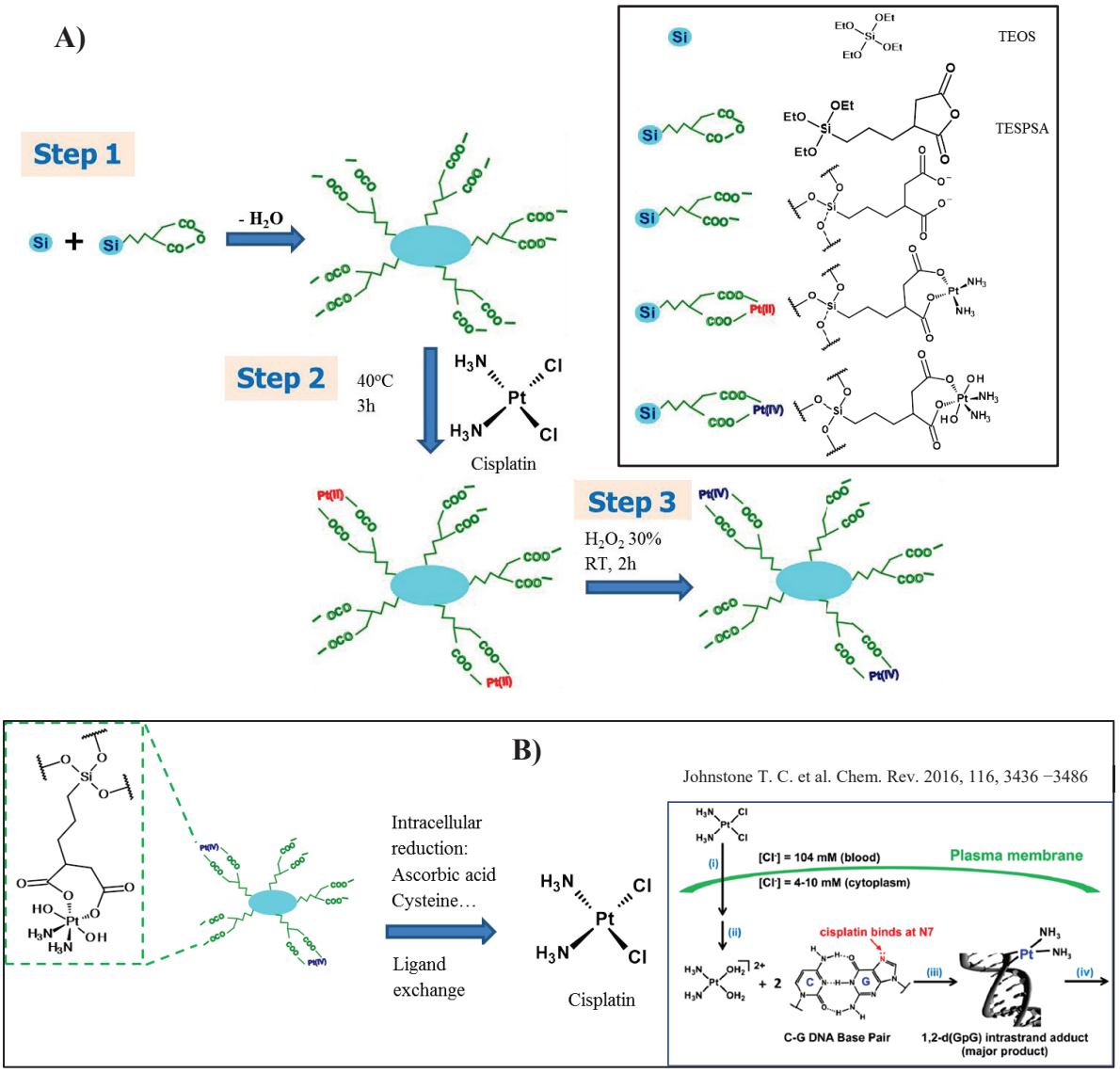

Figure A3. Schematic representation of A) The strategy for the synthesis of USNPPt(IV) and B) The expected working mechanism[247]

A3.2. Synthesis strategy

The synthesis were described schematically in Figure A3-A. Since amine groups can form very strong bonds with Pt and inactivate it, carboxyl groups were preferred to graft Pt on USNPs. Therefore, APTES were dropped out from the formula and replaced by a dicarboxylate silane, (3-triethoxysilyl)propylsuccinic anhydride (TESPSA, abcr GmbH, Germany). A similar one-pot protocol was applied to synthesize USNP. Then, cisplatin was added to react with dicarboxylate functions.[253,254] Afterwards, hydrogen peroxide was added to oxidize Pt(II) into Pt(IV).[255] Unexpectedly, the viscosity of the new particles was quite high and made the concentration step by the tangential filtration too slow. Therefore, the product was lyophilized instead to remove the most part of water (90%). Then, the particles was purified by tangential filtration in NaCl 1 M to remove physically adsorbed cisplatin and re-purified in water to remove the excess of NaCl.

A3.3. Experimental protocol

To 60 ml of water were added 410 µl (1.8 mmol) of TEOS and 540 µl (1.8 mmol) of TESPSA so that the total concentration of silane stayed at 60 mM. The solution was stirred and heated

at 40°C overnight to hydrolyze the silanes and form the particles. Then, 180 mg of cisplatin (cis-diamineplatinum(II) dichloride, Sigma-Aldrich, France) was poured directly to the solution. The solution was kept stirring at 40°C for 3h until a clear yellow solution was obtained. The solution was cooled down to room temperature before 3 ml of hydrogen peroxide was added. The solution was kept stirring for 2h and appeared as a pale blue solution. Solution was lyophilized 2 days until ~ 6 ml remained. This solution was purified by tangential filtration with NaCl 1M as washing solvent for 100 purification factor and re-purified with water for another 100 purification factor.

A3.4. Characterization of USNPPt(IV)

Due to limited amount of time, only some preliminary characterizations have been conducted. The results were summarized in Table A1.

Table A1. Characterization of USNPPt(IV)

Properties	Method(s)	USNPPt(IV)
D_H before lyophilized (nm)	DLS	3.2 ± 1.0
D_H after lyophilized (nm)	DLS	3.8 ± 1.2
Retention time (min)	HPLC (305 nm)	15.9
	HPLC (255 nm)	15.9
FWHM (min)	HPLC (305 nm)	2.425
	HPLC (255 nm)	2.425
Purity (%)	HPLC (305 nm)	94.5
	HPLC (255 nm)	96.4
Presence of Pt(IV)	OPDA colorimetry	Peak at 428 nm
Pt content (µmol/g)	OPDA colorimetry	9.80

DLS results show a D_H around 3.8 nm of particles after lyophilized which demonstrates that USNP was created and maintained during the process. Chromatograms show a quite symmetrical peak around 15.9 min that can be assigned to the USNP accompanied by a small peak at the beginning (< 5%) that can be assigned to free silanes coexisting in an equilibrium with the particles. The chromatograms were recorded at 305 nm as specific absorption region of Pt(IV)[256] and 255 nm as UV cutoff of acetonitrile (Figure A4-A, B).

The content of Pt in USNP can be determined by colorimetry. Pt(II) and Pt(IV) can react with OPDA (o-phenylenediamine) to give a complex that absorb strongly at around 706 nm. By simply establishing a calibration curve at 706 nm of a series of cisplatin samples with increasing concentrations, the amount of Pt complexes in a solution can be determined.[257,258] According to this method, the content of Pt in USNPPt(IV) was 9.8 µmol/g. Moreover, when Pt(IV) is present in the solution, it will be reduced first by OPDA before being complexed. The appearance of a peak at 428 nm in USNPPt(IV) sample signified the presence of oxidized product of OPDA which implies the presence of Pt(IV) in the solution (Figure A4-C, D).[257]

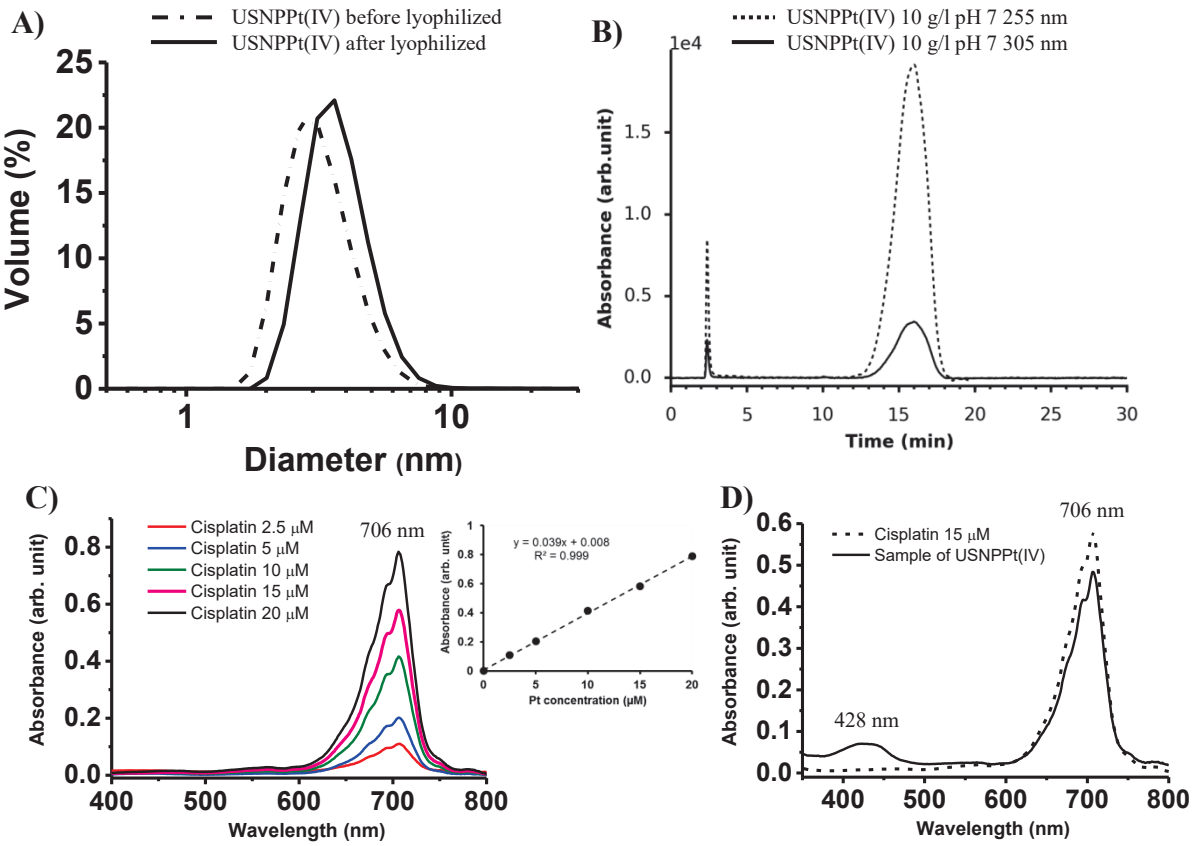

Figure A4. Characterization of USNPPt(IV): A) DLS diagrams of particle before lyophilized (dash-dotted line) and after lyophilized (solid line); B) Chromatograms of particle after lyophilized at 255 nm (dotted line) and 305 nm (solid line); C) Absorption spectra of calibrating samples of cisplatin at different concentration after complexed with OPDA, inset: calibration curve and equation; D) Absorption spectra of diluted USNPPt(IV) sample after complexed with OPDA (solid line), calibrating sample at 15 μM cisplatin was added for comparison (dashed line).

A3.5. Conclusion

This small experiment demonstrates the possibility of using different types of silanes apart from chelating ones in the one-pot synthesis to create ultrasmall particles. However, there are still several things to be done such as to improve the loading ratio, the yield in Pt and to test the release profile under normal and reducing conditions. Moreover, eventually, aminosilanes should be introduced somehow to the surface of the particle to neutralize the surface zeta potential and prevent proteins adsorption on the particles before this particle can be used for any biological experiments.

A4. Assignment of infra-red spectra of DOTAGA and APTES-DOTAGA

Table A2. Assignment of the main peaks in infra-red spectra of DOTAGA and APTES-DOTAGA

Wave number (cm^{-1})	Assignment
3385.3	Si-OH stretching or primary amine N-H stretching
3238.7	Si-OH stretching or secondary amide N-H stretching or carboxylic O-H stretching
3079.2	Secondary amide II overtone or carboxylic O-H stretching
2932.6	Methylene asymmetric C-H stretching
2885.2	Methylene symmetric C-H stretching
1712.7	Carboxylic acid C=O stretching
1677.0	Secondary amide C=O stretching
1622.2	Amine NH_2 scissoring, N-H bending
1385.1	Carboxylic acid C-O-H in-plane bending
1221.3	Carboxylic acid C-O stretching or Aliphatic C-N stretching
1122.1	Si-O-Si asymmetric stretching or Aliphatic C-N stretching
1087.6	Si-O-C stretching

A5. Behaviors of USNP in human serum (supplementary information)

A5.1. Characterization of the second batch of USNP@DOTA$_{IS}$-5-Gd

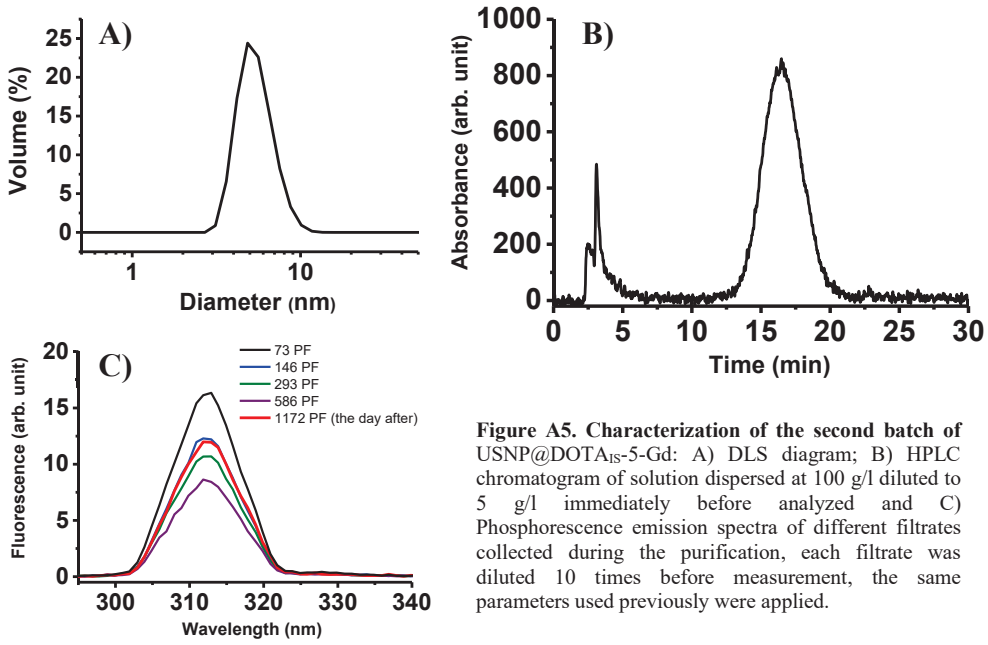

Figure A5. Characterization of the second batch of USNP@DOTA$_{IS}$-5-Gd: A) DLS diagram; B) HPLC chromatogram of solution dispersed at 100 g/l diluted to 5 g/l immediately before analyzed and C) Phosphorescence emission spectra of different filtrates collected during the purification, each filtrate was diluted 10 times before measurement, the same parameters used previously were applied.

A5.2. Relaxation velocities of concentrated sample and kinetics measurement of diluted sample of USNP@DOTA$_{IS}$-5-Gd in human serum normalized by the volume of solution

Table A3. Longitudinal (r_1*) and transverse (r_2*) relaxation velocities normalized by the amount of Gd in NP and the volume of solution of the second batch of USNP@DOTA$_{IS}$-5-Gd in human serum (94 g/L or 56.3 mM) (37°C, 60 MHz).

r_1* ((mM^{-1}.s^{-1})	r_2*/r_1*
21.4	1.68
21.2	1.68

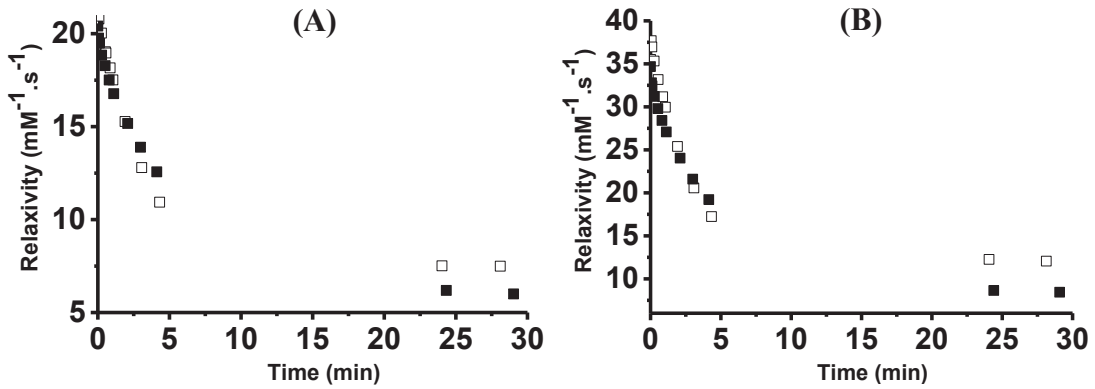

Figure A6. Kinetics of degradation measured by relaxometry of the second batch of USNP@DOTA$_{IS}$-5-Gd in water (solid symbols) and in human serum (open symbols) at 1 g/L (or 0.6 mM) (37°C, 60 MHz): A) longitudinal and B) transverse relaxation velocities. The results were normalized with mmol of Gd in NP in the samples and the volume of solutions.

A6. Publications

A6.1. Receipt of submission for Patent 1: Method for synthesizing silica nanoparticles EP17305701

Europäisches Patentamt | European Patent Office | Office européen des brevets

Acknowledgement of receipt

We hereby acknowledge receipt of your request for grant of a European patent as follows:

Submission number	1000407984	
Application number	EP17305701.9	
File No. to be used for priority declarations	EP17305701	
Date of receipt	09 June 2017	
Your reference	BEP170263EP	
Applicant	NH THERAGUIX	
Country	FR	
Title	METHOD FOR SYNTHESIZING SILICA NANOPARTICLES	
Documents submitted	package-data.xml	ep-request.xml
	application-body.xml	ep-request.pdf (5 p.)
	SPECEPO-1.pdf\2017.06.09 - BEP170263 EP - texte depot.pdf (54 p.)	f1002-1.pdf (2 p.)
Submitted by	EMAIL=bourgarel@plass.com,CN=Denis BOURGAREL,O=CABINET PLASSERAUD,C=FR	
Method of submission	Online	
Date and time receipt generated	09 June 2017, 17:51:03 (CEST)	
Official Digest of Submission	C6:6F:C1:EE:50:E7:BF:FA:7A:23:A3:92:42:A7:CB:55:62:EE:F6:19	

/INPI, section dépôt/

Form 1002 - 1: Public inventor(s)

Designation of inventor

User reference: BEP170263EP
Application No:

Public

	Inventor	
	Name:	LUX, Mr. François
	Address:	272 cours Lafayette 69003 Lyon France
	The applicant has acquired the right to the European patent:	As employer
	Inventor	
	Name:	TILLEMENT, Mr. Olivier
	Address:	305 rue des fours 69270 Fontaines Saint Martin France
	The applicant has acquired the right to the European patent:	As employer
	Inventor	
	Name:	ROSSETI, Mr. Fabien
	Address:	33 rue de la Filature 69100 Villeurbanne France
	The applicant has acquired the right to the European patent:	As employer
	Inventor	
	Name:	TRAN, Mr. Vu-Long
	Address:	91/19 Chuong Duong, Linh Chieu, Thu Duc Ho Chi Minh Viet Nam
	The applicant has acquired the right to the European patent:	As employer
	Inventor	
	Name:	THAKARE, Mr. Vivek
	Address:	Flat A-406, Sai Galaxy Apartments, Vanavaibhav, Indiranagar 422009 Nasik, Maharashtra India
	The applicant has acquired the right to the European patent:	As employer

Signature(s)

User reference: BEP170263EP
Application No:

Place:	**Lyon**
Date:	**09 June 2017**
Signed by:	**FR, CABINET PLASSERAUD, Denis BOURGAREL**
Association:	**CABINET PLASSERAUD**
Representative name:	**Denis BOURGAREL**
Capacity:	**(Representative)**

A6.2. Receipt of submission for Patent 2: Nanovecteurs et utilisations FR1759607

R E P U B L I Q U E F R A N C A I S E

INSTITUT NATIONAL DE LA PROPRIÉTÉ INDUSTRIELLE

BREVET D'INVENTION
CERTIFICAT D'UTILITE

Réception électronique de la soumission

Il est certifié par la présente qu'une demande de brevet (ou d'un certificat d'utilité) a été reçue par le biais du dépôt électronique sécurisé de l'INPI. Après réception, un numéro d'enregistrement et une date de réception ont été automatiquement attribués.

Numéro de demande	1759607	
Numéro de soumission	1000426736	
Date de réception	13 octobre 2017	
Vos références	BFF170323	
Demandeur	NH THERAGUIX	
Pays	FR	
Titre de l'invention	NANOVECTEURS ET UTILISATIONS	
Documents envoyés	package-data.xml	requetefr.xml
	application-body.xml	fr-fee-sheet.xml
	requetefr.pdf (3 p.)	validation-log.xml
	comment.pdf (2 p.)	indication-bio-deposit.xml
	design.pdf (2 p.)	fr-office-specific-info.xml
	textebrevet.pdf (45 p.)	dessins.pdf (10 p.)
	redtax-1.pdf (1 p.)	
Déposé par	EMAIL=bourgarel@plass.com,CN=Denis BOURGAREL,O=CABINET PLASSERAUD,C=FR	
Méthode de dépôt	Dépôt électronique	
Date et heure de réception électronique	13 octobre 2017, 14:00:13 (CEST)	
Empreinte officielle du dépôt	52:60:92:77:28:CF:08:9F:A5:A6:EA:20:B7:74:36:D3:9C:B5:0D:3A	

/INPI, section dépôt/

INPI - 15 RUE DES MINIMES - CS 50001 - 92677 COURBEVOIE CEDEX - TELEPHONE : 0820 210 211 (service 0,10 €/min + prix appel) - TELECOPIE : +33 (0)1 56 65 86 00
ETABLISSEMENT PUBLIC NATIONAL CREE PAR LA LOI No 51-444 DU 19 AVRIL 1951

INSTITUT NATIONAL DE LA PROPRIÉTÉ INDUSTRIELLE

15 rue des Minimes - CS 50001 - 92677 Courbevoie Cedex
INPI Direct : 0820 210 211 (Service 0,10 €/min + prix appel)
Pour déposer par télécopie : 33 (0)1 56 65 86 00

BREVET D'INVENTION

Code de la propriété intellectuelle - Livre VI

cerfa

DÉSIGNATION D'INVENTEUR(S)

Vos références pour ce dossier	BFF170323
N° D'ENREGISTREMENT NATIONAL	
TITRE DE L'INVENTION	
Titre	NANOVECTEURS ET UTILISATIONS
LE(S) DEMANDEUR(S)	NH THERAGUIX, UNIVERSITE CLAUDE BERNARD LYON 1, CENTRE NATIONAL DE LA RECHERCHE SCIENTIFIQUE - CNRS -
DÉSIGNE(NT) EN TANT QU'INVENTEUR(S)	
INVENTEUR 1	
Nom	TILLEMENT
Prénom	Olivier
Rue	305 rue des Fours
Code postal et ville	69270 FONTAINES SAINT-MARTIN
Pays	FR
INVENTEUR 2	
Nom	LUX
Prénom	François
Rue	272 cours Lafayette
Code postal et ville	69003 LYON
Pays	FR
INVENTEUR 3	
Nom	ROSSETTI
Prénom	Fabien
Rue	33 rue de la Filature
Code postal et ville	69100 VILLEURBANNE
Pays	FR
INVENTEUR 4	
Nom	TRAN
Prénom	Vu-Long

Rue	91/19 Chuong Duong, Linh Chieu, Thu Duc
Code postal et ville	Ho Chi Minh
Pays	VN
INVENTEUR 5	
Nom	MATHIEU
Prénom	Clélia
Rue	6 rue des Blagis
Code postal et ville	92340 BOURG-LA-REINE
Pays	FR
INVENTEUR 6	
Nom	DAHAN
Prénom	Myleva
Rue	17 rue de la Part Dieu
Code postal et ville	69003 LYON
Pays	FR
DATE ET SIGNATURE	
Signé numériquement par	Subject: FR, CABINET PLASSERAUD, Denis BOURGAREL; Issuer: FR, INPI, INPI-EN-LIGNE 1.1
Date	13 October 2017
Signataire	Mandataire

Conformément aux dispositions de la loi n° 78-17 du 6.01.1978 modifiée relative à l'informatique, aux fichiers et aux libertés, vous bénéficiez d'un droit d'accès et de rectification pour les données vous concernant auprès de l'INPI. Les données à caractère personnel que vous êtes tenu(e) de nous fournir dans ce formulaire sont exclusivement utilisées pour identifier le titulaire de la demande et son éventuel mandataire.

A6.3. Co-authored paper: Gadolinium-based Nanoparticles and Radiation Therapy for Multiple Brain Melanoma Metastases: Proof of concept before Phase I Trial. Theranostics, 2016, 6 (3), 418 – 427.

IVYSPRING INTERNATIONAL PUBLISHER

Theranostics

2016; 6(3): 418-427. doi: 10.7150/thno.14018

Research Paper

Gadolinium-Based Nanoparticles and Radiation Therapy for Multiple Brain Melanoma Metastases: Proof of Concept before Phase I Trial

Shady Kotb[1], Alexandre Detappe[1,2,3], François Lux[1], Florence Appaix[4], Emmanuel L. Barbier[4,5], Vu-Long Tran[1], Marie Plissonneau[1,3], Hélène Gehan[1,3], Florence Lefranc[6], Claire Rodriguez-Lafrasse[7], Camille Verry[8], Ross Berbeco[2], Olivier Tillement[1], Lucie Sancey[1]✉

1. Institut Lumière Matière, UMR5306, Université Claude Bernard Lyon1-CNRS, Université de Lyon 69622 Villeurbanne Cedex, France
2. Department of Radiation Oncology, Brigham and Women's Hospital, Dana-Farber Cancer Institute and Harvard Medical School, Boston, MA, United States
3. Nano-H, St Quentin Fallavier, 38070, France
4. Grenoble Institut des Neurosciences (GIN), INSERM U836, Grenoble, 38706, France
5. Université Grenoble Alpes, Grenoble, France
6. Service de Neurochirurgie, Hôpital Erasme, Université Libre de Bruxelles, 808 Route de Lennik, 1070 Brussels, Belgium
7. Laboratoire de Radiobiologie Cellulaire et Moléculaire, EMR3738, Faculté de Médecine Lyon-Sud, Université de Lyon, Université Lyon 1, Oullins, France
8. Radiotherapy Department, Grenoble University Hospital, 38043 Grenoble.

✉ Corresponding author: Lucie Sancey PhD. Institut Lumière Matière, Equipe FENNEC - UMR CNRS 5306 - Univ. Lyon 1, Bâtiment Jules Raulin, 2, rue V. Grignard, 69622 Villeurbanne Cedex FRANCE. E-mail: lucie.sancey@univ-lyon1.fr. Phone: +33 4.27.46.57.24

Received: 2015.10.01; Accepted: 2015.12.12; Published: 2016.01.20

Abstract

Nanoparticles containing high-Z elements are known to boost the efficacy of radiation therapy. Gadolinium (Gd) is particularly attractive because this element is also a positive contrast agent for MRI, which allows for the simultaneous use of imaging to guide the irradiation and to delineate the tumor. In this study, we used the Gd-based nanoparticles, AGuIX®. After intravenous injection into animals bearing B16F10 tumors, some nanoparticles remained inside the tumor cells for more than 24 hours, indicating that a single administration of nanoparticles might be sufficient for several irradiations. Combining AGuIX® with radiation therapy increases tumor cell death, and improves the life spans of animals bearing multiple brain melanoma metastases. These results provide pre-clinical proof-of-concept for a phase I clinical trial.

Key words: AGuIX, radiosensitizer, radiation therapy, brain metastases, nanoparticles, imaged-guided therapy, personalized medicine

Introduction

Despite recent outcome progress,[1-3] melanoma is still difficult to treat due to multidrug- and radio-resistance and high metastatic capacity.[4] In approximately 80% of cases, malignant melanomas tend to metastasize into the central nervous system;[5] this specific dissemination has a considerable effect on overall patient survival. Neurosurgeons and neuro-oncologists have attained limited success using conventional treatments such as surgical resection[6, 7] when possible, and radiation therapy with local approach,[8] stereotactic radiosurgery,[9] or *in toto* radiation with whole-brain radiotherapy (WBRT).[10]

One method for enhancing the effect of radiotherapy is to combine X-ray radiation exposure with metallic nanoparticles containing high-Z atoms. This approach has been known for at least 10 years,[11] and is based on the interaction of low-energy photons with these elements.[12-14] During this interaction, photons are absorbed by the nanoparticles, which subsequently release photoelectrons and Auger electrons, leading to a local dose enhancement and the creation of reactive oxygen species (ROS), damaging the neighboring cells.[15] After IV injection, the particles can reach the tumor site through the passive en-

A6.4. Co-authored book chapter: New research in ionizing radiation and nanoparticles: the ARGENT project in Nanoscale Insights into Ion-Beam Cancer Therapy, Springer 2017.

New Research in Ionizing Radiation and Nanoparticles: The ARGENT Project

Marta Bolsa Ferruz, Vladimir Ivošev, Kaspar Haume, Lilian Ellis-Gibbings, Ali Traore, Vivek Thakare, Soraia Rosa, Pablo de Vera, Vu-Long Tran, Arkadiusz Mika, Daria Boscolo, Sophie Grellet, Alexey Verkhovtsev, Bernd A. Huber, Karl T. Butterworth, Kevin M. Prise, Frederick J. Currell, Nigel J. Mason, Jon Golding, Emanuele Scifoni, Gustavo García, Frédéric Boschetti, F. Lux, O. Tillement, Cédric Louis, Kurt Stokbro, Andrey V. Solov'yov and Sandrine Lacombe

Abstract This chapter gives an overview of "ARGENT" ("Advanced Radiotherapy, Generated by Exploiting Nanoprocesses and Technologies"), an ongoing international Initial Training Network project, supported by the European Commission. The project, bringing together world-leading researchers in physics, medical physics, chemistry, and biology, aims to train 13 Early Stage Researchers (ESRs) whose research activities are linked to understanding and exploiting the nanoscale processes that drive physical, chemical, and biological effects induced by ionizing radiation in the presence of radiosensitizing nanoparticles. This research is at the forefront of current practices and involves many experts from the respective scientific disciplines. In this chapter, we overview research topics covered by ARGENT and briefly describe the research projects of each ESR.

S. Lacombe—On behalf of the ARGENT consortium, see http://www.itn-argent.eu.

M. Bolsa Ferruz (✉) · V. Ivošev · S. Lacombe
Institut des Sciences Moléculaires d'Orsay (ISMO), CNRS,
Univ. Paris-Sud, Université Paris-Saclay, 91405 Orsay Cedex, France
e-mail: marta.bolsa-ferruz@u-psud.fr

V. Ivošev
e-mail: vladimir.ivosev@u-psud.fr

S. Lacombe
e-mail: sandrine.lacombe@u-psud.fr

K. Haume · P. de Vera · N.J. Mason
Department of Physical Sciences, The Open University,
Milton Keynes MK7 6AA, UK
e-mail: Kaspar.Haume@open.ac.uk

P. de Vera
e-mail: p.devera@qub.ac.uk

N.J. Mason
e-mail: nigel.mason@open.ac.uk

K. Haume · P. de Vera · A. Verkhovtsev
MBN Research Center, 60438 Frankfurt am Main, Germany
e-mail: verkhovtsev@iff.csic.es

A.V. Solov'yov (ed.), *Nanoscale Insights into Ion-Beam Cancer Therapy*,
DOI 10.1007/978-3-319-43030-0_12

A6.5. List of publications and patents

Publications

[1] S. Kotb, A. Detappe, F. Lux, F. Appaix, E. L. Barbier, **V.L. Tran**, M. Plissonneau, H. Gehan, F. Lefranc, C. Rodriguez-Lafrasse, C. Verry, R. Berbeco, O. Tillment, L. Sancey. *Gadolinium-Based Nanoparticles and Radiation Therapy for Multiple Brain Melanoma Metastases: Proof of Concept before Phase I Trial.* **Theranostics, 2016, 6 (3), 418 – 427.**

[2] M. B. Ferruz, V. Ivosev, K. Haume, E.G. Lilian, A. Traore, V. Thakare, S. Rosa, P. de Vera, **V.L. Tran**, A. Mika, D. Boscolo, S. Grellet, A. Verkhovtsev, B.A. Huber, K. T. Butterworth, K. M. Prise, F. J. Currell, N. J. Mason, J. Golding, E. Scifoni, G. Garcia, F. Boschetti, F. Lux, O. Tillement, C. Louis, K. Stokbro, A. V. Solov'yov, S. Lacombe. *New Research in Ionizing Radiation and Nanoparticles: The ARGENT Project*. In: Andrey Solov'yov (Ed.), **Nanoscale Insights into Ion-Beam Cancer Therapy, Springer 2017.**

[3] **V.L. Tran**, V. Thakare, F. Rosetti, A. Marais, E. Thomas, A. Baudouin, G. Ramniceanu, B. T. Doan, N. Mignet, C. Zerbino, R. Antoine, M. Martini, F. Boschetti, F. Lux, O. Tillement. *One-pot Direct Synthesis for Multifunctional Ultrasmall Hybrid Silica Nanoparticles.* In preparation.

Patents

[1] **V.L. Tran**, F. Lux, O. Tillement, F. Rosetti, V. Thakare. *Method for synthesizing silica nanoparticles.* **European Patent EP17305701, 2017.** Submitted.

[2] O. Tillement, F. Lux, F. Rosetti, **V.L. Tran**, M. Clélia, D. Myleva. *Nanovecteurs et utilisations.* **French patent FR1759607, 2017.** Submitted.

REFERENCES

REFERENCES

1. Min, Y., Caster, J. M., Eblan, M. J. & Wang, A. Z. Clinical Translation of Nanomedicine. *Chem. Rev.* **115,** 11147–11190 (2015).
2. Huang, H.-C., Barua, S., Sharma, G., Dey, S. K. & Rege, K. Inorganic nanoparticles for cancer imaging and therapy. *J. Controlled Release* **155,** 344–357 (2011).
3. Zarschler, K., Rocks, L., Licciardello, N., Boselli, L., Polo, E., Garcia, K. P., De Cola, L., Stephan, H. & Dawson, K. A. Ultrasmall inorganic nanoparticles: State-of-the-art and perspectives for biomedical applications. *Nanomedicine Nanotechnol. Biol. Med.* **12,** 1663–1701 (2016).
4. Hainfeld, J. F., Slatkin, D. N. & Smilowitz, H. M. The use of gold nanoparticles to enhance radiotherapy in mice. *Phys. Med. Biol.* **49,** N309–N315 (2004).
5. Zheng, Y., Hunting, D. J., Ayotte, P. & Sanche, L. Radiosensitization of DNA by Gold Nanoparticles Irradiated with High-Energy Electrons. *Radiat. Res.* **169,** 19–27 (2008).
6. Kwatra, D., Venugopal, A. & Anant, S. Nanoparticles in radiation therapy: a summary of various approaches to enhance radiosensitization in cancer. *Transl. Cancer Res.* **2,** 330–342 (2013).
7. Retif, P., Pinel, S., Toussaint, M., Frochot, C., Chouikrat, R., Bastogne, T. & Barberi-Heyob, M. Nanoparticles for Radiation Therapy Enhancement: the Key Parameters. *Theranostics* **5,** 1030–1044 (2015).
8. Mi, Y., Shao, Z., Vang, J., Kaidar-Person, O. & Wang, A. Z. Application of nanotechnology to cancer radiotherapy. *Cancer Nanotechnol.* **7,** (2016).
9. Bonvalot, S., Le Pechoux, C., Debaere, T., Kantor, G., Buy, X., Stoeckle, E., Sargos, P., Terrier, P., Coindre, J., Lassau, N. & others. First human study testing a new radio enhancer using nanoparticles (NBTXR3) activated by radiation therapy in patients with locally advanced soft tissue sarcomas. *Clin. Cancer Res.* clincanres–1297 (2016).
10. Soo Choi, H., Liu, W., Misra, P., Tanaka, E., Zimmer, J. P., Itty Ipe, B., Bawendi, M. G. & Frangioni, J. V. Renal clearance of quantum dots. *Nat. Biotechnol.* **25,** 1165–1170 (2007).
11. Longmire, M., Choyke, P. L. & Kobayashi, H. Clearance properties of nano-sized particles and molecules as imaging agents: considerations and caveats. *Nanomed.* **3,** 703–717 (2008).
12. Liu, J., Yu, M., Zhou, C. & Zheng, J. Renal clearable inorganic nanoparticles: a new frontier of bionanotechnology. *Mater. Today* **16,** 477–486 (2013).
13. Lin, Z., Monteiro-Riviere, N. A. & Riviere, J. E. Pharmacokinetics of metallic nanoparticles. *Wiley Interdiscip. Rev. Nanomed. Nanobiotechnol.* **7,** 189–217 (2015).
14. Yu, M. & Zheng, J. Clearance Pathways and Tumor Targeting of Imaging Nanoparticles. *ACS Nano* **9,** 6655–6674 (2015).
15. Liang, X., Wang, H., Zhu, Y., Zhang, R., Cogger, V. C., Liu, X., Xu, Z. P., Grice, J. E. & Roberts, M. S. Short- and Long-Term Tracking of Anionic Ultrasmall Nanoparticles in Kidney. *ACS Nano* **10,** 387–395 (2016).
16. Chen, G., Roy, I., Yang, C. & Prasad, P. N. Nanochemistry and Nanomedicine for Nanoparticle-based Diagnostics and Therapy. *Chem. Rev.* **116,** 2826–2885 (2016).
17. Maeda, H. Macromolecular therapeutics in cancer treatment: The EPR effect and beyond. *J. Controlled Release* **164,** 138–144 (2012).
18. Kunjachan, S., Ehling, J., Storm, G., Kiessling, F. & Lammers, T. Noninvasive Imaging of Nanomedicines and Nanotheranostics: Principles, Progress, and Prospects. *Chem. Rev.* **115,** 10907–10937 (2015).
19. Braddock, M. *Biomedical Imaging The Chemistry of Labels, Probes and Contrast Agents*. (RSCPublishing, 2012).
20. Mundt, A. J. & Roeske, J. *Image-Guided Radiation Therapy: A Clinical Perspective*. (People's Medical Publishing House-USA, 2011).
21. Haume, K., Rosa, S., Grellet, S., Śmiałek, M. A., Butterworth, K. T., Solov'yov, A. V., Prise, K. M., Golding, J. & Mason, N. J. Gold nanoparticles for cancer radiotherapy: a review. *Cancer Nanotechnol.* **7,** (2016).
22. McMahon, S. J., Hyland, W. B., Muir, M. F., Coulter, J. A., Jain, S., Butterworth, K. T., Schettino, G., Dickson, G. R., Hounsell, A. R., O'Sullivan, J. M., Prise, K. M., Hirst, D. G. & Currell, F. J. CORRIGENDUM: Biological consequences of nanoscale energy deposition near irradiated heavy atom nanoparticles. *Sci. Rep.* **3,** (2013).
23. Butterworth, K. T., Nicol, J. R., Ghita, M., Rosa, S., Chaudhary, P., McGarry, C. K., McCarthy, H. O., Jimenez-Sanchez, G., Bazzi, R., Roux, S., Tillement, O., Coulter, J. A. & Prise, K. M. Preclinical evaluation of gold-DTDTPA nanoparticles as theranostic agents in prostate cancer radiotherapy. *Nanomed.* **11,** 2035–2047 (2016).
24. Laurent, S., Elst Vander, L. & Muller, R. N. in *The Chemistry of Contrast Agents in Medical Magnetic Resonance Imaging* 427–448 (John Wiley & Sons, Ltd., 2013).

25. Maldiney, T., Byk, G., Wattier, N., Seguin, J., Khandadash, R., Bessodes, M., Richard, C. & Scherman, D. Synthesis and functionalization of persistent luminescence nanoparticles with small molecules and evaluation of their targeting ability. *Int. J. Pharm.* **423,** 102–107 (2012).
26. Shen, D., Henry, M., Trouillet, V., Comby-Zerbino, C., Bertorelle, F., Sancey, L., Antoine, R., Coll, J.-L., Josserand, V. & Le Guével, X. Zwitterion functionalized gold nanoclusters for multimodal near infrared fluorescence and photoacoustic imaging. *APL Mater.* **5,** 053404 (2017).
27. Truillet, C. NANOSONDES AGUIX® POUR LE THERAGNOSTIQUE ETUDES DES MARQUAGES PAR DES RADIONUCLEIDES ET EMETTEURS PDT. (University of Claude Bernard Lyon I, 2013).
28. Knapp, F. F. (Russ) & Dash, A. *Radiopharmaceuticals for Therapy*. (Springer India, 2016).
29. Jadvar, H. & Parker, J. A. *Clinical PET and PET/CT*. (Springer-Verlag, 2005).
30. Harisinghani, M. G., Barentsz, J., Hahn, P. F., Deserno, W. M., Tabatabaei, S., van de Kaa, C. H., de la Rosette, J. & Weissleder, R. Noninvasive detection of clinically occult lymph-node metastases in prostate cancer. *N. Engl. J. Med.* **348,** 2491–2499 (2003).
31. Thill, M., Kurylcio, A., Welter, R., van Haasteren, V., Grosse, B., Berclaz, G., Polkowski, W. & Hauser, N. The Central-European SentiMag study: Sentinel lymph node biopsy with superparamagnetic iron oxide (SPIO) vs. radioisotope. *The Breast* **23,** 175–179 (2014).
32. Winter, A., Woenkhaus, J. & Wawroschek, F. A Novel Method for Intraoperative Sentinel Lymph Node Detection in Prostate Cancer Patients Using Superparamagnetic Iron Oxide Nanoparticles and a Handheld Magnetometer: The Initial Clinical Experience. *Ann. Surg. Oncol.* **21,** 4390–4396 (2014).
33. Karakatsanis, A., Christiansen, P. M., Fischer, L., Hedin, C., Pistioli, L., Sund, M., Rasmussen, N. R., Jørnsgård, H., Tegnelius, D., Eriksson, S., Daskalakis, K., Wärnberg, F., Markopoulos, C. J. & Bergkvist, L. The Nordic SentiMag trial: a comparison of super paramagnetic iron oxide (SPIO) nanoparticles versus Tc99 and patent blue in the detection of sentinel node (SN) in patients with breast cancer and a meta-analysis of earlier studies. *Breast Cancer Res. Treat.* **157,** 281–294 (2016).
34. Maier-Hauff, K., Ulrich, F., Nestler, D., Niehoff, H., Wust, P., Thiesen, B., Orawa, H., Budach, V. & Jordan, A. Efficacy and safety of intratumoral thermotherapy using magnetic iron-oxide nanoparticles combined with external beam radiotherapy on patients with recurrent glioblastoma multiforme. *J. Neurooncol.* **103,** 317–324 (2011).
35. Haldemann Heusler, R. C., Wight, E. & Marincek, B. Oral superparamagnetic contrast agent (ferumoxsil): tolerance and efficacy in MR imaging of gynecologic diseases. *J. Magn. Reson. Imaging* **5,** 385–391 (1995).
36. Scheidler, J., Heuck, A. F., Meier, W. & Reiser, M. F. MRI of pelvic masses: efficacy of the rectal superparamagnetic contrast agent Ferumoxsil. *J. Magn. Reson. Imaging* **7,** 1027–1032 (1997).
37. Wallengren, N.-O., Holt\a as, S. & Andrén-Sandberg, \AA. Preoperative staging of rectal carcinoma using double-contrast MR imaging: Technical aspects and early clinical experiences. *Acta Radiol.* **37,** 791–798 (1996).
38. Blomqvist, L., Ohlsen, H., Hindmarsh, T., Jonsson, E. & Holm, T. Local recurrence of rectal cancer: MR imaging before and after oral superparamagnetic particles vs contrast-enhanced computed tomography. *Eur. Radiol.* **10,** 1383–1389 (2000).
39. Boraschi, P., Braccini, G., Gigoni, R., Cartei, F. & Perri, G. Mr enteroclysis using iron oxide particles (ferristene) as an endoluminal contrast agent: An open phase III trial. *Magn. Reson. Imaging* **22,** 1085–1095 (2004).
40. Singh, A., Patel, T., Hertel, J., Bernardo, M., Kausz, A. & Brenner, L. Safety of Ferumoxytol in Patients With Anemia and CKD. *Am. J. Kidney Dis.* **52,** 907–915 (2008).
41. Spinowitz, B. S., Kausz, A. T., Baptista, J., Noble, S. D., Sothinathan, R., Bernardo, M. V., Brenner, L. & Pereira, B. J. G. Ferumoxytol for Treating Iron Deficiency Anemia in CKD. *J. Am. Soc. Nephrol.* **19,** 1599–1605 (2008).
42. Balakrishnan, V. S., Rao, M., Kausz, A. T., Brenner, L., Pereira, B. J. G., Frigo, T. B. & Lewis, J. M. Physicochemical properties of ferumoxytol, a new intravenous iron preparation. *Eur. J. Clin. Invest.* **39,** 489–496 (2009).
43. Provenzano, R., Schiller, B., Rao, M., Coyne, D., Brenner, L. & Pereira, B. J. G. Ferumoxytol as an Intravenous Iron Replacement Therapy in Hemodialysis Patients. *Clin. J. Am. Soc. Nephrol.* **4,** 386–393 (2009).
44. Paciotti, G. F., Myer, L., Weinreich, D., Goia, D., Pavel, N., McLaughlin, R. E. & Tamarkin, L. Colloidal Gold: A Novel Nanoparticle Vector for Tumor Directed Drug Delivery. *Drug Deliv.* **11,** 169–183 (2004).
45. Goel, R., Shah, N., Visaria, R., Paciotti, G. F. & Bischof, J. C. Biodistribution of TNF-α-coated gold nanoparticles in an in vivo model system. *Nanomed.* **4,** 401–410 (2009).
46. Libutti, S. K., Paciotti, G. F., Byrnes, A. A., Alexander, H. R., Gannon, W. E., Walker, M., Seidel, G. D., Yuldasheva, N. & Tamarkin, L. Phase I and Pharmacokinetic Studies of CYT-6091, a Novel PEGylated Colloidal Gold-rhTNF Nanomedicine. *Clin. Cancer Res.* **16,** 6139–6149 (2010).
47. Day, E. S., Thompson, P. A., Zhang, L., Lewinski, N. A., Ahmed, N., Drezek, R. A., Blaney, S. M. & West, J. L. Nanoshell-mediated photothermal therapy improves survival in a murine glioma model. *J. Neurooncol.* **104,** 55–63 (2011).

48. Schwartz, J. A., Shetty, A. M., Price, R. E., Stafford, R. J., Wang, J. C., Uthamanthil, R. K., Pham, K., McNichols, R. J., Coleman, C. L. & Payne, J. D. Feasibility Study of Particle-Assisted Laser Ablation of Brain Tumors in Orthotopic Canine Model. *Cancer Res.* **69,** 1659–1667 (2009).
49. Stern, J. M., Stanfield, J., Kabbani, W., Hsieh, J.-T. & Cadeddu, J. A. Selective Prostate Cancer Thermal Ablation With Laser Activated Gold Nanoshells. *J. Urol.* **179,** 748–753 (2008).
50. Pottier, A., Borghi, E. & Levy, L. The future of nanosized radiation enhancers. *Br. J. Radiol.* **88,** 20150171 (2015).
51. Pottier, A., Borghi, E. & Levy, L. Metals as radio-enhancers in oncology: The industry perspective. *Biochem. Biophys. Res. Commun.* **468,** 471–475 (2015).
52. Pottier, A., Borghi, E. & Levy, L. New use of metals as nanosized radioenhancers. *Anticancer Res.* **34,** 443–453 (2014).
53. Phillips, E., Penate-Medina, O., Zanzonico, P. B., Carvajal, R. D., Mohan, P., Ye, Y., Humm, J., Gonen, M., Kalaigian, H., Schoder, H., Strauss, H. W., Larson, S. M., Wiesner, U. & Bradbury, M. S. Clinical translation of an ultrasmall inorganic optical-PET imaging nanoparticle probe. *Sci. Transl. Med.* **6,** 260ra149-260ra149 (2014).
54. Benezra, M., Penate-Medina, O., Zanzonico, P. B., Schaer, D., Ow, H., Burns, A., DeStanchina, E., Longo, V., Herz, E., Iyer, S., Wolchok, J., Larson, S. M., Wiesner, U. & Bradbury, M. S. Multimodal silica nanoparticles are effective cancer-targeted probes in a model of human melanoma. *J. Clin. Invest.* **121,** 2768–2780 (2011).
55. Burns, A. A., Vider, J., Ow, H., Herz, E., Penate-Medina, O., Baumgart, M., Larson, S. M., Wiesner, U. & Bradbury, M. Fluorescent Silica Nanoparticles with Efficient Urinary Excretion for Nanomedicine. *Nano Lett.* **9,** 442–448 (2009).
56. Caltagirone, C., Bettoschi, A., Garau, A. & Montis, R. Silica-based nanoparticles: a versatile tool for the development of efficient imaging agents. *Chem Soc Rev* **44,** 4645–4671 (2015).
57. Deen, W. M., Lazzara, M. J. & Myers, B. D. Structural determinants of glomerular permeability. *Am. J. Physiol.-Ren. Physiol.* **281,** F579–F596 (2001).
58. Zarschler, K., Rocks, L., Licciardello, N., Boselli, L., Polo, E., Garcia, K. P., De Cola, L., Stephan, H. & Dawson, K. A. Ultrasmall inorganic nanoparticles: State-of-the-art and perspectives for biomedical applications. *Nanomedicine Nanotechnol. Biol. Med.* **12,** 1663–1701 (2016).
59. Petros, R. A. & DeSimone, J. M. Strategies in the design of nanoparticles for therapeutic applications. *Nat. Rev. Drug Discov.* **9,** 615–627 (2010).
60. Mahon, E., Salvati, A., Baldelli Bombelli, F., Lynch, I. & Dawson, K. A. Designing the nanoparticle–biomolecule interface for "targeting and therapeutic delivery". *J. Controlled Release* **161,** 164–174 (2012).
61. Bonitatibus, P. J., Torres, A. S., Kandapallil, B., Lee, B. D., Goddard, G. D., Colborn, R. E. & Marino, M. E. Preclinical Assessment of a Zwitterionic Tantalum Oxide Nanoparticle X-ray Contrast Agent. *ACS Nano* **6,** 6650–6658 (2012).
62. Garcia, K. P., Zarschler, K., Barbaro, L., Barreto, J. A., O'Malley, W., Spiccia, L., Stephan, H. & Graham, B. Zwitterionic-Coated "Stealth" Nanoparticles for Biomedical Applications: Recent Advances in Countering Biomolecular Corona Formation and Uptake by the Mononuclear Phagocyte System. *Small* **10,** 2516–2529 (2014).
63. Liu, J., Yu, M., Zhou, C., Yang, S., Ning, X. & Zheng, J. Passive Tumor Targeting of Renal-Clearable Luminescent Gold Nanoparticles: Long Tumor Retention and Fast Normal Tissue Clearance. *J. Am. Chem. Soc.* **135,** 4978–4981 (2013).
64. Liu, J., Yu, M., Ning, X., Zhou, C., Yang, S. & Zheng, J. PEGylation and Zwitterionization: Pros and Cons in the Renal Clearance and Tumor Targeting of Near-IR-Emitting Gold Nanoparticles. *Angew. Chem. Int. Ed.* **52,** 12572–12576 (2013).
65. Popat, K., McQueen, K. & Feeley, T. W. The global burden of cancer. *Best Pract. Res. Clin. Anaesthesiol.* **27,** 399–408 (2013).
66. Stewart, B. W., Wild, C., International Agency for Research on Cancer & World Health Organization. *World cancer report 2014*. (International Agency for Research on Cancer ; Distributed by WHO Press, 2014). at <http://search.ebscohost.com/login.aspx?direct=true&scope=site&db=nlebk&db=nlabk&AN=979458>
67. Fitzmaurice, C. *et al.* The Global Burden of Cancer 2013. *JAMA Oncol.* **1,** 505 (2015).
68. Atun, R., Jaffray, D. A., Barton, M. B., Bray, F., Baumann, M., Vikram, B., Hanna, T. P., Knaul, F. M., Lievens, Y., Lui, T. Y. & others. Expanding global access to radiotherapy. *Lancet Oncol.* **16,** 1153–1186 (2015).
69. Baumann, M., Krause, M., Overgaard, J., Debus, J., Bentzen, S. M., Daartz, J., Richter, C., Zips, D. & Bortfeld, T. Radiation oncology in the era of precision medicine. *Nat. Rev. Cancer* **16,** 234–249 (2016).
70. Rosenblatt, E. & Zubizarreta, E. *Radiotherapy in cancer care: facing the global challenge*. (International Atomic Energy Agency, 2017).
71. Cooper, D. R., Bekah, D. & Nadeau, J. L. Gold nanoparticles and their alternatives for radiation therapy enhancement. *Front. Chem.* **2,** (2014).

72. Bolsa Ferruz, M. *et al.* in *Nanoscale Insights into Ion-Beam Cancer Therapy* (ed. Solov'yov, A. V.) 379–434 (Springer International Publishing, 2017). doi:10.1007/978-3-319-43030-0_12
73. Hubbell, J. H. & Seltzer, S. M. X-Ray Mass Attenuation Coefficients. Available at: http://www.nist.gov/pml/data/xraycoef/.
74. McMahon, S. J., Hyland, W. B., Muir, M. F., Coulter, J. A., Jain, S., Butterworth, K. T., Schettino, G., Dickson, G. R., Hounsell, A. R., O'Sullivan, J. M., Prise, K. M., Hirst, D. G. & Currell, F. J. Nanodosimetric effects of gold nanoparticles in megavoltage radiation therapy. *Radiother. Oncol.* **100,** 412–416 (2011).
75. Butterworth, K. T., McMahon, S. J., Currell, F. J. & Prise, K. M. Physical basis and biological mechanisms of gold nanoparticle radiosensitization. *Nanoscale* **4,** 4830 (2012).
76. Porcel, E., Tillement, O., Lux, F., Mowat, P., Usami, N., Kobayashi, K., Furusawa, Y., Le Sech, C., Li, S. & Lacombe, S. Gadolinium-based nanoparticles to improve the hadrontherapy performances. *Nanomedicine Nanotechnol. Biol. Med.* **10,** 1601–1608 (2014).
77. Shady, K. Safety and radiosensitization properties of theranostic Gadolinium-based nanoparticles AGuIX. (University of Claude Bernard Lyon I, 2016).
78. Prise, K. M. & O'Sullivan, J. M. Radiation-induced bystander signalling in cancer therapy. *Nat. Rev. Cancer* **9,** 351–360 (2009).
79. Butterworth, K. T., McMahon, S. J., Hounsell, A. R., O'Sullivan, J. M. & Prise, K. M. Bystander Signalling: Exploring Clinical Relevance Through New Approaches and New Models. *Clin. Oncol.* **25,** 586–592 (2013).
80. Conde, J., Dias, J. T., GrazÃº, V., Moros, M., Baptista, P. V. & de la Fuente, J. M. Revisiting 30 years of biofunctionalization and surface chemistry of inorganic nanoparticles for nanomedicine. *Front. Chem.* **2,** (2014).
81. Her, S., Jaffray, D. A. & Allen, C. Gold nanoparticles for applications in cancer radiotherapy: Mechanisms and recent advancements. *Adv. Drug Deliv. Rev.* **109,** 84–101 (2017).
82. Chen, Y.-S., Hung, Y.-C., Liau, I. & Huang, G. S. Assessment of the In Vivo Toxicity of Gold Nanoparticles. *Nanoscale Res. Lett.* **4,** 858–864 (2009).
83. Laurent, G. *et al.* Minor changes in the macrocyclic ligands but major consequences on the efficiency of gold nanoparticles designed for radiosensitization. *Nanoscale* **8,** 12054–12065 (2016).
84. Alric, C., Miladi, I., Kryza, D., Taleb, J., Lux, F., Bazzi, R., Billotey, C., Janier, M., Perriat, P., Roux, S. & Tillement, O. The biodistribution of gold nanoparticles designed for renal clearance. *Nanoscale* **5,** 5930 (2013).
85. Grellet, S., Tzelepi, K., Roskamp, M., Williams, P., Sharif, A., Slade-Carter, R., Goldie, P., Whilde, N., Śmiałek, M. A., Mason, N. J. & Golding, J. P. Cancer-selective, single agent chemoradiosensitising gold nanoparticles. *PLOS ONE* **12,** e0181103 (2017).
86. Zhang, X.-D., Luo, Z., Chen, J., Song, S., Yuan, X., Shen, X., Wang, H., Sun, Y., Gao, K., Zhang, L., Fan, S., Leong, D. T., Guo, M. & Xie, J. Ultrasmall Glutathione-Protected Gold Nanoclusters as Next Generation Radiotherapy Sensitizers with High Tumor Uptake and High Renal Clearance. *Sci. Rep.* **5,** (2015).
87. Fang, X., Wang, Y., Ma, X., Li, Y., Zhang, Z., Xiao, Z., Liu, L., Gao, X. & Liu, J. Mitochondria-targeting Au nanoclusters enhance radiosensitivity of cancer cells. *J Mater Chem B* **5,** 4190–4197 (2017).
88. Levy, L., Pottier, A., Rouet, A., Marill, J., Devaux, C. & Germain, M. Inorganic nanoparticles of high density to destroy cells in-vivo. (2011). at <https://google.com/patents/EP2300054A2?cl=ar>
89. Tóth, É., Lothar, Helm & Merbach, A. in *The Chemistry of Contrast Agents in Medical Magnetic Resonance Imaging* 25–82 (John Wiley & Sons, Ltd., 2013).
90. Le Duc, G., Miladi, I., Alric, C., Mowat, P., Bräuer-Krisch, E., Bouchet, A., Khalil, E., Billotey, C., Janier, M., Lux, F., Epicier, T., Perriat, P., Roux, S. & Tillement, O. Toward an Image-Guided Microbeam Radiation Therapy Using Gadolinium-Based Nanoparticles. *ACS Nano* **5,** 9566–9574 (2011).
91. Lux, F., Sancey, L., Bianchi, A., Crémillieux, Y., Roux, S. & Tillement, O. Gadolinium-based nanoparticles for theranostic MRI-radiosensitization. *Nanomed.* 1–15 (2015). doi:10.2217/nnm.15.30
92. Grobner, T. Gadolinium - a specific trigger for the development of nephrogenic fibrosing dermopathy and nephrogenic systemic fibrosis? *Nephrol. Dial. Transplant.* **21,** 1104–1108 (2005).
93. Faucher, L., Guay-Bégin, A.-A., Lagueux, J., Côté, M.-F., Petitclerc, É. & Fortin, M.-A. Ultra-small gadolinium oxide nanoparticles to image brain cancer cells in vivo with MRI. *Contrast Media Mol. Imaging* **6,** 209–218 (2011).
94. Moriggi, L., Cannizzo, C., Dumas, E., Mayer, C. R., Ulianov, A. & Helm, L. Gold Nanoparticles Functionalized with Gadolinium Chelates as High-Relaxivity MRI Contrast Agents. *J. Am. Chem. Soc.* **131,** 10828–10829 (2009).
95. Ferreira, M. F., Gonçalves, J., Mousavi, B., Prata, M. I. M., Rodrigues, S. P. J., Calle, D., López-Larrubia, P., Cerdan, S., Rodrigues, T. B., Ferreira, P. M., Helm, L., Martins, J. A. & Geraldes, C. F. G. C. Gold nanoparticles functionalised with fast water exchanging Gd^{3+} chelates: linker effects on the relaxivity. *Dalton Trans* **44,** 4016–4031 (2015).

96. Endres, P. J., Paunesku, T., Vogt, S., Meade, T. J. & Woloschak, G. E. DNA–TiO $_2$ Nanoconjugates Labeled with Magnetic Resonance Contrast Agents. *J. Am. Chem. Soc.* **129,** 15760–15761 (2007).
97. Townley, H. E., Kim, J. & Dobson, P. J. In vivo demonstration of enhanced radiotherapy using rare earth doped titania nanoparticles. *Nanoscale* **4,** 5043 (2012).
98. Tokumitsu, H., Hiratsuka, J., Sakurai, Y., Kobayashi, T., Ichikawa, H. & Fukumori, Y. Gadolinium neutron-capture therapy using novel gadopentetic acid–chitosan complex nanoparticles: in vivo growth suppression of experimental melanoma solid tumor. *Cancer Lett.* **150,** 177–182 (2000).
99. Ichikawa, H., Uneme, T., Andoh, T., Arita, Y., Fujimoto, T., Suzuki, M., Sakurai, Y., Shinto, H., Fukasawa, T., Fujii, F. & Fukumori, Y. Gadolinium-loaded chitosan nanoparticles for neutron-capture therapy: Influence of micrometric properties of the nanoparticles on tumor-killing effect. *Appl. Radiat. Isot.* **88,** 109–113 (2014).
100. Ghaemi, B., Mashinchian, O., Mousavi, T., Karimi, R., Kharrazi, S. & Amani, A. Harnessing the Cancer Radiation Therapy by Lanthanide-Doped Zinc Oxide Based Theranostic Nanoparticles. *ACS Appl. Mater. Interfaces* **8,** 3123–3134 (2016).
101. Yong, Y., Zhou, L., Zhang, S., Yan, L., Gu, Z., Zhang, G. & Zhao, Y. Gadolinium polytungstate nanoclusters: a new theranostic with ultrasmall size and versatile properties for dual-modal MR/CT imaging and photothermal therapy/radiotherapy of cancer. *NPG Asia Mater.* **8,** e273 (2016).
102. Song, G., Liang, C., Gong, H., Li, M., Zheng, X., Cheng, L., Yang, K., Jiang, X. & Liu, Z. Core-Shell MnSe@Bi $_2$ Se $_3$ Fabricated via a Cation Exchange Method as Novel Nanotheranostics for Multimodal Imaging and Synergistic Thermoradiotherapy. *Adv. Mater.* **27,** 6110–6117 (2015).
103. Alqathami, M., Blencowe, A., Geso, M. & Ibbott, G. Quantitative 3D Determination of Radiosensitization by Bismuth-Based Nanoparticles. *J. Biomed. Nanotechnol.* **12,** 464–471 (2016).
104. DiPalma, J. R. Bismuth Toxicity, Often Mild, Can Result in Severe Poisonings. *Emerg. Med. News* **23,** (2001).
105. Porcel, E., Liehn, S., Remita, H., Usami, N., Kobayashi, K., Furusawa, Y., Sech, C. L. & Lacombe, S. Platinum nanoparticles: a promising material for future cancer therapy? *Nanotechnology* **21,** 085103 (2010).
106. Schlatholter, Lacombe, S., Eustache, P., Porcel, E., Salado, D., Stefancikova, L., Tillement, O., Lux, F., Mowat, P., van Goethem, M.-J., Remita, H. & Biegun, A. Improving proton therapy by metal-containing nanoparticles: nanoscale insights. *Int. J. Nanomedicine* 1549 (2016). doi:10.2147/IJN.S99410
107. Liu, X., Zhang, X., Zhu, M., Lin, G., Liu, J., Zhou, Z., Tian, X. & Pan, Y. PEGylated Au@Pt Nanodendrites as Novel Theranostic Agents for Computed Tomography Imaging and Photothermal/Radiation Synergistic Therapy. *ACS Appl. Mater. Interfaces* **9,** 279–285 (2017).
108. Luna, A., Vilanova, J. C., Hygino Da Cruz Jr., L. C. & Rossi, S. E. *Functional Imaging in Oncology: Biophysical Basis and Technical Approaches*. (Springer, 2014).
109. Cortes, S., Brucher, E., Geraldes, C. F. G. C. & Sherry, A. D. Potentiometry and NMR studies of 1,5,9-triazacyclododecane-N,N',N''-triacetic acid and its metal ion complexes. *Inorg. Chem.* **29,** 5–9 (1990).
110. Pan, D., Schmieder, A. H., Wickline, S. A. & Lanza, G. M. Manganese-based MRI contrast agents: past, present, and future. *Tetrahedron* **67,** 8431–8444 (2011).
111. de Sá, A., Bonnet, C. S., Geraldes, C. F. G. C., Tóth, É., Ferreira, P. M. T. & André, J. P. Thermodynamic stability and relaxation studies of small, triaza-macrocyclic Mn(ii) chelates. *Dalton Trans.* **42,** 4522 (2013).
112. Hao, D., Ai, T., Goerner, F., Hu, X., Runge, V. M. & Tweedle, M. MRI contrast agents: Basic chemistry and safety. *J. Magn. Reson. Imaging* **36,** 1060–1071 (2012).
113. Broome, D. R. Nephrogenic systemic fibrosis associated with gadolinium based contrast agents: A summary of the medical literature reporting. *Eur. J. Radiol.* **66,** 230–234 (2008).
114. Bennett, P., Oza, U. D., Trout, A. T. & Mintz, A. *Diagnostic Imaging: Nuclear Medicine*. (Elsevier, 2016).
115. Weissleder, R. & others. A clearer vision for in vivo imaging. *Nat. Biotechnol.* **19,** 316–316 (2001).
116. Gianolio, E., Giovenzana, G. B., Longo, D., Longo, I., Menegotto, I. & Aime, S. Relaxometric and Modelling Studies of the Binding of a Lipophilic Gd-AAZTA Complex to Fatted and Defatted Human Serum Albumin. *Chem. - Eur. J.* **13,** 5785–5797 (2007).
117. Zhou, Z., Wang, L., Chi, X., Bao, J., Yang, L., Zhao, W., Chen, Z., Wang, X., Chen, X. & Gao, J. Engineered Iron-Oxide-Based Nanoparticles as Enhanced T_1 Contrast Agents for Efficient Tumor Imaging. *ACS Nano* **7,** 3287–3296 (2013).
118. Eriksson, P.-O., Aaltonen, E., Petoral, R., Lauritzson, P., Miyazaki, H., Pietras, K., Månsson, S., Hansson, L., Leander, P. & Axelsson, O. Novel Nano-Sized MR Contrast Agent Mediates Strong Tumor Contrast Enhancement in an Oncogene-Driven Breast Cancer Model. *PLoS ONE* **9,** e107762 (2014).
119. Tamion, A., Hillenkamp, M., Hillion, A., Maraloiu, V. A., Vlaicu, I. D., Stefan, M., Ghica, D., Rositi, H., Chauveau, F., Blanchin, M.-G., Wiart, M. & Dupuis, V. Ferritin surplus in mouse spleen 14 months after intravenous injection of iron oxide nanoparticles at clinical dose. *Nano Res.* **9,** 2398–2410 (2016).
120. PILGRIMM, H. SUPER-PARAMAGNETIC PARTICLES WITH INCREASED R1 RELAXIVITY, PROCESSES FOR PRODUCING SAID PARTICLES AND USE THEREOF.
121. Taupitz, M., Schnorr, J., Abramjuk, C., Wagner, S., Pilgrimm, H., Hünigen, H. & Hamm, B. New generation of monomer-stabilized very small superparamagnetic iron oxide particles (VSOP) as contrast

medium for MR angiography: Preclinical results in rats and rabbits. *J. Magn. Reson. Imaging* **12,** 905–911 (2000).
122. Wagner, M., Wagner, S., Schnorr, J., Schellenberger, E., Kivelitz, D., Krug, L., Dewey, M., Laule, M., Hamm, B. & Taupitz, M. Coronary MR angiography using citrate-coated very small superparamagnetic iron oxide particles as blood-pool contrast agent: Initial experience in humans. *J. Magn. Reson. Imaging* **34,** 816–823 (2011).
123. Taupitz, M., Wagner, S., Schnorr, J., Kravec, I., Pilgrimm, H., Bergmann-Fritsch, H. & Hamm, B. Phase I Clinical Evaluation of Citrate-coated Monocrystalline Very Small Superparamagnetic Iron Oxide Particles as a New Contrast Medium for Magnetic Resonance Imaging: *Invest. Radiol.* **39,** 394–405 (2004).
124. Kim, B. H., Lee, N., Kim, H., An, K., Park, Y. I., Choi, Y., Shin, K., Lee, Y., Kwon, S. G., Na, H. B., Park, J.-G., Ahn, T.-Y., Kim, Y.-W., Moon, W. K., Choi, S. H. & Hyeon, T. Large-Scale Synthesis of Uniform and Extremely Small-Sized Iron Oxide Nanoparticles for High-Resolution T_1 Magnetic Resonance Imaging Contrast Agents. *J. Am. Chem. Soc.* **133,** 12624–12631 (2011).
125. Zeng, L., Ren, W., Zheng, J., Cui, P. & Wu, A. Ultrasmall water-soluble metal-iron oxide nanoparticles as T1-weighted contrast agents for magnetic resonance imaging. *Phys. Chem. Chem. Phys.* **14,** 2631 (2012).
126. Shen, L., Bao, J., Wang, D., Wang, Y., Chen, Z., Ren, L., Zhou, X., Ke, X., Chen, M. & Yang, A. One-step synthesis of monodisperse, water-soluble ultra-small Fe3O4 nanoparticles for potential bio-application. *Nanoscale* **5,** 2133 (2013).
127. Walter, A., Garofalo, A., Parat, A., Jouhannaud, J., Pourroy, G., Voirin, E., Laurent, S., Bonazza, P., Taleb, J., Billotey, C., Vander Elst, L., Muller, R. N., Begin-Colin, S. & Felder-Flesch, D. Validation of a dendron concept to tune colloidal stability, MRI relaxivity and bioelimination of functional nanoparticles. *J Mater Chem B* **3,** 1484–1494 (2015).
128. Walter, A., Parat, A., Garofalo, A., Laurent, S., Elst, L. V., Muller, R. N., Wu, T., Heuillard, E., Robinet, E., Meyer, F., Felder-Flesch, D. & Begin-Colin, S. Modulation of Relaxivity, Suspension Stability, and Biodistribution of Dendronized Iron Oxide Nanoparticles as a Function of the Organic Shell Design. *Part. Part. Syst. Charact.* **32,** 552–560 (2015).
129. Liberman, A., Mendez, N., Trogler, W. C. & Kummel, A. C. Synthesis and surface functionalization of silica nanoparticles for nanomedicine. *Surf. Sci. Rep.* **69,** 132–158 (2014).
130. Arkles, B. *Silane Coupling Agents: Connecting Across Boundaries*. (Gellest, Inc., 2014).
131. Sancey, L., Kotb, S., Truillet, C., Appaix, F., Marais, A., Thomas, E., van der Sanden, B., Klein, J.-P., Laurent, B., Cottier, M., Antoine, R., Dugourd, P., Panczer, G., Lux, F., Perriat, P., Motto-Ros, V. & Tillement, O. Long-Term in Vivo Clearance of Gadolinium-Based AGuIX Nanoparticles and Their Biocompatibility after Systemic Injection. *ACS Nano* **9,** 2477–2488 (2015).
132. Kotb, S., Piraquive, J., Lamberton, F., Lux, F., Verset, M., Di Cataldo, V., Contamin, H., Tillement, O., Canet-Soulas, E. & Sancey, L. Safety Evaluation and Imaging Properties of Gadolinium-Based Nanoparticles in nonhuman primates. *Sci. Rep.* **6,** 35053 (2016).
133. Mignot, A. *et al.* A Top-Down Synthesis Route to Ultrasmall Multifunctional Gd-Based Silica Nanoparticles for Theranostic Applications. *Chem. - Eur. J.* **19,** 6122–6136 (2013).
134. Sancey, L. *et al.* The use of theranostic gadolinium-based nanoprobes to improve radiotherapy efficacy. *Br. J. Radiol.* **87,** 20140134 (2014).
135. Kotb, S., Detappe, A., Lux, F., Appaix, F., Barbier, E. L., Tran, V.-L., Plissonneau, M., Gehan, H., Lefranc, F., Rodriguez-Lafrasse, C., Verry, C., Berbeco, R., Tillement, O. & Sancey, L. Gadolinium-Based Nanoparticles and Radiation Therapy for Multiple Brain Melanoma Metastases: Proof of Concept before Phase I Trial. *Theranostics* **6,** 418–427 (2016).
136. Le Duc, G., Roux, S., Paruta-Tuarez, A., Dufort, S., Brauer, E., Marais, A., Truillet, C., Sancey, L., Perriat, P., Lux, F. & Tillement, O. Advantages of gadolinium based ultrasmall nanoparticles vs molecular gadolinium chelates for radiotherapy guided by MRI for glioma treatment. *Cancer Nanotechnol.* **5,** 4 (2014).
137. Lux, F. *et al.* Ultrasmall Rigid Particles as Multimodal Probes for Medical Applications. *Angew. Chem. Int. Ed.* **50,** 12299–12303 (2011).
138. Truillet, C., Bouziotis, P., Tsoukalas, C., Brugière, J., Martini, M., Sancey, L., Brichart, T., Denat, F., Boschetti, F., Darbost, U., Bonnamour, I., Stellas, D., Anagnostopoulos, C. D., Koutoulidis, V., Moulopoulos, L. A., Perriat, P., Lux, F. & Tillement, O. Ultrasmall particles for Gd-MRI and ^{68} Ga-PET dual imaging. *Contrast Media Mol. Imaging* **10,** 309–319 (2015).
139. Truillet, C., Thomas, E., Lux, F., Huynh, L. T., Tillement, O. & Evans, M. J. Synthesis and Characterization of ^{89} Zr-Labeled Ultrasmall Nanoparticles. *Mol. Pharm.* **13,** 2596–2601 (2016).
140. Verry, C., Dufort, S., Barbier, E. L., Montigon, O., Peoc'h, M., Chartier, P., Lux, F., Balosso, J., Tillement, O., Sancey, L. & Le Duc, G. MRI-guided clinical 6-MV radiosensitization of glioma using a unique gadolinium-based nanoparticles injection. *Nanomed.* **11,** 2405–2417 (2016).
141. Bouziotis, P., Stellas, D., Thomas, E., Truillet, C., Tsoukalas, C., Lux, F., Tsotakos, T., Xanthopoulos, S., Paravatou-Petsotas, M., Gaitanis, A., Moulopoulos, L. A., Koutoulidis, V., Anagnostopoulos, C. D. & Tillement, O. ^{68} Ga-radiolabeled AGuIX nanoparticles as dual-modality imaging agents for PET/MRI-guided radiation therapy. *Nanomed.* **12,** 1561–1574 (2017).

142. Luchette, M., Korideck, H., Makrigiorgos, M., Tillement, O. & Berbeco, R. Radiation dose enhancement of gadolinium-based AGuIX nanoparticles on HeLa cells. *Nanomedicine Nanotechnol. Biol. Med.* **10,** 1751–1755 (2014).
143. Miladi, I., Aloy, M.-T., Armandy, E., Mowat, P., Kryza, D., Magné, N., Tillement, O., Lux, F., Billotey, C., Janier, M. & Rodriguez-Lafrasse, C. Combining ultrasmall gadolinium-based nanoparticles with photon irradiation overcomes radioresistance of head and neck squamous cell carcinoma. *Nanomedicine Nanotechnol. Biol. Med.* **11,** 247–257 (2015).
144. Detappe, A., Kunjachan, S., Rottmann, J., Robar, J., Tsiamas, P., Korideck, H., Tillement, O. & Berbeco, R. AGuIX nanoparticles as a promising platform for image-guided radiation therapy. *Cancer Nanotechnol.* **6,** (2015).
145. Detappe, A., Kunjachan, S., Drané, P., Kotb, S., Myronakis, M., Biancur, D. E., Ireland, T., Wagar, M., Lux, F., Tillement, O. & Berbeco, R. Key clinical beam parameters for nanoparticle-mediated radiation dose amplification. *Sci. Rep.* **6,** 34040 (2016).
146. Detappe, A., Kunjachan, S., Sancey, L., Motto-Ros, V., Biancur, D., Drane, P., Guieze, R., Makrigiorgos, G. M., Tillement, O., Langer, R. & Berbeco, R. Advanced multimodal nanoparticles delay tumor progression with clinical radiation therapy. *J. Controlled Release* **238,** 103–113 (2016).
147. Štefančíková, L., Porcel, E., Eustache, P., Li, S., Salado, D., Marco, S., Guerquin-Kern, J.-L., Réfrégiers, M., Tillement, O., Lux, F. & Lacombe, S. Cell localisation of gadolinium-based nanoparticles and related radiosensitising efficacy in glioblastoma cells. *Cancer Nanotechnol.* **5,** 6 (2014).
148. Štefančíková, L., Lacombe, S., Salado, D., Porcel, E., Pagáčová, E., Tillement, O., Lux, F., Depeš, D., Kozubek, S. & Falk, M. Effect of gadolinium-based nanoparticles on nuclear DNA damage and repair in glioblastoma tumor cells. *J. Nanobiotechnology* **14,** (2016).
149. Bianchi, A., Dufort, S., Lux, F., Fortin, P.-Y., Tassali, N., Tillement, O., Coll, J.-L. & Cremillieux, Y. Targeting and in vivo imaging of non-small-cell lung cancer using nebulized multimodal contrast agents. *Proc. Natl. Acad. Sci.* **111,** 9247–9252 (2014).
150. Morlieras, J., Chezal, J.-M., Miot-Noirault, E., Vidal, A., Besse, S., Kryza, D., Truillet, C., Mignot, A., Antoine, R., Dugourd, P., Redini, F., Sancey, L., Lux, F., Perriat, P., Janier, M. & Tillement, O. In vivo evidence of the targeting of cartilaginous tissue by pyridinium functionalized nanoparticles. *Chem. Commun.* **49,** 3046 (2013).
151. Miot-Noirault, E., Vidal, A., Morlieras, J., Bonazza, P., Auzeloux, P., Besse, S., Dauplat, M.-M., Peyrode, C., Degoul, F., Billotey, C., Lux, F., Rédini, F., Tillement, O., Chezal, J.-M., Kryza, D. & Janier, M. Small rigid platforms functionalization with quaternary ammonium: Targeting extracellular matrix of chondrosarcoma. *Nanomedicine Nanotechnol. Biol. Med.* **10,** 1887–1895 (2014).
152. Morlieras, J., Chezal, J.-M., Miot-Noirault, E., Roux, A., Heinrich-Balard, L., Cohen, R., Tarrit, S., Truillet, C., Mignot, A., Hachani, R., Kryza, D., Antoine, R., Dugourd, P., Perriat, P., Janier, M., Sancey, L., Lux, F. & Tillement, O. Development of gadolinium based nanoparticles having an affinity towards melanin. *Nanoscale* **5,** 1603 (2013).
153. Morlieras, J., Dufort, S., Sancey, L., Truillet, C., Mignot, A., Rossetti, F., Dentamaro, M., Laurent, S., Vander Elst, L., Muller, R. N., Antoine, R., Dugourd, P., Roux, S., Perriat, P., Lux, F., Coll, J.-L. & Tillement, O. Functionalization of Small Rigid Platforms with Cyclic RGD Peptides for Targeting Tumors Overexpressing $\alpha_v\beta_3$ -Integrins. *Bioconjug. Chem.* **24,** 1584–1597 (2013).
154. Dentamaro, M., Lux, F., Vander Elst, L., Dauguet, N., Montante, S., Moussaron, A., Burtea, C., Muller, R. N., Tillement, O. & Laurent, S. Chemical and *in vitro* characterizations of a promising bimodal AGuIX probe able to target apoptotic cells for applications in MRI and optical imaging. *Contrast Media Mol. Imaging* (2016). doi:10.1002/cmmi.1702
155. Plissonneau, M., Pansieri, J., Heinrich-Balard, L., Morfin, J.-F., Stransky-Heilkron, N., Rivory, P., Mowat, P., Dumoulin, M., Cohen, R., Allémann, É., Tóth, É., Saraiva, M. J., Louis, C., Tillement, O., Forge, V., Lux, F. & Marquette, C. Gd-nanoparticles functionalization with specific peptides for ß-amyloid plaques targeting. *J. Nanobiotechnology* **14,** (2016).
156. Pansieri, J., Plissonneau, M., Stransky-Heilkron, N., Dumoulin, M., Heinrich-Balard, L., Rivory, P., Morfin, J.-F., Toth, E., Saraiva, M. J., Allémann, E., Tillement, O., Forge, V., Lux, F. & Marquette, C. Multimodal imaging Gd-nanoparticles functionalized with Pittsburgh compound B or a nanobody for amyloid plaques targeting. *Nanomed.* **12,** 1675–1687 (2017).
157. Stöber, W., Fink, A. & Bohn, E. Controlled growth of monodisperse silica spheres in the micron size range. *J. Colloid Interface Sci.* **26,** 62–69 (1968).
158. Osterholtz, F. D. & Pohl, E. R. Kinetics of the hydrolysis and condensation of organofunctional alkoxysilanes: a review. *J. Adhes. Sci. Technol.* **6,** 127–149 (1992).
159. Hench, L. L. & West, J. K. The sol-gel process. *Chem. Rev.* **90,** 33–72 (1990).
160. Yokoi, T., Sakamoto, Y., Terasaki, O., Kubota, Y., Okubo, T. & Tatsumi, T. Periodic arrangement of silica nanospheres assisted by amino acids. *J. Am. Chem. Soc.* **128,** 13664–13665 (2006).
161. Rahman, I. A., Vejayakumaran, P., Sipaut, C. S., Ismail, J., Bakar, M. A., Adnan, R. & Chee, C. K. An optimized sol–gel synthesis of stable primary equivalent silica particles. *Colloids Surf. Physicochem. Eng. Asp.* **294,** 102–110 (2007).

162. Hartlen, K. D., Athanasopoulos, A. P. T. & Kitaev, V. Facile Preparation of Highly Monodisperse Small Silica Spheres (15 to >200 nm) Suitable for Colloidal Templating and Formation of Ordered Arrays. *Langmuir* **24,** 1714–1720 (2008).
163. Bradbury, M., Wiesner, U., Medina, O. P., Burns, A., Lewis, J., Larson, S. & Quinn, T. Multimodal silica-based nanoparticles. (2014). at <https://www.google.com/patents/US20140248210>
164. Benezra, M., Phillips, E., Overholtzer, M., Zanzonico, P. B., Tuominen, E., Wiesner, U. & Bradbury, M. S. Ultrasmall Integrin-Targeted Silica Nanoparticles Modulate Signaling Events and Cellular Processes in a Concentration-Dependent Manner. *Small* **11,** 1721–1732 (2015).
165. Yoo, B., Ma, K., Zhang, L., Burns, A., Sequeira, S., Mellinghoff, I., Brennan, C., Wiesner, U. & Bradbury, M. S. Ultrasmall dual-modality silica nanoparticle drug conjugates: Design, synthesis, and characterization. *Bioorg. Med. Chem.* **23,** 7119–7130 (2015).
166. Bradbury, M. S., Pauliah, M., Zanzonico, P., Wiesner, U. & Patel, S. Intraoperative mapping of sentinel lymph node metastases using a clinically translated ultrasmall silica nanoparticle: SLN mapping using ultrasmall fluorescent silica particles. *Wiley Interdiscip. Rev. Nanomed. Nanobiotechnol.* **8,** 535–553 (2016).
167. Ma, K., Mendoza, C., Hanson, M., Werner-Zwanziger, U., Zwanziger, J. & Wiesner, U. Control of Ultrasmall Sub-10 nm Ligand-Functionalized Fluorescent Core–Shell Silica Nanoparticle Growth in Water. *Chem. Mater.* **27,** 4119–4133 (2015).
168. Murray, E., Born, P., Weber, A. & Kraus, T. Robust, ultrasmall organosilica nanoparticles without silica shells. *J. Nanoparticle Res.* **16,** (2014).
169. Martini, M., Perriat, P., Montagna, M., Pansu, R., Julien, C., Tillement, O. & Roux, S. How Gold Particles Suppress Concentration Quenching of Fluorophores Encapsulated in Silica Beads. *J. Phys. Chem. C* **113,** 17669–17677 (2009).
170. Martini, M., Roux, S., Montagna, M., Pansu, R., Julien, C., Tillement, O. & Perriat, P. How gold inclusions increase the rate of fluorescein energy homotransfer in silica beads. *Chem. Phys. Lett.* **490,** 72–75 (2010).
171. Wiesner, U. & Ma, K. Mesoporous oxide nanoparticles and methods of making and using same. (2015). at <https://www.google.com/patents/WO2013192609A1?cl=en>
172. Bazzi, R., Flores, M. ., Louis, C., Lebbou, K., Zhang, W., Dujardin, C., Roux, S., Mercier, B., Ledoux, G., Bernstein, E., Perriat, P. & Tillement, O. Synthesis and properties of europium-based phosphors on the nanometer scale: Eu2O3, Gd2O3:Eu, and Y2O3:Eu. *J. Colloid Interface Sci.* **273,** 191–197 (2004).
173. Truillet, C., Lux, F., Tillement, O., Dugourd, P. & Antoine, R. Coupling of HPLC with Electrospray Ionization Mass Spectrometry for Studying the Aging of Ultrasmall Multifunctional Gadolinium-Based Silica Nanoparticles. *Anal. Chem.* **85,** 10440–10447 (2013).
174. Mignot, A. A top-down synthesis route to ultrasmall multifunctional Gd-based silica nanoparticles for theranostic applications. (University of Claude Bernard Lyon I, 2012).
175. Thomas, E. Développement d'une seconde génération de nanoparticules AGuIX pour des applications théranostiques en oncologie. (University of Claude Bernard Lyon I, 2017).
176. Marais, A. *Etude des propriétés structurales et de la dégradation de nanoparticules de type AGuIX®*. (University of Claude Bernard Lyon I, 2014).
177. Arkles, B., Steinmetz, J. R., Zazyczny, J. & Mehta, P. Factors contributing to the stability of alkoxysilanes in aqueous solution. *J. Adhes. Sci. Technol.* **6,** 193–206 (1992).
178. Etienne, M. Analytical investigation of the chemical reactivity and stability of aminopropyl-grafted silica in aqueous medium. *Talanta* **59,** 1173–1188 (2003).
179. Asenath Smith, E. & Chen, W. How To Prevent the Loss of Surface Functionality Derived from Aminosilanes. *Langmuir* **24,** 12405–12409 (2008).
180. Putnam, C. D., Hammel, M., Hura, G. L. & Tainer, J. A. X-ray solution scattering (SAXS) combined with crystallography and computation: defining accurate macromolecular structures, conformations and assemblies in solution. *Q. Rev. Biophys.* **40,** (2007).
181. Svergun, D. I. & Koch, M. H. J. Small-angle scattering studies of biological macromolecules in solution. *Rep. Prog. Phys.* **66,** 1735 (2003).
182. Patterson, J. P., Robin, M. P., Chassenieux, C., Colombani, O. & O'Reilly, R. K. The analysis of solution self-assembled polymeric nanomaterials. *Chem. Soc. Rev.* **43,** 2412 (2014).
183. Durand, E., Clemancey, M., Quoineaud, A.-A., Verstraete, J., Espinat, D. & Lancelin, J.-M. ^{1}H Diffusion-Ordered Spectroscopy (DOSY) Nuclear Magnetic Resonance (NMR) as a Powerful Tool for the Analysis of Hydrocarbon Mixtures and Asphaltenes. *Energy Fuels* **22,** 2604–2610 (2008).
184. Balci, M. *Basic 1H- and 13C-NMR Spectroscopy*. (Elsevier Science, 2005).
185. Keire, D. A. & Kobayashi, M. NMR Studies of the Metal-Loading Kinetics and Acid−Base Chemistry of DOTA and Butylamide-DOTA. *Bioconjug. Chem.* **10,** 454–463 (1999).
186. Stejskal, E. O. & Tanner, J. E. Spin Diffusion Measurements: Spin Echoes in the Presence of a Time-Dependent Field Gradient. *J. Chem. Phys.* **42,** 288–292 (1965).
187. Claridge, T. D. W. *High-Resolution NMR Techniques in Organic Chemistry*. (Elsevier Ltd., 2009).

188. Lehman, S. E., Tataurova, Y., Mueller, P. S., Mariappan, S. V. S. & Larsen, S. C. Ligand Characterization of Covalently Functionalized Mesoporous Silica Nanoparticles: An NMR Toolbox Approach. *J. Phys. Chem. C* **118,** 29943–29951 (2014).
189. Brambilla, R., Poisson, J., Radtke, C., Miranda, M. S. L., Cardoso, M. B., Butler, I. S. & dos Santos, J. H. Z. Sol–gel preparation of aminopropyl-silica-magnesia hybrid materials. *J. Sol-Gel Sci. Technol.* **59,** 135–144 (2011).
190. Bernhard, C., Moreau, M., Lhenry, D., Goze, C., Boschetti, F., Rousselin, Y., Brunotte, F. & Denat, F. DOTAGA-Anhydride: A Valuable Building Block for the Preparation of DOTA-Like Chelating Agents. *Chem. - Eur. J.* **18,** 7834–7841 (2012).
191. Chernushevich, I. V., Loboda, A. V. & Thomson, B. A. An introduction to quadrupole-time-of-flight mass spectrometry. *J. Mass Spectrom.* **36,** 849–865 (2001).
192. Bruker Daltonik. micrOTOF-Q II User Manual. (2007).
193. Gross, J. H. *Mass Spectrometry a textbook*. (Springer-Verlag, 2011).
194. Hagen, J. J. & Monnig, C. A. Method for estimating molecular mass from electrospray spectra. *Anal. Chem.* **66,** 1877–1883 (1994).
195. Arkles, B., Pan, Y., Larson, G. L. & Singh, M. Enhanced Hydrolytic Stability of Siliceous Surfaces Modified with Pendant Dipodal Silanes. *Chem. - Eur. J.* **20,** 9442–9450 (2014).
196. Zhu, M., Lerum, M. Z. & Chen, W. How To Prepare Reproducible, Homogeneous, and Hydrolytically Stable Aminosilane-Derived Layers on Silica. *Langmuir* **28,** 416–423 (2012).
197. Ashley, C. E. *et al.* The targeted delivery of multicomponent cargos to cancer cells by nanoporous particle-supported lipid bilayers. *Nat Mater* **10,** 389–397 (2011).
198. Stuart, B. *Infrared Spectroscopy: Fundamentals and Applications*. (John Wiley & Sons, Ltd, 2004). at <10.1002/0470011149>
199. Jokanović, V., Dramićanin, M. D. & Andrić, Ž. Nanodesigning of SiO2: Eu3+Particles Obtained by Spray Pyrolysis Method and Their Luminescence Properties. *Acta Chim Slov* **53,** 23–28 (2006).
200. Ma, L., Chen, L., Wen, J., Wang, Q. & Tan, C. Eu3+ chelate with phenanthroline derivative gives selective emission responses to Cu(II) ions. *J. Organomet. Chem.* **696,** 829–831 (2011).
201. Giraud, L., Nadarajah, R., Matar, Y., Bazin, G., Sun, J., Zhu, X. X. & Giasson, S. Amino-functionalized monolayers covalently grafted to silica-based substrates as a robust primer anchorage in aqueous media. *Appl. Surf. Sci.* **370,** 476–485 (2016).
202. Sagliano, N., Floyd, T. R., Hartwick, R. A., Dibussolo, J. M. & Miller, N. T. Studies on the stabilization of reversed phases for liquid chromatography. *J. Chromatogr. A* **443,** 155–172 (1988).
203. Miller, N. T. & DiBussolo, J. M. Studies on the stability of n-alkyl-bonded silica gels under basic pH conditions. *J. Chromatogr. A* **499,** 317–332 (1990).
204. Kirkland, J. J. Development of some stationary phases for reversed-phase HPLC. *J. Chromatogr. A* **1060,** 9–21 (2004).
205. Drahoš, B., Kubíček, V., Bonnet, C. S., Hermann, P., Lukeš, I. & Tóth, É. Dissociation kinetics of Mn2+ complexes of NOTA and DOTA. *Dalton Trans.* **40,** 1945 (2011).
206. Mei, B. C., Oh, E., Susumu, K., Farrell, D., Mountziaris, T. J. & Mattoussi, H. Effects of Ligand Coordination Number and Surface Curvature on the Stability of Gold Nanoparticles in Aqueous Solutions. *Langmuir* **25,** 10604–10611 (2009).
207. Brinker, C. J. Hydrolysis and condensation of silicates: Effects on structure. *Glas. Glass Ceram. Gels* **100,** 31–50 (1988).
208. Wadas, T. J., Wong, E. H., Weisman, G. R. & Anderson, C. J. Coordinating Radiometals of Copper, Gallium, Indium, Yttrium, and Zirconium for PET and SPECT Imaging of Disease. *Chem. Rev.* **110,** 2858–2902 (2010).
209. Atsumi, H., Yoshimoto, K., Saito, S., Ohkuma, M., Maeda, M. & Nagasaki, Y. Luminescence-based colorimetric discrimination of single-nucleotide transversions by the combined use of the derivatives of DOTA-conjugated naphthyridine and its terbium complex. *Tetrahedron Lett.* **50,** 2177–2180 (2009).
210. Detappe, A., Thomas, E., Tibbitt, M. W., Kunjachan, S., Zavidij, O., Parnandi, N., Reznichenko, E., Lux, F., Tillement, O. & Berbeco, R. Ultrasmall Silica-Based Bismuth Gadolinium Nanoparticles for Dual Magnetic Resonance–Computed Tomography Image Guided Radiation Therapy. *Nano Lett.* **17,** 1733–1740 (2017).
211. Plissonneau, M. Vectorisation de nanoparticules d'imagerie multimodale a base de gadolinium p our un ciblage actif des plaques amyloıdes et de cellules hepatocytes. (University of Claude Bernard Lyon I, 2015).
212. Csajbók, É., Baranyai, Z., Bányai, I., Brücher, E., Király, R., Müller-Fahrnow, A., Platzek, J., Radüchel, B. & Schäfer, M. Equilibrium, ^{1}H and ^{13}C NMR Spectroscopy, and X-ray Diffraction Studies on the Complexes Bi(DOTA)$^{-}$ and Bi(DO3A-Bu). *Inorg. Chem.* **42,** 2342–2349 (2003).
213. Moutiez, E., Prognon, P., Mahuzier, G., Bourrinet, P., Zehaf, S. & Dencausse, A. Time-resolved Luminescence as a Novel Detection Mode for the Simultaneous High-performance Liquid Chromatographic Determination of Gadolinium–DOTA and Gd3+. *Analyst* **122,** 1347–1352 (1997).

214. Boselli, L., Polo, E., Castagnola, V. & Dawson, K. A. Regimes of Biomolecular Ultrasmall Nanoparticle Interactions. *Angew. Chem. Int. Ed.* **56,** 4215–4218 (2017).
215. Kopp, M., Kollenda, S. & Epple, M. Nanoparticle–Protein Interactions: Therapeutic Approaches and Supramolecular Chemistry. *Acc. Chem. Res.* **50,** 1383–1390 (2017).
216. Giardiello, M., Botta, M. & Lowe, M. P. Synthesis of lanthanide(III) complexes appended with a diphenylphosphinamide and their interaction with human serum albumin. *J. Incl. Phenom. Macrocycl. Chem.* **71,** 435–444 (2011).
217. Vandesquille, M., Li, T., Po, C., Ganneau, C., Lenormand, P., Dudeffant, C., Czech, C., Grueninger, F., Duyckaerts, C., Delatour, B., Dhenain, M., Lafaye, P. & Bay, S. Chemically-defined camelid antibody bioconjugate for the magnetic resonance imaging of Alzheimer's disease. *mAbs* **9,** 1016–1027 (2017).
218. Ke, N. & Abassi, Y. Focus Application-Compound induced cytotoxicity with XCELLigence. at <https://aceabio.com/wp-content/uploads/Compound-Mediated-Cytotoxicity-Using-xCELLigence-to-Optimize-Endpoint-Viability-and-Cytotoxicity-Assays.pdf>
219. Raatschen, H.-J., Fu, Y., Shames, D. M., Wendland, M. F. & Brasch, R. C. Magnetic resonance imaging enhancement of normal tissues and tumors using macromolecular Gd-based cascade polymer contrast agents: preclinical evaluations. *Invest. Radiol.* **41,** 860–867 (2006).
220. Jensen, K. J., Shelton, P. T. & Pedersen, S. L. *Peptide Synthesis and Applications*. (Humana Press, 2013).
221. Ciccione, J., Jia, T., Coll, J.-L., Parra, K., Amblard, M., Jebors, S., Martinez, J., Mehdi, A. & Subra, G. Unambiguous and Controlled One-Pot Synthesis of Multifunctional Silica Nanoparticles. *Chem. Mater.* **28,** 885–889 (2016).
222. Bevilacqua, A., Gelb, R. I., Hebard, W. B. & Zompa, L. J. Equilibrium and thermodynamic study of the aqueous complexation of 1, 4, 7-triazacyclononane-N, N', N"-triacetic acid with protons, alkaline-earth-metal cations, and copper (II). *Inorg. Chem.* **26,** 2699–2706 (1987).
223. Prasanphanich, A. F., Nanda, P. K., Rold, T. L., Ma, L., Lewis, M. R., Garrison, J. C., Hoffman, T. J., Sieckman, G. L., Figueroa, S. D. & Smith, C. J. [64Cu-NOTA-8-Aoc-BBN (7-14) NH2] targeting vector for positron-emission tomography imaging of gastrin-releasing peptide receptor-expressing tissues. *Proc. Natl. Acad. Sci.* **104,** 12462–12467 (2007).
224. Zhang, Y., Hong, H., Engle, J. W., Bean, J., Yang, Y., Leigh, B. R., Barnhart, T. E. & Cai, W. Positron Emission Tomography Imaging of CD105 Expression with a 64Cu-Labeled Monoclonal Antibody: NOTA Is Superior to DOTA. *PLoS ONE* **6,** e28005 (2011).
225. Ghosh, S. C., Pinkston, K. L., Robinson, H., Harvey, B. R., Wilganowski, N., Gore, K., Sevick-Muraca, E. M. & Azhdarinia, A. Comparison of DOTA and NODAGA as chelators for 64Cu-labeled immunoconjugates. *Nucl. Med. Biol.* **42,** 177–183 (2015).
226. Lux, J., White, A. G., Chan, M., Anderson, C. J. & Almutairi, A. Nanogels from Metal-Chelating Crosslinkers as Versatile Platforms Applied to Copper-64 PET Imaging of Tumors and Metastases. *Theranostics* **5,** 277–288 (2015).
227. Yang, X., Shi, C., Tong, R., Qian, W., Zhau, H. E., Wang, R., Zhu, G., Cheng, J., Yang, V. W., Cheng, T., Henary, M., Strekowski, L. & Chung, L. W. K. Near IR Heptamethine Cyanine Dye-Mediated Cancer Imaging. *Clin. Cancer Res.* **16,** 2833–2844 (2010).
228. Yang, X., Shao, C., Wang, R., Chu, C.-Y., Hu, P., Master, V., Osunkoya, A. O., Kim, H. L., Zhau, H. E. & Chung, L. W. K. Optical Imaging of Kidney Cancer with Novel Near Infrared Heptamethine Carbocyanine Fluorescent Dyes. *J. Urol.* **189,** 702–710 (2013).
229. Shi, C., Wu, J. B., Chu, G. C., Li, Q., Wang, R., Zhang, C., Zhang, Y., Kim, H. L., Wang, J., Zhau, H. E. & others. Heptamethine carbocyanine dye-mediated near-infrared imaging of canine and human cancers through the HIF-1α/OATPs signaling axis. *Oncotarget* **5,** 10114 (2014).
230. Wu, J. B., Shao, C., Li, X., Shi, C., Li, Q., Hu, P., Chen, Y.-T., Dou, X., Sahu, D., Li, W., Harada, H., Zhang, Y., Wang, R., Zhau, H. E. & Chung, L. W. K. Near-infrared fluorescence imaging of cancer mediated by tumor hypoxia and HIF1α/OATPs signaling axis. *Biomaterials* **35,** 8175–8185 (2014).
231. Wu, J. B., Lin, T.-P., Gallagher, J. D., Kushal, S., Chung, L. W. K., Zhau, H. E., Olenyuk, B. Z. & Shih, J. C. Monoamine Oxidase A Inhibitor–Near-Infrared Dye Conjugate Reduces Prostate Tumor Growth. *J. Am. Chem. Soc.* **137,** 2366–2374 (2015).
232. Wu, J. B., Shi, C., Chu, G. C.-Y., Xu, Q., Zhang, Y., Li, Q., Yu, J. S., Zhau, H. E. & Chung, L. W. K. Near-infrared fluorescence heptamethine carbocyanine dyes mediate imaging and targeted drug delivery for human brain tumor. *Biomaterials* **67,** 1–10 (2015).
233. Hermanson, G. *Bioconjugate Techniques*. (Elsevier Inc., 2013).
234. Mathieu, C. *Développement de nanoparticules ultrafines pour le ciblage de l'angiogenèse en oncologie*. (University of Claude Bernard Lyon I, 2017).
235. Theocharis, A. D., Skandalis, S. S., Tzanakakis, G. N. & Karamanos, N. K. Proteoglycans in health and disease: novel roles for proteoglycans in malignancy and their pharmacological targeting: Proteoglycans as potential pharmacological targets. *FEBS J.* **277,** 3904–3923 (2010).
236. Iozzo, R. V. & Schaefer, L. Proteoglycan form and function: A comprehensive nomenclature of proteoglycans. *Matrix Biol.* **42,** 11–55 (2015).

237. Nelson, D. L. & Cox, M. M. in *Lehninger Principles of Biochemistry* (W. H. Freeman and Company, 2013).
238. Giraud, I., Rapp, M., Maurizis, J.-C. & Madelmont, J.-C. Application to a Cartilage Targeting Strategy: Synthesis and in Vivo Biodistribution of 14C-Labeled Quaternary Ammonium- Glucosamine Conjugates. *Bioconjug. Chem.* **11,** 212–218 (2000).
239. Maurizis, J.-C., Rapp, M., Nicolas, C., Ollier, M., Verny, M. & Madelmont, J.-C. Disposition in Rats of N-Pyridinium-propyl-cyclam, N-Triethylammonium-propyl-cyclam, andN-[Triethylammonium]-3-propyl-[15] ane-N5, Potential Cartilage Imaging Agents. *Drug Metab. Dispos.* **28,** 418–422 (2000).
240. Vidal, A., Gaumet, V., Galmier, M.-J., Besse, S., Leal, F., Gachon, F., Viot, G., Métin, J., Chezal, J.-M., Miot-Noirault, E. & Auzeloux, P. Development of a freeze-dried kit formulation for the preparation of 99mTc-NTP 15-5, a radiotracer for scintigraphic imaging of proteoglycans. *Appl. Radiat. Isot.* **101,** 1–9 (2015).
241. Peyrode, C., Weber, V., David, E., Vidal, A., Auzeloux, P., Communal, Y., Dauplat, M. M., Besse, S., Gouin, F., Heymann, D., Chezal, J. M., Rédini, F. & Miot-Noirault, E. Quaternary ammonium-melphalan conjugate for anticancer therapy of chondrosarcoma: in vitro and in vivo preclinical studies. *Invest. New Drugs* **30,** 1782–1790 (2012).
242. Angelini, A., Guerra, G., Mavrogenis, A. F., Pala, E., Picci, P. & Ruggieri, P. Clinical outcome of central conventional chondrosarcoma: Central Conventional Chondrosarcoma. *J. Surg. Oncol.* **106,** 929–937 (2012).
243. Peyrode, C., Weber, V., Voissière, A., Maisonial-Besset, A., Vidal, A., Auzeloux, P., Gaumet, V., Borel, M., Dauplat, M.-M., Quintana, M., Degoul, F., Rédini, F., Chezal, J.-M. & Miot-Noirault, E. Proteoglycans as Target for an Innovative Therapeutic Approach in Chondrosarcoma: Preclinical Proof of Concept. *Mol. Cancer Ther.* **15,** 2575 (2016).
244. Salis, A., Boström, M., Medda, L., Cugia, F., Barse, B., Parsons, D. F., Ninham, B. W. & Monduzzi, M. Measurements and Theoretical Interpretation of Points of Zero Charge/Potential of BSA Protein. *Langmuir* **27,** 11597–11604 (2011).
245. Salgin, S., Salgin, U. & Bahadir, S. Zeta potentials and isoelectric points of biomolecules: the effects of ion types and ionic strengths. *Int J Electrochem Sci* **7,** 12404–12414 (2012).
246. Lincheneau, C., Leonard, J. P., McCabe, T. & Gunnlaugsson, T. Lanthanide directed self-assembly formations of Tb(iii) and Eu(iii) luminescent complexes from tryptophan based pyridyl amide ligands. *Chem. Commun.* **47,** 7119 (2011).
247. Johnstone, T. C., Suntharalingam, K. & Lippard, S. J. The Next Generation of Platinum Drugs: Targeted Pt(II) Agents, Nanoparticle Delivery, and Pt(IV) Prodrugs. *Chem. Rev.* **116,** 3436–3486 (2016).
248. McKeuge, M. J. in *Platinum-Based Drugs in Cancer Therapy* 251–276 (Humana Press, 2000).
249. Bhargava, A. & Vaishampayan, U. N. Satraplatin: leading the new generation of oral platinum agents. *Expert Opin. Investig. Drugs* **18,** 1787–1797 (2009).
250. Pichler, V., Göschl, S., Schreiber-Brynzak, E., Jakupec, M. A., Galanski, M. & Keppler, B. K. Influence of reducing agents on the cytotoxic activity of platinum(IV) complexes: induction of G $_2$ /M arrest, apoptosis and oxidative stress in A2780 and cisplatin resistant A2780cis cell lines. *Metallomics* **7,** 1078–1090 (2015).
251. Rocca, J. D., Werner, M. E., Kramer, S. A., Huxford-Phillips, R. C., Sukumar, R., Cummings, N. D., Vivero-Escoto, J. L., Wang, A. Z. & Lin, W. Polysilsesquioxane nanoparticles for triggered release of cisplatin and effective cancer chemoradiotherapy. *Nanomedicine Nanotechnol. Biol. Med.* **11,** 31–38 (2015).
252. Ravera, M., Gabano, E., Zanellato, I., Perin, E., Arrais, A. & Osella, D. Functionalized nonporous silica nanoparticles as carriers for Pt(IV) anticancer prodrugs. *Dalton Trans* (2016). doi:10.1039/C6DT03133A
253. Harrison, R. C., McAuliffe, C. A. & Zaki, A. M. An efficient route for the preparation of highly soluble platinum (II) antitumour agents. *Inorganica Chim. Acta* **46,** L15–L16 (1980).
254. Azure, M. T., Sastry, K. S. R., Archer, R. D., Howell, R. W. & Rao, D. V. *Microscale synthesis of carboplatin labeled with the Auger emitter platinum-193m: Radiotoxicity versus chemotoxicity of the antitumor drug in mammalian cells*. (American Inst of Physics, Inc, 1992).
255. Varbanov, H. P., Valiahdi, S. M., Kowol, C. R., Jakupec, M. A., Galanski, M. & Keppler, B. K. Novel tetracarboxylatoplatinum(iv) complexes as carboplatin prodrugs. *Dalton Trans.* **41,** 14404 (2012).
256. Ramos, Y., Hernández, C., Fernandez, L. A., Bataller, M., Veliz, E. & Small, R. Optimization of a HPLC procedure for simultaneous determination of cisplatin and the complex cis, cis, trans-diamminedichlorodihydroxoplatinum (IV) in aqueous solutions. *Quím. Nova* **34,** 1450–1454 (2011).
257. Golla, E. D. & Ayres®, G. H. Spectrophotometric determination of platinum with o-phenylenediamine. *Talanta* **20,** 199–210 (1973).
258. Basotra, M., Singh, S. K. & Gulati, M. Development and Validation of a Simple and Sensitive Spectrometric Method for Estimation of Cisplatin Hydrochloride in Tablet Dosage Forms: Application to Dissolution Studies. *ISRN Anal. Chem.* **2013,** 1–8 (2013).

RÉSUMÉ

Les nanoparticules (NPs) hybrides peuvent combiner les propriétés physiques uniques des éléments inorganiques pour des applications en imagerie et en thérapeutique avec la biocompatibilité des structures organiques. Cependant, leur utilisation en médecine est encore limitée par des risques potentiels de toxicité à long terme. Dans ce contexte, des NPs hybrides ultrafines pouvant être éliminées rapidement par la voie rénale apparaissent comme de bonnes candidates pour la nanomédicine. La NP à base de silice contenant des chélates du gadolinium appelée AGuIX (Activation et Guidage de l'Irradiation par rayon-X) a été développée avec un diamètre hydrodynamique de moins de 5 nm qui lui permet d'être éliminée rapidement via l'urine après injection intraveineuse. Cette NP s'est révélée être une sonde efficace en imagerie multimodale et un amplificateur local en radiothérapie pour le diagnostic et le traitement du cancer. Elle est en train d'être évaluée dans un essai clinique de phase I par radiothérapie des métastases cérébrales (NANO-RAD, NCT02820454). Néanmoins, la synthèse d'AGuIX est un procédé multi-étapes qui est difficilement modulable.

Ce manuscrit rapporte, pour la première fois, le développement d'un protocole « one-pot » direct pour des nanoparticules de silice ultrafines (USNP) contenant des chélateurs complexés ou non à partir des précurseurs silanes chélatants moléculaires. Dans ce nouveau protocole, la taille des particules et les types des métaux chélatés peuvent être contrôlés facilement. Certaines des propriétés chimiques des USNP ont été clarifiées davantage pendant ce travail exploratoire. Les particules élaborées ont été caractérisées par différentes techniques analytiques complémentaires. Ces nouvelles nanoparticules USNPs présentent des caractéristiques similaires aux AGuIX en terms de propriétes biologiques et de biodistribution.

Dans un second temps, un nouveau protocole de fonctionnalisation d'USNP par des précurseurs silanes chélatants a été développé. Ces chélatants libres fonctionnalisés sur la particule peuvent être alors utilisés afin de complexer des radiométaux pour l'imagerie bimodale. Enfin, d'autres stratégies de fonctionnalisation sont aussi décrites. La nouvelle sonde (17VTh031) combinant un petit chélateur cyclique (NODA) et un fluorophore proche-infrarouge tumeur ciblant (IR783) ainsi que le pyridinium quaternaire ont été greffés sur l'AGuIX pour créer une nouvelle sonde en imagerie multimodale et cibler des tumeurs chondrosarcomes respectivement.

Mots-clés : *nanoparticule de silice ultrafine, cancer, sonde en imagerie multimodale, radiosensibilisateur*